Contribution to the Decentralized Energy Management of Autonomous AC-Microgrid

Hassan Moussa

UNIVERSITÉ DE LORRAINE
École Doctorale “Informatique Automatique Électronique-Électrotechnique Mathématiques”
Département de Formation Doctorale “Électronique-Électrotechnique”

THÈSE

Présentée à
L’UNIVERSITÉ DE LORRAINE
En vue de l’obtention du
DOCTORAT DE L’UNIVERSITÉ DE LORRAINE
Spécialité: Génie Électrique
Par:

Hassan MOUSSA

Contribution to the Decentralized Energy Management of Autonomous AC-Microgrid

Soutenue publiquement le 07/07/2017 devant un jury composé de :

Président	Manuela SECHILARIU	Professeur-UTC
Rapporteurs	Eric MONMASSON	Professeur-Université de Cergy-P.
	Seddik BACHA	Professeur-Université de Grenoble
Examinateur	Xuefang Lin-Shi	Professeur-INSA-Lyon
Invité	Nazih MOUBAYED	Professeur-Université Libanaise
Directeur de thèse	Serge PIERFEDERICI	Professeur-Université de Lorraine
Encadrant de thèse	Jean-Philippe MARTIN	MdC-Université de Lorraine

Laboratoire GREEN (Groupe de Recherche en Electrotechnique et Electronique de Nancy) Ecole Nationale Supérieure d’Electricité et de Méchanique-Université de Lorraine 2, avenue de la Forêt de Haye 54516 Vandoeuvre-Lès-Nancy Cedex

Thèse réalisée au Laboratoire GREEN
Pôle, Université de Lorraine
2, avenue de la Forêt de Haye
54518 Vandoeuvre-Lès-Nancy Cedex

Tél : +33 3 83 59 56 54
Fax : +33 3 83 59 56 53

Web : http://green.univ-lorraine.fr/

Sous la direction de Serge Pierfederici serge.pierfederici@univ-lorraine.fr

Co-encadrement Jean-Philippe Martin jean-philippe.martin@univ-lorraine.fr

Financement This project has been funded with support of the European Commission and laboratory GREEN.

Résumé en Français

De par le monde, l'utilisation d'énergie conventionnelle est confrontée aux problèmes d'épuisement progressif des ressources en combustibles fossiles, à une mauvaise efficacité énergétique et une pollution environnementale importante. Ces problèmes ont conduit à une nouvelle tendance visant à transformer localement l'énergie de sources non conventionnelles/renouvelables en énergie électrique et l'intégrer dans un réseau de distribution électrique. Parmi ces sources d'énergie conventionnelles, on peut trouver le biogaz, l'énergie éolienne, l'énergie hydrauliques, l'énergie photovoltaïques, les piles à combustible à travers l'hydrogène, la production combinée de chaleur, la cogénération et les moteurs Stirling. Ce type de production d'électricité est qualifié de génération décentralisée (DG) et les sources d'énergie sont désignées comme des ressources énergétiques distribuées (DER). Le terme "Génération décentralisée" (DG) a été conçu pour distinguer ce concept de la génération centralisée. Un micro-réseau est un réseau de distribution électrique actif conçu pour fournir l'énergie électrique à un regroupement d'habitation et/ou d'industrie de petite taille, comme par exemple un lotissement urbain ou suburbain, une zone universitaire, un quartier commerçant, un site industriel, etc... Un micro-réseau doit permettre l'intégration des DER et des consommateurs locaux. Il peut être connecté à d'autres réseaux électriques ou fonctionner en mode îloté pour garantir un niveau de fiabilité élevée. Ainsi, le développement récent des micro-réseaux dans la distribution locale d'électricité nécessite d'importantes études par rapport aux problématiques suivantes :

- Amélioration de l'efficacité énergétique impliquant des changements technologiques,
- Amélioration des systèmes de stockage d'énergie,
- Amélioration de la fiabilité globale et de la disponibilité du réseau,
- Intégration accrue de ressources d'énergie distribuée,
- Amélioration de qualité d'énergie,
- Alimentation des lois de gestion décentralisée de l'énergie.

Cette thèse a été réalisée au "Groupe de Recherche en Électronique et Électrotechnique de Nancy" (GREEN) de Université de lorraine - Nancy, France. Le principal objectif porte sur l'amélioration des lois de gestion d'énergie décentralisées dans des micro-réseaux AC îlotés. L'interconnexion des DER à un micro-réseau électrique AC s'effectue généralement en utilisant des convertisseurs d'interface distribué (DIC), réalisé autour d'onduleurs de

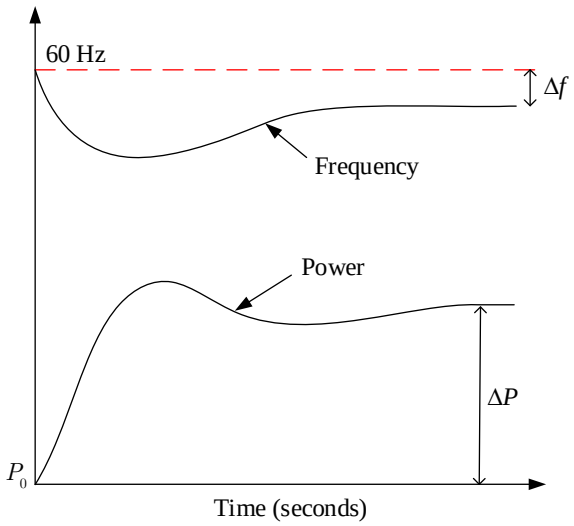

FIGURE 1 : Réponse transitoire d'un générateur synchrone.

tension (VSI) à base de composant d'électronique de puissance, associé à un module de contrôle. La thèse commence par un état de l'art des différentes lois de contrôle décentralisées. Le principe général porte sur les fonctions de statisme de type "Droop Control" permettant d'équilibrer la distribution de puissance entre les différentes sources reliées au micro-réseau et les différentes charges. Ceci garanti une flexibilité élevée du système et un fonctionnement optimal. L'idée principale associée aux lois de contrôle décentralisées s'inspire du comportement d'un générateur synchrone. Lors d'une modification du point de fonctionnement de la source ou de la charge conduisant à une modification de la fréquence du réseau électrique, l'énergie stockée dans les générateurs synchrones est utilisée pour maintenir l'équilibre entre la production et la consommation par le biais de la décélération ou l'accélération de la vitesse de rotation des générateurs. La variation de la fréquence du système évolue proportionnellement à l'inertie totale du système. La Figure 1 illustre la réponse dynamique d'un générateur synchrone lors d'une augmentation de la puissance absorbée par la charge. L'augmentation de la charge $\triangle P$ génère une diminution de la fréquence électrique $\triangle f$ du réseau.

Le contrôleur interne de l'onduleur de tension (VSI) est conçu pour assurer les meilleures performances du système. L'architecture la plus généralement utilisée reste le contrôleur linéaire de type PI. Dans les applications industrielles, le régulateur PI présente l'avantage d'être mis en œuvre aussi bien de manière analogique que numérique. Cependant, en présence de fortes non linéarités, les performances en régulation sont réduites. Dans ce cas, il est préférable de mettre en œuvre des contrôleurs non linéaires. De nombreux algorithmes sont présents dans la littérature. Suite à des travaux antérieurs réalisés au le laboratoire GREEN, des contrôleurs basés sur les propriétés de platitude ont été adaptés pour le contrôle d'un onduleur DC/AC avec filtre LC en sortie. Ceci formant la brique de base du contrôleur des DIC dans un micro-réseau. Les avantages d'un contrôle basée sur les propriétés de platitude sont :

- Lorsque le système est parfaitement connu, il est possible de contrôler le système en

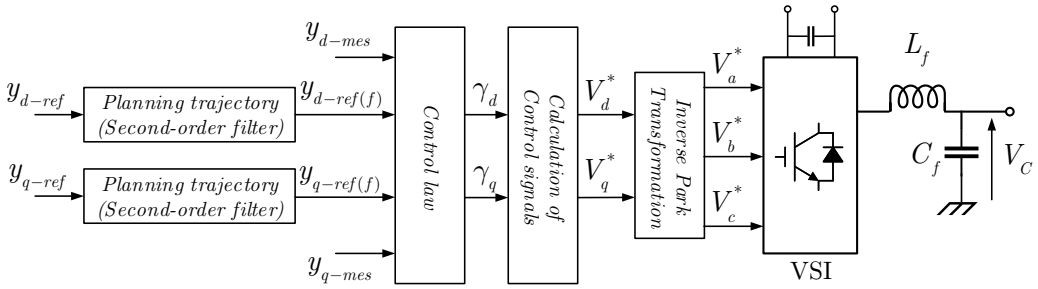

FIGURE 2 : Schéma fonctionnel de la commande basée sur la platitude.

boucle ouverte. Le correcteur ne sera là que pour compenser les erreurs de modélisation.

- La génération de trajectoire de référence permet de prendre en compte les contraintes physiques du système. Et ceci aussi bien pour le convertisseur statique que pour la source. Elle assure également un fonctionnement en toute sécurité notamment lors des séquences de démarrage et transitoires.

- Les contrôleurs par platitude utilisent les références au lieu de mesures dans les lois de commande. Ainsi, l'impact du bruit est limité.

- Pour un système plat, la linéarisation entrée-sortie n'entraîne pas de zéros dynamiques instables.

La figure 2 présente le schéma fonctionnel de la méthode de contrôle par platitude à une boucle. On peut noter que seuls les capteurs de tension sont utilisés pour la commande. Les capteurs de courant de charge peuvent être utilisées pour augmenter la dynamique de régulation lors de perturbations de la charge.

Pour présenter les avantages et l'efficacité de l'approche proposée, une modélisation du système et des simulations numériques ont été effectués lors de phases de démarrage et de régimes transitoires. Des résultats expérimentaux valident l'efficacité de la commande utilisée avec un taux de distorsion harmonique très faible de la tension de sortie. De plus, dans le but d'augmenter la puissance pouvant être transférée entre la source et le réseau, une mise en parallèle de convertisseur a été réalisée. La commande utilisée pour ce DIC est également basée sur les propriétés de platitude du système et garantie la répartition des puissances entre les différents onduleurs tout en minimisant le courant de circulation entre les convertisseurs. En effet, ceux-ci ne participent pas au transfert de puissance. La commande proposée permet également de réduire les effets transitoires lors de la déconnexion d'un onduleur. La partie suivante porte sur l'amélioration des algorithmes de type "droop". De nombreux travaux présent dans la littérature montrent que, pour des réseaux de nature inductif (réseau moyenne et haute tension), la chute de tension à travers les impédances de ligne influe sur la répartition de la puissance réactive entre différents convertisseurs. Une amélioration a donc été proposée pour assurer la répartition des puissances réactives, en fonction des puissances nominales de chaque DG. Cette amélioration est basée sur la chute de tension à travers l'impédance de ligne de chaque DG. Cette chute

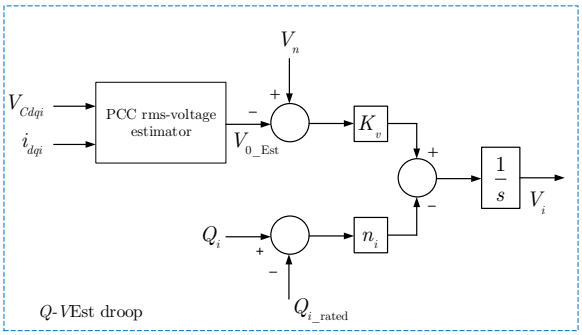

FIGURE 3 : Schéma du controleur $Q - VEst$.

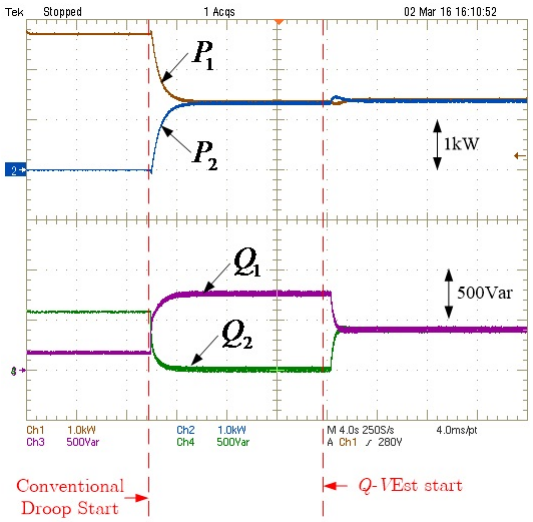

FIGURE 4 : Résultats expérimentaux : Répartition des puissances active et réactive entre deux DGs avant et après l'activation de l'algorithme proposé.

de tension est obtenue via la mise en place d'un estimateur d'état appliquée à l'estimation de la tension RMS au point de connexion (PCC). La modification de l'algorithme "droop" ($Q - VEst$) permet de contrôler la valeur de la tension au point de connexion à la tension nominale. Aucune communication n'est ajoutée entre les différents DG. Le schéma du contrôleur proposé est représenté sur la figure 3. Ce contrôleur est basé sur la définition de deux coefficients. Le premier (K_v) permet de définir la tension au point de connexion et le second (n_i) permet de prendre en compte la puissance nominale de chaque DG. Des résultats de simulation et des résultats expérimentaux montrent l'efficacité de l'algorithme "droop" proposée. La figure 4 présente des résultats expérimentaux obtenu sur un système avec deux générateurs. On observe que l'utilisation des algorithmes "droop" conventionnel ne permettent pas d'équilibré les puissances réactives des générateurs. Par contre, lorsque l'on met en œuvre l'algorithme $Q - VEst$ proposé, la puissance réactive est équilibrée entre les deux DG.

La connexion de charges non-linéaire sur le micro-réseau génère des harmoniques de tension. La réduction de ces harmoniques a été une des thématiques de cette thèse. Une

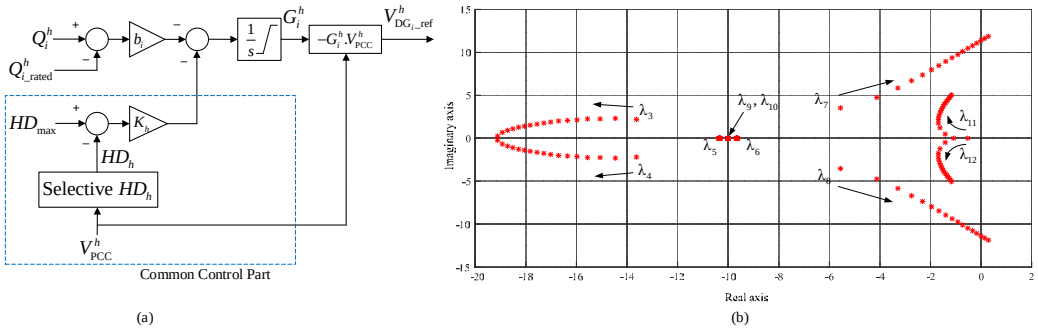

FIGURE 5 : Schéma du controleur harmonique droop.

modélisation a été effectuée pour représenter la génération d'harmonique. Une méthode permettant de réduire le THD tension et d'équilibrer la puissance harmonique entre chaque DG en fonction de leur puissance nominale a été mise au point. Le schéma du contrôleur proposé pour la prise en compte des harmoniques est représenté sur la figure 5. La prise en compte des puissances nominales pour chaque DG est considérée via le paramètre b_i. L'amplitude des harmoniques de tension au point de connexion est mesurée et transmise à chaque DG. Le taux de distorsion harmonique au point de connexion est pris en compte via le paramètre K_h. La définition de la tension de référence est obtenue par la multiplication de l'amplitude de la tension de chaque harmonique avec un gain positif non linéaire G_i^h obtenu à la sortie de l'intégrateur, comme présenté à gauche de la figure 5. Pour effectuer le dimensionnement de la valeur des différents coefficients de l'algorithme proposé, une étude de stabilité petit-signal a été effectuée. L'évolution des valeurs propres du système linéarisé sont représenté sur la figure 5b lorsque le coefficient b_i varie.

Des résultats de simulation et des résultats expérimentaux valident l'efficacité de la méthode proposée. Les figures 6 et 7 montrent les résultats expérimentaux obtenus pour un système avec deux générateurs, la charge non-linéaire étant réalisée via un redressement à diodes. La figure 6 illustre l'efficacité des algorithmes proposés pour équilibrer les puissances réactives harmoniques fournies par les DG. Pour ces essais, seul les harmoniques de tension de rang 5 et 7 sont considérés. Sur cette figure est également représenté l'évolution de la valeur d'un paramètre interne défini dans l'algorithme proposé. La figure 7 montre la réduction des harmoniques de tension de rang 5 et 7. En effet, l'amplitude de l'harmonique 5 passe de 1,85% à 0,6%, et l'amplitude de l'harmonique 7 passe de 1,37% à 0,34%. La THD global de la tension est ainsi réduit puisqu'il passe de 2.88% à 1.88%.

De par sa construction, l'utilisation des algorithmes "droop" classiques ne permettent pas de garantir la valeur de la fréquence et l'amplitude de la tension aux points de connexion à leur valeur nominale. Des boucles de restaurations doivent être ajoutées pour rétablir la fréquence et l'amplitude de la tension à leurs valeurs nominales. Dans les cas habituels, un système de communication est mis en place à cet effet. Des algorithmes supplémentaires sont nécessaires et la dynamique de ces boucles secondaires doit être prise en considération pour assurer la stabilité du système. Dans cette thèse, de nouveaux algorithmes de type "angle droop" sont proposés pour la gestion décentralisée d'énergie dans les micro-réseaux AC îlotés. La figure 8 propose une représentation du réseau considéré

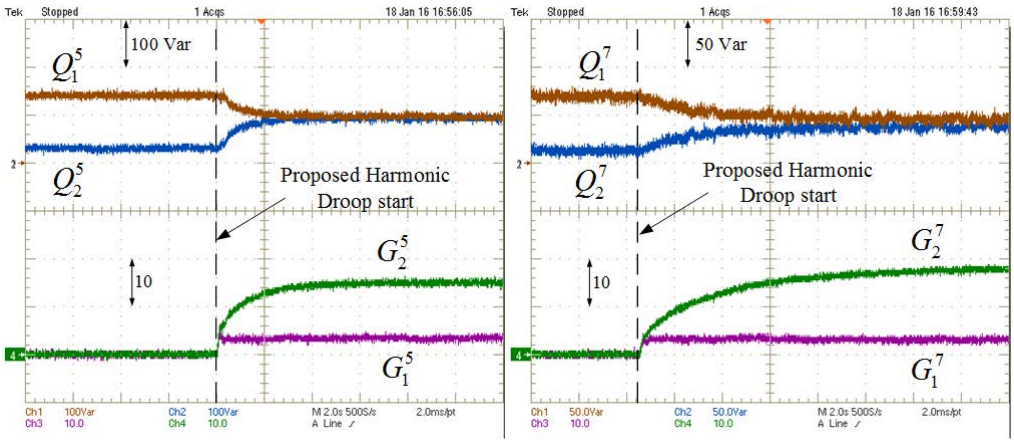

FIGURE 6 : Résultats expérimentaux : puissances réactives harmoniques de rang 5 et 7 fournies par les deux DG et évolution du gain interne.

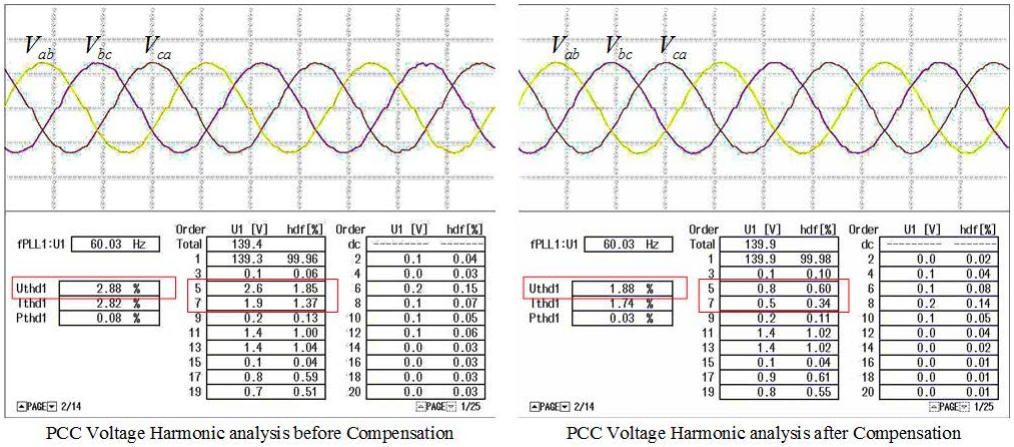

FIGURE 7 : Résultats expérimentaux : Tensions composés aux bornes du PCC avec analyse harmonique avant et après compensation.

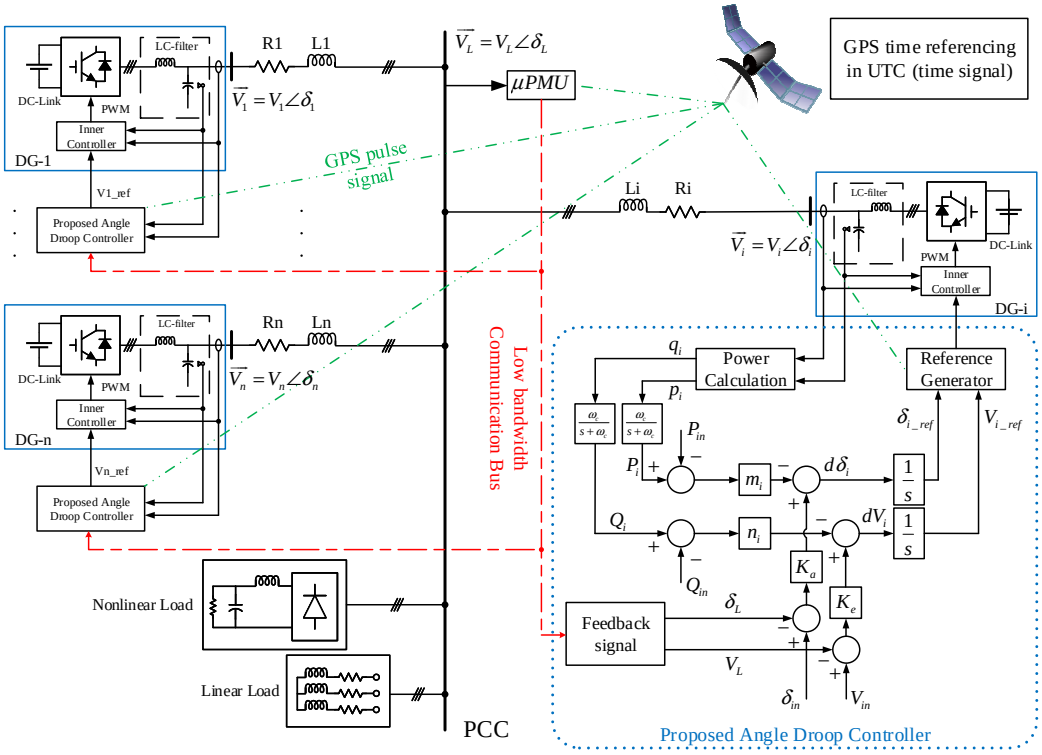

FIGURE 8 : Micro-réseaux avec schéma ensemble Angle s'affaisser contrôle proposé.

ainsi qu'une représentation schématique de ce nouveau controller. Par rapport au "droop" conventionnel, le contrôleur de type "angle droop" garanti la valeur de la fréquence du réseau, quel que soit le point de fonctionnement et une chute de tension limité au point de connexion. La boucle de restauration n'est donc plus nécessaire.

Cet algorithme nécessite l'utilisation de système permettant de mesurer la tension et la phase au point de connexion et transmettre ces valeurs à tous les DG. De plus, la synchronisation de tous les DG est réalisée à l'aide d'un signal GPS. Pour cela, un système de mesure de déphasage et d'amplitude de tension est nécessaire (µPMU : micro phasor measurement unit), une nouvelle technologie de mesure prometteuse pour le micro-réseaux AC, permet d'utiliser un signal de rétroaction par rapport à la phase et l'amplitude de la tension au point de connexion. Le schéma du contrôleur est présent sur la figure 8. La prise en compte des puissances nominales pour chaque DG est considérée via le paramètre m_i et n_i. Les signaux transmis par le µPMU sont comparés avec les valeurs nominales et introduit dans le contrôleur via les coefficients K_a et K_e. Un intégrateur est ajouté en sortie pour garantir une erreur nulle en régime permanent.

Le dimensionnement des paramètres du contrôle "angle droop" est réalisé grâce à une étude de stabilité petit signal. L'évolution des valeurs du système complet sont représentées sur la figure 9 lorsque les coefficients du contrôleur varient. Des résultats de simulation et des résultats expérimentaux valident l'efficacité de la méthode proposée ainsi que le dimensionnement des paramètres. La figure ci-dessous montre des résultats expérimentaux. Sur la figure 10a est représenté le partage de puissance active et réactive. Comme repré-

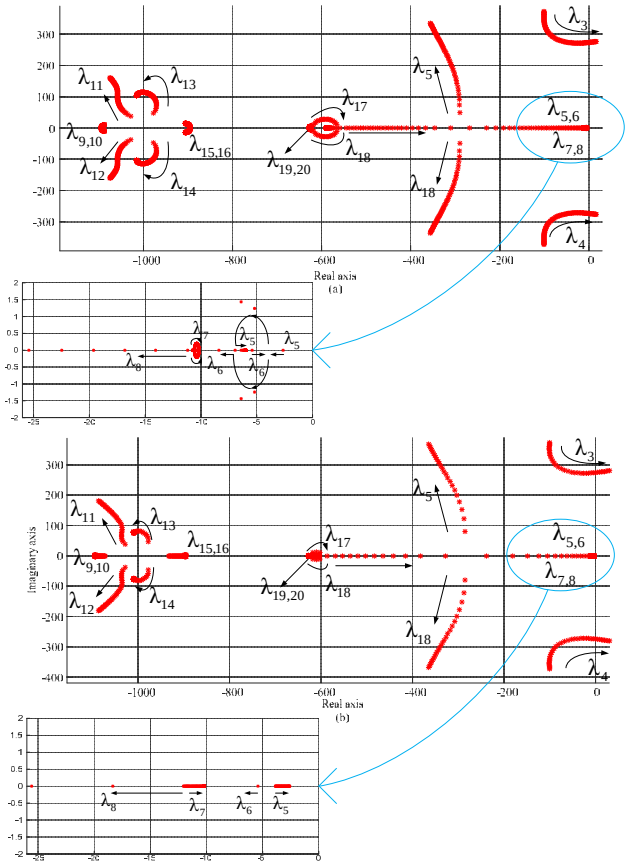

FIGURE 9 : Lieu des pôles pour différentes valeurs des coefficients du contrôleur "angle droop" proposé.

senté sur la figure, la méthode proposée permet d'équilibrer le partage des puissances à travers les différents DG. Les figures 10b et 10c représentent les formes d'onde de tension et de courant les deux DIC.

Les charges précédemment utilisées étaient constituées exclusivement de charges passives linéaires et non linéaires. Cependant, de plus en plus de charge contrôlées sont utilisées. Ces charges absorbent généralement une puissance constante. Associé à leur filtres d'entrées permettant de réduire les ondulations, les interactions dynamiques avec les générateurs peuvent engendrer des comportements instables conduisant à des oscillations de grandes amplitudes pouvant conduire à la destruction de plusieurs éléments du réseau. Pour pouvoir garantir la stabilité du réseau quelles que soit les perturbations extérieures, une étude de stabilité doit être réalisée. Dans de nombreux travaux présents dans la littérature, l'analyse de stabilité est réalisée via une approche petit-signal, obtenue par linéarisation du système autour d'un point de fonctionnement. Cette approche considère de très faible variation autour d'un point de fonctionnement. Elle ne permet pas de garantir le comportement lors de grande variations de la charge ou de la source. Pour une analyse complète, l'utilisation de méthode d'analyse large signal est nécessaire. Dans cette thèse, l'impact de l'intégration massive des charges à puissance constante est considéré via une étude de stabilité. Une étude de sensibilité associée à une analyse petit

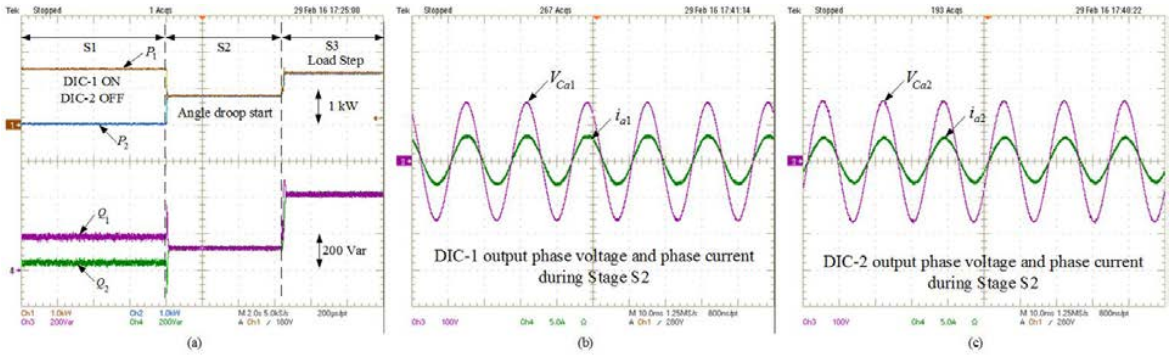

FIGURE 10 : Résultats expérimentaux : (a) Puissances active et réactive entre deux DG ; (b-c) Tension et courant pour chaque DIC-1 et DIC-2.

signal a permis de montrer que la dynamique du droop peut être négligé par rapport à la dynamique de la boucle de contrôle interne. Dans ce cadre, un modèle simplifié a pu être défini pour appréhender l'impact de la variation des différentes charges. Ce modèle simplifié a été représenté par un multi-modèle de type Tagaki-Sugeno. Cette représentation génère $2k$ modèle linéaires associés via des fonction d'appartenances, avec k le nombre de non linéarités dans le modèle. L'utilisation d'une fonction de Lyapunov et sa condition de convergence associée permet de définir des inéquations matricielles linéaires. L'existence de solution garanti la stabilité large signal du système. Une estimation du bassin d'attraction est définie en fonction de l'amplitude des non-linéarités autour d'un point d'équilibre. Ce bassin d'attraction permet de garantir que pour toutes perturbation à l'intérieur du bassin, le système reviendra sur le point d'équilibre initial. Ces outils ont été appliqués pour notre micro-réseau comportant deux DG et plusieurs charges de nature différentes. On a considéré des charges résistives, des charges absorbant un courant constant et des charges absorbant une puissance constante. Le tracé de l'estimation d'un bassin d'attraction dans le cas ou uniquement la charge résistive varie est présenté sur la figure 11. Cette figure montre que lorsque la puissance absorbée par la charge résistive diminue, le bassin d'attraction estimé est également réduit. Ceci montre que le délestage massif de charges résistives peut conduire à un comportement instable d'un réseau comportant des charges à puissance constante. De plus, l'impact de l'utilisation d'inductance virtuelle dans les algorithmes droop a également été analysé. Ces éléments virtuels permettent de répartir les puissances proportionnellement entre les différentes sources. Sur la figure 12 est tracé le bassin d'attraction estimé pour différentes valeurs de l'inductance virtuel. Celle-ci montre l'impact négatif de l'inductance virtuelle sur la stabilité du réseau électrique possédant des charges à puissance constante.

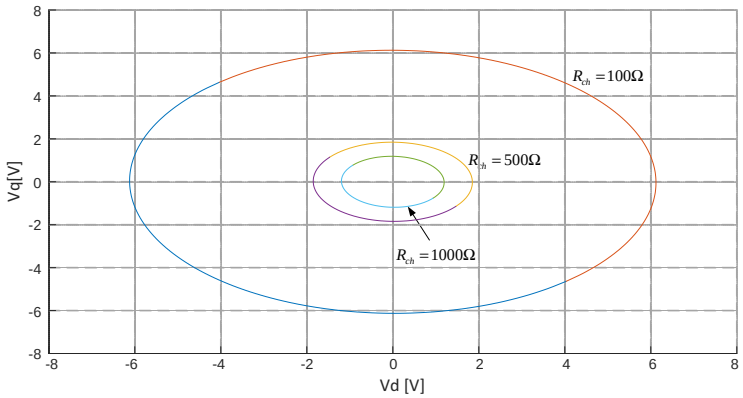

FIGURE 11 : Bassin d'attraction estimé pour le système sous l'effet de la charge résistive.

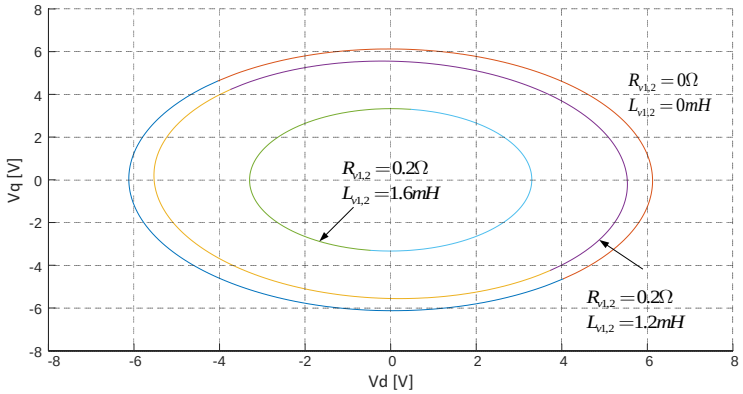

FIGURE 12 : Effet de l'inductance virtuelle L_v sur le bassin estimé de la stabilité asymptotique.

Abstract

This thesis deals with islanded AC microgrid that allows any integration of Distributed Energy Resources (DERs) that may provide their existing supply energy in a controlled manner to insure overall system functioning. The interconnection of a DER to a microgrid is done usually by using a Distributed Interface Converter (DIC), a general power electronics interface block, which consists of a source input converter module, a Voltage Source Inverter module (VSI), an output interface module, and the controller module. The thesis realizes several control laws based on decentralized methods. The major focus is on the Droop functions that are responsible for providing a power distribution balance between different Energy Resources connected to a microgrid. The aim is to insure system stability and better dynamic performance when sharing the power between different DGs as function to their nominal power. Developing a closed loop stability analysis is useful for studying system dynamics in order to obtain a desired transient response that allows identifying the proper loop control parameters. Power Quality enhancement in microgrids is also a purpose of this research. The reduction of harmonic distortions of the output voltage when supplying linear and non-linear loads are taken in consideration in this thesis. Further aspects will be studied about how to deal with constant power loads connected to the grid and the large perturbations exerted. This results to further research studies that deal with large-signal stability of microgrids.

Keywords: AC Microgrid, Distributed Interface Converter (DIC), Decentralized control, Droop method, Power Quality, Total Harmonic Distortion (THD), System stability.

Acknowledgments

The work presented in this report was carried out at "Groupe de Recherche en Electronique et Electrotechnique de Nancy" (GREEN) Laboratory, Lorraine University, Nancy-France. Acknowledgments are given to these institutes, as well as the Erasmus Mundus Program for their financial support during the four year's Ph.D. study.

This project was finished under supervision of Prof. Serge PIERFEDERICI, and Associate Prof. Jean-Philippe MARTIN. I would like to express my deepest appreciation to my supervisor Prof. Serge PIERFEDERICI, for his professional and constructive guidance, inspiration and trust. It is my greatest honor to work with him and I do believe his earnestness and dedication to work will consistent encourage me in my future life. I also would like to give my sincere appreciation to my co-supervisor, Associate Prof. Jean-Philippe MARTIN, for his patient suggestions, continuous encouragement and support during my Ph.D. period.

I also have the honor and pleasure to thank all the members of the Jury:

- Manuela SECHILARIU, Professor at the University of Technology of Compiègne (UTC), for presiding over this jury and accepting to be one of my examiners. I really appreciated her great interest in our work, as well as the relevance of her questions on day of the defense.

- Eric MONMASSON, Professor at the University of Cergy-Pontoise, for agreeing to be one of my rapporteurs. I really like appreciates his great interest in our work.

- Seddik BACHA, Professor at the University of Grenoble, for accepting the heavy task of rapporteur. I really appreciated his very constructive remarks during the defense as well as his vast knowledge in this area.

- Xuefang LIN-SHI, Professor at the National Institute of Applied Sciences of Lyon (INSA-Lyon), to have participated in this jury as an examiner. I very much appreciated her look at our work and her valuable remarks.

- Nazih MOUBAYED, Professor at the Lebanese University, by agreeing to sit in this jury and for his valuable advice throughout my thesis.

I would like to thank the GREEN staff, researchers, secretaries and technicians for their friendships. I would also like to thank my dear friends, who encouraged and supported me throughout these four years. I extend the huge gratitude to my parents and my fiancee for their exceptional love and encouragement.

Finally, I would like to express my deepest appreciation to the one whom I really miss: My mother. My mother is the greatest reason that enlightened my path and led me the way till here. Unfortunately, after she drove me this far, she changed her path and went away. Unluckily I didn't have the chance neither to thank nor to express my grateful towards her. I would like to dedicate my work to her soul wishing her to be resting in peace and suffering from no pain anymore.

Contents

List of Figures

List of Tables

GENERAL INTRODUCTION

Around the world, conventional power system is facing the problems of gradual depletion of fossil fuel resources, poor energy efficiency and environmental pollution. These problems have led to a new trend of generating power locally at distribution voltage level by using non-conventional/renewable energy sources like natural gas, biogas, wind power, solar photovoltaic cells, fuel cells, combined heat and power (CHP) systems, microturbines, and Stirling engines and their integration into the utility distribution network. This type of power generation is termed as distributed generation (DG) and the energy sources are termed as distributed energy resources (DERs). The term 'Distributed Generation' has been devised to distinguish this concept of generation from centralized conventional generation. The distribution network becomes active with the integration of DG and hence is termed as active distribution network. Microgrids, an active distribution networks, are designed to supply power for its local area, such as a housing estate or a suburban locality, or an academic or public areas such as university or school, a commercial area, an industrial site. A microgrid can offer integration of DERs with local loads, which can operate in parallel with the grid or in an islanded mode to provide a customized level of high reliability and resistance to grid disturbances. Thus, the recent advantages of using microgrids in electricity production have open the door for urgent studies of this microgrids that are helpful to fulfill the maximization of the following issues:

1. Efficiency and demand trends involving technological changes.
2. Advanced energy storage systems.
3. Improving reliability of the system.
4. Increased integration of Distributed Generation Resources.
5. Power quality and system reliability.
6. Decentralized Power Management.

This PhD has been conducted in the "Groupe de Recherche en Électronique et Électrotechnique de Nancy" (GREEN) laboratory, part of Université de lorraine, Nancy, FRANCE. The main objective of this thesis is to solve problems and find improvements related to the control and power management of distributed generation (DG) systems based on microgrid application. The thesis deals with islanded AC microgrid which allows any integration of Distributed Energy Resources (DERs) that may provide their existing supply

energy in a controlled manner to insure overall system functioning. The interconnection of a DER to a microgrid is done usually by using a Distributed Interface Converter (DIC), a general power electronics interface block that constitutes of a source input converter module, a Voltage Source Inverter module (VSI), an output interface module, and the controller module. The thesis start a review of several control laws based on decentralized methods. The major focus is on the Droop functions that are responsible for providing a power distribution balance between different Energy Resources connected to a microgrid. Then, the Flatness-based method is realized by modeling and developing the control law for DC/AC inverter with output LC filter which is applicable for other DICs in a microgrid. Furthermore, the Flatness-based control (FBC) is implemented on parallel inverters system. The proposed control allows equal current sharing between parallel inverters with minimized circulating current. The droop control methods implemented through out this thesis aim to insure system stability and dynamic performance when sharing the power between different DGs as function to their nominal power. Developing a closed loop stability analysis can be useful for studying system dynamics in order to obtain a desired transient response that allows identifying the proper loop control parameters. Power Quality enhancement in microgrids is also a purpose of this research. The reduction of harmonic distortions of the output voltage when supplying linear and non-linear loads are taken into consideration in this thesis. Another target to be achieved, is the accuracy in power sharing when using several Droop Control laws. Off course, the power sharing accuracy is affected by mismatch in power lines and configurations. Further aspects will be studied about how to deal with the interaction of tightly regulated power converter loads, especially the constant power load, connected to the grid and the large perturbations they will exert. This gives rise to further research studies that deal with small-signal and large-signal stability analysis of microgrids before ending up with a general conclusion of the overall work and the future perspectives to follow after.

Chapter 1

STATE OF THE ART - POWER SHARING WITH INTERFACED CONVERTERS IN A MICROGRID

1.1 Introduction

Nowadays, Electricity Networks are in the era of major transition from stable passive distributed networks with unidirectional electricity transportation to active distributed networks with bidirectional electricity transportation. Distributed networks without Distributed Generators (DGs) are expected to be passive. Whereas, integration of different DG units to a distributed system leads to bidirectional flow of Power between source thus forming an active distributed network. Microgrids are small-scale Low Voltage (LV) active distributed networks that are produced from localized grouping of Distributed Energy Resources (DERs) and loads that normally operate connected and synchronized to the traditional centralized grid (main utility grid) or can disconnect and function alone as physical and/or economic conditions dictate. The supply sources may include reciprocating engine generator sets, microturbines, fuel cells, photovoltaic and other small-scale renewable generators, storage devices, and controllable end-use loads. All controlled sources and sinks are interconnected in a manner that enable devices to perform the microgrid control functions unnecessary for traditional DER. From operational point of view, many resources must be equipped with Distributed Generation Interfaced Converters (DICs) and controls to provide the required flexibility to ensure operation as a single aggregated system and to maintain the specified power quality and energy output.

To ensure the flexibility of the system, optimal operation, energy management and seamless transfer from one operational mode to another, microgrids require wide range of control. This control can be achieved by the Interfaced Converter Local Controllers (LCs) and a Central Controller (CC). This chapter focuses in the Local Control of those Interfaced converters. What are their main functions? How they coordinate with each other's?

1.2 Local Control of parallel Interfaced Converters in a Microgrid

In autonomous microgrid, usually a converter is integrated with a DC power source that represents a photovoltaic sources, energy storage systems, small wind generator, and others, a full bridge and LC filter [3], [4]. The full bridge converter, more specifically a Voltage Source Inverter (VSI), produces an AC output voltage from a DC source. This conversion is resulted from a fully controllable semiconductor power switches. The output LC filter is there to filter out undesired switching frequency components from the output current spectrum [5].

In the design point of view, the Local Control in microgrid aims to autonomously share the power between different Distributed Generators, they can independently control the active and the reactive power produced by the Interfaced Converters and to provide a control of its output voltage to ensure the overall stability and reliability of the microgrid. In this sense, the converter local controller will be addressed in details, and the several research studies applied recently are introduced here. The Local control can be decomposed into two different parts:

1) A Power Controller, that is responsible for setting a voltage magnitude and frequency (and hence phase angle) reference for the inverter output voltage according to certain characteristics to set the real and reactive powers.

2) An Inner Controller, which is designed to track the voltage reference and to reject high frequency disturbances.

Figure 1.1 shows a complete configuration of an Interfaced Converter with control blocks representing the Power Controller and Inverter Inner Control loop. Parallel Interfaced Converters have been locally controlled so as to deliver the desired power to the microgrid system. In this case, only local signals are used as feedback to control converters. In real microgrid, this topology is more practical since the distance between the converters would make communication difficult. Nowadays, all advanced Interfaced Converters are based on what is called “Plug and Play” feature that describes this matter. From Fig. 1.1, the local signals are identified by the line current i_L and capacitor voltage V_C.

1.2.1 Inner Controller: Flatness based Control

The Inner Controller of the VSI is designed to ensure better performance of the converter. So far, the most used technique stays the PI controller. In industrial applications, the PI controller is very well known and it presents advantages of being implemented both analogically or numerically [6, 7, 8, 9]. However, in the presence of strong nonlinear effects, their performance is below. Several interested applications have been reported in the control community, with the nonlinear theories being more attracted.

Following some previous work on the subject in the GREEN laboratory [10, 1, 11], it has been chosen to use the flatness property of the power converter to design their control. Indeed, the differential flatness theory has been proved to be very interesting

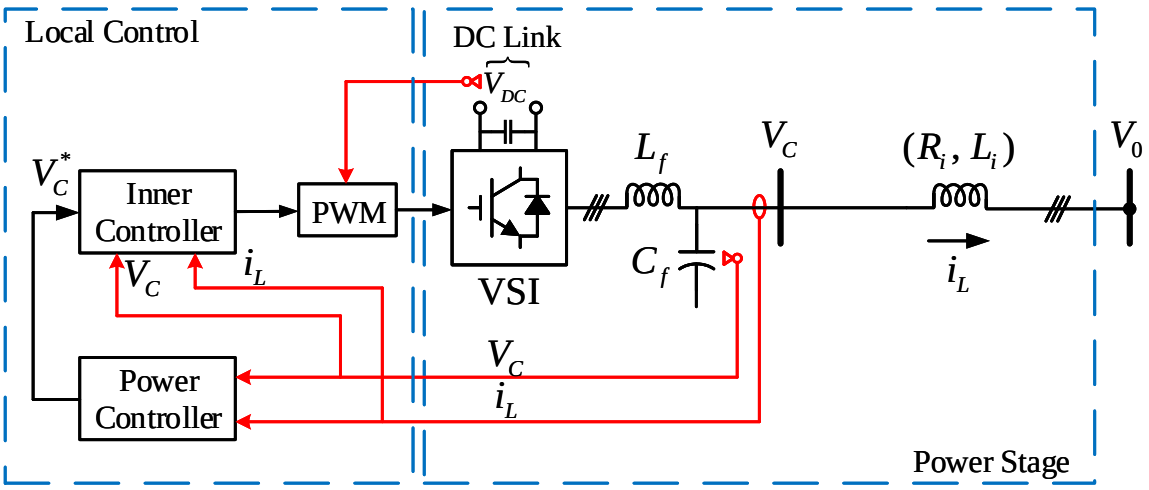

Figure 1.1: Interfaced Converter Control Block Diagram.

when applied on power converter control. In [1], the flatness-based control strategy is proposed for a three-phase inverter with an output LC filter. A comparison with two other control methods (PI, Feedback Linearization control-FL) shows that the proposed control allows obtaining a lowest voltage total harmonic distortion (THD), high dynamic performances, safety start up, and good robustness against parameter variations.

The concept of the flat system was introduced by *Fliess et al.* [12] using the formalism of differential algebra. In differential algebra, a system is considered to be differentially flat if a set of variables (flat output components) can be found such that all state variables and input components can be determined from these output components without any integration [12, 13]. More precisely, if the system has a state vector $x \in \Re^n$ and the input vector $u \in \Re^m$(n and m are two integers), then the system is considered to be differentially flat if and only if there exist an output $y \in \Re^m$, of dimension m, that can be found of the form

$$\begin{cases} y = & \phi(x, \dot{u}, \ddot{u}, \cdots, u^{(l)}) \\ x = & \varphi(y, \dot{y}, \cdots, y^{(r)}) \\ u = & \psi(y, \dot{y}, \cdots, y^{(r+1)}) \end{cases} \tag{1.1}$$

with rank(φ)=n, rank(ψ)=m, and rank(ϕ)=m. Where, l and r are the finite derivatives of input variable u and output y respectively.

One major property of differential flatness is that, due to (1.1), the state and the input variables can be directly expressed, without integrating any differential equation, in terms of the flat output and a finite number of its derivatives. Then, by imposing an adapted trajectory on the flat output, it can be guaranteed to control every variables of the system both in steady-state and during transients. Details on trajectory planning can be found in [14, 15]. For simplicity, it has been chosen to use a second order filter to generate the flat output reference trajectories. It allows to easily ensure the continuity conditions for the flat output and its first derivative. Advantages of the flatness-based control are underlined in [14]. Among them, some can be underlined:

- If the system is perfectly known, it offers possibility to control the system in open-loop. Regulation will only be there to compensate modeling errors.
- The use of feasible trajectory generation ensures every physical constraint respected at any time. It also ensures safe functioning especially during starting-sequences and transients.
- Flatness-based controllers use references instead of measurements in the command laws. Then, impact of the noise is limited.
- For flat systems, input-output linearization does not lead to any unstable dynamic zeroes.

Figure 1.2 shows the functional diagram of the one-loop Flatness based control method. It can be noted that the measure of the inductive filter currents is not useful to implement the control law. Only the capacitor voltage sensors are used for generating equations, while the load current sensors could be useful for increasing dynamics of Flatness Controller as regard to load perturbation. More details about the controller are introduced precisely in Chapter 2.

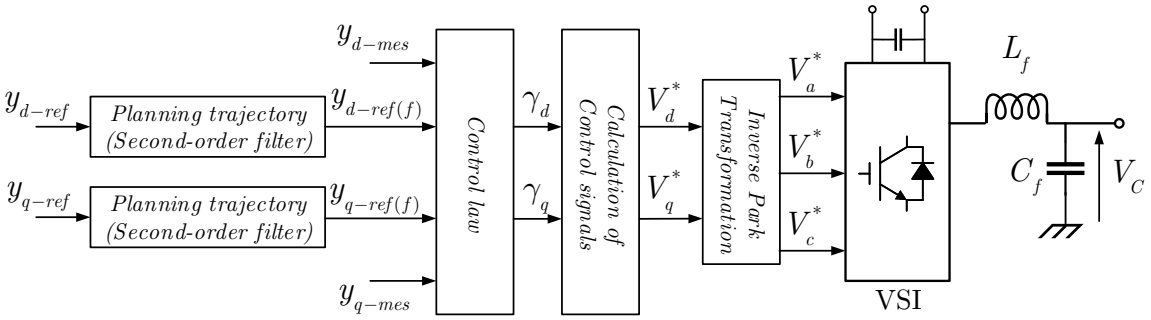

Figure 1.2: Flatness Control Functional Diagram.

1.2.2 Decentralized Power Controller

Usually, the external power control loop is based on Frequency Droop Control [16, 17, 18, 19, 20, 21, 22], also called autonomous or decentralized control. Its purpose is to share active and reactive power among Distributed Generator (DG) units using their local measurments to improve the system performance and reliability. The main idea behind Droop Control for DG Interfaced Converters (DICs) is taken from the behavior of synchronous generator. After the event leading to frequency deviation, a load power increase for example, the rotational energy stored in large synchronous machines is utilized to keep the balance between production and consumption through deceleration of the rotors. The system frequency will decrease at a rate mainly determined by the total inertia of the system. Fig. 1.3 shows the dynamic and static droop response of a synchronous generator describing this event. In this context, Droop control is proposed among DIC

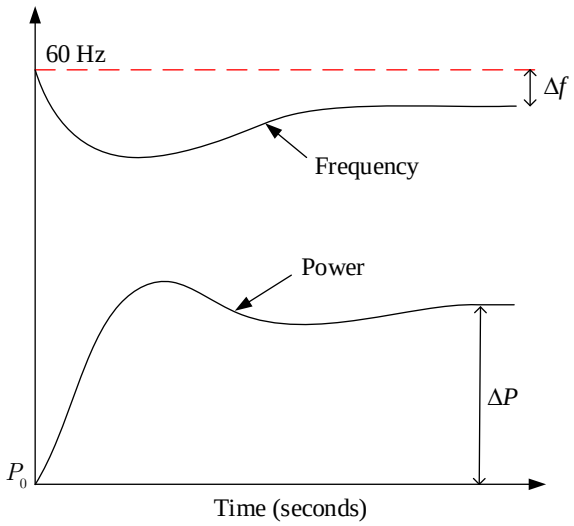

Figure 1.3: Synchronous Generator transient response.

modules to share the power autonomously to increase system performance. In this way, the frequency and amplitude of the output voltage must be fine-tuned in the control loop to obtain a desired power sharing.

1.2.2.1 Power Delivered to a Voltage Source

Figure 1.4 illustrates a voltage source which describes a distributed generator delivering power to the common bus modeled by a voltage source $v_0 = V_0\angle -\delta_0$ through an impedance $Z_i\angle\theta_i$. Where V_0 and V_i is the rms-value of the voltage sources. and Z_i is the impedance module. Since the current flowing through the terminal is written as

$$\bar{I} = \frac{V_i\angle\delta_i - V_0\angle 0^\circ}{Z_i\angle\theta_i} \tag{1.2}$$

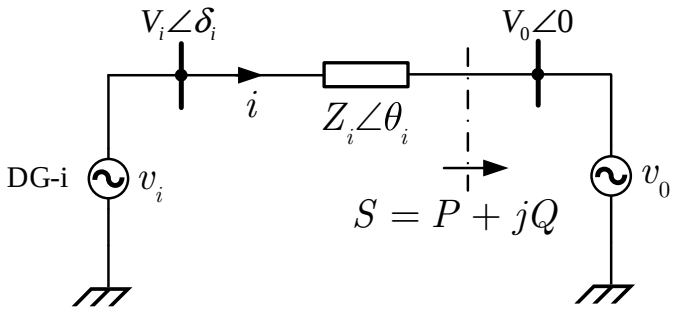

Figure 1.4: Distributed Generator Delivering power to infinite bus through impedance $\bar{Z}_i$.

The real and reactive power delivered by the source to the common bus terminal via the impedance can be obtained by

$$\begin{aligned} P &= \left(\frac{V_i V_0}{Z_i}\cos\delta_i - \frac{V_0^2}{Z_i}\right)\cos\theta_i + \frac{V_i V_0}{Z_i}\sin\delta_i \sin\theta_i \\ Q &= \left(\frac{V_i V_0}{Z_i}\cos\delta_i - \frac{V_0^2}{Z_i}\right)\sin\theta_i - \frac{V_i V_0}{Z_i}\sin\delta_i \cos\theta_i \end{aligned} \tag{1.3}$$

where δ_i is the phase difference between the supply and the terminal, often called the power angle. This demonstration reflects the situation when a distributed generator is connected in a microgrid via a feeder line to an infinite bus of terminal voltage v_0.

1.2.2.2 Conventional Droop Control

As shown in Fig. 1.4, the voltage-controlled inverter is modeled as an ideal voltage source v_i in series with a line impedance $Z_i \angle \theta_i$. For different types of line impedances, different droop control strategies can be obtained.

For purely Resistive Line impedance:

When the line impedance is purely resistive, $\theta_i = 0°$. Then

$$\begin{aligned} P &= \frac{V_i V_0}{Z_i}\cos\delta_i - \frac{V_0^2}{Z_i} \\ Q &= -\frac{V_i V_0}{Z_i}\sin\delta_i \end{aligned} \tag{1.4}$$

When δ_i is small,

$$\begin{aligned} P &\approx \frac{V_0}{Z_i}V_i - \frac{V_0^2}{Z_i} \\ Q &\approx -\frac{V_i V_0}{Z_i}\delta_i \end{aligned} \tag{1.5}$$

and roughly,

$$P \sim V \text{ and } Q \sim -\delta$$

where $\sim$ means in proportion to. Hence, the conventional droop control strategy takes the form

$$\begin{aligned} V_i &= V_n - n_i P_i \\ \omega_i &= \omega_n + m_i Q_i \end{aligned} \tag{1.6}$$

This strategy, consisting of $Q-\omega$ and $P-V$ droop [23, 24, 25], is illustrated in Fig. 1.5(a).

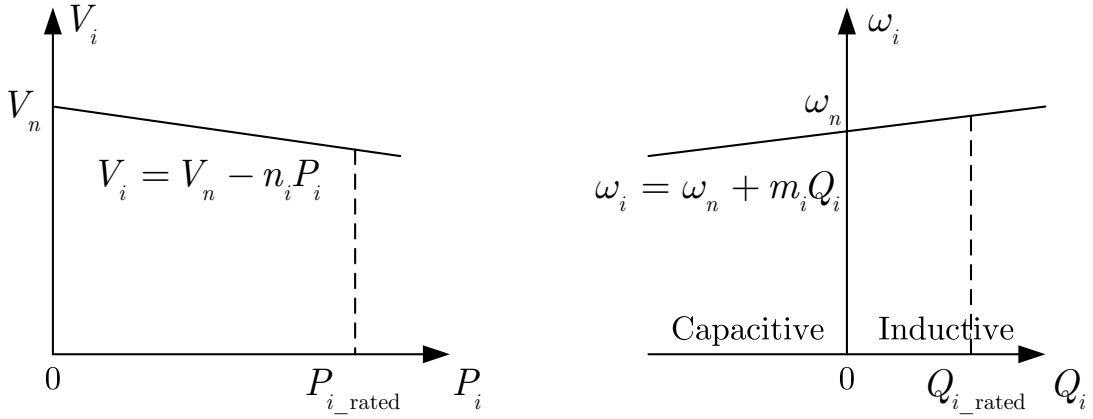

For Resistive Impedance
(a)

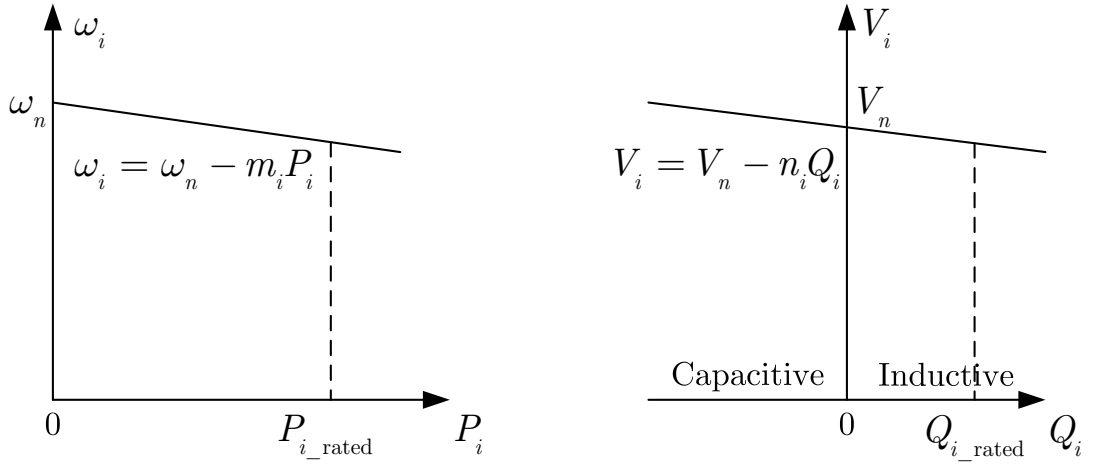

For Inductive Impedance
(b)

Figure 1.5: Droop Control Strategies.

For purely Inductive Line impedance:

When the line impedance is inductive, $\theta_i = 90°$. Then

$$\begin{aligned} P &= \frac{V_i V_0}{Z_i} \sin \delta_i \\ Q &= \frac{V_i V_0}{Z_i} \cos \delta_i - \frac{V_0^2}{Z_i} \end{aligned} \tag{1.7}$$

When δ_0 is small,

$$\begin{aligned} P &\approx \frac{V_i V_0}{Z_i} \delta_i \\ Q &\approx \frac{V_0}{Z_i} V_i - \frac{V_0^2}{Z_i} \end{aligned} \tag{1.8}$$

and roughly,

$$P \sim \delta \text{ and } Q \sim V$$

As a result, the conventional droop control strategy for inverters with inductive line impedance takes the form:

$$\begin{aligned} V_i &= V_n - n_i Q_i \\ \omega_i &= \omega_n - m_i P_i \end{aligned} \tag{1.9}$$

This strategy, consisting of the $Q - V$ and $P - \omega$ droop, is illustrated in Fig. 1.5(b).

To implement the Droop method, equation (1.9) is used, to generate a reference voltage based on the measured active and reactive power that are averaged and evaluated at fundamental frequency. This operation can be done by means of low-pass filters with a reduced bandwidth.

In electrical power transmission systems, the line impedance is mainly inductive ($\theta_i \approx 90°$), this is the reason why it is adopted to use $P - \omega$ and $Q - V$ slopes. Hence, the interfaced converter can inject desired active and reactive power to the grid, regulating the output voltage and responding to some linear load changes. Fig. 1.6 describes the Droop controller for one interfaced Converter where a similar structure is also used for others in a Microgrid.

1.2.2.3 Droop Control limitations

Droop Control methods are based on local measurements of the network state variables which make converters truly distributed. Such approach has desirable features such as high expandability, modularity and flexibility of the system as well as easy implementation without communication. However, the Droop Control has some limitations including:

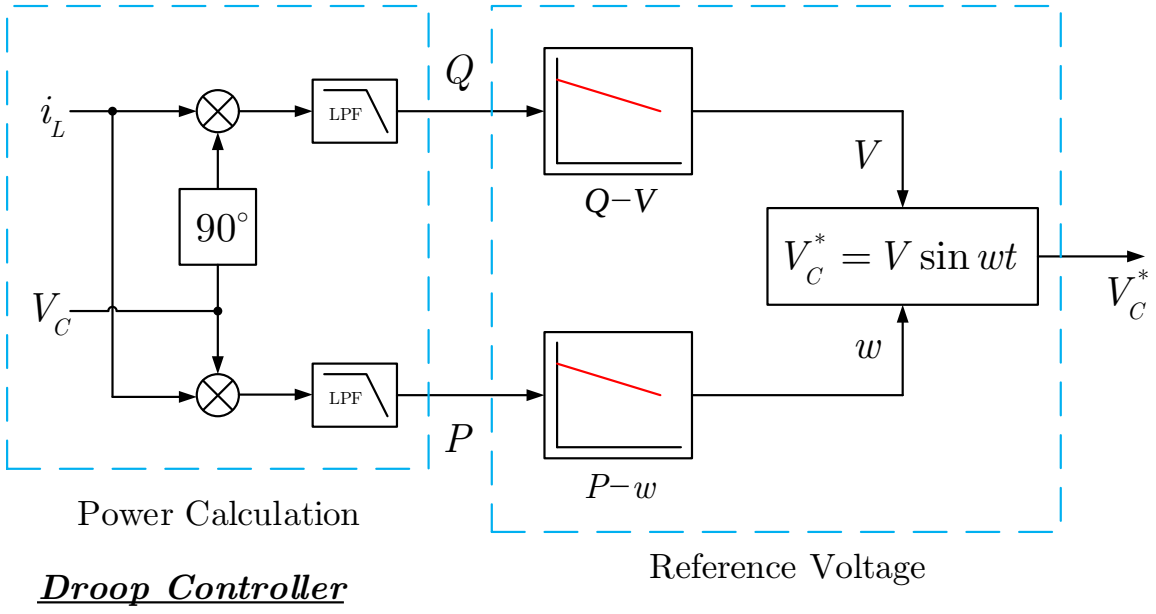

Figure 1.6: Droop Controller Block Diagram.

1. *Frequency and Amplitude deviations*: In Islanding mode, the voltage and frequency of the microgrid are load dependent. High droop gains (i.e.: steeper droop) ensure better load sharing. However, they result in large frequency and voltage deviations and can deteriorate the stability of the microgrid. An inherent tradeoff between the frequency and voltage regulation and power sharing accuracy exists. In practice, these deviations are acceptable if for instance, they are less 2% in frequency and 5% in amplitude.

2. *Slow dynamic response*: the dynamic response depends mainly on the droop parameters and the cutoff frequency of the low-pass filter, which should be carefully chosen in order not to interact with the inner control. On the other hand, the limitation of the droop parameter values will result in power variation, therefore the system dynamics response is not optimized and slow transient response may arise.

3. *Power Sharing is affected by physical parameters of the network*: The line impedances between the paralleled interfaced converters affect the power sharing performance. If the line impedance is mixed resistive and inductive, then the active and reactive power will be strongly coupled. When the line impedance mismatches between inverters and the common bus exist, there is possibility of circulating current among inverters.

4. *Poor Harmonic sharing*: The original droop control is designed only to share fundamental positive sequence component of the load power. The harmonic power sharing is not taken into account in the case of nonlinear load, which leads to harmonic circulating currents and poor power quality.

5. *Fluctuant and Changeable Output Power of DGs*: Another drawback of the original droop method appears in the poor performance with renewable energy resources because the output active power of micro-source is usually fluctuant and changeable.

1.3 Droop Control improvements and different structures

The Droop method has increasing widespread attention with the intensive study of microgrid decentralized control. The importance of the Droop control in microgrids led many researchers to work toward enhancing it and introducing different solutions to overcome all the mentioned limitations. These improved Droop methods fall into three categories: 1) Modified Droop Structure; 2) Virtual structure Droop; 3) Compensated Droop Control.

1.3.1 Modified Droop Structure

1.3.1.1 Complex Line Impedance-Based Droop Method

The impact of considering a complex line impedance can be solved by using the conventional droop method. In, [26], the authors propose a controller that can simplify and couple the active and reactive power relationships. Thus, the modified droop control method will be more convenient when the line resistance is similar to the reactance value (i.e. $R_i \approx X_i$) in Medium Voltage (MV) microgrids. In this case, the droop functions can be expressed as

$$\begin{cases} \omega = & \omega_n - m_P.(P - Q) \\ V = & V_n - n_Q.(P + Q) \end{cases} \tag{1.10}$$

The idea behind this control is that for a microgrid with complex line impedance, the active and reactive power both affect the voltage magnitude and frequency. The proposed droop control loop design is shown in Fig. 1.7. The controller can simplify the couple effect between active and reactive powers, offer good dynamic performance. However, it is more convenient only in particular cases when impedance resistance and inductance parts are similar.

1.3.1.2 Angle Droop Control

In further investigation of the droop concept, some researchers have proposed power-angle droop control, in which the voltage angle of each interfaced converter is set relative to a common timing reference [27, 28, 29]. Unlike the conventional $P - f$ and $Q - V$ droop control that indirectly control the angle by varying the frequency of the grid, the $P - \delta$ and $Q - V$ droop control directly drops the voltage magnitude and angle as:

$$\begin{aligned} \delta_i &= \delta_{i\_\text{rated}} - m_i \left(P_i - P_{i\_\text{rated}}\right) \\ V_i &= V_{i\_\text{rated}} - n_i \left(Q_i - Q_{i\_\text{rated}}\right) \end{aligned} \tag{1.11}$$

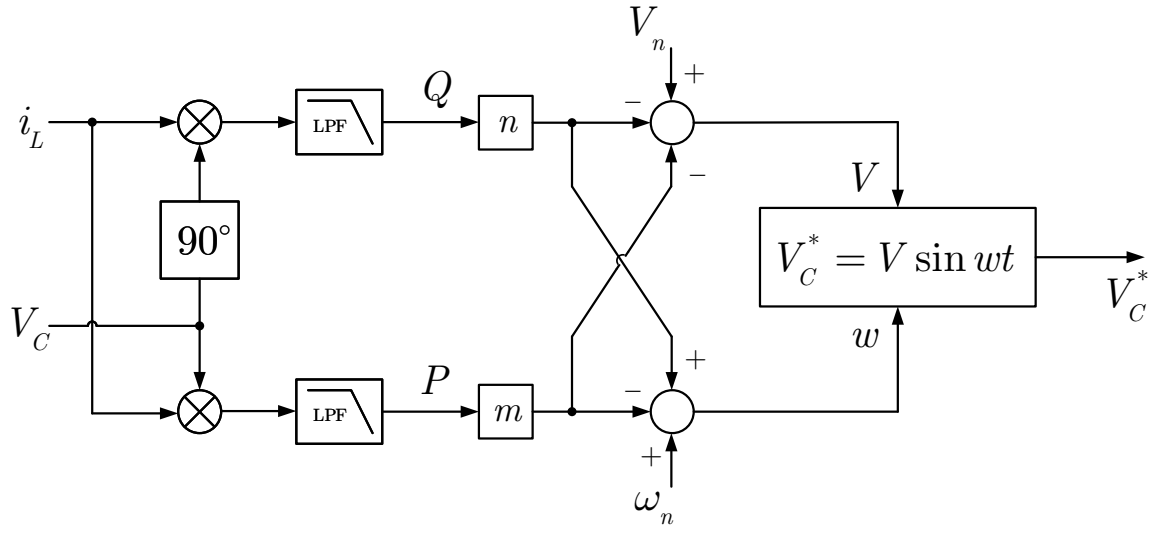

Figure 1.7: Droop Control for complex line impedance.

where δ_{i_rated} and V_{i_rated} are, respectively, the rated voltage angle and magnitude of DG_i. P_{i_rated} and Q_{i_rated} are the rated real and reactive power levels for DG_i. The coefficients m_i and n_i are selected to set the voltage angle and magnitude drop. These coefficients are chosen for different DGs to share the load in proportion to their rating at a desired drop ratio, i.e., $m_i = \triangle\delta/P_{i\_\text{rated}}$ and $n_i = \triangle V/Q_{i\_\text{rated}}$.

The angle droop is able to provide a load sharing among the DGs without a significant steady-state drop in system frequency and it has advantage as the maximum frequency variation restricts the choice of droop gain in case of conventional frequency droop. Moreover, no communication is needed between DGs, but only a time signal is needed to ensure the local control boards are synchronized to each other. Some authors suggest a controller area network bus or even a signal from global positioning system (GPS) to synchronize DGs. Similar to frequency droop, the error in proportional power sharing is due to line impedance mismatches. High droop gains will play a dominant role in alleviating power sharing error as presented in [29]. However, high droop gains have a negative impact on the overall stability of the system.

1.3.2 Virtual Structure Droop

1.3.2.1 Virtual Output Impedance Loop

In order to avoid the active and reactive power coupling (resistive-inductive lines), a typical and popular approach is based on virtual output impedance method [30, 31, 32, 33, 26]. This control method is implemented by including a fast control loop in the droop method, as shown in Fig. 1.8. As a result, the modified voltage reference can be expressed as

$$V_{ref} = V_C^* - Z_v(s).i_L \tag{1.12}$$

where $Z_v(s)$ is the virtual output impedance, V_C^* is the reference voltage given by the droop and V_{ref} is the modified reference voltage.

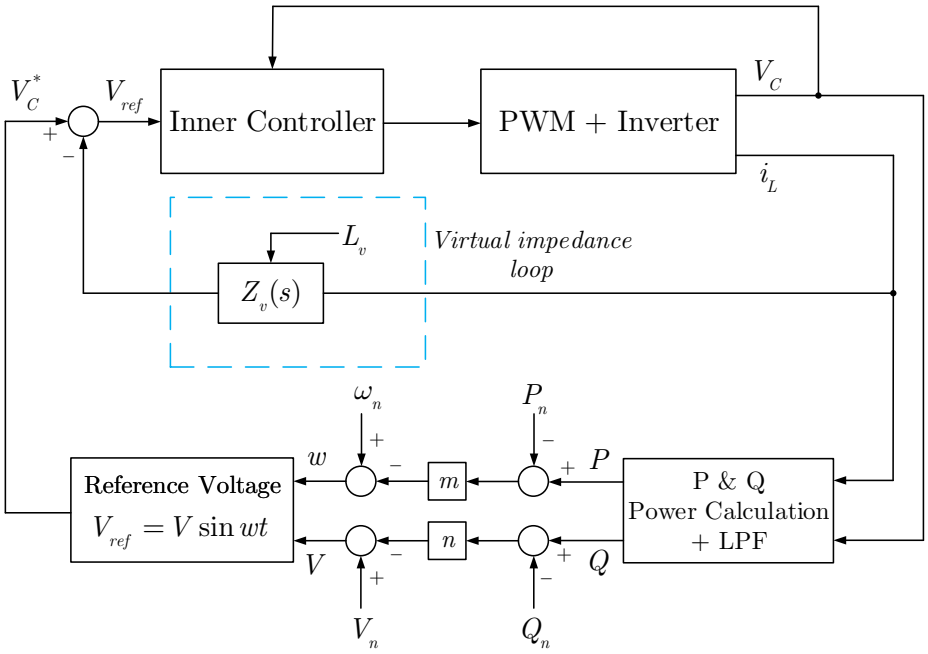

Figure 1.8: Droop Control overall scheme with virtual output impedance.

In general, the virtual impedance is used by emulating an inductive behavior to fix the output impedance of the inverter. The main objective is to insure an inductive line to allow active/reactive power decoupling and to validate the power flow equations used in droop control (1.9).

This can be achieved by drooping the output voltage proportionally to the derivative of the output current with respect to time, i.e. $Z_v(s) = sL_v$. However, differentiation can amplify high frequency noise, which may destabilize the DG inner control scheme, especially during transients. This issue can be overcome by adding a low-pass filter to the measured output current [31].

$$V_C^* = V_{ref} - sL_v \frac{1}{s + \omega_c} i_L \tag{1.13}$$

If the virtual impedance $Z_v(s)$ is properly adjusted, it can prevent occurrence of current spikes when the DG is initially connected to the microgrid. Recently, the virtual output impedance method is used for harmonic current sharing [34, 35, 36]. In a microgrid with intensive use of nonlinear loads, an inaccurate sharing of harmonic power can lead to DG over capacity. Furthermore, harmonics can cause overheating, increased losses, distorted current and voltage waveforms, etc. To realize a better reactive power and harmonic power sharing, *He et al.* [37] proposed an enhanced control method using virtual impedance for fundamental and selective harmonic frequencies. The proposed overall scheme of the droop control with enhanced virtual impedance is shown in Fig. 1.9. While effective in

preventing the power coupling, this approach may increase the reactive power control and sharing error due to the increased voltage drops.

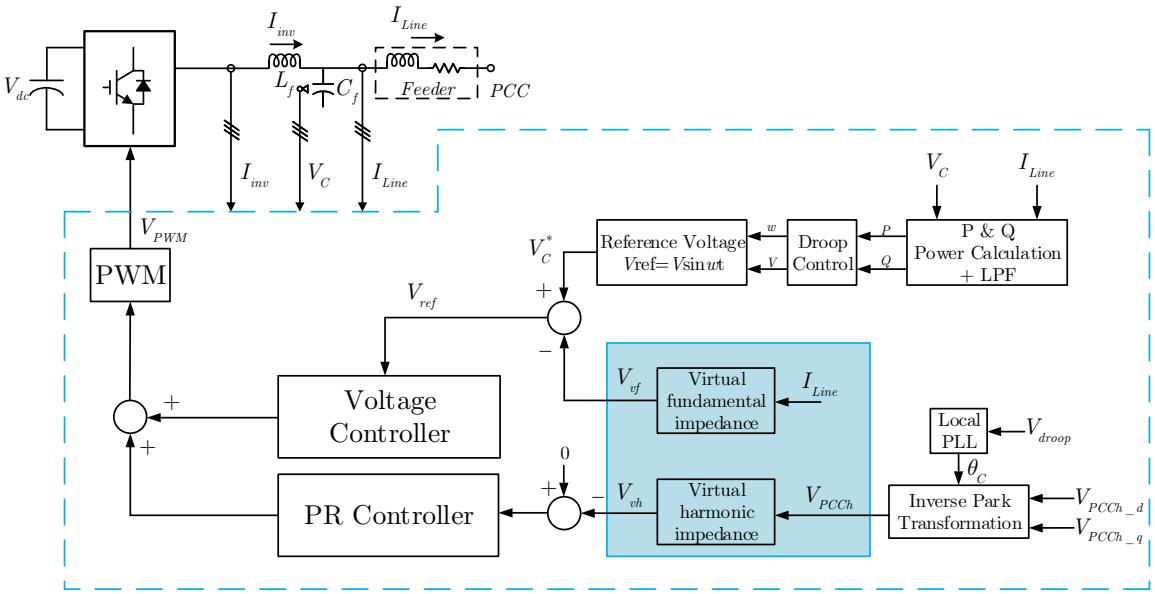

Figure 1.9: Droop Control with enhanced virtual impedance.

1.3.2.2 Virtual Power method

Another way of virtual structure is the virtual power transformation method presented in [20], [38, 39, 40, 41], which could decouple the power flows by rotating the power vectors with the impedance angle. In this case, both the line reactance X and resistance R need to be considered. Using equation (1.3), the real and reactive power can be rewritten as

$$\begin{bmatrix} P \\ Q \end{bmatrix} = \begin{bmatrix} \sin\theta_i & \cos\theta_i \\ -\cos\theta_i & \sin\theta_i \end{bmatrix} \begin{bmatrix} \frac{V_i V_0}{Z_i}\sin\delta_0 \\ \frac{V_i V_0}{Z_i}\cos\delta_0 - \frac{V_0^2}{Z_i} \end{bmatrix} \tag{1.14}$$

If we define the virtual power P' and Q' as

$$\begin{bmatrix} P' \\ Q' \end{bmatrix} = \begin{bmatrix} \frac{V_i V_0}{Z_i}\sin\delta_0 \\ \frac{V_i V_0}{Z_i}\cos\delta_0 - \frac{V_0^2}{Z_i} \end{bmatrix} \tag{1.15}$$

Then

$$\begin{bmatrix} P' \\ Q' \end{bmatrix} = \begin{bmatrix} \sin\theta_i & -\cos\theta_i \\ \cos\theta_i & \sin\theta_i \end{bmatrix} \begin{bmatrix} P \\ Q \end{bmatrix} \tag{1.16}$$

Hence, for a small δ_0,

$$\begin{aligned} P' &= \frac{V_i V_0}{Z_i}\sin\delta_0 \approx \frac{V_i V_0}{Z_i}\delta_0 \\ Q' &= \frac{V_i V_0}{Z_i}\cos\delta_0 - \frac{V_0^2}{Z_i} \approx \frac{V_i - V_0}{Z_i}V_0 \end{aligned} \tag{1.17}$$

which means that P' and Q' can be controlled by controlling δ_0 and V_i respectively. What is important is that a transformation involving the impedance angle θ_i should be applied to calculate the real power P and reactive power Q.

The virtual active and reactive power is respectively related to the frequency and voltage amplitude without coupling each other. The Droop control is adopted in the virtual frame to ensure the virtual power is shared properly. The virtual active and reactive power (P' and Q') are obtained by using an orthogonal transformation matrix T to rotate the active and reactive power vectors by the impedance angle as expressed in (1.16).

However, one problem with the virtual power method exist when the frame transformation angle is different between DGs and a power sharing error will appear. If the rotation angle is set to be a unified value, the relationship between the actual power P and Q and virtual power $P'$and Q' will have nothing to do with the impedance angle of transmission line and thus will be identical for parallel inverters. Therefore, as long as the virtual power are shared, both the actual active power and the actual reactive power will be accurately shared despite the difference of line impedance [41]. The overall block diagram of the virtual power droop is shown in Fig. 1.10.

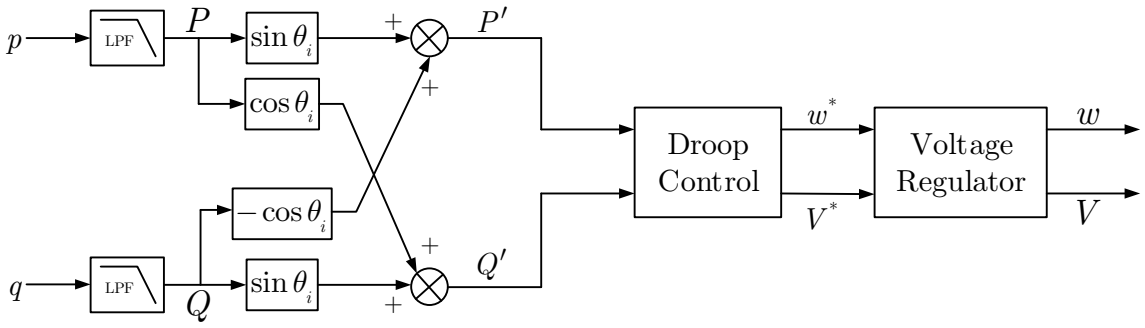

Figure 1.10: Virtual Power Droop Control Block diagram.

1.3.3 Compensated Droop Control

1.3.3.1 Additional Control loop based Droop methods

In order to improve the dynamic performances of inverters in DG system, a "wireless controller" is proposed in [42], where power derivative-integral terms are added to the conventional droop to improve transient response. Fig. 1.12 shows the proposed droop for this case.

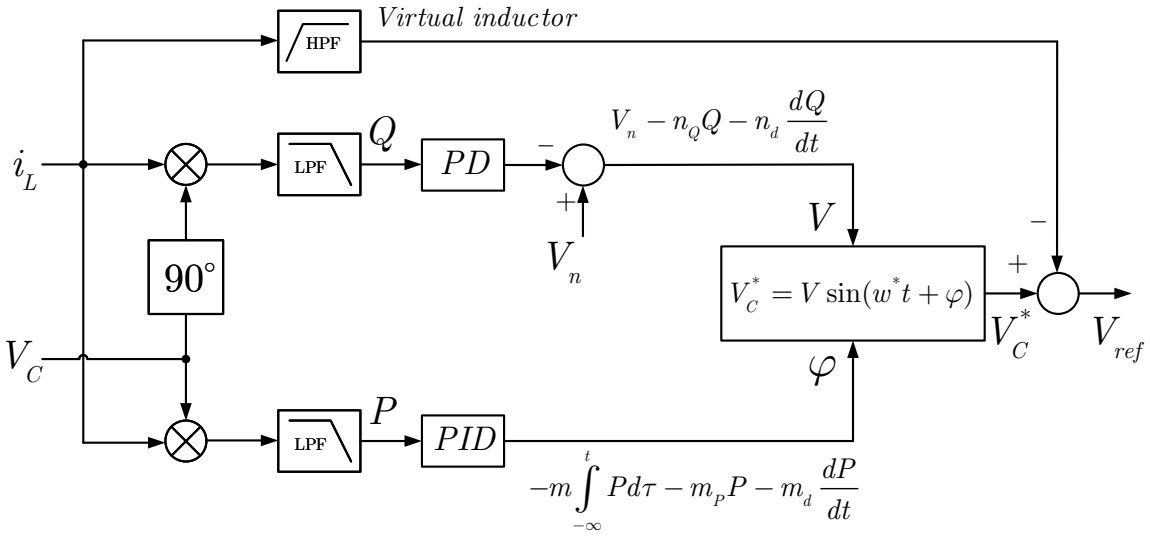

Figure 1.11: Additional control loop Droop Controller.

$$\begin{aligned} \phi &= -m\int_{-\infty}^{t} Pd\tau - m_P P - m_d\frac{dP}{dt} \\ E &= E^* - n_Q Q - n_d\frac{dQ}{dt} \end{aligned} \tag{1.18}$$

In a relatively small ac microgrid, large load changes can be expected. Then an adaptive derivative term is used to add damping and to avoid large start-up transients and circulating currents [43, 44], as

$$\begin{aligned} \omega &= \omega^* + K_P\left(P - P_{ref}\right) + K_{Pd}\frac{dP}{dt} \\ V &= V^* + K_Q\left(Q - Q_{ref}\right) + K_{Qd}\frac{dQ}{dt} \end{aligned} \tag{1.19}$$

Additionally, there are some other solutions to improve dynamic response of the droop control: droop based on coupling filter parameters [45], Additional Virtual inertia Droop [46]. In order to comprise a decoupled and accurate power sharing, other authors introduce estimator loop in addition to the use of virtual inductor at the Interfacing Converter output. An estimation of the impedance voltage drop to the reactive power ratio [47] or the grid parameters [48] (in case of grid connected and islanded microgrid) can be substituted in the droop control to improve the reactive power sharing.

1.3.3.2 Adaptive Voltage Droop

Recently, in [49], researchers propose an adaptive voltage droop scheme for voltage converters in an islanded microgrid. In this scheme, the voltage droop coefficient is defined

as a function of respective VSI active and reactive power outputs. Thus, each VSI voltage reference is adaptively drooped as a non-linear function of its active and reactive power outputs. In this case, two terms are added to the conventional $Q - V$ droop. One term is used to compensate the voltage drop across transmission line by the elimination of the connecting impedance between each VSI and the common voltage point. The other term is added to improve the reactive power sharing under heavy load conditions and hold the system stability. To demonstrate this control technique, two DG-system with generic output impedances is shown in Fig. 1.12. The voltage of a single DG can be derived as

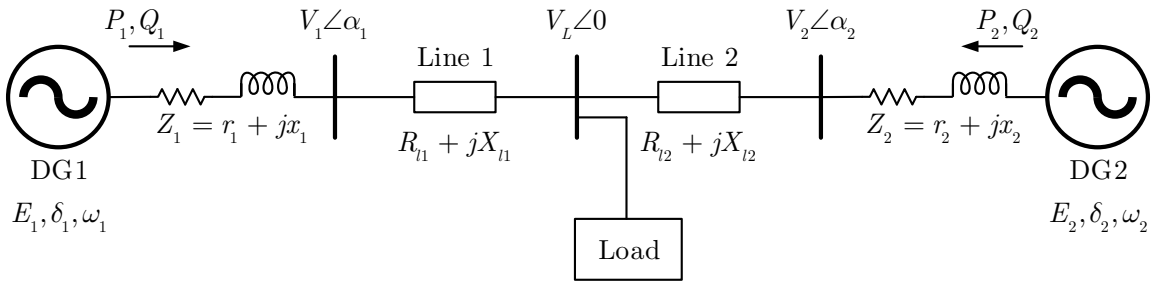

Figure 1.12: Two DG-system.

$$V_i = E_i^* - D_{Qi}Q_i - \frac{r_i P_i}{E_i^*} - \frac{x_i Q_i}{E_i^*} \tag{1.20}$$

The two later terms represent the voltage drop on the internal line impedance. Thus, to improve the voltage regulation at the load buses, the conventional voltage droop equation can be modified the voltage drop on the connecting impedances as

$$E_i = E_i^* - D_{Qi}Q_i + \left(\frac{r_i P_i}{E_i^*} + \frac{x_i Q_i}{E_i^*}\right) \tag{1.21}$$

Since the reactive power control cannot operate independently of the real power and system parameters and to meet control objective, that is reduction of the reactive power control dependence on real power control and system parameters, a novel reactive power sharing scheme is proposed as

$$\begin{aligned} E_i &= E_i^* - D_i(P_i, Q_i) + \left(\frac{r_i P_i}{E_i^*} + \frac{x_i Q_i}{E_i^*}\right) \\ D_i(P_i, Q_i) &= D_{Qi} + m_{Qi}Q_i^2 + m_{Pi}P_i^2 \end{aligned} \tag{1.22}$$

where D_{Qi}, m_{Qi} and m_{Pi} are the droop coefficients. The three terms can minimize the negative impacts of the real power and the system parameters on the reactive power control, as well as improving the system stability and reactive power sharing under heavy loading conditions. However, this method requires a good knowledge of the power line parameters [49]. Small errors may result in a positive feedback, and thus may cause system instability.

1.3.3.3 Q-Vdot Droop Control method

This Control law develops a dynamic relation between the reactive power Q and the rate of change of the DG output voltage ($\dot{V}$) [50, 51, 52]. The proposed $Q - \dot{V}$ can avoid the coupling dependence between the reactive power flow and the line impedance by placing the droop relationship $\dot{V}$ on rather than V. The rate of change of voltage $\dot{V}$ will drive the voltage V continuously until the desired reactive power Q flows through the line, and its performance will be less dependent on the line impedances. The $Q - \dot{V}$ droop controller is expressed as

$$\begin{aligned} \dot{V}_i &= \dot{V}_{ni} - n_i \left(Q_{ni} - Q_i\right) \\ V_i^* &= V_{ni} + \int_t \dot{V}_i d\tau \end{aligned} \tag{1.23}$$

where n_i is the droop coefficient, $\dot{V}_{ni}$ is the nominal value of $\dot{V}_i$ which is set to 0 V/sec, and Q_{ni} is the reactive power set point at the nominal $\dot{V}_i$, which is related to the reactive power capacity of DG. Also, V_{ni} is the nominal phase voltage magnitude and V_x^* is the output voltage magnitude command. A restoration mechanism is also proposed to bring $\dot{V}$ to zero at steady state and to maintain a constant level voltage. The restoration of $\dot{V}_i$ is designed as

$$\frac{d}{dt} Q_{ni} = K_{res}.Q_{Rx} \left(\dot{V}_{ni} - \dot{V}_i\right) \tag{1.24}$$

The control diagram of $Q - \dot{V}$ droop and the DG block diagram are shown in Fig. 1.13. In the $Q - \dot{V}$ control strategy, the error in reactive power sharing can be reduced but not eliminated due to its sensitivity to computational errors. Secondly, the restoration loop that tries to restore the voltage depends on the initial state of the integrator which would lead to system instability.

1.3.3.4 Common Variable-Based Control Method

It is well addressed that the voltage is not a global variable in a microgrid contrary to the frequency. Thus the reactive power, which is related to the Voltage, is difficult to share between parallel inverters and may result in circulating reactive current. Some researchers have proposed an adjustable reactive power sharing method by adding a common variable in the $Q - V$ droop, where an integral controller is used to regulate the common bus voltage (V_{PCC}) around the nominal value [53, 25, 54]. Thus, the controller can be independent from the voltage drop across mismatched line impedances and robust against grid perturbations. The voltage drop can be written as:

$$\triangle E_i = E_i - E^* = -n_i Q_i \tag{1.25}$$

and the voltage E_i can be implemented via integrating $\triangle E_i$, as

$$E_i = \int \triangle E_i dt \tag{1.26}$$

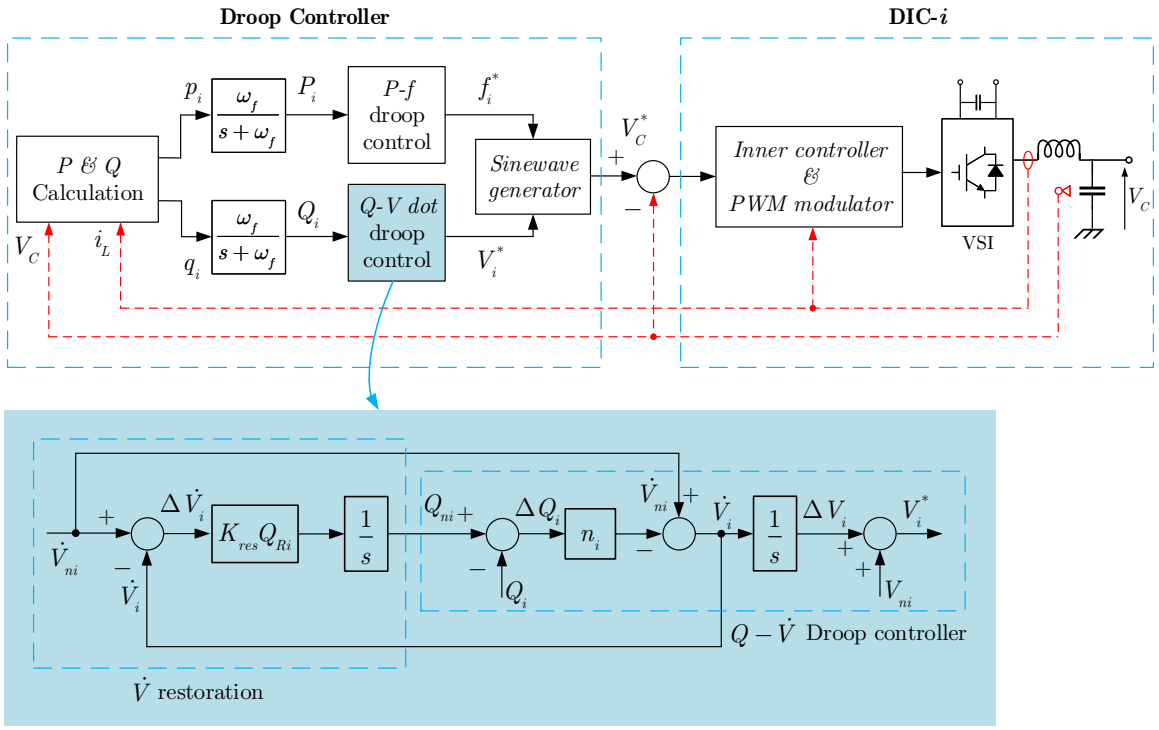

Figure 1.13: $Q - \dot{V}$ droop Controller and the overall control block diagram of DIC-i.

In order to make sure that the load voltage remains in a certain range, the load voltage drop $E^* - V_{PCC}$ needs to be fed back in a certain way. It can be added to $\triangle E_i$ as

$$E_i = \int \left[K_e \left(E^* - V_{PCC}\right) - n_i Q_i\right] dt \tag{1.27}$$

In steady state, the input of the integrator is zero, hence:

$$K_e \left(E^* - V_{PCC}\right) = n_i Q_i \tag{1.28}$$

$K_e \left(E^* - V_{PCC}\right)$ is the same for all DGs, if K_e is the same, thus an accurate reactive power sharing can be achieved, which is no longer depend on the line impedance and immune from system parameter variations.

In summary, the PCC rms-voltage (V_{PCC}) is measured and compared to the rated value E^*. The difference will be integrated to reach static error equal to zero. However, the main drawback is that the common bus voltage should be measured all the way between converters to enhance the reactive power sharing.

1.3.3.5 Hierarchical Droop Control method

Conventional droop control cannot ensure a constant voltage and frequency, neither an exact power sharing. But an advantage of the control can avoid communication among the DGs. For developing a flexible microgrid, it is necessary to distribute the control tasks over levels. The later decouples the power flows and develop a restoration system

for frequency and voltage, reactive power compensation, mode transfer, power settings [55, 56, 57, 58]. Functionally, the microgrid operate within three control hierarchical levels:

- *Primary Control*: P/Q Droop Control
  The primary control is based on classical droop control to allow the connection of different sources in parallel and to share the load wirelessly. In addition, it is responsible for the voltage and current regulation in terms of a particular reference. A virtual impedance loop is used for decoupling the control parameters and eliminate the circulation currents between DGs and reactive power oscillations.

- *Secondary Control*: Frequency/Voltage Restoration and synchronization
  In order to restore the microgrid voltage and frequency to nominal voltage, supervisor system must send the corresponding signals using low-bandwidth communication. A synchronization loop can be added in this level to transfer from islanding to grid-connected modes.

- *Tertiary Control*: P/Q Import and Export
  The third control hierarchy allows import/export active and reactive power to the grid based on economic data decisions, estimates the grid parameters and detects non-planed islanding operation.

In [55], a PI controller was proposed to implement the secondary and tertiary control after sensing the voltage, current and frequency at both sides of the static transfer switch (STS) and sending them by low-bandwidth communication link. This controller is represented in Fig. 1.14, where the frequency and voltage restoration controllers G_ω and G_E, shown in Fig. 1.14(a) are PI controllers. The phase between the grid and the microgrid will be synchronized by means of the synchronization control loop shown in Fig. 1.14(b), which can be seen as a conventional PLL.

1.4 Conclusion

Droop Control methods are based on local measurements of the network state variables to provide power sharing among parallel interfaced converters, which make microgrid control truly distributed, as they do not depend on cables for reliable operation. It has many desirable features such as expandability, modularity, flexibility and redundancy. However, the droop control concept has some limitations including frequency and voltage variations, slow transient response, and possibility of circulating current between inverters due to line impedance mismatches between inverters and the common bus.

Recently, many researchers have improved the conventional droop control to overcome those limitations. From the introduced methods, it is difficult for only one control scheme to overcome all the mentioned drawbacks for all applications. However, further investigation of these control techniques would help improve the design and implementation of future distributed ac microgrid architecture. Table 1.1 summarizes the potential advantages and disadvantages of the different droop methods presented in this chapter.

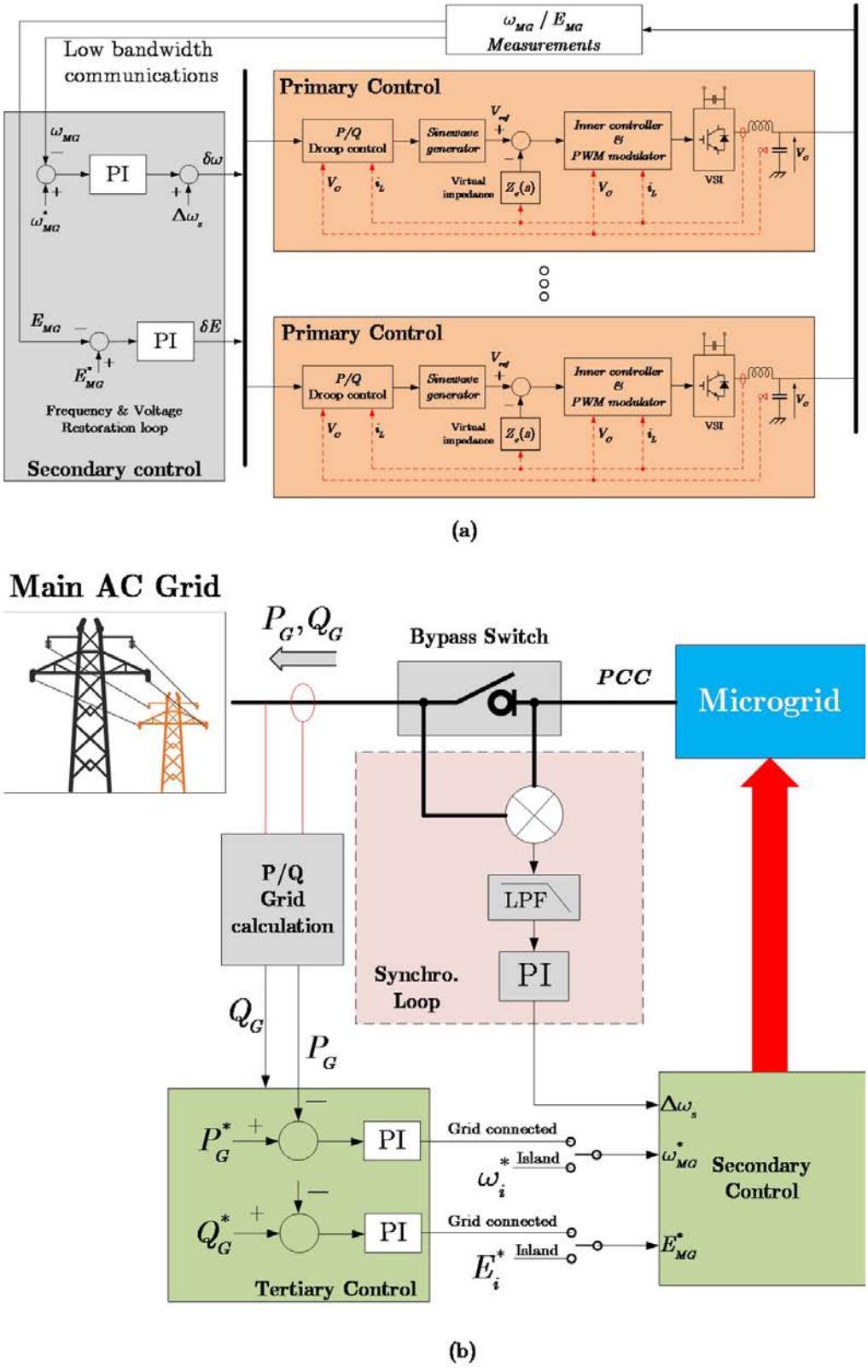

Figure 1.14: Block diagrams of the hierarchical control of an AC microgrid: (a) Primary and secondary controls. (b) Tertiary Control and synchronization loop.

In addition, the research about the impacts of stability and reliability with a specific load are still behind. The stability of microgrid has been studied for long years, but it is not studied perfectly when a microgrid supplies some complex loads, such as a dynamic load, a constant load, inductor motor etc. So it is necessary to propose special models and control methods to solve the voltage, frequency and power-angle instabilities for complex loads. From those issues, this thesis has specified the way of improving ac microgrids and highlighted on the techniques and future studies that should close the gaps. Our later proposed droop methods are studied in details in the next chapters. Chapter Two will deal with modeling and control of Flatness -based Interface Converters for autonomous as microgrid application. Furthermore, an improved frequency droop control based on voltage estimator is introduced.

Droop Control Methods		**Potential Advantages**	**Potential Disadvantages**
Conventional Droop Method	$P-\omega/Q-V$ Or $P-V/Q-\omega$ Droop Methods	☑ Easy Implementation Without Communication. ☑ Expandable, Modular And Flexible. ☑ For Highly Inductive\Resistive Transmission Lines.	☒ Affected By Physical Parameters. ☒ Poor Voltage-frequency Regulation. ☒ Slow Dynamic Response. ☒ Poor Harmonic Sharing.
Modified Droop Structure	Complex Line Impedance-based Droop	☑ Decoupled Active And Reactive Controls. ☑ Improved Voltage Regulation.	☒ Line Impedances Should Be Known In Advance. ☒ Slow Dynamic Response. ☒ Poor Harmonic Sharing.
	Angle Droop Method	☑ Constant Frequency Regulation. ☑ Good Power Quality.	☒ Require GPS Signals. ☒ Poor Performance Of Power Sharing. ☒ Slow Dynamic Response. ☒ Poor Harmonic Sharing.
Virtual Droop Method	Virtual Output Impedance Loop	☑ Not Affected By Physical Parameters. ☑ Improved Performance Of Power Sharing And System Stability.	☒ Voltage Regulation Is Not Guaranteed. ☒ Requires Relatively High Bandwidth For Controller. ☒ Require Low Bandwidth Communication In Some Cases. ☒ The Physical Parameters Should Be Known In Specific Application.
	Virtual Power Method	☑ Decoupled Active And Reactive Power Controls.	☒ Hard To Extract The Same Transformation Angle For All DGs. ☒ The Physical Parameters Should Be Known In Advance.
Compensated Droop Control	Additional Control Loop Based Droop Method	☑ Decoupled Active And Reactive Controls. ☑ Improved Voltage Regulation.	☒ Line Impedance Should Be Known In Advance. ☒ Slow Dynamic Response. ☒ Poor Harmonic Sharing.
	Q-Vdot Droop Control Method	☑ Same As Conventional Droop.	☒ Depend On Initial Conditions. ☒ Steady-state Solution May Not Exist. ☒ Easy To Destabilize.
	Common Variable-based Control Method	☑ Accurate Reactive Power Sharing. ☑ Not Affected By The Physical Parameters.	☒ Hard To Measure The Common Voltage Due To Long Distance. ☒ Frequency Is Load Dependent. ☒ Poor Harmonic Sharing.
	Hierarchical Droop Control Method	☑ Same As Conventional Droop.	☒ Trade-off Between Voltage Regulation And Power Sharing. ☒ Slow Dynamic Response. ☒ Need Low Bandwidth Communication For Voltage/Frequency Restoration.

Table 1.1: Potential Advantages and Disadvantages of different types of Droop Controllers

Chapter 2

FLATNESS BASED CONTROL FOR INTERFACED CONVERTER WITH DROOP CONTROL ENHANCEMENTS

2.1 Introduction

In chapter 1, we discussed the different strategies used for decentralized control based-Islanded AC Microgrid. All the design strategies are based on Droop Control which can autonomously manage the active and reactive powers between distributed generators (DGs), based on their ratings, with no communication between them. Thus, enhancing reliability and flexibility of the system. The inner controller of the Interfaced Converter has had a portion in the first chapter, where the Flatness-based Control was introduced and its advantages over other Controllers were given. This chapter focuses on the development of the Flatness-based Control for Interfaced Converter. Modeling, analysis and implementation of the controller are done for DC/AC inverter with LC filter which is applicable for other DICs in a microgrid. Furthermore, the Flatness-based control (FBC) is implemented on parallel inverters system. The proposed control allows equal current sharing between parallel inverters, reduces the circulating currents and minimizes the impact of a full disconnection of any faulty inverter in the system. The next part of this chapter, deals with a proposed Droop Control based on a state estimation of the common bus voltage (V_{PCC}) which is then used as a feedback signal for the Droop Control to accurately share the reactive power between parallel interfaced Converters. This is done without adding communication link and without adding a supplementary loop to inject a virtual impedance. Thus the proposed method keeps the advantages of the conventional Droop control method to manage the power between distributed generations in autonomous fashion. Simulation and experiments of the proposed droop method are presented in this chapter.

2.2 Flatness-based Control for inverter

Figure 2.1 represents the full power electronics scheme of an Interfaced Converter based microgrid, where the Distributed Energy Resource (DER) is modeled by a DC source of fixed voltage with a value chosen so that to ensure the controllability of the voltage source inverter (VSI). The three phase inverter which assures the conversion DC/AC, is controlled by a pulse width modulation (PWM) signals. The LC type passive filter is there to reduce the high frequency harmonic contents.

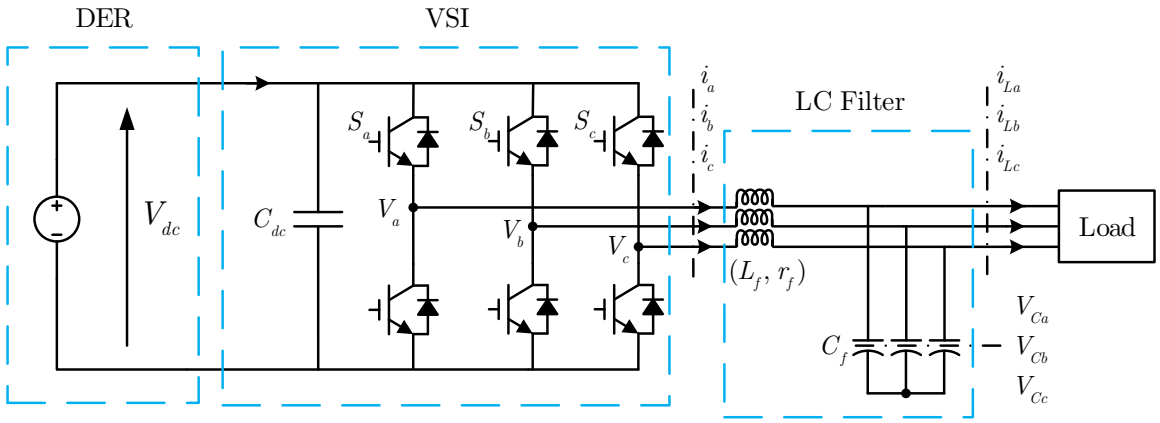

Figure 2.1: Distributed Generator with DER modeled as a DC source.

Firstly, The work of Azeddine Houari, in his PhD thesis [1] has been reviewed where the definition of the flatness controller for DC/AC Converter was introduced and a comparison with other control law recently published was done. The Criteria's in comparison were focused on:

- The Total Harmonic Distortion (THD) in the AC-side capacitors.
- Rapidity in the response during load transient state.
- Robustness according parameters variation.

In Houari thesis, a conclusion was drawn out for the advantages of Flatness-based control, compared with PID and Linearization MIMO [59], in terms of network quality, parametric robustness and stability. The results are summarized in table 2.1.

2.2.1 System Modeling

The modeling equations of a three phase system, Fig. 2.1, are given as:

$$L_f \frac{d}{dt} \begin{pmatrix} i_a \\ i_b \\ i_c \end{pmatrix} = \begin{pmatrix} V_a \\ V_b \\ V_c \end{pmatrix} - r_f \begin{pmatrix} i_a \\ i_b \\ i_c \end{pmatrix} - \begin{pmatrix} V_{Ca} \\ V_{Cb} \\ V_{Cc} \end{pmatrix} \tag{2.1}$$

	PID	Linearization [59]	Flatness
Start-up ability	Exceeding 55%	Exceeding 100%	No overshoot
THD under load (Linear and non linear)	Medium	Good	Good
Dynamic response	Medium (Two loops)	Rapid	Rapid
Parametric robustness	Medium	Lower than the PID	Good
Stability 'Local'	Unstable beyond a certain power	Unstable beyond a certain power (knowing that load currents are estimated)	Unstable beyond a certain power (knowing that load currents are not measured) Stable system in the whole field of controllability (if the load currents are measured)
Number of sensors	7	7 with current measuring, 5 with estimation	5 with current measuring, 3 with estimation

Table 2.1: Summary of results obtained in Houari thesis [1]

$$C_f \frac{d}{dt}\begin{pmatrix} V_{Ca} \\ V_{Cb} \\ V_{Cc} \end{pmatrix} = \begin{pmatrix} i_a - i_{La} \\ i_b - i_{Lb} \\ i_c - i_{Lc} \end{pmatrix} \tag{2.2}$$

For system control, a practical common method for developing the control laws for three-phase systems is the transition to the rotating frame of Park. Moving to this reference frame is done using the change of base matrix P.

$$P = \sqrt{\frac{2}{3}}\begin{pmatrix} \frac{1}{\sqrt{2}} & \frac{1}{\sqrt{2}} & \frac{1}{\sqrt{2}} \\ \cos\theta & \cos\left(\theta - \frac{2\pi}{3}\right) & \cos\left(\theta + \frac{2\pi}{3}\right) \\ -\sin\theta & -\sin\left(\theta - \frac{2\pi}{3}\right) & -\sin\left(\theta + \frac{2\pi}{3}\right) \end{pmatrix} \tag{2.3}$$

with $\theta = \omega t + \theta_0$, ω is the electrical pulsation of the network and is selected in function of the constraints imposed by the choice of control strategy. The sum of the inverter output currents ($[i_a, i_b, i_c]^t$), the sum of the load currents ($[i_{La}, i_{Lb}, i_{Lc}]^t$) and that of the capacitor currents ($[i_{Ca}, i_{Cb}, i_{Cc}]^t$) are all zeros (i.e. $i_a + i_b + i_c = 0$, $i_{La} + i_{Lb} + i_{Lc} = 0$, and $i_{Ca} + i_{Cb} + i_{Cc} = 0$).

Thus, the three-phase system described in (2.1) and (2.2) in (abc) frame, is reduced to a system described respectively by the following equations in (dq) Park transformation.

$$\frac{d}{dt}\begin{pmatrix} V_{Cd} \\ V_{Cq} \end{pmatrix} = \begin{pmatrix} 0 & \omega \\ -\omega & 0 \end{pmatrix}\begin{pmatrix} V_{Cd} \\ V_{Cq} \end{pmatrix} + \frac{1}{C_f}\begin{pmatrix} i_d \\ i_q \end{pmatrix} - \frac{1}{C_f}\begin{pmatrix} i_{Ld} \\ i_{Lq} \end{pmatrix} \tag{2.4}$$

$$\frac{d}{dt}\begin{pmatrix} i_d \\ i_q \end{pmatrix} = \begin{pmatrix} \frac{-r_f}{L_f} & \omega \\ -\omega & \frac{-r_f}{L_f} \end{pmatrix}\begin{pmatrix} i_d \\ i_q \end{pmatrix} + \frac{1}{L_f}\begin{pmatrix} V_d \\ V_q \end{pmatrix} - \frac{1}{L_f}\begin{pmatrix} V_{Cd} \\ V_{Cq} \end{pmatrix} \tag{2.5}$$

with: $[V_d, V_q]^t = P.[V_a, V_b, V_c]^t$, $[V_{Cd}, V_{Cq}]^t = P.[V_{Ca}, V_{Cb}, V_{Cc}]^t$,
$[i_d, i_q]^t = P.[i_a, i_b, i_c]^t$, $[i_{Ld}, i_{Lq}]^t = P.[i_{La}, i_{Lb}, i_{Lc}]^t$.

2.2.2 Flatness Control for the Modeled System

To illustrate the flatness property of the modeled system, the differentially flat conditions described early in Chapter 1 by relation (1.1) must hold. We propose to use the following candidate flat output associated with the system described by the equations (2.4) and (2.5):

$$y = \begin{pmatrix} y_d \\ y_q \end{pmatrix} = \begin{pmatrix} V_{Cd} \\ V_{Cq} \end{pmatrix} = \phi(x, u) \tag{2.6}$$

where x represents the state vector ($x = [V_{Cd}, V_{Cq}, i_d, i_q]^t$), u is the input vector ($u = [V_d, V_q]^t$).

The first condition for the differential system is confirmed since the flat output is expressed as function of the state vector x. Referring to equations (2.4) and (2.5) and the expression of the candidate flat outputs in (2.6), the state vector x can be expressed by the following expression:

$$\begin{pmatrix} V_{Cd} \\ V_{Cq} \\ i_d \\ i_q \end{pmatrix} = C_f \cdot \begin{pmatrix} 0 \\ 0 \\ \dot{y}_d \\ \dot{y}_q \end{pmatrix} - \begin{pmatrix} 1 & 0 \\ 0 & 1 \\ 0 & C_f\omega \\ -C_f\omega & 0 \end{pmatrix} \cdot \begin{pmatrix} y_d \\ y_q \end{pmatrix} + \begin{pmatrix} 0 \\ 0 \\ i_{Ld} \\ i_{Lq} \end{pmatrix} \tag{2.7}$$

The above expression can be written in the form:

$$\begin{pmatrix} V_{Cd} \\ V_{Cq} \\ i_d \\ i_q \end{pmatrix} = \begin{pmatrix} \varphi_{V_{cd}}(y_d, y_q, \dot{y}_d) \\ \varphi_{V_{Cq}}(y_d, y_q, \dot{y}_q) \\ \varphi_{i_d}(y_d, y_q, \dot{y}_d) \\ \varphi_{i_q}(y_d, y_q, \dot{y}_q) \end{pmatrix} \tag{2.8}$$

The first derivative of the flat output enables to bring up the state variables. Indeed, the system can be considered differentially flat, if the input, $u = [V_d, V_q]^t$, can be expressed in terms of flat output components and their successive derivatives.

$$\frac{d}{dt}\begin{pmatrix} i_d \\ i_q \end{pmatrix} = C_f . \begin{pmatrix} \ddot{y}_d \\ \ddot{y}_q \end{pmatrix} - \begin{pmatrix} 0 & C_f\omega \\ -C_f\omega & 0 \end{pmatrix} \begin{pmatrix} \dot{y}_d \\ \dot{y}_q \end{pmatrix} + \frac{d}{dt}\begin{pmatrix} i_{Ld} \\ i_{Lq} \end{pmatrix} \tag{2.9}$$

We then set:

$$\frac{d}{dt}\begin{pmatrix} i_d \\ i_q \end{pmatrix} = \begin{pmatrix} \varphi_{di_d}(y_d, \dot{y}_d, \dot{y}_q, \ddot{y}_d) \\ \varphi_{di_q}(y_q, \dot{y}_d, \dot{y}_q, \ddot{y}_q) \end{pmatrix} \tag{2.10}$$

Finally, substituting (2.6), (2.8) and (2.10) in (2.5), the expression of the control input, u=$[V_d, V_q]^t$, as function of the flat output and its successive derivatives can be expressed in the form:

$$\begin{pmatrix} V_d \\ V_q \end{pmatrix} = L_f . \begin{pmatrix} \varphi_{di_d}(y_d, \dot{y}_d, \dot{y}_q, \ddot{y}_d) \\ \varphi_{di_q}(y_q, \dot{y}_d, \dot{y}_q, \ddot{y}_q) \end{pmatrix} - \begin{pmatrix} -r_f & \omega L_f \\ -\omega L_f & -r_f \end{pmatrix} \begin{pmatrix} \varphi_{i_d}(y_d, y_q, \dot{y}_d) \\ \varphi_{i_q}(y_d, y_q, \dot{y}_q) \end{pmatrix} + \begin{pmatrix} y_d \\ y_q \end{pmatrix} \tag{2.11}$$

$$\begin{pmatrix} V_d \\ V_q \end{pmatrix} = \begin{pmatrix} \psi(y_d, y_q, \dot{y}_d, \dot{y}_q, \ddot{y}_d) \\ \psi(y_d, y_q, \dot{y}_d, \dot{y}_q, \ddot{y}_q) \end{pmatrix} \tag{2.12}$$

In summary, the differential flatness expressed in (1.1) are verified in (2.6), (2.8) and (2.12). Thus, the modeled system can be considered as flat, of vector $y = [V_{Cd}, V_{Cq}]^t$ being the flat output associated with the input $u = [V_d, V_q]^t$.

So far, we have demonstrated that the studied system, shown in Fig. 2.1, can be considered differentially flat. In the next sections, we will present the synthesis of the controller, as well as the reference trajectory planning algorithm.

2.2.2.1 Implementation of the control algorithm

As detailed in [1, 11, 10], the input-output linearization technique can be used to insure the control of the flat output, $y = [y_d, y_q]^t$ to its trajectory reference, $y_{ref} = \left[y_{d_{ref}}, y_{q_{ref}}\right]^t$. This technique involves introducing the control vector, $\gamma = [\gamma_d, \gamma_q]^t$, defined as follows:

$$\begin{cases} \ddot{y}_d = & \gamma_d \\ \ddot{y}_q = & \gamma_q \end{cases} \tag{2.13}$$

The calculation of the control components γ_d and γ_q is obtained by the control laws described respectively in (2.14) and (2.15). These laws govern the evaluation of the error ($\varepsilon = y_{ref} - y$), so that an asymptotic convergence of the error tends to zero.

$$0 = \left(\ddot{y}_{d_{ref}} - \gamma_d\right) + k_1\left(\dot{y}_{d_{ref}} - \dot{y}_d\right) + k_2\left(y_{d_{ref}} - y_d\right) + k_3\int\left(y_{d_{ref}} - y_d\right)d\tau \tag{2.14}$$

$$0 = \left(\ddot{y}_{q_{ref}} - \gamma_q\right) + k_1\left(\dot{y}_{q_{ref}} - \dot{y}_q\right) + k_2\left(y_{q_{ref}} - y_q\right) + k_3\int\left(y_{q_{ref}} - y_q\right)d\tau \tag{2.15}$$

The integral terms are introduced to ensure zero static errors in steady state and can compensate the modeling errors and/or errors related to parametric uncertainties. Each of these equations is equivalent to a third order equation on the error of the form:

$$\dddot{\varepsilon} + k_1\ddot{\varepsilon} + k_2\dot{\varepsilon} + k_3\varepsilon = 0 \tag{2.16}$$

The optimal choice of parameters k_1, k_2, k_3, can be obtained by polynomial identification (2.16) to a characteristic polynomial given by equation (2.17), whose roots are predetermined [1].

$$p(s) = (s + p_1).(s^2 + 2\xi\omega_n.s + \omega_n^2) \tag{2.17}$$

Thus, we obtain by identification:

$$\begin{cases} k_1 = & 2\xi\omega_n + p_1 \\ k_2 = & 2\xi\omega_n p_1 + \omega_n^2 \\ k_3 = & p_1\omega_n^2 \end{cases} \tag{2.18}$$

where ξ is the damping coefficient and ω_n is the cut-off frequency of the controller. They are designed to achieve desired control performance (fast dynamic with noise reduction). p_1 is an additional pole which must regulate the dynamics of the followed set-point. It is proposed to set the pole equal to the cut-off frequency of the controller. The numerical values of these parameters are given in section (2.2.2.3).

2.2.2.2 Trajectory Planning

For the generation of the reference trajectory, related to the flat outputs, we use a second order low-pass filter with damping factor equal 1. From a practical point of view, this choice is better than the polynomial approach when the number of constraint is low. Indeed, the computing time is minimized during the planning phases. This solution allows naturally integrate the constraints of continuity of paths (which must be of class

C2 in this case, due to double derivative terms), the derivatives are zero at the start and the finish [1]. The reference trajectories are expressed as follows:

$$\begin{pmatrix} y_{d_{ref-f}} \\ y_{q_{ref-f}} \end{pmatrix} = \left(1 - e^{\frac{t-t_{init}}{\tau_1}} - \frac{t-t_{init}}{\tau_1} e^{\frac{t-t_{init}}{\tau_1}}\right) . \begin{pmatrix} y_{d_{ref}} - y_{d_{init}} \\ y_{q_{ref}} - y_{q_{init}} \end{pmatrix} + \begin{pmatrix} y_{d_{init}} \\ y_{q_{init}} \end{pmatrix} \quad (2.19)$$

where: t and t_{init} represent respectively time and the initial time, τ_1 represents the time constant of the filter, where its value is chosen so that the dq components of the inverter voltage $[V_d, V_q]^t$ remain always in the interval $[-(V_{dc}/2), (V_{dc}/2]$ when using SPWM, to ensure the system is almost controllable. $y_{d_{init}}$and $y_{q_{init}}$ are respectively the initial values of the flat output components y_d and y_q. In this relation, $y_{d_{ref}}$ and $y_{q_{ref}}$ are defined as $\left[y_{d_{ref}}, y_{q_{ref}}\right]^t = \left[V_{Cd_{ref}}, V_{Cq_{ref}}\right]^t$. $V_{Cd_{ref}}, V_{Cq_{ref}}$ represent the dq components of the reference voltage across capacitors. The choice of reference values is generated by the droop control that guarantee the desired output power delivered by the interfaced converter to the grid.

Finally, the use of the filtered reference outputs (Fig. 2.2), $y_{d_{ref-f}}$and $y_{q_{ref-f}}$, and the established control variable, $\gamma = [\gamma_d, \gamma_q]^t$, allow for the generation of reference commands associated to the voltage of the inverter.

$$\begin{pmatrix} V_{d_{ref}} \\ V_{q_{ref}} \end{pmatrix} = \begin{pmatrix} \psi_{V_{d_{ref}}}(y_{d_{ref-f}}, y_{q_{ref-f}}, \dot{y}_{d_{ref-f}}, \dot{y}_{q_{ref-f}}, \gamma_d) \\ \psi_{V_{qref}}(y_{d_{ref-f}}, y_{q_{ref}-f}, \dot{y}_{d_{ref-f}}, \dot{y}_{q_{ref-f}}, \gamma_q) \end{pmatrix} \quad (2.20)$$

We highlight that the measure of inductive filter currents is not necessary to implement the control law, (2.20). Only the capacitor voltage sensors are used for generating equations, while the load current sensors, that are used for power measuring in droop controller, could be useful for increasing dynamics of Flatness Controller as regard to load perturbation. The block diagram of the proposed control is presented in Fig. 2.2.

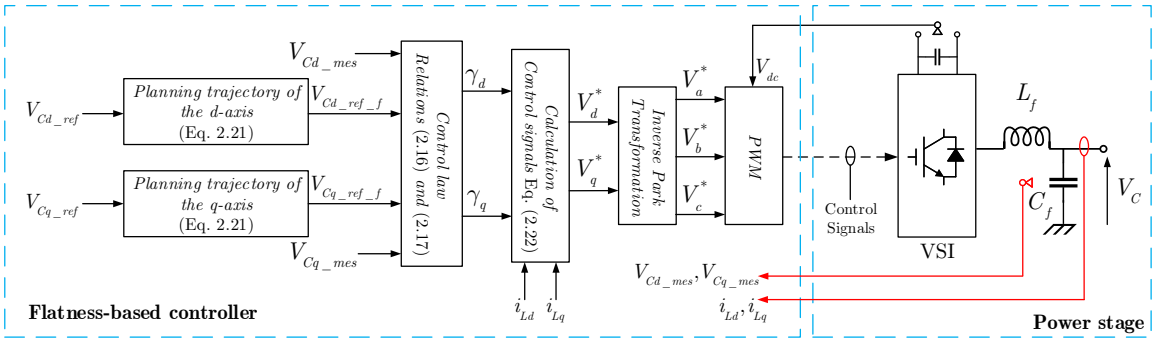

Figure 2.2: Functional diagram of the proposed Control.

2.2.2.3 Verification of the proposed Control

To check the flatness-based control for a DIC, i.e. the possibility to show the evolution of the system state variables from the flat outputs, it is proposed to demonstrate the

system behavior at the starting phase and at a load transient state by using MATLAB-Simulink. A state-space average model for a three-phase SPWM inverter is designed with the system parameters used for this simulation are given in Table 2.2. A balanced three-phase star connected R-L load with 25Ω resistance and 9.3 mH inductance per phase was used. Figure 2.3 represents the evolution of the flat outputs (V_{Cd}, V_{Cq}) after applying an rms-voltage level ranging from 0 to 110V. As shown in Figure 2.3, the measured flat outputs perfectly follow their trajectory references. Thus, the proposed control with its trajectory planing algorithm allows forcing the system to follow a predefined trajectories during the start phase.

Symbol	Designation	Value
r_f	The internal resistance of the output filter inductor	0.7 Ω
L_f	The inductance of the filter inductor	3.4 mH
C_f	The capacitance of the output filter capacitor	40 μF
V_n	The nominal RMS single-line voltage	110 V
ω	Microgrid angular frequency	$2\pi 60$
V_{dc}	DC voltage	500 V
Flatness Controller parameters		
ξ	The damping factor	0.7
ω_n	The cut-off frequency	5000 rad/sec
p_1	Additional pole	6000 rad/sec
Trajectory Filter		
ξ	The damping factor	1
ω_c	The cut-off frequency	1000 rad/sec

Table 2.2: Flatness Control system parameters.

Figure 2.4 shows the system response during a load change from 800W to 3600W. Figure 2.4(a) shows the power consumed by the load. Figure 2.4(b) shows the *dq* components of the inverter output current (i_d, i_q) perfectly follow the state variables predicted by the command, i.e. φ_{i_d} and φ_{i_q}as expressed in (2.8).

2.3 Flatness-based control for parallel-connected inverters

The parallel connection of three-phase converters is a well known solution for large-scale inverter-based microgrid when the capacities of the switching devices are limited or constrained by economic considerations [60]. For many applications, the parallel operation could be crucial in systems with high reliability requirements. Parallel inverters allow reducing the components size, especially the inductive components by segmenting the total power and distributing it between inverters. The global efficiency becomes better and the voltage stress on each inverter can be reduced. The parallel inverter system allows creating redundancy, achieving compact design, high power density compared to single

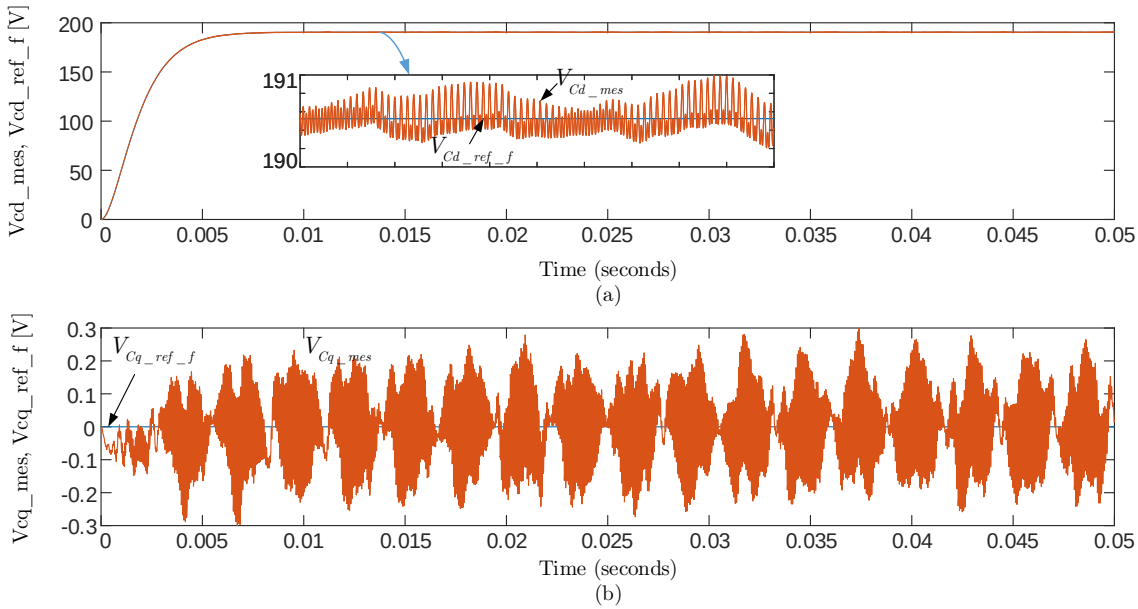

Figure 2.3: Behavior of the Flat outputs (V_{cd}, V_{cq}) at starting phase.

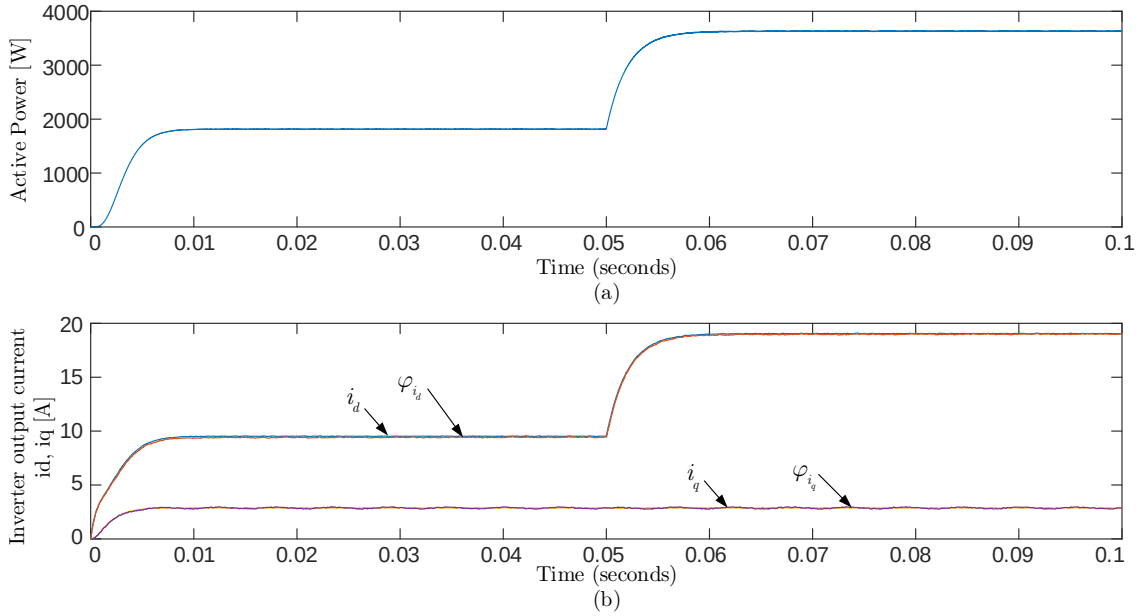

Figure 2.4: Current response during a load transient change from 800 to 3600W.

large power inverter and making the load power expansion between the parallel inverters more flexible [61, 62, 63, 64, 65, 66, 67]. One method for controlling parallel inverters is to define one inverter as master which imposes the output voltage while the others as slave units where only currents or power is regulated. Master-slave control has been used in [68, 69, 70]. However, the major concern for parallel operation is the circulating currents in the conduction paths resulting at the common connection of the DC/AC terminals of each inverter. Definition of the phenomenon is detailed in [71, 72, 73, 65, 74, 75, 76]. Commonly, it is possible to prove that the circulating currents are essentially generated from the difference of the switching operation associated with the individual units, or due to non-identical components, or open circuit of any switch or at the moment of fully disconnection of any unit in the parallel system. Those currents can be separated into two types; low-frequency component close to the fundamental frequency, and a high-frequency component close to the switching frequency [75, 76]. While the high-frequency component can be effectively limited by means of passive components, the low-frequency component needs a special attention. Traditionally, in order to avoid this problem, transformers are used to isolate the output current flow [77, 78]. However, the transformers are heavy and they increase both core and copper losses. Basically, the recommended solutions in literature are based on modifying the PWM operation [76, 71, 79].

The Flatness-based controller, detailed in this work, manages the currents between the parallel units either on healthy or faulty operation mode. It is able to minimize the effect of the circulating current or the influence of any faulty unit at the disconnection or reconnection moment of any inverter in the parallel system. The proposed control method does not need physical or complicated model of control and is independent of the load conditions.

2.3.1 System structure and modeling

Referring to Fig. 2.5, the sum of the load currents and the sum of the N modules output current are equal to zero

$$i_{La} + i_{Lb} + i_{Lc} = 0 \tag{2.21}$$

$$\sum_{k=1}^{N} (i_{ak} + i_{bk} + i_{ck}) = 0 \tag{2.22}$$

Then, the sum of the filter capacitors input current is zero. Assuming that, the zero-sequence voltage component V_{c0} is always zero. Actually, for each inverter of the system, there is a zero current path by the anti-parallel diodes of the full bridge of the other inverters. To confirm this fact, simply, the zero-sequence current of an inverter can be left free and the other $N-1$ zero-sequence components of the output currents of the other inverters are kept as independent state variables. Then, the zero-sequence current component of the first inverter can be given as $i_{01} = -\sum_{k=2}^{N} i_{0k}$. Controlling the zero-sequence currents of $N-1$ modules involves the cancellation of the first inverter zero-sequence current i_{01}. The first inverter of the system is considered as the reference to the

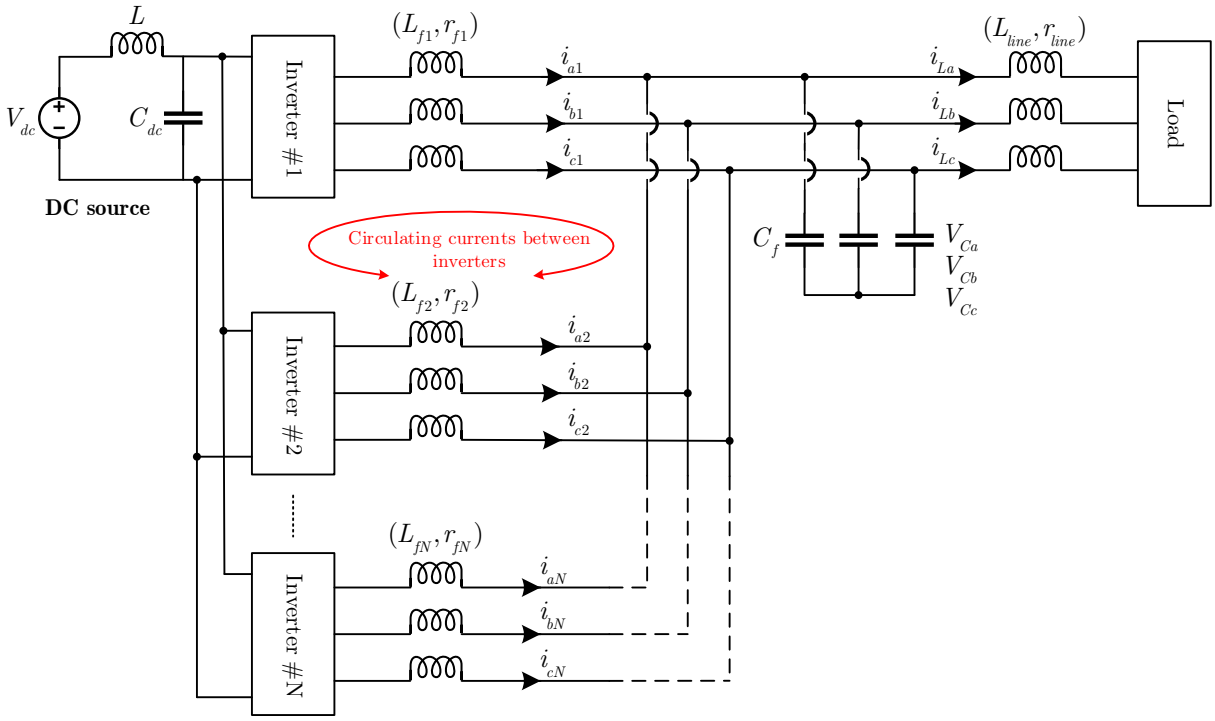

Figure 2.5: System with N-parallel inverters.

given parallel inverters system. It is obvious that another inverter can be considered as the reference or *master* and the others as *slave* for the control purpose.

In order to establish the control laws in the continuous domain, the voltage-current model is transformed from three-phase static frame into synchronous $0dq$ frame using Park transformation. Derivatives of the output voltages in $0dq$ frame, with $V_{c0} = 0$ at the common filter capacitors, are obtained as

$$\frac{d}{dt}\begin{pmatrix} V_{cd} \\ V_{cq} \end{pmatrix} = \begin{pmatrix} 0 & \omega \\ -\omega & 0 \end{pmatrix} \cdot \begin{pmatrix} V_{cd} \\ V_{cq} \end{pmatrix} + \frac{1}{C_f}\left(\begin{pmatrix} \sum_{k=1}^{N} i_{dk} \\ \sum_{k=1}^{N} i_{qk} \end{pmatrix} - \begin{pmatrix} i_{Ld} \\ i_{Lq} \end{pmatrix} \right) \tag{2.23}$$

The derivatives of the dq components of the first inverter output current as function of the controlled voltages V_{d1} and V_{q1}, similarly the derivatives of the kth inverter output currents in the system with $k \in \{2, \cdots, N\}$, can be obtained as

$$\frac{d}{dt}\begin{pmatrix} i_{d1} \\ i_{q1} \end{pmatrix} = \begin{pmatrix} \frac{-r_{f1}}{L_{f1}} & \omega \\ -\omega & \frac{-r_{f1}}{L_{f1}} \end{pmatrix} \cdot \begin{pmatrix} i_{d1} \\ i_{q1} \end{pmatrix} + \frac{1}{L_{f1}}\begin{pmatrix} V_{d1} \\ V_{q1} \end{pmatrix} - \frac{1}{L_{f1}}\begin{pmatrix} V_{cd} \\ V_{cq} \end{pmatrix} \tag{2.24}$$

$$\frac{d}{dt}\begin{pmatrix} i_{0k} \\ i_{dk} \\ i_{qk} \end{pmatrix} = \begin{pmatrix} \frac{-r_{fk}}{L_{fk}} & 0 & 0 \\ 0 & \frac{-r_{fk}}{L_{fk}} & \omega \\ 0 & -\omega & \frac{-r_{fk}}{L_{fk}} \end{pmatrix} \cdot \begin{pmatrix} i_{0k} \\ i_{dk} \\ i_{qk} \end{pmatrix} + \frac{1}{L_{fk}}\begin{pmatrix} V_{0k} \\ V_{dk} \\ V_{qk} \end{pmatrix} - \frac{1}{L_{fk}}\begin{pmatrix} V_{c0} \\ V_{cd} \\ V_{cq} \end{pmatrix} \tag{2.25}$$

where the variables V_{0k}, V_{dk} and V_{qk} are the controlled voltages of the kth inverter in the system of N-parallel inverters.

2.3.2 Control strategy for parallel-inverters

A one-loop Flatness-based control (FBC) is presented for controlling the system of N-parallel inverters. The FBC strategy was introduced in section 2.2 where the chosen candidate flat output was the voltage across the output filter capacitor. Of course, the flat output may include any other variables of the system depending on the control purposes. For this control objectives, we are going to choose two different flat outputs and verify that the Flatness-based control still efficient in both cases.

2.3.2.1 System modeling with Capacitor voltage as Flat output

The flat output vector y is defined as $y = [y_c,\, y_z]^t$, where the first part $y_c = [y_d,\, y_q]^t$ is defined by the dq voltage across the ac capacitor output filter

$$y_c = \begin{pmatrix} y_d \\ y_q \end{pmatrix} = \begin{pmatrix} V_{cd} \\ V_{cq} \end{pmatrix} \tag{2.26}$$

The second part of the candidate flat output vector y corresponds to the current error vector y_z, which represents the current errors referred to the reference. Each component of y_z allows to minimize the circulating currents and to balance the powers between the ith reference inverter and all other kth working inverters. The current error vector $y_z = [y_{z1},\, y_{z2}, \ldots, y_{zi-1},\, y_{zi+1}, \ldots, y_{zN}]^t$ and its components y_{zk}, $\forall k \in \{1, \ldots, N\}$, $k \neq i$ are expressed as

$$y_{zk} = \begin{pmatrix} y_{z0k} \\ y_{zdk} \\ y_{zqk} \end{pmatrix} = \begin{pmatrix} z_{0k} \\ z_{dk} \\ z_{qk} \end{pmatrix} = \begin{pmatrix} i_{0k} \\ i_{di} - i_{dk} \\ i_{qi} - i_{qk} \end{pmatrix} = \phi_{yzk}(x) \tag{2.27}$$

The flat output $y = [y_c,\, y_z]^t$ can be written in the form

$$y = \begin{pmatrix} y_c \\ y_z \end{pmatrix} = \begin{pmatrix} V_{cd} \\ V_{cq} \\ i_{01} \\ i_{di} - i_{d1} \\ i_{qi} - i_{q1} \\ \vdots \\ i_{0k} \\ i_{di} - i_{dk} \\ i_{qi} - i_{qk} \end{pmatrix} = \begin{pmatrix} \phi_{yc}(x) \\ \phi_{yz1}(x) \\ \vdots \\ \phi_{yzk}(x) \end{pmatrix} \; \forall k \in \{1, \ldots, N\},\, k \neq i \tag{2.28}$$

where, $x = [V_{cd}, V_{cq}, i_{01}, i_{d1}, i_{q1}, \ldots, i_{di}, i_{qi}, \ldots i_{0k}, i_{dk}, i_{qk}]^t$, $dim(x) = 3N + 1$ is the state variables vector. Equation (2.23), the derivative of the voltage vector $[V_{cd},\, V_{cq}]^t$, can be rewritten as:

$$\begin{pmatrix} \dot{V}_{cd} \\ \dot{V}_{cq} \end{pmatrix} = \begin{pmatrix} \dot{y}_d \\ \dot{y}_q \end{pmatrix} = \begin{pmatrix} 0 & \omega \\ -\omega & 0 \end{pmatrix} \begin{pmatrix} y_d \\ y_q \end{pmatrix} + \frac{1}{C_f} \left(\begin{pmatrix} N.i_{di} - \sum\limits_{\substack{k=1 \\ k\neq i}}^{N} z_{dk} \\ N.i_{qi} - \sum\limits_{\substack{k=1 \\ k\neq i}}^{N} z_{qk} \end{pmatrix} - \begin{pmatrix} i_{Ld} \\ i_{Lq} \end{pmatrix} \right) \tag{2.29}$$

Thus, the ith inverter output currents $[i_{di},\, i_{qi}]^t$ can be expressed as function of y_c and its derivative $\dot{y}_c$ and y_{zk}

$$\begin{pmatrix} i_{di} \\ i_{qi} \end{pmatrix} = \frac{1}{N} \begin{pmatrix} C_f \dot{y}_d + \sum\limits_{\substack{k=1 \\ k\neq i}}^{N} z_{dk} + i_{Ld} \\ C_f \dot{y}_q + \sum\limits_{\substack{k=1 \\ k\neq i}}^{N} z_{qk} + i_{Lq} \end{pmatrix} - \begin{pmatrix} 0 & \omega C_f/N \\ -\omega C_f/N & 0 \end{pmatrix} \begin{pmatrix} V_{cd} \\ V_{cq} \end{pmatrix} = \begin{pmatrix} \varphi_{id_i}(y_c, \dot{y}_c, y_z) \\ \varphi_{iq_i}(y_c, \dot{y}_c, y_z) \end{pmatrix} \tag{2.30}$$

The expression of the output currents for the remaining inverters $i_{0dqk} (k \in \{1, \ldots, N\}, k \neq i)$ can be derived using (2.37) and (2.30) as

$$\begin{pmatrix} i_{0k} \\ i_{dk} \\ i_{qk} \end{pmatrix} = \begin{pmatrix} z_{0k} \\ \varphi_{i_{di}}(y_c,\, \dot{y}_c,\, y_z) - z_{dk} \\ \varphi_{i_{qi}}(y_c,\, \dot{y}_c,\, y_z) - z_{qk} \end{pmatrix} = \begin{pmatrix} \varphi_{i_{0k}}(y_{zk}) \\ \varphi_{i_{dk}}(y_c,\, \dot{y}_c,\, y_{zk}) \\ \varphi_{i_{qk}}(y_c,\, \dot{y}_c,\, y_{zk}) \end{pmatrix} \tag{2.31}$$

Thus, the system state vector $x = [V_{cd}, V_{cq}, i_{01}, i_{d1}, i_{q1}, \ldots, i_{di}, i_{qi}, \ldots i_{0k}, i_{dk}, i_{qk}]^t$, $dim(x) = 3N + 1$, can be redefined as function of the flat output vector y as:

$$\begin{pmatrix} V_{cd} \\ V_{cq} \\ i_{01} \\ i_{d1} \\ i_{q1} \\ \vdots \\ i_{di} \\ i_{qi} \\ \vdots \\ i_{0k} \\ i_{dk} \\ i_{qk} \end{pmatrix} = \begin{pmatrix} y_d \\ y_q \\ \varphi_{i_{01}}(y_{z1}) \\ \varphi_{i_{d1}}(y_c,\, \dot{y}_c,\, y_{z1}) \\ \varphi_{i_{q1}}(y_c,\, \dot{y}_c,\, y_{z1}) \\ \vdots \\ \varphi_{i_{di}}(y_c,\, \dot{y}_c,\, y_z) \\ \varphi_{i_{qi}}(y_c,\, \dot{y}_c,\, y_z) \\ \vdots \\ \varphi_{i_{0k}}(y_{zk}) \\ \varphi_{i_{dk}}(y_c,\, \dot{y}_c,\, y_{zk}) \\ \varphi_{i_{qk}}(y_c,\, \dot{y}_c,\, y_{zk}) \end{pmatrix}$$

The derivatives of the reference inverter output currents (ith inverter) can be obtained by using (2.30) as:

$$\frac{d}{dt}\begin{pmatrix} i_{di} \\ i_{qi} \end{pmatrix} = \frac{1}{N}\begin{pmatrix} C_f\ddot{y}_d + \sum_{\substack{k=1 \\ k\neq i}}^{N} \dot{z}_{dk} + \frac{d}{dt}i_{Ld} \\ C_f\ddot{y}_q + \sum_{\substack{k=1 \\ k\neq i}}^{N} \dot{z}_{qk} + \frac{d}{dt}i_{Lq} \end{pmatrix} - \begin{pmatrix} 0 & \omega C_f/N \\ -\omega C_f/N & 0 \end{pmatrix}\begin{pmatrix} \dot{y}_d \\ \dot{y}_q \end{pmatrix}$$
$$= \begin{pmatrix} \varphi_{di_{di}}(y_c, \dot{y}_c, \ddot{y}_c, y_z, \dot{y}_z) \\ \varphi_{di_{qi}}(y_c, \dot{y}_c, \ddot{y}_c, y_z, \dot{y}_z) \end{pmatrix} \tag{2.32}$$

The derivatives of the remaining output currents, $i_{0dqk}\, \forall k \in \{1, \ldots, N\}$, $k \neq i$, verify

$$\frac{d}{dt}\begin{pmatrix} i_{0k} \\ i_{dk} \\ i_{qk} \end{pmatrix} = \begin{pmatrix} \dot{z}_{0k} \\ \varphi_{di_{di}}(y_c,\, \dot{y}_c,\, \ddot{y}_c,\, y_z,\, \dot{y}_z) - \dot{z}_{dk} \\ \varphi_{di_{qi}}(y_c,\, \dot{y}_c,\, \ddot{y}_c,\, y_z,\, \dot{y}_z) - \dot{z}_{qk} \end{pmatrix}$$
$$= \begin{pmatrix} \varphi_{di_{0k}}(\dot{y}_z) \\ \varphi_{di_{dk}}(y_c,\, \dot{y}_c,\, \ddot{y}_c,\, y_z,\, \dot{y}_z) \\ \varphi_{di_{qk}}(y_c,\, \dot{y}_c,\, \ddot{y}_c,\, y_z,\, \dot{y}_z) \end{pmatrix} \tag{2.33}$$

From (2.30)-(2.33), the output currents and their corresponding derivatives are found as function of the candidate flat output as being presented in Chapter 1, Eq. (1.1). The input controlled vector $u = [V_{di},\, V_{qi}, \ldots, V_{0k},\, V_{dk},\, V_{qk}]^t$ can be obtained as

$$\begin{pmatrix} V_{di} \\ V_{qi} \end{pmatrix} = L_{fi}\begin{pmatrix} \varphi_{di_{di}} \\ \varphi_{di_{qi}} \end{pmatrix} - L_{fi}\begin{pmatrix} \frac{-r_{fi}}{L_{fi}} & \omega \\ -\omega & \frac{-r_{fi}}{L_{fi}} \end{pmatrix}\begin{pmatrix} \varphi_{i_{di}} \\ \varphi_{i_{qi}} \end{pmatrix}$$
$$+ \begin{pmatrix} \varphi_{V_{cd}} \\ \varphi_{V_{cq}} \end{pmatrix} = \begin{pmatrix} \psi_{V_{di}}(y_c,\, \dot{y}_c,\, \ddot{y}_c,\, y_z,\, \dot{y}_z) \\ \psi_{V_{qi}}(y_c,\, \dot{y}_c,\, \ddot{y}_c,\, y_z,\, \dot{y}_z) \end{pmatrix} \tag{2.34}$$

With the same procedure, the input vector for the remaining $N-1$ inverters ($\forall k \in \{1, \ldots, N\}$, $k \neq i$) can be obtained as

$$\begin{pmatrix} V_{0k} \\ V_{dk} \\ V_{qk} \end{pmatrix} = L_{fk}\begin{pmatrix} \varphi_{di_{0k}} \\ \varphi_{di_{dk}} \\ \varphi_{di_{qk}} \end{pmatrix} - L_{fk}\begin{pmatrix} \frac{-r_{fk}}{L_{fk}} & 0 & 0 \\ 0 & \frac{-r_{fk}}{L_{fk}} & \omega \\ 0 & -\omega & \frac{-r_{fk}}{L_{fk}} \end{pmatrix} \times \begin{pmatrix} \varphi_{i_{0k}} \\ \varphi_{i_{dk}} \\ \varphi_{i_{qk}} \end{pmatrix}$$
$$+ \begin{pmatrix} V_{c0} \\ \varphi_{V_{cd}} \\ \varphi_{V_{cq}} \end{pmatrix} = \begin{pmatrix} \psi_{V_{0k}}(y_z,\, \dot{y}_z) \\ \psi_{V_{dk}}(y_c,\, \dot{y}_c,\, \ddot{y}_c,\, y_z,\, \dot{y}_z) \\ \psi_{V_{qk}}(y_c,\, \dot{y}_c,\, \ddot{y}_c,\, y_z,\, \dot{y}_z) \end{pmatrix} \tag{2.35}$$

Thus, the differential flatness property expressed early in Chapter 1, equation (1.1) are verified by (2.28), (2.30), (2.31), (2.34) and (2.35). We can consider the modeled system as flat, with vector $y = [y_c, y_z]^t$ being the flat output associated with the input

vector $u = [V_{01}, V_{d1}, V_{q1}, \cdots, V_{di}, V_{qi}, \cdots, V_{0k}, V_{dk}, V_{qk}]^t$, where $y_c = [V_{cd}, V_{cq}]^t$ is the output capacitor voltages. In the next subsection, we are going to demonstrate that another flat output can be considered for modeling the system. The flatness property will be verified by ensuring equation (**??**) with the control of the flat output to its reference. The reference trajectory planning algorithm and the control law are given after to complete the synthesis of the control process.

2.3.2.2 System modeling with Electrostatic Energy as Flat output

The electrostatic energy and the current error vector between the parallel inverters are chosen as the candidate flat outputs to regulate the output ac-voltage and balance the currents between the parallel inverters. The flat output vector y is defined as $y = [y_c,\, y_z]^t$, where the first part $y_c = [y_d,\, y_q]^t$ is defined by the dq electrostatic energies stored in the ac capacitor output filter

$$y_c = \begin{pmatrix} y_d \\ y_q \end{pmatrix} = \frac{1}{2} C_f \begin{pmatrix} sign(V_{cd}) \cdot V_{cd}^2 \\ sign(V_{cq}) \cdot V_{cq}^2 \end{pmatrix} = \phi_{yc}(x) \tag{2.36}$$

There is no difference regarding the second part of the candidate flat output y_z, which is defined as the current error vector. The expression of y_z remains as

$$y_{zk} = \begin{pmatrix} y_{z0k} \\ y_{zdk} \\ y_{zqk} \end{pmatrix} = \begin{pmatrix} z_{0k} \\ z_{dk} \\ z_{qk} \end{pmatrix} = \begin{pmatrix} i_{0k} \\ i_{di} - i_{dk} \\ i_{qi} - i_{qk} \end{pmatrix} = \phi_{yzk}(x) \tag{2.37}$$

The flat output $y = [y_c,\, y_z]^t$ can be written in the form

$$y = \begin{pmatrix} y_c \\ y_z \end{pmatrix} = \begin{pmatrix} \frac{1}{2} C_f \cdot sign(V_{cd}) \cdot V_{cd}^2 \\ \frac{1}{2} C_f \cdot sign(V_{cq}) \cdot V_{cq}^2 \\ i_{01} \\ i_{di} - i_{d1} \\ i_{qi} - i_{q1} \\ \vdots \\ i_{0k} \\ i_{di} - i_{dk} \\ i_{qi} - i_{qk} \end{pmatrix} = \begin{pmatrix} \phi_{yc}(x) \\ \phi_{yz1}(x) \\ \vdots \\ \phi_{yzk}(x) \end{pmatrix} \quad \forall k \in \{1, \ldots, N\},\, k \neq i \tag{2.38}$$

Using $y_c = [y_d,\, y_q]^t$ given by (2.36), the output voltage vector $[V_{cd},\, V_{cq}]^t$ can be redefined as a function of the flat output vector y_c regarding the sign of the energy vector y_c as

$$\begin{pmatrix} V_{cd} \\ V_{cq} \end{pmatrix} = \begin{pmatrix} sign(y_d)\sqrt{2y_d/C_f} \\ sign(y_q)\sqrt{2y_q/C_f} \end{pmatrix} = \begin{pmatrix} \varphi_{V_{cd}}(y_d) \\ \varphi_{V_{cq}}(y_q) \end{pmatrix} \tag{2.39}$$

From (2.23) and (2.39), the derivative of the voltage vector $[V_{cd},\, V_{cq}]^t$ can be expressed as:

$$\begin{pmatrix} \dot{V}_{cd} \\ \dot{V}_{cq} \end{pmatrix} = \begin{pmatrix} 0 & \omega \\ -\omega & 0 \end{pmatrix} \begin{pmatrix} \varphi_{V_{cd}}(y_d) \\ \varphi_{V_{cq}}(y_q) \end{pmatrix} + \frac{1}{C_f} \left(\begin{pmatrix} \sum_{j=1}^{N} i_{dj} \\ \sum_{j=1}^{N} i_{qj} \end{pmatrix} - \begin{pmatrix} i_{Ld} \\ i_{Lq} \end{pmatrix} \right) \tag{2.40}$$

Globally, from (2.39) and (2.40), the ith inverter output currents $[i_{di},\, i_{qi}]^t$ can be expressed as function of y_c and its derivative $\dot{y}_c$ and y_{zk}

$$\begin{aligned} \begin{pmatrix} i_{di} \\ i_{qi} \end{pmatrix} &= \frac{1}{N} \begin{pmatrix} sign(y_d)\dot{y}_d/\sqrt{2y_d/C_f} + \sum_{\substack{k=1 \\ k\neq i}}^{N} z_{dk} + i_{Ld} \\ sign(y_q)\dot{y}_q/\sqrt{2y_q/C_f} + \sum_{\substack{k=1 \\ k\neq i}}^{N} z_{qk} + i_{Lq} \end{pmatrix} \\ &\quad - \begin{pmatrix} 0 & \frac{\omega C_f}{N} \\ \frac{-\omega C_f}{N} & 0 \end{pmatrix} \begin{pmatrix} sign(y_d)\sqrt{2y_d/C_f} \\ sign(y_q)\sqrt{2y_q/C_f} \end{pmatrix} = \begin{pmatrix} \varphi_{i_{di}}(y_c,\, \dot{y}_c,\, y_z) \\ \varphi_{i_{qi}}(y_c,\, \dot{y}_c,\, y_z) \end{pmatrix} \end{aligned} \tag{2.41}$$

The expression of the output currents for the remaining inverters $i_{0dqk}(k \in \{1, \ldots, N\}, k \neq i)$ can be derived using (2.37) and (2.41) as

$$\begin{pmatrix} i_{0k} \\ i_{dk} \\ i_{qk} \end{pmatrix} = \begin{pmatrix} z_{0k} \\ \varphi_{i_{di}}(y_c,\, \dot{y}_c,\, y_z) - z_{dk} \\ \varphi_{i_{qi}}(y_c,\, \dot{y}_c,\, y_z) - z_{qk} \end{pmatrix} = \begin{pmatrix} \varphi_{i_{0k}}(y_{zk}) \\ \varphi_{i_{dk}}(y_c,\, \dot{y}_c,\, y_{zk}) \\ \varphi_{i_{qk}}(y_c,\, \dot{y}_c,\, y_{zk}) \end{pmatrix} \tag{2.42}$$

Thus, the system state vector $x = [V_{cd}, V_{cq}, i_{01}, i_{d1}, i_{q1}, \ldots, i_{di}, i_{qi}, \ldots i_{0k}, i_{dk}, i_{qk}]^t$, $dim(x) = 3N + 1$, can be redefined as function of the flat output vector y as

$$\begin{pmatrix} V_{cd} \\ V_{cq} \\ i_{01} \\ i_{d1} \\ i_{q1} \\ \vdots \\ i_{di} \\ i_{qi} \\ \vdots \\ i_{0k} \\ i_{dk} \\ i_{qk} \end{pmatrix} = \begin{pmatrix} \varphi_{V_{cd}}(y_d) \\ \varphi_{V_{cq}}(y_q) \\ \varphi_{i_{01}}(y_{z1}) \\ \varphi_{i_{d1}}(y_c,\, \dot{y}_c,\, y_{z1}) \\ \varphi_{i_{q1}}(y_c,\, \dot{y}_c,\, y_{z1}) \\ \vdots \\ \varphi_{i_{di}}(y_c,\, \dot{y}_c,\, y_z) \\ \varphi_{i_{qi}}(y_c,\, \dot{y}_c,\, y_z) \\ \vdots \\ \varphi_{i_{0k}}(y_{zk}) \\ \varphi_{i_{dk}}(y_c,\, \dot{y}_c,\, y_{zk}) \\ \varphi_{i_{qk}}(y_c,\, \dot{y}_c,\, y_{zk}) \end{pmatrix}$$

The derivatives of the reference inverter output currents (ith inverter) can be obtained by using (2.40) and (2.41) as:

$$\frac{d}{dt}\begin{pmatrix} i_{di} \\ i_{qi} \end{pmatrix} = \frac{1}{N}\left(\begin{array}{c} \begin{pmatrix} \frac{sign(y_d)\ddot{y}_d}{V_{cd}} - \frac{sign(y_d)\dot{y}_d}{C_f V_{cd}^2}\left(\sum_{j=1}^{N} i_{dj} - i_{Ld} + \omega C_f V_{cq}\right) \\ \frac{sign(y_q)\ddot{y}_q}{V_{cq}} - \frac{sign(y_q)\dot{y}_q}{C_f V_{cq}^2}\left(\sum_{j=1}^{N} i_{qj} - i_{Lq} - \omega C_f V_{cd}\right) \end{pmatrix} \\ + \begin{pmatrix} \sum_{\substack{k=1 \\ k\neq i}}^{N} \dot{z}_{dk} + \frac{d}{dt} i_{Ld} \\ \sum_{\substack{k=1 \\ k\neq i}}^{N} \dot{z}_{qk} + \frac{d}{dt} i_{Lq} \end{pmatrix} - \begin{pmatrix} 0 & \omega \\ -\omega & 0 \end{pmatrix} \begin{pmatrix} \left(\sum_{j=1}^{N} i_{dj} - i_{Ld} + \omega C_f V_{cq}\right) \\ \left(\sum_{j=1}^{N} i_{qj} - i_{Lq} - \omega C_f V_{cd}\right) \end{pmatrix} \end{array} \right)$$
$$= \begin{pmatrix} \varphi_{di_{di}}(y_c,\, \dot{y}_c,\, \ddot{y}_c,\, y_z,\, \dot{y}_z) \\ \varphi_{di_{qi}}(y_c,\, \dot{y}_c,\, \ddot{y}_c,\, y_z,\, \dot{y}_z) \end{pmatrix} \tag{2.43}$$

The derivatives of the remaining output currents, $i_{0dqk}\, \forall k \in \{1, \ldots, N\}$, $k \neq i$, verify

$$\begin{aligned} \frac{d}{dt}\begin{pmatrix} i_{0k} \\ i_{dk} \\ i_{qk} \end{pmatrix} &= \begin{pmatrix} \dot{z}_{0k} \\ \varphi_{di_d}(y_c,\, \dot{y}_c,\, \ddot{y}_c,\, y_z,\, \dot{y}_z) - \dot{z}_{dk} \\ \varphi_{di_q}(y_c,\, \dot{y}_c,\, \ddot{y}_c,\, y_z,\, \dot{y}_z) - \dot{z}_{qk} \end{pmatrix} \\ &= \begin{pmatrix} \varphi_{di_{0k}}(\dot{y}_z) \\ \varphi_{di_{dk}}(y_c,\, \dot{y}_c,\, \ddot{y}_c,\, y_z,\, \dot{y}_z) \\ \varphi_{di_{qk}}(y_c,\, \dot{y}_c,\, \ddot{y}_c,\, y_z,\, \dot{y}_z) \end{pmatrix} \end{aligned} \tag{2.44}$$

From (2.41)-(2.44), the output currents and their corresponding derivatives are found as function of the candidate flat output as being presented in (1.1). The input controlled vector $u = [V_{di},\, V_{qi}, \ldots, V_{0k},\, V_{dk},\, V_{qk}]^t$ can be obtained as

$$\begin{aligned} \begin{pmatrix} V_{di} \\ V_{qi} \end{pmatrix} &= L_{fi}\begin{pmatrix} \varphi_{di_{di}} \\ \varphi_{di_{qi}} \end{pmatrix} - L_{fi}\begin{pmatrix} \frac{-r_{fi}}{L_{fi}} & \omega \\ -\omega & \frac{-r_{fi}}{L_{fi}} \end{pmatrix}\begin{pmatrix} \varphi_{i_{di}} \\ \varphi_{i_{qi}} \end{pmatrix} \\ &\quad + \begin{pmatrix} \varphi_{V_{cd}} \\ \varphi_{V_{cq}} \end{pmatrix} = \begin{pmatrix} \psi_{V_{di}}(y_c,\, \dot{y}_c,\, \ddot{y}_c,\, y_z,\, \dot{y}_z) \\ \psi_{V_{qi}}(y_c,\, \dot{y}_c,\, \ddot{y}_c,\, y_z,\, \dot{y}_z) \end{pmatrix} \end{aligned} \tag{2.45}$$

With the same procedure, the input vector for the remaining $N-1$ inverters ($\forall k \in \{1, \ldots, N\}$, $k \neq i$) can be obtained as

$$\begin{aligned} \begin{pmatrix} V_{0k} \\ V_{dk} \\ V_{qk} \end{pmatrix} &= L_{fk}\begin{pmatrix} \varphi_{di_{0k}} \\ \varphi_{di_{dk}} \\ \varphi_{di_{qk}} \end{pmatrix} - L_{fk}\begin{pmatrix} \frac{-r_{fk}}{L_{fk}} & 0 & 0 \\ 0 & \frac{-r_{fk}}{L_{fk}} & \omega \\ 0 & -\omega & \frac{-r_{fk}}{L_{fk}} \end{pmatrix} \times \begin{pmatrix} \varphi_{i_{0k}} \\ \varphi_{i_{dk}} \\ \varphi_{i_{qk}} \end{pmatrix} \\ &\quad + \begin{pmatrix} V_{c0} \\ \varphi_{V_{cd}} \\ \varphi_{V_{cq}} \end{pmatrix} = \begin{pmatrix} \psi_{V_{0k}}(y_z,\, \dot{y}_z) \\ \psi_{V_{dk}}(y_c,\, \dot{y}_c,\, \ddot{y}_c,\, y_z,\, \dot{y}_z) \\ \psi_{V_{qk}}(y_c,\, \dot{y}_c,\, \ddot{y}_c,\, y_z,\, \dot{y}_z) \end{pmatrix} \end{aligned} \tag{2.46}$$

If one inverter (including the reference one) or more of the parallel modules are disconnected under normal or faulty condition, the previous analysis is always valid and the rank of the state vector x will be reduced by $3f$, where f is the number of the faulty inverters (i.e., $x \in R^{n-3f}$). The ranks of the flat output vector y and the input u will also be reduced by $3f$, but the rank of y_c rests the same (i.e., $y \in R^{m-3f}$). When the reference inverter (the first one by example) is fully disconnected, the current expression given by (2.43) will be referred to the next inverter (by example, the second one). Consequently, (2.37) will be referred to the new reference. The flatness conditions can always be verified for the studied system with the reduced state and input vectors associated with the candidate flat output y regarding the new vector y_{zk}. The reference $y_{zk_{ref}}$ of the current error vector y_{zk} is assumed to be zero in normal case (i.e., $z_{0k_{ref}} = z_{dk_{ref}} = z_{qk_{ref}} = 0$). This choice minimizes the circulating currents and ensures that the total power is equally distributed between the parallel inverters. When one inverter (number j for example) of the parallel system is fully disconnected, the reference $y_{zj_{ref}}$ of the current error vector y_{zj} becomes equal to the reference inverter currents (i.e., $z_{0j_{ref}} = 0$, $z_{dj_{ref}} = i_{di}$, $z_{qj_{ref}} = i_{qi}$). Thus, in the case of healthy or faulty conditions of any inverter in the parallel system, the relations (2.41) and (2.43) can always be used. For both cases, the reference of y_c is calculated as

$$y_{c_{ref}} = \begin{pmatrix} y_{d_{ref}} \\ y_{q_{ref}} \end{pmatrix} = \frac{1}{2} C_f \begin{pmatrix} V_{cd_{ref}}^2 \\ V_{cq_{ref}}^2 \end{pmatrix} \tag{2.47}$$

where $V_{cd_{ref}} = V_{cq_{ref}} = V_{rms}\sqrt{3/2}$ and V_{rms} represents the RMS value of the reference output voltage of theLC filter.

The last step consists of the formulation of the input vector u as function of the candidate flat output references $y_{ref} = [y_{c_{ref}}, y_{z_{ref}}]^t$ and their respective derivatives. The relations (2.45) and (2.46) can be expressed for each active inverter as

$$\begin{pmatrix} V_{di} \\ V_{qi} \end{pmatrix} = \begin{pmatrix} \psi_{V_{di}}(y_{c_{ref}}, \dot{y}_{c_{ref}}, \ddot{y}_{c_{ref}}, y_{z_{ref}}, \dot{y}_{z_{ref}}) \\ \psi_{V_{qi}}(y_{c_{ref}}, \dot{y}_{c_{ref}}, \ddot{y}_{c_{ref}}, y_{z_{ref}}, \dot{y}_{z_{ref}}) \end{pmatrix} \tag{2.48}$$

$$\begin{pmatrix} V_{0k} \\ V_{dk} \\ V_{qk} \end{pmatrix} = \begin{pmatrix} \psi_{V_{0k}}(y_{zk_{ref}}, \dot{y}_{zk_{ref}}) \\ \psi_{V_{dk}}(y_{c_{ref}}, \dot{y}_{c_{ref}}, \ddot{y}_{c_{ref}}, y_{zk_{ref}}, \dot{y}_{zk_{ref}}) \\ \psi_{V_{qk}}(y_{c_{ref}}, \dot{y}_{c_{ref}}, \ddot{y}_{c_{ref}}, y_{zk_{ref}}, \dot{y}_{zk_{ref}}) \end{pmatrix} \tag{2.49}$$

2.3.2.3 Reference Trajectory

To plan the desired trajectory of the candidate flat output y and consequently their sub-respective components as given by (2.36) and (2.37), a second order low-pass filter is used, which allows limiting the power during transient state due to the variations of the voltage reference value V_{rms}. This formulation, allows respecting the conditions of the candidate flat output derivatives at initial and steady states. At these instants, the values of these derivatives have to be zero. Therefore, the desired reference trajectory $y_{ref} = [y_{c_{ref}}, y_{z_{ref}}]^t \forall k \in \{1, \ldots, N\}$, $k \neq i$ can be expressed as

$$y_{c_{ref-f}} = \left(1 - \left(1 + \frac{t - t_{initc}}{\tau_c}\right) e^{-\frac{t-t_{initc}}{\tau_c}}\right) \times (y_{c_{ref}} - y_{c_{init}}) + y_{c_{init}} \tag{2.50}$$

$$y_{zk_{ref-f}} = \left(1 - \left(1 + \frac{t - t_{initz}}{\tau_z}\right) e^{-\frac{t-t_{initz}}{\tau_z}}\right) \times (y_{zkref} - y_{zk_{init}}) + y_{zk_{init}} \tag{2.51}$$

where t and $t_{initc/z}$ represent the time and the initial time for both reference trajectories, respectively. τ_c and τ_z are the time constants of the planned reference trajectories for the electrostatic energy and the current error.

2.3.2.4 Control law and Linearization

To ensure the control of both flat output components y_c and y_{zk} to their respective reference trajectories $y_{c_{ref}}$ and $y_{zk_{ref}}$ for the healthy and faulty conditions, the classical input-output linearization is used. Feedback linearization is a common approach used in the control of nonlinear systems and it is well applied to the nonlinear parallel inverters system. This technique consists of introducing fictitious control variables $\gamma_c = [\gamma_d, \gamma_q]^t$ associated to the output energy vector and $\gamma_z = [\gamma_{z1}, \ldots, \gamma_{zi-1}, \gamma_{zi+1}, \ldots, \gamma_{zN}]^t$ to the current error vector. For the output energy vector, the fictitious control variable can be expressed as

$$\begin{cases} \gamma_d = & \ddot{y}_d \\ \gamma_q = & \ddot{y}_q \end{cases} \tag{2.52}$$

These control laws allow an asymptotic convergence of the measured variables to their respective reference trajectories and can be deduced as

$$(\ddot{y}_{d_{ref}} - \gamma_d) + k_{11}(\dot{y}_{d_{ref}} - \dot{y}_d) + k_{12}(y_{d_{ref}} - y_d) + k_{13} \int (y_{d_{ref}} - y_d) d\tau = 0 \tag{2.53}$$

$$(\ddot{y}_{qref} - \gamma_q) + k_{11}(\dot{y}_{q_{ref}} - \dot{y}_q) + k_{12}(y_{q_{ref}} - y_q) + k_{13} \int (y_{q_{ref}} - y_q) d\tau = 0 \tag{2.54}$$

The integral term is introduced to ensure zero static error in steady state and to compensate the effects introduced by the system modeling errors. For each current error vector y_{zk}, the fictitious control variable $\gamma_{zk} = [\gamma_{z0k}, \gamma_{zdk}, \gamma_{zqk}]^t$ is expressed in the same way as

$$\gamma_{zk} = \begin{cases} \dot{z}_{0k} = & \gamma_{z0k} \\ \dot{z}_{dk} = & \gamma_{zdk} \\ \dot{z}_{qk} = & \gamma_{zqk} \end{cases} \forall k \in \{1, \ldots, N\},\ k \neq i. \tag{2.55}$$

Second-order laws are used to ensure that the current error vector y_{zk} follows its planned reference $y_{zk_{ref}}$:

$$(\dot{y}_{zk_{ref}} - \gamma_{zk}) + k_{21}(y_{zk_{ref}} - y_{zk}) + k_{22}\int (y_{zk_{ref}} - y_{zk})d\tau = 0 \tag{2.56}$$

To simplify (2.53), (2.54) and (2.56), a variable ϵ is introduced to express the dynamics of the error

$$\dddot{\epsilon}_{y_c} + k_{11}\ddot{\epsilon}_{y_c} + k_{12}\dot{\epsilon}_{y_c} + k_{13}\epsilon_{y_c} = 0 \tag{2.57}$$

$$\ddot{\epsilon}_{y_{zk}} + k_{21}\dot{\epsilon}_{y_{zk}} + k_{22}\epsilon_{y_{zk}} = 0 \tag{2.58}$$

where, $\epsilon_{y_c} = y_{c_{ref}} - y_c$ and $\epsilon_{y_{zk}} = y_{zk_{ref}} - y_{zk}$.

The parallel system operating point will be stable if the coefficients $k_{11}, k_{12}, k_{13}, k_{21}, k_{22}$ are strictly positive values. The dynamics of the system will be fixed by these gains associated with the control laws. To determine the values of the gain coefficients, a classical pole placement method is used thanks to a comparison between the characteristic polynomials associated to (2.57) and (2.58) with the polynomials given by (2.59):

$$\begin{cases} p_{y_c}(s) = & (s + p_1)(s^2 + 2\xi\omega_n \cdot s + \omega_n^2) \\ p_{y_z}(s) = & (s^2 + 2\xi\omega_n \cdot s + \omega_n^2) \end{cases} \tag{2.59}$$

Therefore, the control gain parameters can be defined as

$$\begin{cases} k_{11} = & 2\xi_c\omega_{y_c} + p_1 \\ k_{12} = & 2\xi_c\omega_{y_c} \cdot p_1 + \omega_{y_c}^2 \\ k_{13} = & p_1 \cdot \omega_{y_c}^2 \end{cases} \tag{2.60}$$

$$\begin{cases} k_{21} = & 2\xi_z\omega_{y_z} \\ k_{22} = & \omega_{y_z}^2 \end{cases} \tag{2.61}$$

It is possible to get formulation of u in closed loop by

$$\begin{pmatrix} V_{di} \\ V_{qi} \end{pmatrix} = \begin{pmatrix} \psi_{V_{di}}(y_{c_{ref-f}}, \dot{y}_{c_{ref-f}}, \gamma_c, y_{z_{ref-f}}, \gamma_z) \\ \psi_{V_{qi}}(y_{c_{ref-f}}, \dot{y}_{c_{ref-f}}, \gamma_c, y_{z_{ref-f}}, \gamma_z) \end{pmatrix} \tag{2.62}$$

$$\begin{pmatrix} V_{0k} \\ V_{dk} \\ V_{qk} \end{pmatrix} = \begin{pmatrix} \psi_{V_{0k}}(y_{zk_{ref-f}}, \gamma_z) \\ \psi_{V_{dk}}(y_{c_{ref-f}}, \dot{y}_{c_{ref-f}}, \gamma_c, y_{z_{ref-f}}, \gamma_z) \\ \psi_{V_{qk}}(y_{c_{ref-f}}, \dot{y}_{c_{ref-f}}, \gamma_c, y_{z_{ref-f}}, \gamma_z) \end{pmatrix} \tag{2.63}$$

2.3.3 Simulation Results

To validate the proposed control method in both cases with different selection of flat output, a model of three parallel inverters, based on MATLAB-Simulink, has been performed (i.e., $N = 3$). The system parameters and the control gains which are associated to the voltage, energy and current balancing trajectories are listed in Table 2.3.

First, the system model with output capacitor voltage as flat output is tested. Figure 2.6 shows the behavior of the capacitor voltages flat output y_d and y_q that corresponds

to V_{cd} and V_{cq} under normal condition with a reference step rms-voltage from 90 to 110V at $t = 50$ms. The measured components follow perfectly their reference trajectories. As shown in Fig. , the current error in dq frame between inverter 1 and 2 is zero as exposed by the reference value, which indicates that the current controller effectively supress the circulating current between parallel inverters.

System parameters	
DC side line inductance	$L = 400\mu$H, $r_L = 0.2\Omega$
Output ac filter inductances	$L_1 = L_2 = L_3 = 1$mH, $r_1 = r_2 = r_3 = 0.7\Omega$
DC bus capacitance	$C_{dc} = 1100\mu$F
AC output voltage	110 V-60 Hz
DC input voltage	500 V
Switching frequency	$f_{sw} = 15$ kHz
Voltage/Energy control dynamics	$\xi_c = 0.7$, $\omega_{y_c} = 5000$ rad/s, $p_1 = 6000$ rad/s
Current control dynamics	$\xi_z = 0.7$, $\omega_{y_z} = 5000$ rad/s
Time constant (τ_c) for voltage/energy trajectory filter	1 ms
Time constant (τ_z) for current trajectory filter	10 ms

Table 2.3: Parallel inverters system parameters.

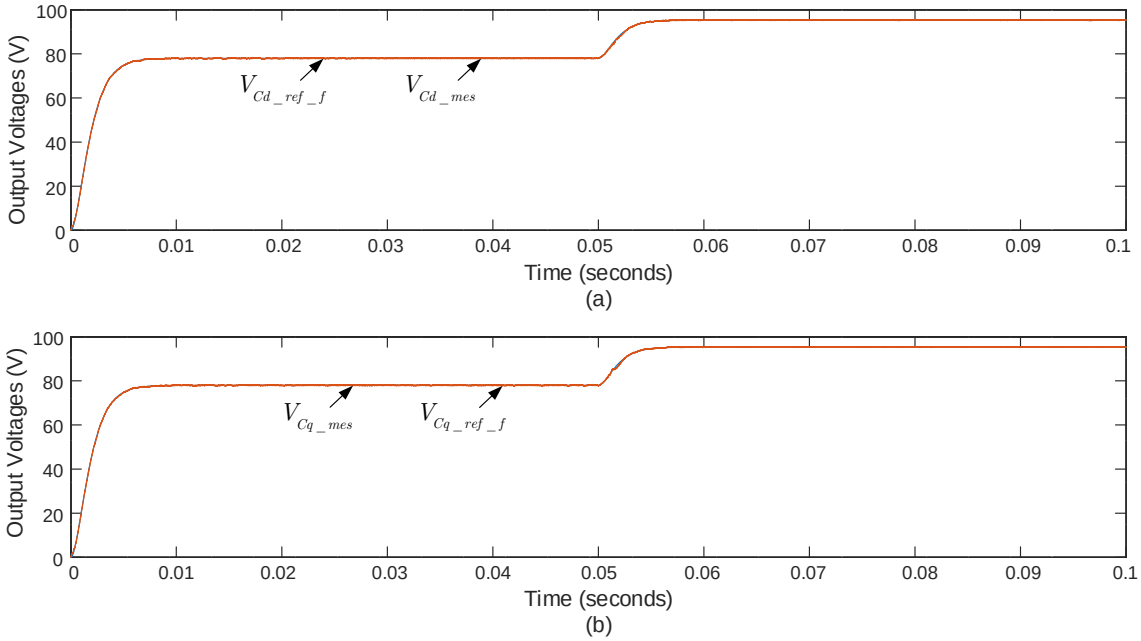

Figure 2.6: *dq* output voltages of parallel system under the proposed control method. (a) Voltage V_{cd}, (b) Voltage V_{cq} from the startup to a step in V_{rms} voltage at $t = 50$ms from 90 to 110V.

Secondly, for the other case study, where the electrostatic energy is considered as the flat output, The schematic diagram of the proposed control system is given in Fig. 2.8. Under the normal conditions, the proposed control method regulates the output ac bus

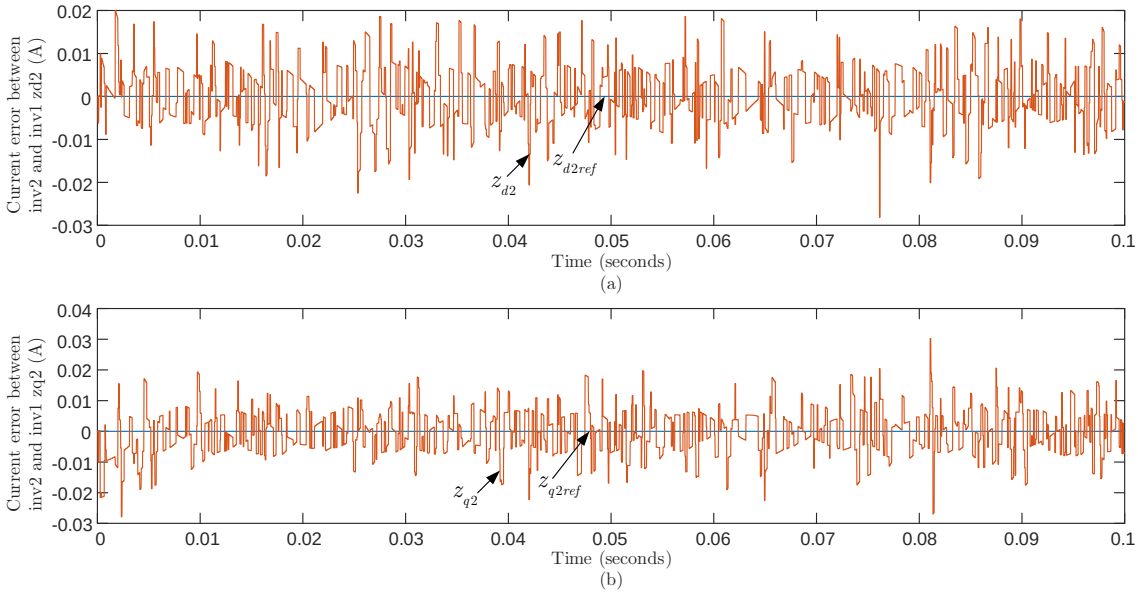

Figure 2.7: *dq* current error between inverter 1 and 2 under the proposed control method. (a) current error z_{d2}, (b) current error z_{q2}.

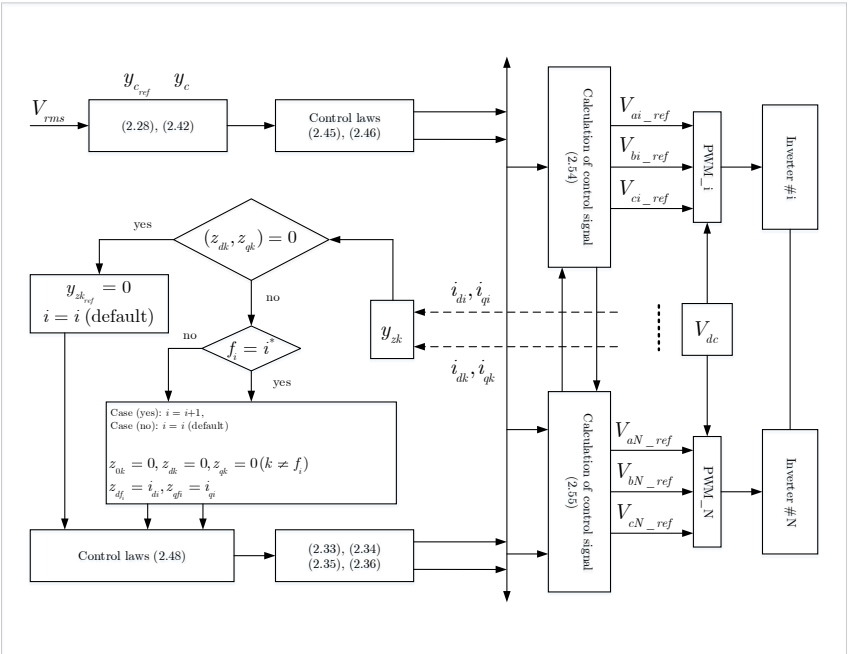

Figure 2.8: Operational block diagram of the proposed control method for N-parallel inverters with the circulating current and balancing method.

voltages. The current balancing controller allows sharing the power equally between the parallel inverters with minimization of circulating currents, so the current error vector y_{zk} equals zero. Under a fault condition of any inverter, the corresponding current error vector y_{zk} referred to the reference inverter is no more zero. This method can be used for multiple inverters failure identification. If the value of the individual current error vector y_{zk} equals the reference inverter dq currents, this value will be an identification for the full disconnection of the faulty inverter. Thus, the proposed control given by (2.37) and (2.56) is verified for both healthy and faulty conditions. Fig. 2.9(a) and (b) show, respectively, the behavior of the electrostatic energies y_d and y_q and the corresponding output voltages V_{cd} and V_{cq} under normal conditions for a step in the RMS reference voltage from 90 to 110V at $t = 50$ms. The measured components follow perfectly their reference trajectories. The components y_0 and V_{c0} are equal to zero. In this case, when the three modules are identical, there is no circulating current.

Fig. 2.10(a) shows the behavior of the line currents i_{a1}, i_{a2} and i_{a3} and the corresponding powers P_1, P_2 and P_3 of the three inverters at the common ac bus, during a faulty condition when adding 1.5Ω per phase for the second inverter. When the the current balancing controller is switched OFF at t=40 ms, the healthy inverters carry more power than the faulty one. So, there is a circulating current between the parallel inverters as given by the difference between line currents i_{a1} and i_{a2}.

Fig. 2.10(b) shows the power sharing between the three inverters. The three powers are supposed to be equal as indicated by the normal zone ZN. The load power P_L is divided equally to P_1, P_2 and P_3, at the common ac bus, between the three inverters for a given load of 3.2 kW. If a fault involves the fully disconnection of one inverter, by example the second inverter at t=20 ms, the reference inverter and the third one continue supplying equally the load power during the abnormal zone ZF2. At t=40 ms, when the second inverter problem was cleared and restarted, the load power is equally shared as previous state ZN. The same operation can be applied for the third inverter which is disconnected in ZF3 when the disconnection and reclosure are effectuated at t=60 ms and t=80 ms respectively. In the zones ZF2 and ZF3, the first inverter is the reference as viewed by the current error vector y_{zk}. But if it is disconnected, the currents will be referred to the second inverter as given by (2.37) and operational diagram given in Fig. 2.8 (i.e. $i = 2$).

Fig. 2.11(a) shows the current error during the healthy and faulty conditions. The current error is equal to zero for ZN and when the second inverter is fully disconnected, the current error vector for both dq components equals the current of the reference inverter. Fig. 2.11(b) shows the behavior of the electrostatic energies dq components when the second inverter or the third one is disconnected, some perturbations about 6% of the steady state value are observed at both t=20ms and t=60ms in the measured dq components. This is due to the variation of the electromagnetic energy stored in the inductances which affects the energy of output LC filter. When the faults are cleared and the inverter is reconnected to the system, the perturbations are negligible as indicated at t=40ms and t=80ms for the dq components due to the current balance controller which limits the rate of variations of the references at the moment of inverter reconnection. The behavior of the voltage V_{cd}, V_{cq} components and the three phase voltages V_{ca}, V_{cb} and V_{cc} of the output filter capacitors is shown in Fig. 2.11(c) when one inverter is disconnected.

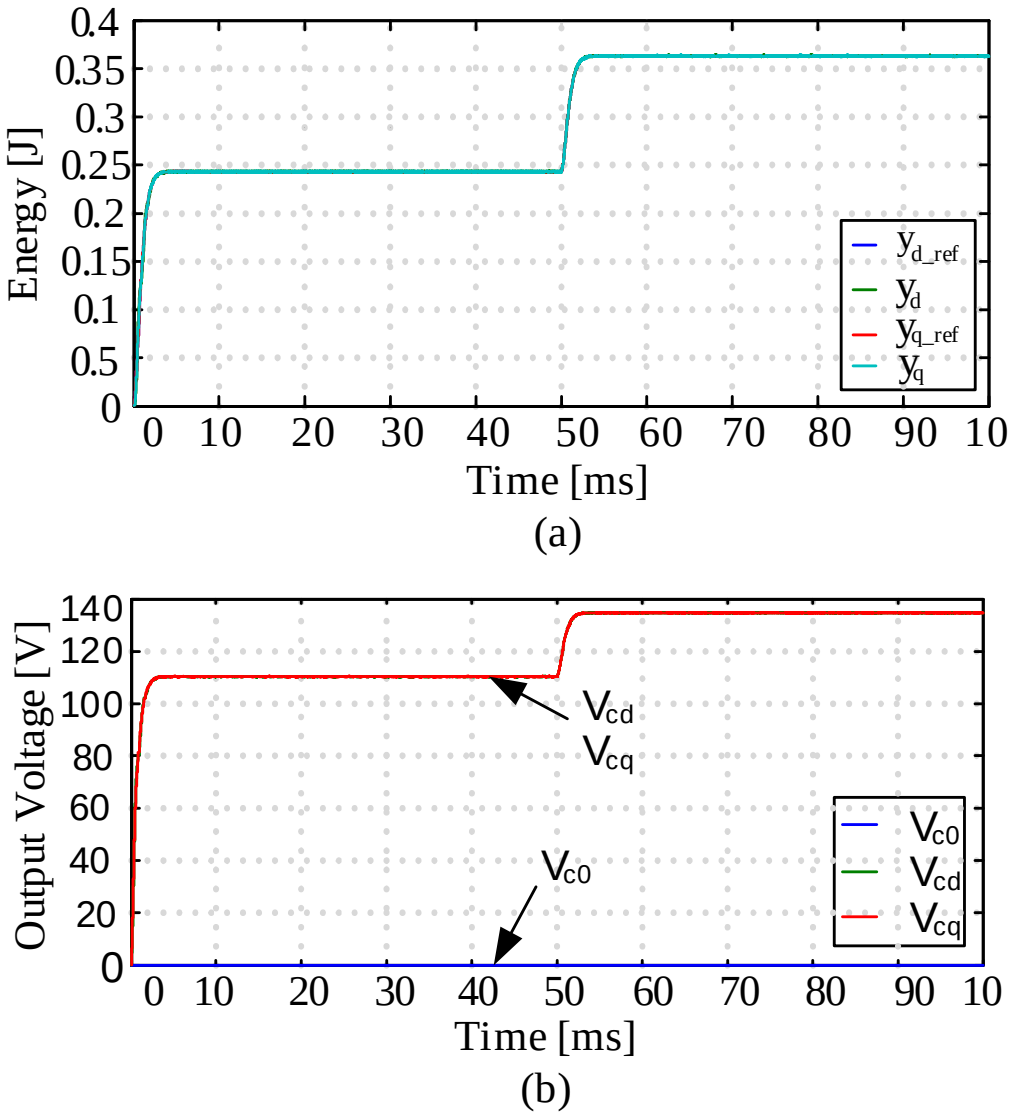

Figure 2.9: Waveforms of the output ac bus of parallel system under the proposed control method. (a) Behavior of electrostatic energies y_d and y_q. (b) Voltages V_{c0}, V_{cd},and V_{cq} from the startup to a step in V_{rms} voltage at $t = 50$ms from 90 to 110V.

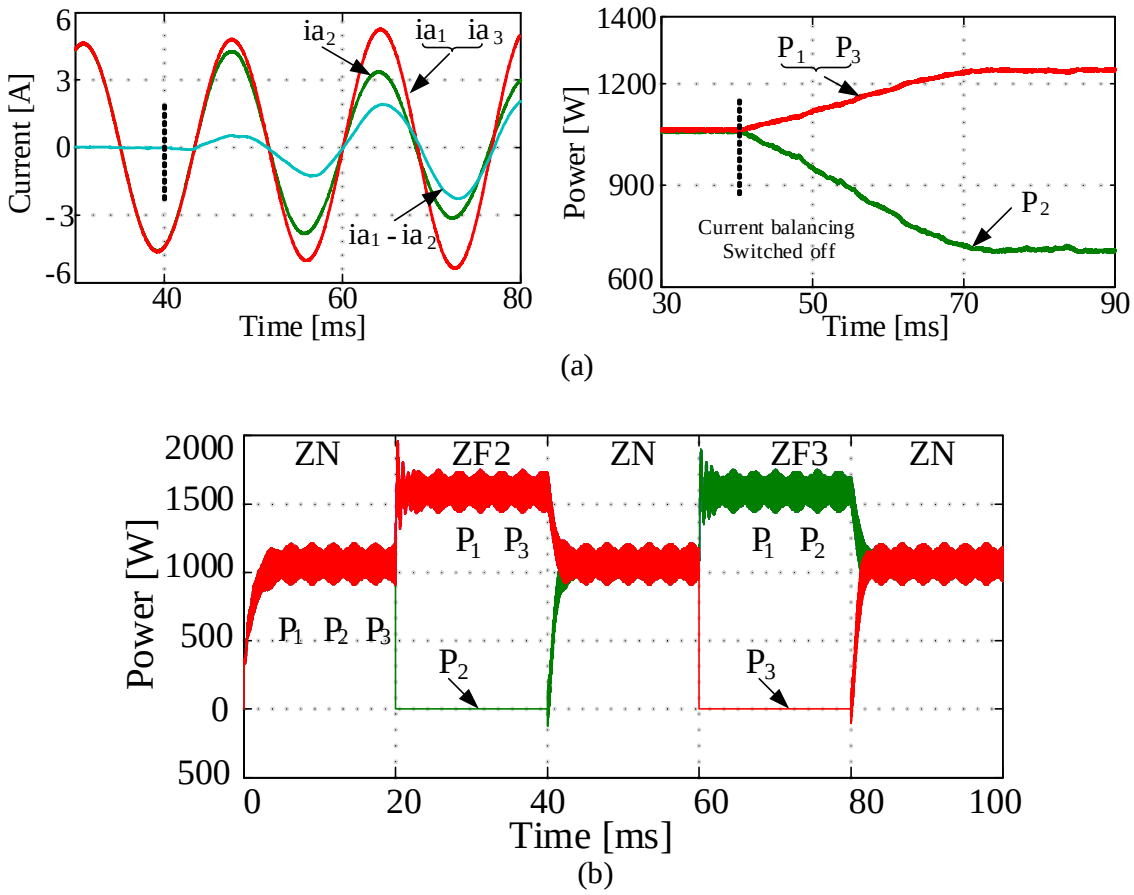

Figure 2.10: Behavior of the parallel inverters system under the proposed control method (V_{dc} = 500V, V_{rms} = 110V, P_{load} = 3.2kW). (a) Line currents and power sharing between parallel inverters when the current balancing controller is switched OFF. (b) Load power sharing between parallel inverters for a load of 3.2 kW during healthy and faulty conditions for each inverter with the proposed current balancing method.

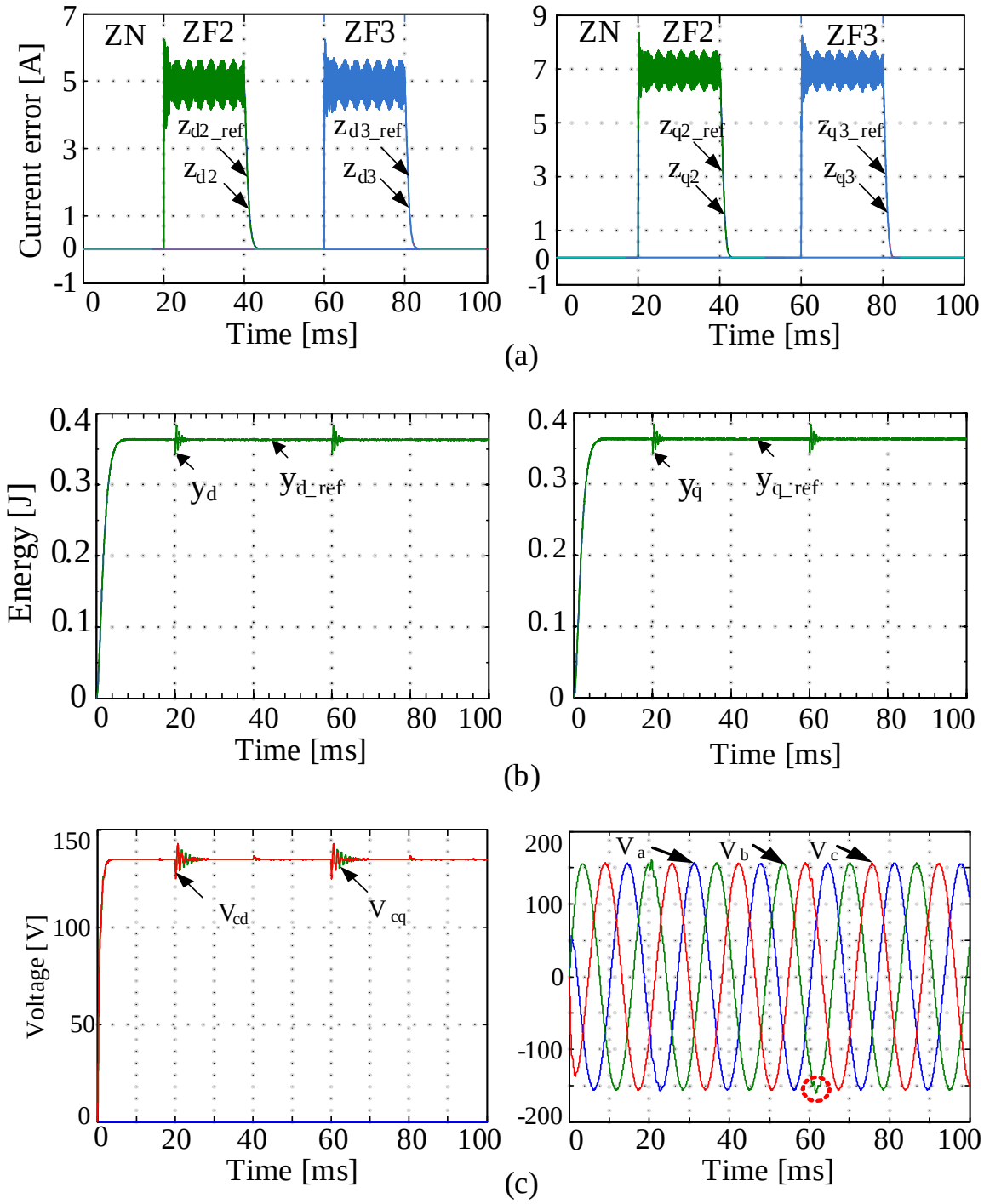

Figure 2.11: Behavior of the parallel inverters system under the proposed control method (V_{dc} = 500V, V_{rms} = 110V, P_{load} = 3.2kW). (a) Behavior of current error during healthy and faulty conditions. (b) Behavior of electrostatic energies y_d, y_q under the proposed current balancing method with minimal perturbation. (c) Behavior of V_{cd}, V_{cq} and the output three phase voltages in different zones.

The output energies and voltages follow perfectly their respective references and the three phase voltages of the output LC filter are pure sine waves.

2.3.4 Experimental Results

To verify the effectiveness of the proposed control method, experiments are performed on a 5-kW test bench consisted of two parallel inverters under the proposed control method as shown in Fig. 2.12 with the parameters listed in Table 2.3. The proposed control is realized with Matlab-Simulink-RTW software and implemented owing to dSPACE-1105 real-time control card. Fig. 2.13(a) shows the output ac voltages of the LC filter for a balanced resistive load of 3.2 kW. The voltage THD is 1.8% for the FBC. Fig. 2.13(b) shows the behavior of both the dq energies and the voltages components of the output ac bus after a step variation in the voltage reference from 55 to 110 V with a resistive load power set to 3.2 kW in steady state. The measured values follow perfectly their respective references trajectories. Fig. 2.13(c) shows the experimental results of the output energies which follow perfectly the planed energy references for step variation from 120 to 80 V and then again to 120 V. The behavior of the output energy stays well controlled thanks to the proposed flat control method after a step of the load power from 3.2 kW to 5 kW. The system exhibits efficiency about 87% under the given load conditions. When there is non-similarity of the components, there will be a circulating currents between the parallel inverters. Unbalanced system is introduced by adding 1.5Ω per phase for the second inverter, this resistance artificially represents the nonequivalent condition. The currents i_{d1}, i_{d2} and i_{q1}, i_{q2} at the common ac bus is still equally divided between the two inverters using the current balancing controller, and the circulating current is reduced to zero as shown in Fig. 2.13(d) and (e). The respective current differences are equal to zero with the proposed currents balancing method. These results put emphasis on the minimization of the circulating currents for unbalanced parallel systems. Fig. 2.13(f) shows the power P_1, P_2 which are balanced between the two parallel inverters, but the second inverter exhibits more losses than the first one under the given nonequivalent condition. These figures show the efficiency of the current balancing method used to balance the currents and the power between inverters. Also, the balancing system is still efficient during transient state.

Fig. 2.14(a) shows the power P_1, P_2 and the power sharing ratio α_1, α_2 between the two inverters under a resistive balanced load of 3.2 kW when the current balancing system is switched OFF under the abnormal condition by adding 1.5Ω per phase for the second inverter. The healthy inverter provide more power than the faulty one. So, there is a circulating current about 2A between the parallel inverters as shown in Fig. 2.14(b). The system exhibits efficiency about 86% and 84% with and without the current balancing method under the abnormal and same load conditions. Fig. 2.14(c) shows the behavior of electrostatic energies y_d (similarly y_q) and the output ac bus voltages V_{abc} during the faulty condition of the second inverter which is fully disconnected from the system for the given values of V_{dc}=500 V, V_{rms} =110 V and the load power of 3.2 kW. A perturbation around 7% in comparison of the values in steady state is observed for the energy and output ac bus voltages due to the change of the electromagnetic energy level in filter

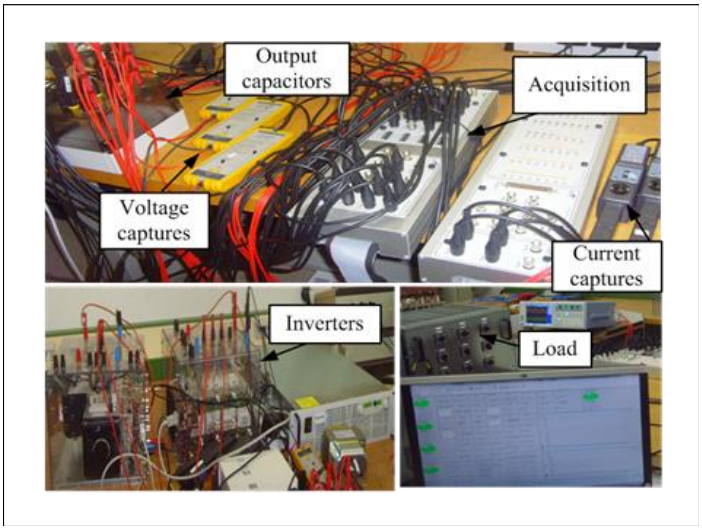

Figure 2.12: The experimental test bench of two parallel inverters.

inductors. The corresponding behavior of the power P_1, P_2 and the current error vector z_d, z_q and their respective reference trajectories is shown in Fig. 2.14(d) and Fig. 2.14(e). The first inverter is switched OFF at the beginning of ZF1 and the full load power is provided by the second inverter which becomes the reference (i.e., inv1=s, inv2=m) and continues as a reference. However, at the moment of reconnecting the first inverter at the end of ZF1, the second inverter stays the reference unit which is disconnected at the beginning of ZF2, and the first inverter becomes the reference as in the initial state.

To verify the performance of the proposed controller under nonlinear load condition, a three-phase diode bridge rectifier with a resistive load is used. Fig. 2.15 shows the waveforms of the output ac bus voltages and load currents. The THD is 2.71% for the output ac bus voltages under the proposed control method. The lower THD value for the line voltages under the flatness controller is mainly due to use of the reference reactions instead of disturbance reactions. The performance of the proposed control method can be tested under abnormal condition like open-switch fault. Fig. 2.16(a) shows the experimental results for the output ac bus voltages under open-switch fault of the first inverter represented by S11 (a detection variable flag). In this case, the control continues to operate in normal mode (no disconnection of the faulty inverter). The measured current error values are negative for the upper open-switch case as shown in Fig. 2.16(b). The faulty phase has negative unidirectional current and zero for the positive half as shown in Fig. 2.16(c). The experimental results show the validity of the proposed FBC method for regulating the output voltage or minimize the circulating currents between the parallel inverters and minimizing the transient effects due to changes of the configurations of the parallel system.

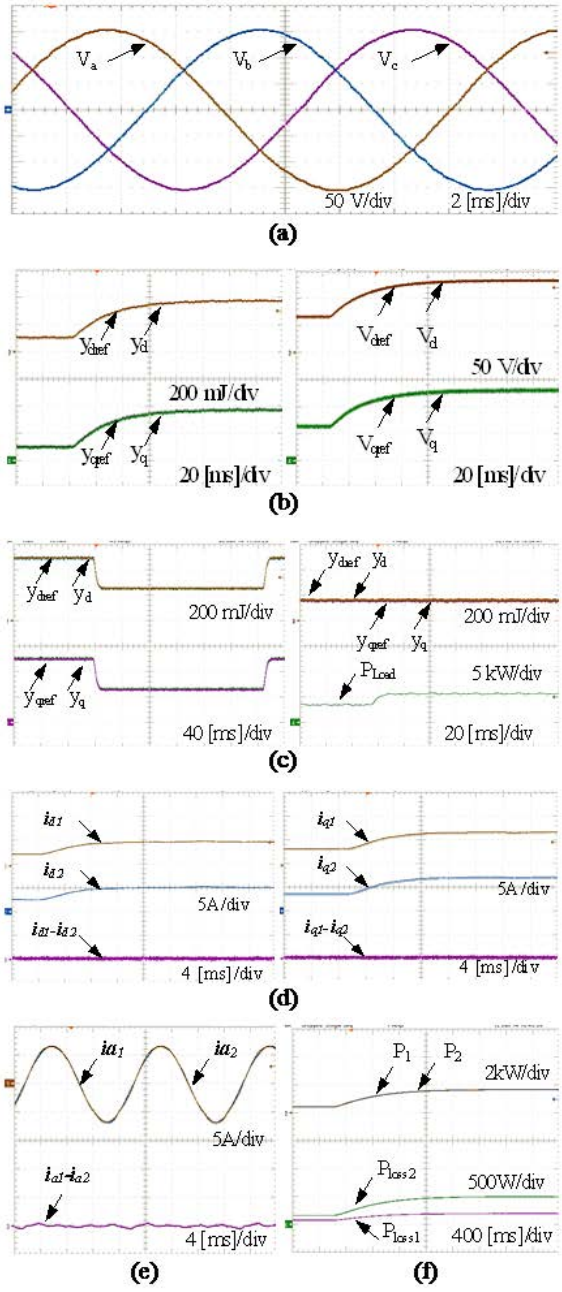

Figure 2.13: Experimental results: (a) Output voltages for Vrms=110 V under 3.2 kW balanced resistive load. (b) Behavior of measured dq energies and voltages of output ac bus for step in reference voltage Vrms from 55V to 110V. (c) Experimental results during step variations of measured energies after step variation of Vrms from 120 to 80 V and then again to 120 V and with step of load power from 3.2 kW to 5 kW. (d) Experimental results of currents i_{d1}, i_{d2} and i_{q1}, i_{q2} and their respective differences when current balancing controller in ON state. (e) Line currents ia1, ia2, their respective differences when current balancing controller in ON state. (f) Corresponding behavior of supplied power at output ac bus; P_1, P_2, losses P_{loss1} and P_{loss2}.

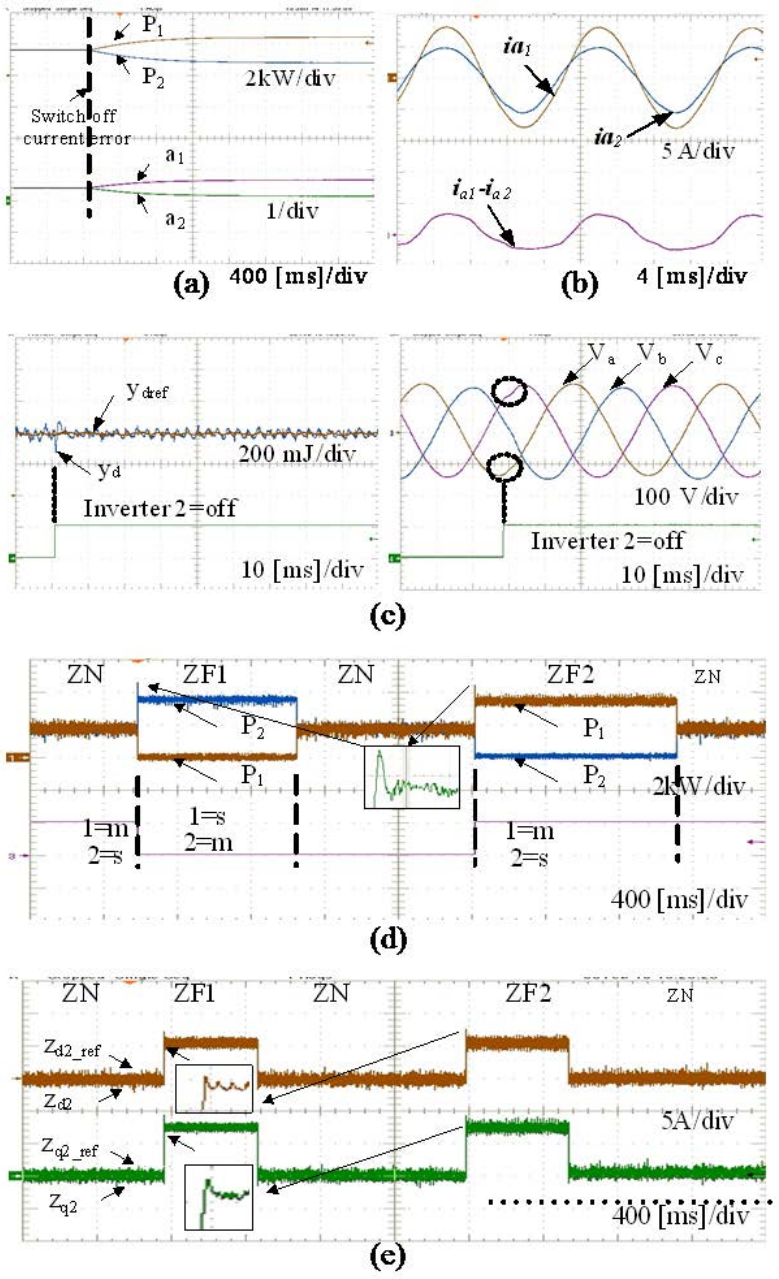

Figure 2.14: Experimental results: (a) Power P_1, P_2 and their ratio at common ac bus under resistive balanced load of 3.2 kW when current balancing is in OFF state. (b) output currents i_{a1}, i_{a2} and their respective differences when current balancing controller is in OFF state. (c) Electrostatic energies y_d, y_q during full disconnection of second inverter and corresponding three phase voltages with perturbation of 7%. (d) Powers P_1 and P_2 at output ac bus under resistive balanced load of 3.2 kW for full disconnection of first and second inverter respectively. (e) Current error vector z_{d2} and z_{q2} components under resistive balanced load of 3.2 kW for disconnection condition of inverters.

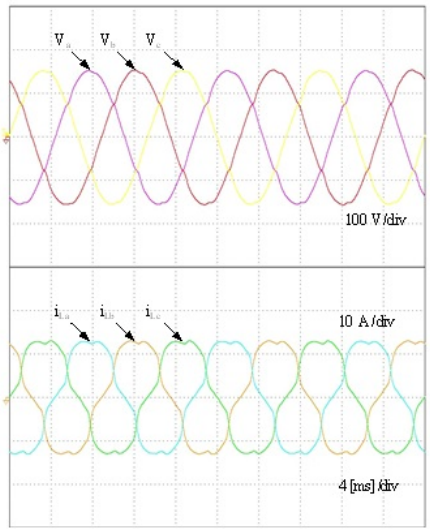

Figure 2.15: Experimental results for output ac voltages and currents with a nonlinear load, (Vdc=500 V, Vrms =110 V, Pload=3.2 kW).

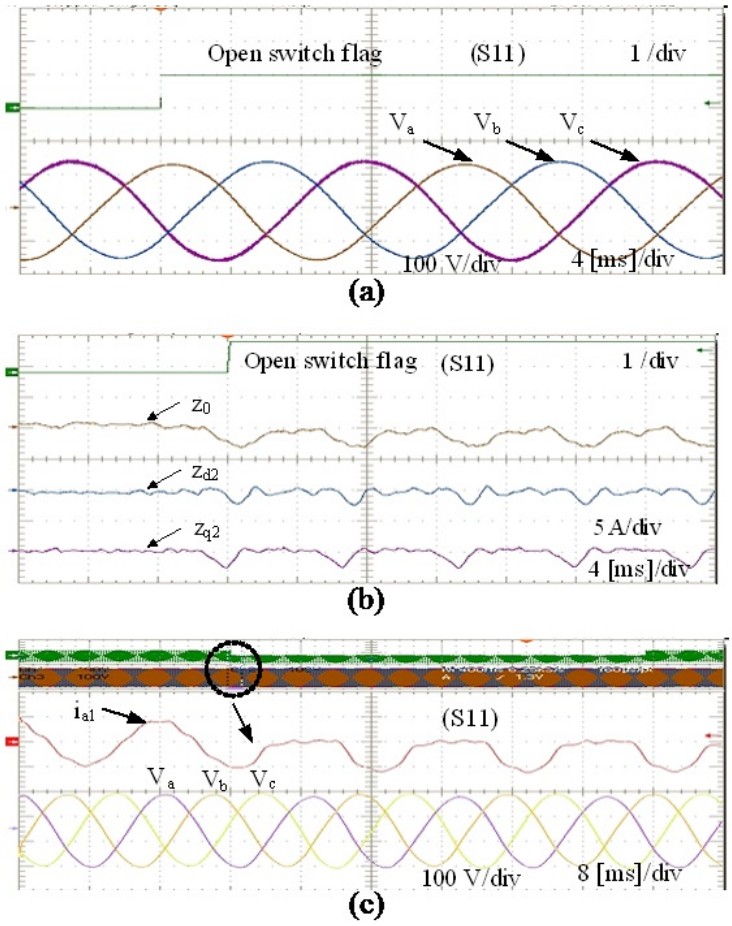

Figure 2.16: Experimental results: (a) waveforms of output ac bus voltages, (b) current errors and (c) output currents under open-switch fault.

2.4 Power sharing enhancement based Droop Control

In recent years, many research attention was paid on improving the $Q-V$ droop control to enhance the accuracy in reactive power sharing and to get better dynamics and steady state performance. For example, better transient response with voltage drop minimization was obtained by introducing a derivative or integral terms into the droop controller [53, 54, 46]. The conventional droop control with virtual output impedance [30, 31, 32, 33, 26, 55, 37, 80] was proposed to obtain a mainly inductive feeder line to increase the power sharing accuracy. Another way to decouple the active and reactive powers was introduced in [39], by adding a virtual power frame transformation. Recently, communication link has been introduced in the Droop control strategy to improve microgrid power sharing performance [81, 82, 36, 83]. Thus the microgrid characteristics play an important role in the performance of the droop control, and undesirable parameters affect the accuracy of power sharing. It is well known that, the voltage drops across the line affect the $Q-V$ function performance. In [47], the line voltage magnitude drop was estimated and the converter reactive power output information during grid connection were used to design the slope of the droop function during islanded mode.

In a different manner, the voltage at the point of common coupling (PCC) could be estimated to improve the reactive power sharing under mismatched line impedances. Thus, in this part, we are going to propose an online state estimator for the PCC rms-voltage and additional control signal is injected to the $Q-V$ droop to compensate the drop voltage across the line, thus accurate reactive power sharing is achieved. This is done without adding communication link and without adding a supplementary loop to inject a virtual impedance.

To illustrate the failure of the conventional $Q-V$ droop in sharing accurately the reactive power, a cross reference to Chapter 1 Eq. (1.7) is realized and an arrangement of the equation gives rise to:

$$V_i - V_0 = \frac{Z_i Q_i}{V_0} \tag{2.64}$$

The passage from (2.64) to $Q-V$ droop equation ($V_i - V_n = -n_i(Q_i - Q_{in})$) is done by assuming that the voltage (V_0) is controlled to the set point (V_n) which is not physically completed, as it misses the voltage drop across the line impedance. To make sure that the PCC voltage is controlled to the desired set point, we must add the voltage drop across the line in the $Q-V$ droop control model as:

$$V_i = V_n + |Z_i i_{li}| - n_i(Q_i - Q_{in}) \tag{2.65}$$

Equation (2.65) can effectively control the PCC voltage near the constant voltage as desired. From this point of view, a PCC rms-voltage estimator is adopted and compared with the constant desired value, the difference will be added to the $Q-V$ droop function using integral control. In this way, we can ensure that the voltage at the PCC point will rest in a desired range, and the modified $Q-V$ droop will no longer depends on line impedance values.

2.4.1 PCC rms-voltage State-Estimator

In this section, a state-observer of the PCC rms-voltage is proposed. This state-observer, is dedicated to a specific subclass of non-linear systems which are supposed to be observable. It is inspired from the sub-class of state-observers designed through the literature as "Disturbance observers", for example, those studied in [84, 85].

Disturbance observers are indeed very well adapted to the considered problematic consisting of PCC rms-voltage estimation. In microgrid application, the disturbance vector $disturb = \begin{pmatrix} V_{PCCd} & V_{PCCq} \end{pmatrix}^T$ has to be observed in dq rotating frame. The non-linear system can be described as

$$\dot{X} = \begin{pmatrix} \dot{x} \\ \dot{p} \end{pmatrix} = \begin{pmatrix} f(x,u) + g(x,u).p \\ 0 \end{pmatrix} \tag{2.66}$$

where:

- $X \in \Re^{n+m}$ is the vector of variables which are going to be estimated.
- $x \in \Re^n$ is the vector of the system state-variables. Every state variable are proposed to be measured.
- $p \in \Re^m$ is the vector of the unknown parameters to estimate. Parameters p are supposed to vary slowly compared to state-variables (i.e.: $\dot{x} \gg \dot{p}$).
- f and g are non-linear functions of x and u (the command signal vector) respectively of size $\Re^n$ and $\Re^{n \times m}$. Note that, $g(x,u)$ is non singular.

2.4.1.1 Definition of the proposed state-observer

A lot of observation techniques exist in literature. Contrary to the Extended Kalman Filter or Luenberger observers, the proposed observer doesn't use a local model around an operating point and is well adopted for nonlinear systems [10]. Its dynamical equations are given by:

$$\begin{pmatrix} \dot{\hat{x}} \\ \dot{\hat{p}} \end{pmatrix} = \begin{pmatrix} f(x,u) + g(x,u).\hat{p} - S.(\hat{x} - x) \\ K_p.(\dot{\hat{x}} - \dot{x}) + K_i.(\hat{x} - x) - g^T(x,u).(\hat{x} - x) \end{pmatrix} \tag{2.67}$$

where:

- S positive-definite matrix of size $\Re^{n \times n}$.
- $K_p.g(x,u) = -P$.
- $K_i = K_p.S$.
- P positive-definite matrix of size $\Re^{m \times m}$.

2.4.1.2 Stability of the estimator

For demonstrating the convergence of the estimation through the state-observer, estimation errors ε_x and ε_p are defined respectively following Eqs. (2.68) and (2.69).

$$\dot{\varepsilon}_x = \left(\dot{\hat{x}} - \dot{x}\right) = g(x,u).\varepsilon_p - S.\varepsilon_x \tag{2.68}$$

$$\dot{\varepsilon}_p = \left(\dot{\hat{p}} - \dot{p}\right) = K_p.g(x,u).\varepsilon_p - K_p.S.\varepsilon_x + K_i.\varepsilon_x - g^T(x,u).\varepsilon_x \tag{2.69}$$

Exponential stability of the estimation can be demonstrated with the classical Lyapunov approach. In fact, Lyapunov stability theorem gives sufficient conditions for stability, asymptotic stability, and so on. Moreover, we use the Lyapunov stability theorem for exponential stability to show that an equilibrium point of a nonlinear system is exponentially stable if and only if the linearization of the system about that point has an exponentially stable equilibrium at the origin [86]. To state the Lyapunov's stability theorem:

Let $x = 0$ be an equilibrium point for an autonomous system ($\dot{x} = f(x)$) and $D \subset R^n$ be a domain containing $x = 0$. Let $V : D \to R$ be a continuously differential function such that

$$V(0) = 0 \text{ and } V(x) > 0 \text{ in } D - \{0\} \tag{2.70}$$

$$\dot{V}(x) \leq 0 \text{ in } D \tag{2.71}$$

Then, $x = 0$ is stable.
Moreover, if

$$\dot{V}(x) < 0 \text{ in } D - \{0\} \tag{2.72}$$

then $x = 0$ is asymptotically stable.
For this, the Lyapunov candidate function V is considered following Inequality (2.73).

$$V = \frac{1}{2}.\begin{pmatrix} \varepsilon_x & \varepsilon_p \end{pmatrix}.\begin{pmatrix} \varepsilon_x \\ \varepsilon_p \end{pmatrix} \geq 0 \tag{2.73}$$

The derivative of function V can be expressed as Eq. (2.74):

$$\dot{V} = \varepsilon_x^T.\dot{\varepsilon}_x + \varepsilon_p^T.\dot{\varepsilon}_p \tag{2.74}$$

By substituting Eqs. (2.68), (2.69) in (2.74), $\dot{V}$ can be expressed as:

$$\dot{V} = \varepsilon_x^T.g(x,u).\varepsilon_p - \varepsilon_x^T.S.\varepsilon_x + \varepsilon_p^T.K_p.g(x,u).\varepsilon_p - \varepsilon_p^T.K_p.S.\varepsilon_x + \varepsilon_p^T.K_i.\varepsilon_x - \varepsilon_p^T.g^T(x,u).\varepsilon_x \tag{2.75}$$

Then, by introducing expressions of $K_p = -P.g^{-1}(x,u)$ and $K_i = K_p.S = -P.g^{-1}(x,u).S$, in Eq. (2.75), it results to:

$$\dot{V} = \begin{pmatrix} \varepsilon_x & \varepsilon_p \end{pmatrix} \cdot \begin{pmatrix} -S & 0 \\ 0 & -P \end{pmatrix} \cdot \begin{pmatrix} \varepsilon_x \\ \varepsilon_p \end{pmatrix} \tag{2.76}$$

Finally, from Eqs. (2.73) and (2.76), the estimation exponential stability can be ensured as long as S and P are positive-definite matrices.

2.4.1.3 PCC rms-voltage estimation for Microgrid Application

The considered model for deriving the differential system equations is represented by Fig. 2.17(a) while Fig. 2.17(b) depicts the vector diagram in dqi rotating frame.

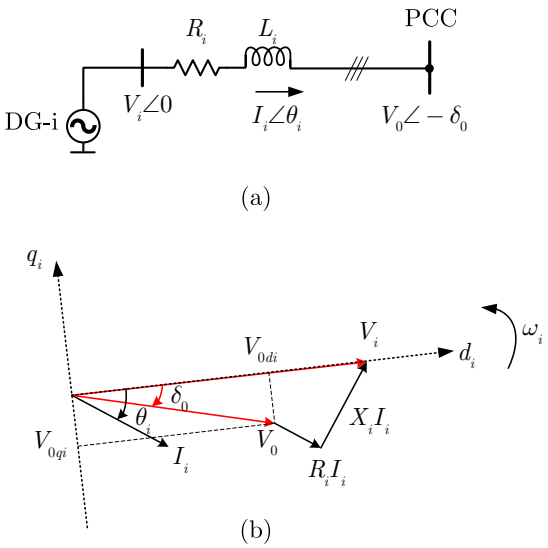

Figure 2.17: Single Line circuit with vector diagram

The PCC rms-voltage is first achieved by estimating the parameters V_{0dqi} in each dqi frame of the corresponding DG-i. The system state equation can be written as Eq. (2.77). For estimation of parametrs, the state-variable I_i, the input vector V_i are measured.

$$\begin{cases} L_i \frac{dI_{di}}{dt} = V_{di} + \omega_i L_i I_{qi} - R_i I_{di} - V_{0di} \\ L_i \frac{dI_{qi}}{dt} = V_{qi} - \omega_i L_i I_{di} - R_i I_{qi} - V_{0qi} \end{cases} \tag{2.77}$$

Before presenting parametres estimation, their observability must be verified since it is proposed to estimate them through state observers. For this purpose, the considered state vector X is given defined as:

$$X = \begin{pmatrix} I_{di} \\ I_{qi} \\ V_{0di} \\ V_{0qi} \end{pmatrix} \tag{2.78}$$

The measured vector Y is defined as:

$$Y = \begin{pmatrix} I_{di} \\ I_{qi} \end{pmatrix} \tag{2.79}$$

Under classical notations, state-variables X and measured ones Y are linked through matrix C which is given be Eq. (2.80)

$$Y = C.X \text{ with} : C = \begin{pmatrix} 1 & 0 & 0 & 0 \\ 0 & 1 & 0 & 0 \end{pmatrix} \tag{2.80}$$

The local observability of such system can be proved by considering the observability vector Θ given by:

$$\Theta = \begin{pmatrix} Y \\ \dot{Y} \end{pmatrix} = \begin{pmatrix} X_1 \\ X_2 \\ \frac{1}{L_i}\left[V_{di} + \omega_i L_i X_2 - R_i X_1 - X_3\right] \\ \frac{1}{L_i}\left[V_{qi} - \omega_i L_i X_1 - R_i X_2 - X_4\right] \end{pmatrix} \tag{2.81}$$

The system model is considered locally observable, if Eq. (2.82) is satisfied. In this case, $dim(X) = 4$ and Eq. (2.82) is verified if $Y = \begin{pmatrix} I_{di} & I_{qi} \end{pmatrix}^T \neq 0$. Then the model is observable if the output power is different from 0, which is practical since the estimated parameters would not be used for null power.

$$rank(Jacob(\Theta)) = dim(X) \tag{2.82}$$

For developing the proposed state-observer, the system represented by Eq. (2.77) is written in the form given in Eq. (2.67). Functions $f(x,u)$ and $g(x,u)$ follow equations (2.83) and (2.84). It is verified that $g(x,u)$ is invertible.

$$f(x,u) = \begin{pmatrix} \frac{1}{L_i}V_{di} + \omega_i I_{qi} - \frac{R_i}{L_i}I_{di} \\ \frac{1}{L_i}V_{qi} - \omega_i I_{di} - \frac{R_i}{L_i}I_{qi} \end{pmatrix} \tag{2.83}$$

$$g(x,u) = \begin{pmatrix} \frac{-1}{L_i} & 0 \\ 0 & \frac{-1}{L_i} \end{pmatrix} \tag{2.84}$$

To complete the proposed state-observer, matrices S and P have to be determined. They are chosen following Eq. (2.85) as:

$$S = \begin{pmatrix} 5000 & 0 \\ 0 & 5000 \end{pmatrix} \; and \; P = \begin{pmatrix} 1000 & 0 \\ 0 & 1000 \end{pmatrix} \tag{2.85}$$

2.4.1.4 The Control Scheme

Before introducing the control scheme used for active and reactive power sharing for parallel inverters in microgrid, we are going to list some benefits for why choosing a state observer for estimating the PCC rms-voltage over other control loops used to enhance power sharing for the droop control in autonomous microgrid.

The benefits of the proposed PCC rms-voltage state estimator over the virtual impedance design or the $Q - V$dot are summarized as follow:

- The state estimation occurred at the same bandwidth as the voltage controller. Thus, the dynamics of the state estimator is three or more times faster than the $Q-V$dot voltage restoration loop [87].
- The improvement of the proposed estimator is that it is simple and does not interact with the dynamic of the droop. In systems with high coupling impedances, the design of virtual impedance scheme is difficult and should be very large. Thus, the dynamics of power sharing can be affected.
- The final advantage of the proposed estimator is that the line impedance is the only constant required, compared to the $Q-V$dot that requires additional parameters to set the restoration loop. Furthermore, the design of virtual output impedance requires, in certain cases, the knowledge of the inverter line impedance as presented in [80].

The new control scheme is shown in Fig. 2.18(a). While the PCC rms-voltage state estimator appears in the modified $Q-V$ droop which is named as $Q-V$Est droop control shown in Fig. 2.18(b). In this case, the estimated PCC rms-voltage is compared with the nominal value to insure less voltage drop at the PCC and eliminating the effect of the drop voltage across mismatched line impedances.

2.4.1.5 Simulation

The proposed droop controller is tested by MATLAB-Simulink for two DGs connected to a common linear and nonlinear load across feeder lines as given in Fig. 2.19. A three-phase network is designed with 110V-60Hz rating voltage. The line impedances are set as $R_1 = 0.1\Omega$, $L_1 = 1$mH and $R_2 = 0.58\Omega$, $L_2 = 5$mH. The system parameters are considered as given in Table 2.4.

System Parameters for simulation		
DG1 P(W)/Q(Var)	3000/1500	
DG2 P(W)/Q(Var)	3000/1500	
m_i (rad/sec/W)	3.34×10^{-4}	
n_i (V/Var)	6.7×10^{-3}	
Integrator gain K_v	10	
System Parameters for experiment		
	Equal ratings	**Different ratings**
P_{i_rated}(W)	3000	3000/1500
Q_{i_rated} (Var)	1500	1500/750
m_i (rad/sec/W)	3.34×10^{-4}	$3.34 \times 10^{-4}/6.66 \times 10^{-4}$
n_i (V/Var)	6.7×10^{-3}	$6.7 \times 10^{-3}/1.33 \times 10^{-2}$

Table 2.4: System parameters for test.

In Simulation test, DG1 and DG2 are supplying the R-L load. The two sources will share the fundamental real power equally by using the droop control with equal droop

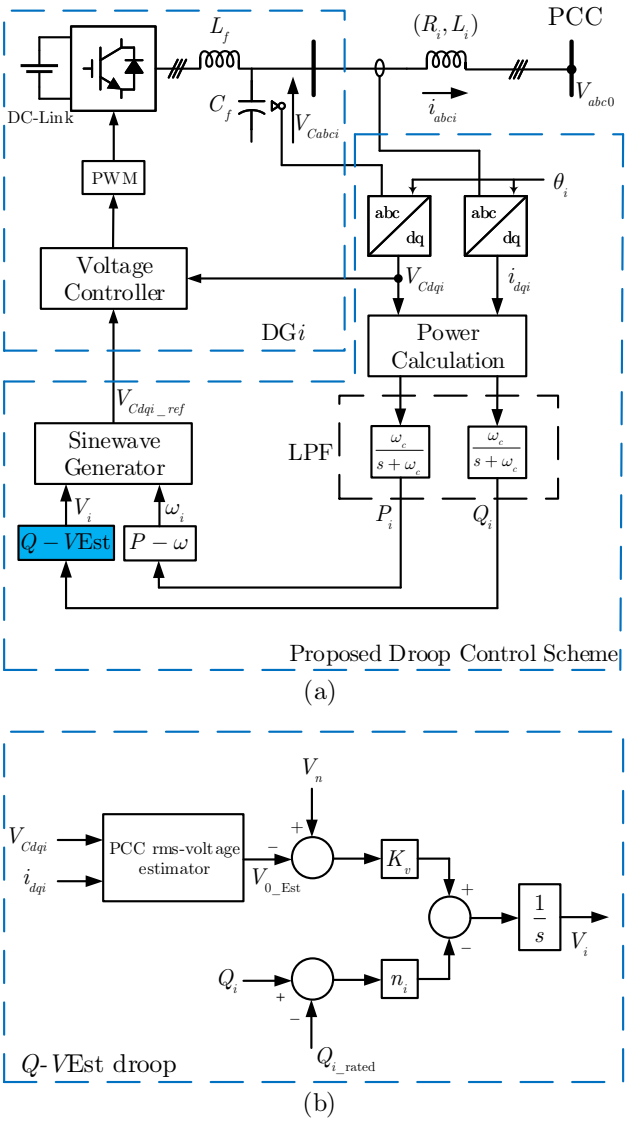

Figure 2.18: Proposed Droop Control scheme with modified $Q-V$Est Droop.

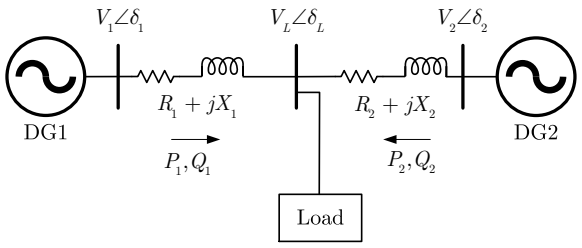

Figure 2.19: Simplified circuit of the system.

coefficients as set in Table 2.4. However, the reactive power is not balanced between the two DICs since the line impedances are different. Fig. 2.20 shows the fundamental power sharing for this case. The proposed online state estimator for the PCC rms-voltage is tested after starting the droop for realizing the difference in reactive power sharing as shown in the figure. Once the estimated PCC rms-voltage is injected in the droop control, so called $Q-V$Est droop, the reactive power is shared equally between the two DGs.

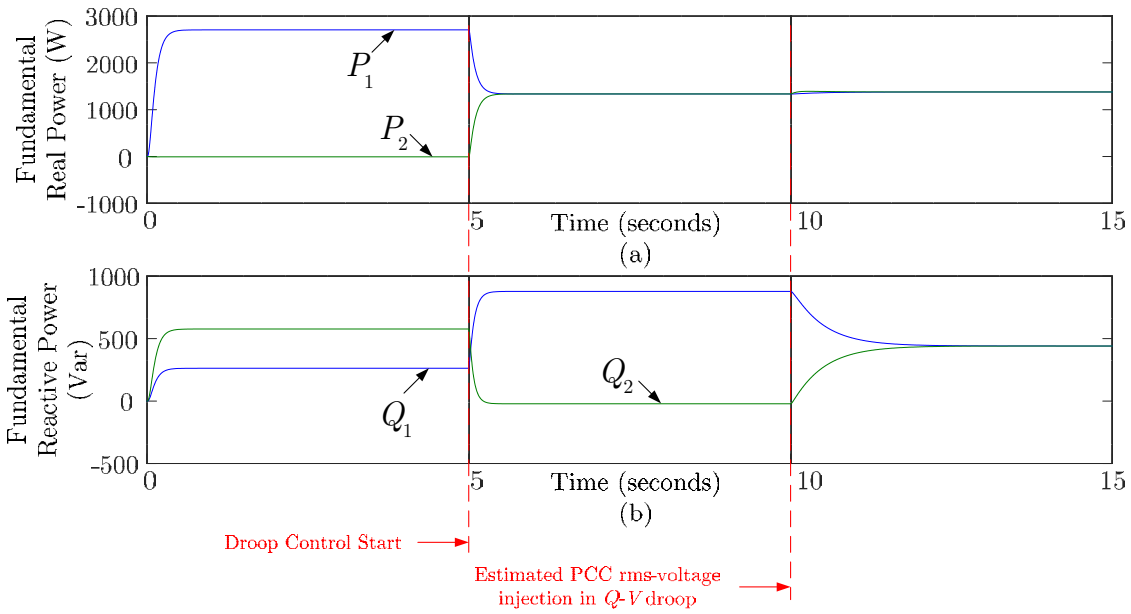

Figure 2.20: Simulation results: (a) Fundamental Real power: P_1, P_2; (b) Fundamental Reactive power: Q_1, Q_2 before and after the intervention of the estimated PCC rms-voltage.

Figure 2.21 shows the Estimator performance by comparing the estimated PCC rms-voltage with its real value for both DGs. It is shown that the estimator is accurately tracking the real value of voltage, since its dynamics is high and is equal to the dynamics of the voltage controller.

Fig. 2.22 shows the $Q-V$Est reference voltages before and after the estimator intervention. The drop voltage across the feeder is well retrieved to each DG reference by applying the proposed Droop controller.

2.4.1.6 Experiment

To validate the performance of the proposed $Q-V$Est Droop controller, a test bench of two DGs is constructed in the laboratory, which consists of two isolated 500V DC voltage supplies, two three-phase inverters controlled by dSPACE 1005 real-time control card, inductors for modeling the line impedance and a three phase R-L load and a full bridge rectifier. The system parameters are considered as follows:

- The system voltage is 110V (RMS, Line-to-neutral), 60Hz.

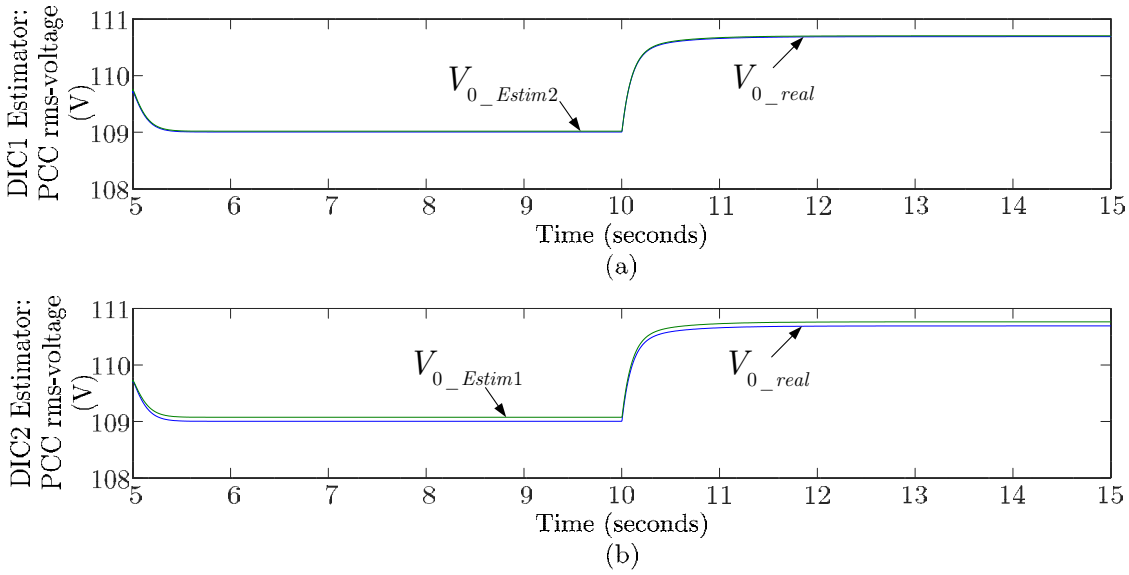

Figure 2.21: Simulation results: (a) DG1 state Estimator PCC rms-voltage compared to real value; (b) DG2 state Estimator PCC rms-voltage compared to real value.

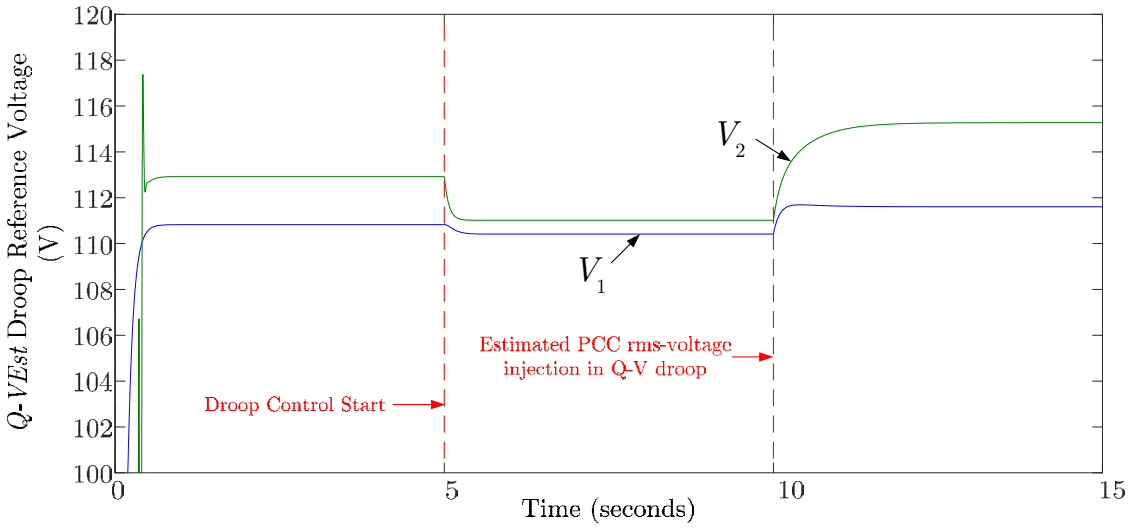

Figure 2.22: $Q - V$Est Droop Reference voltage variation before and after the injection of the estimated PCC rms-voltage.

- Two three-phase PWM inverters, switching frequency 15kHz, the output filter inductor, L_f= 3.4 mH, the output filter capacitor C_f= 40µF.
- The line impedances are set as R_1+jX_1 = 0.1+j0.377Ω and R_2+jX_2 = 0.5+j1.88Ω.
- The Droop Control parameters are considered as given in Table 2.4.

For case 1, we consider equal power ratings of two sources where DG1 is supplying the R-L load, while DG2 is firstly synchronized to the grid voltage using PLL and then the Conventional Droop Control is applied. It is seen from Fig. 2.23 that the reactive power is not shared equally. After applying the PCC rms-voltage state estimator with the proposed $Q-V$Est droop, the Reactive power is balanced between the two DGs even with a mismatch on line impedances. The phase voltage and phase current signals for the two DGs are given in Fig. 2.24(a), (b) after the starting the estimator, which shows an equal magnitude of current in this case.

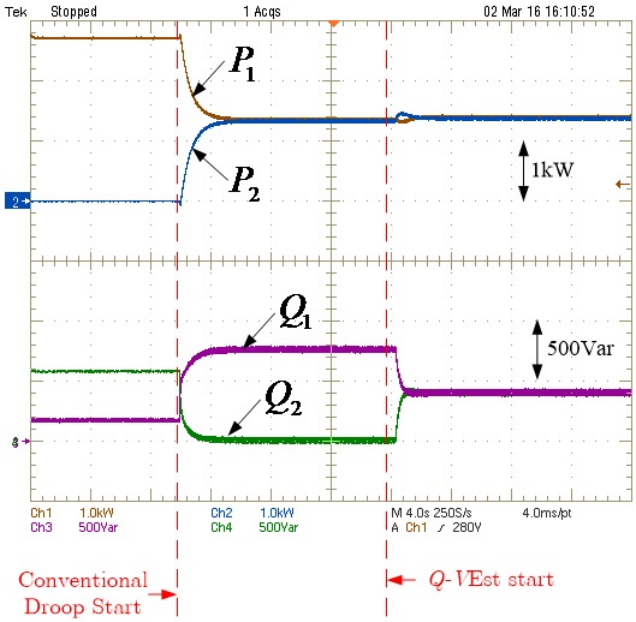

Figure 2.23: Experimental results for Case 1: Fundamental Real power: P_1, P_2; Fundamental Reactive power: Q_1, Q_2 before and after the intervention of the estimated PCC rms-voltage.

For case 2, the ratings of the two sources are different and the load is decomposed of a non-linear rectifier in addition to an R-L load. An identical demonstration as case 1 is given. Fig. 2.25 shows the power sharing for this case. The phase voltage and phase current signals for the two DGs are given in Fig. 2.26(a), (b) after the starting the estimator, which shows the magnitude of i_{Ca2} is half the magnitude of i_{Ca1}. It is to be noted that i_{Ca1} contains more harmonic contents than i_{Ca2} which is due to smaller impedance separating DG1 from the load. The output of the estimator is tested by comparing the estimated PCC rms-voltage to its measured value. Fig. 2.27 shows the estimator result for both DGs.

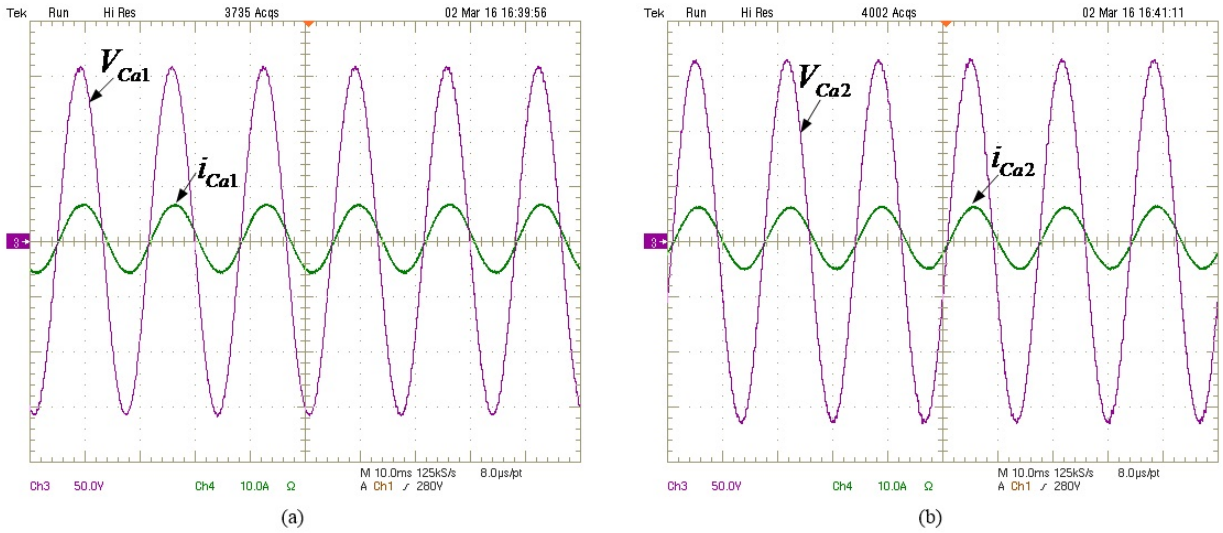

Figure 2.24: Experimental results for Case 1: (a) phase voltage and phase current for DG1; (b) phase voltage and phase current for DG2.

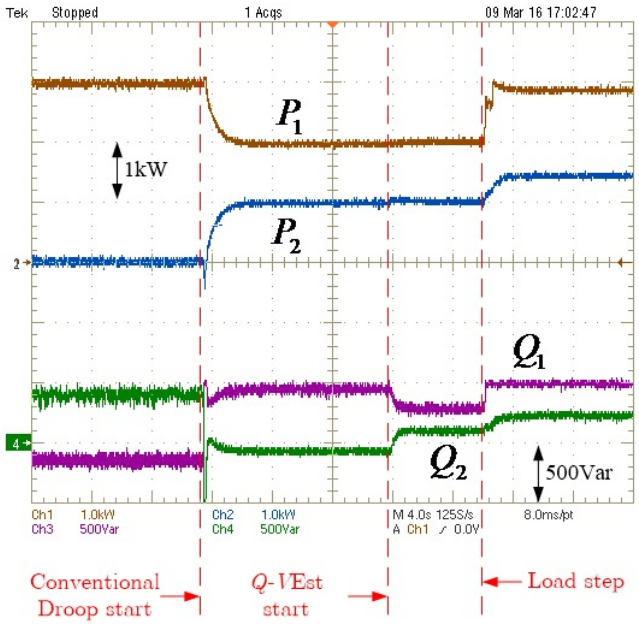

Figure 2.25: Experimental results for Case 2: Fundamental Real power: P1, P2; Fundamental Reactive power: Q_1, Q_2 before and after the intervention of the estimated PCC rms-voltage.

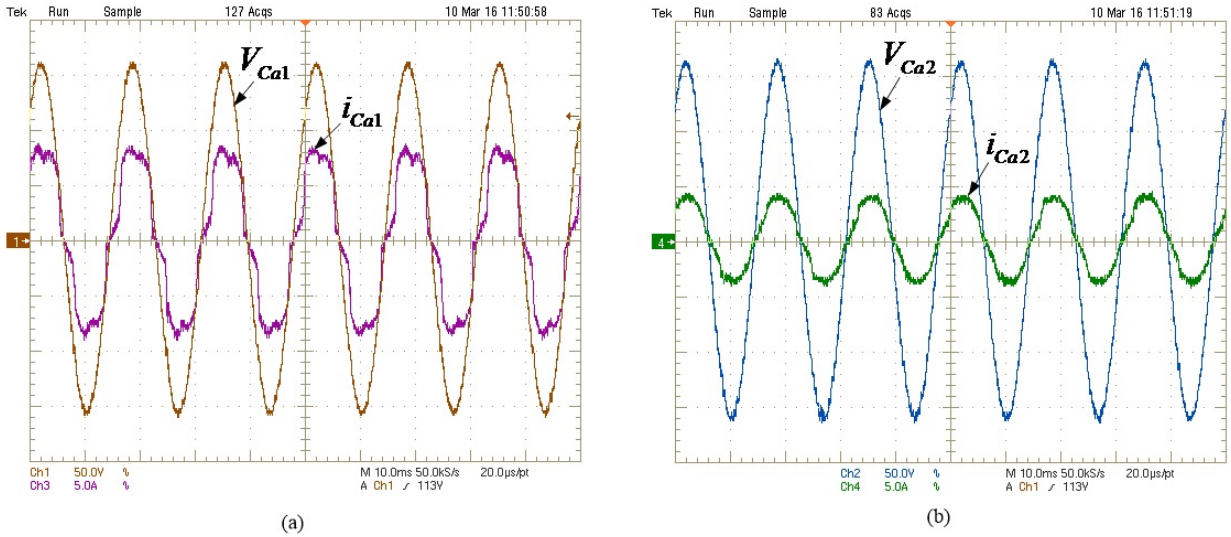

Figure 2.26: Experimental results for Case 2: (a) phase voltage and phase current for DG1; (b) phase voltage and phase current for DG2.

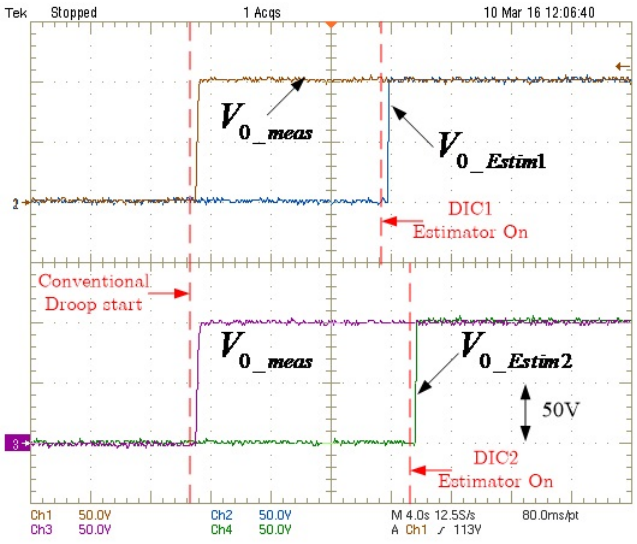

Figure 2.27: Experimental results: Estimated PCC rms-voltage compared to the measured value for each DG.

2.5 Conclusion

In this chapter, we introduce, in details, the inner controller for Distribution Interfaced Converters (DICs). It is described by the Flatness Control concept. To better appreciate the benefits of the proposed approach, Modeling and simulation test were done to check the effectiveness of the controller in starting phase and transients which shows high bandwidth with perfect tracking characteristics. This ensure the capability of using such control in Microgrid application which provides significant advantages over other inner controllers in terms of bandwidth, perfect tracking and number of control loops. Secondly, a parallel system of N-modular inverters was proposed based on flatness control. This strategy involves regulating the ac common bus voltages with minimizing the circulating currents between parallel inverters. The flatness-based control allows reducing the transient effects during a change in configuration when fault presents in one or more inverters that requires a disconnection from the system. The third part of this chapter deals with the proposed droop control for power sharing improvement. Where the proposed State-observer was presented to be used in microgrid application for enhancing the power sharing between parallel inverters. It was shown that, the drop voltage across mismatched line impedances affects the reactive power distribution between different Converters. Retrieving the drop voltage across inverter line impedance is done by proposing a state estimator for the PCC rms-voltage to indirectly sense and control its value around the nominal voltage, thus no communication is added and the droop control performance is no longer depend on the line impedances separating the sources from the common loads. The proposed $Q-V$Est is tested using simulation and experiments which show the effectiveness of the proposed droop control. Its advantages over other proposals are also presented.

Chapter 3

HARMONIC POWER SHARING WITH VOLTAGE DISTORTION COMPENSATION OF DROOP CONTROLLED ISLANDED MICROGRIDS

3.1 Introduction

Modern electrical distribution systems are complicated aggregation of several components and numerous supply points. Microgrids can be categorized into different groups depending on the size, loads, voltages and currents. Three microgrids can be identified: AC, DC and hybrid. In AC microgrids, all distributed energy resources (DER) and loads are connected to the AC bus via DC/AC inverters. In DC microgrids, the common bus is DC, where AC/DC rectifiers are used to connect AC generating units. Some literatures propose hybrid microgrid, that combines both AC and DC microgrids for increasing the system efficiency and reliability [88, 89, 90]. The interaction of components of a microgrid with the power utility results in temporal variations in the characteristics of the power supplied to the customers. These variations usually appear in the form of very short to longer periods of outages or abnormal voltage and/or frequency characteristics. The quality of the supplied power is dependent on these variations. Distributed generation (DG) and integration of distributed energy resources (DERs) in the form of "Microgrids" can be used to improve power quality and reliability significantly. As we have seen in previous chapters, the Distributed Generation interfacing converters (DICs) use the droop method as a decentralized control to regulate the voltage and frequency of the system in case of islanding operation. The droop method also enables DG units to share the real and reactive power required by the load without using any communications between them [30, 87, 46, 54, 55, 91, 92, 93, 94, 95]. The major focus of the droop control is to share the average real and reactive power. Although the traditional droop method shows inconvenient in sharing the reactive power, which depends on the impedance of

DG feeders, it is well addressed in literature and different improvements were made to enhance the reactive power sharing [30, 87, 46, 54, 55, 91, 92, 93, 94, 95]. On the other hand, the islanding microgrid faces a serious problem in power quality due to the intensive use of nonlinear loads. In fact, the droop separately cannot be used since it is only designed to share the fundamental positive sequence component of load power. The traditional way to limit the harmonic distortions in the system is to install passive filters or centralized active power filters [96]. Recently, a new methods of active filtering were proposed for Smart Grid application [97, 98][97, 98]. To further autonomously share the harmonic currents, another popular approach is the virtual output impedance concept, where a load current feedforward loop is introduced together with the output harmonic voltage controller [99, 36, 37, 100, 101, 102, 103]. To attenuate the differences among the feeder impedances of the DGs, a large virtual inductance is needed. As a consequence, additional harmonic voltage distortion may exist. A virtual capacitive impedance loop was used to improve the harmonic current sharing and attenuate the voltage harmonics at the PCC [104, 105]. The basic principle of the capacitive virtual impedance loop is to compensate the non-linear inductive voltage drop by introducing a capacitive component which is equal in magnitude but has an opposite phase shift. The virtual impedance is tuned as regard to transformer and line impedance values. Thus, this control loop is based in knowing the line parameters in advance. In addition to several control methods enhanced with virtual impedance, new design rules are added and the knowledge of physical line impedances are required [106]. In [107], a harmonic and negative-sequence current control in islanded medium-voltage microgrid (MV-microgrid) is presented. The proposed control strategy consists of a multi proportional resonant controller with adjustable resonance frequency to regulate the load voltage under nonlinear and unbalanced load conditions, and a harmonic impedance controller to efficiently share the harmonic currents between DGs. However, for both controllers, this may result a high order feedforward transfer function. In [108], the author proposes a harmonic droop controller to share harmonic power between converters and to damp the voltage distortion at the PCC, where the computational burden is the restriction. Furthermore, in weak microgrid, the THD damping performance is highly affected by line impedances. Another way to achieve harmonic power sharing was presented in [109], based on harmonic conductance-harmonic Var droop (G–H droop). However, it has been found that only the harmonic distortion of DG output voltage can be regulated in this way, whereas the voltage harmonic distortion at the PCC may be undamped when using LCL filters and high line impedance value. In [110], the method presents a voltage controlled method for DGs to compensate the voltage distortions by means of adjusting the DG equivalent harmonic impedance. It should be mentioned that this method can only adjust DG harmonic line current in an indirect control manner. The harmonic current sharing is sensitive to the variation of grid impedance and the disturbance in the main gird. Recently, new proposals are introduced to share accurately reactive, harmonic and imbalanced power based on consensus algorithm [111, 80]. In [112], an enhanced hierarchical control structure for voltage unbalance and harmonics compensation is proposed.

The main purpose of this chapter is to compensate the voltage distortion caused by nonlinear loads, in cooperated manner between different voltage-controlled DGs in islanded

microgrid. Furthermore, the harmonic current of the non-linear loads is distributed between DGs as regard to their ratings. One distinct control loop is being proposed to achieve the targets. The main functionalities of the proposed loop are listed as:

- Define a droop function that allows to share nonlinear current in proportion to DGs harmonic power ratings.
- Compensate the voltage distortion at PCC due to nonlinear load in cooperation between DGs.
- The proposed control loop is immune from grid disturbances and mismatched feeder impedances.
- The proposed control loop is simpler to design. There is no need to know feeder impedances in advance.

This chapter starts with a brief discussion of power sharing for islanding microgrid in Section 3.2. The proposed harmonic droop control for harmonic power sharing is explained in Section 3.3. The strategy is also capable for reducing the voltage distortions at the PCC. The PCC harmonic voltages are modulated to their dc quantities by means of PLL and synchronous frame, and sent to each DG local controller for harmonic distortion reduction. The advantage is that a low bandwidth communication can be used for transmission. A small-signal analysis of the proposed control model is presented in section 3.4, where the eigenvalues are realized to indicate the damping of the oscillatory terms under different operation conditions. This examination allows further identification between system stability and its configuration, such as droop gains and operation conditions. In Section 3.5, the harmonic droop controller is tested using computer simulation with different configurations and case studies. Finally, the system is validated by experiments to verify the effectiveness of the proposed strategy and to show that the proposed method could considerably improve the voltage THD. The results are given in Section 3.6 followed by conclusions made in Section 3.7.

3.2 Islanding Microgrid Power Sharing Principle

Figure 3.1 shows a microgrid formed by n-parallel three-phase interfaced converters linked to the PCC through DG feeders. The microgrid also consists of linear and nonlinear loads at PCC. As shown in Fig. 3.1, the harmonic orders of the PCC voltage are extracted by the measurement block and sent to all DGs via low bandwidth communication bus. Each DG has a local controller which consist of a droop function and an inner control loop to regulate the output voltage to its reference. It is to be noted that, the communication link is only needed to get information about the PCC voltage harmonics and are used for compensation. Thus, the system operation still works even without communication. Nevertheless, the harmonic compensation will be terminated.

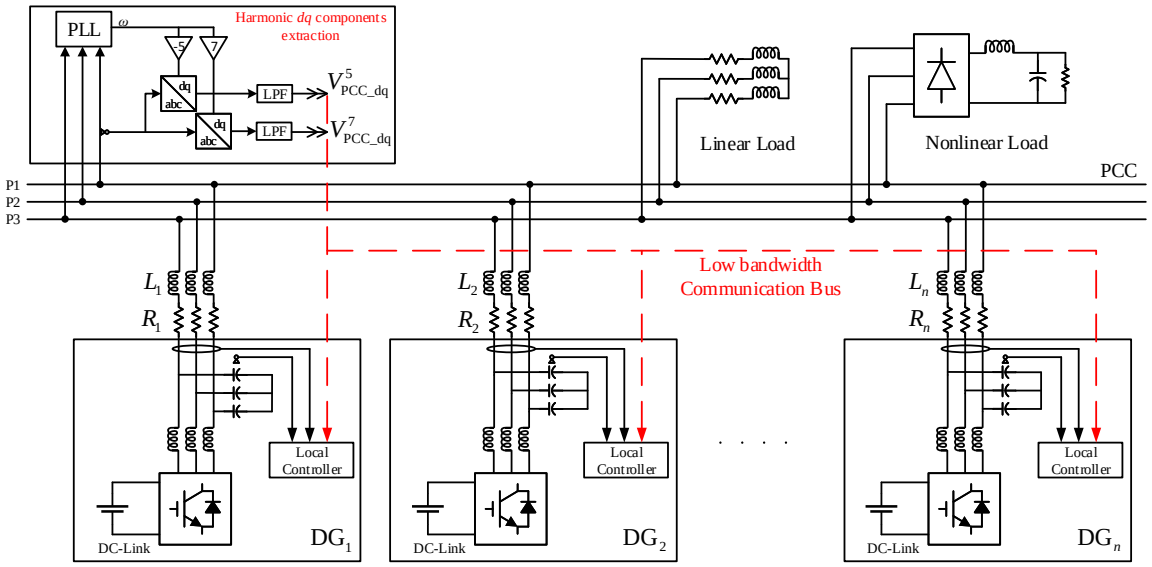

Figure 3.1: Three-phase microgrid with parallel DGs, Linear and nonlinear loads.

3.2.1 Droop control for linear load

The droop control has a long history of use for the synchronous generator control in power system. Recently, it has been used for parallel-inverter control which is developed based on the analysis of steady state power flow in an inductive feeder. The conventional frequency and voltage droop controllers in a DG unit are shown in (3.1) and (3.2) as:

$$\omega_i = \omega_n - m_i(P_i - P_{i\_\text{rated}}) \tag{3.1}$$

$$V_i = V_n - n_i(Q_i - O_{i\_\text{rated}}) \tag{3.2}$$

where ω_n and ω_i are respectively the nominal and reference angular frequency of the DG unit. V_n and V_i are the nominal and reference DG voltage magnitudes. P_i and Q_i are the average power measured after low-pass filtering. P_{i_rated} and Q_{i_rated} are the rated power capacity of a DG unit. m_i and n_i, the droop coefficients of the controller, are designed in inverse proportion to the rated power of DG unit. We have seen in chapter 2 that ,with the conventional droop, an accurate real power sharing is achieved at steady state. However, the accuracy of reactive power sharing is affected by mismatched DG unit feeder impedances. To reduce the impact of the line impedances, several methods can be applied to compensate the accuracy of fundamental reactive power.

3.2.2 Harmonic Power sharing

In a microgrid with significant nonlinear loads, an inaccurate sharing of harmonic power can lead to DG over capacity. Furthermore, harmonics can cause overheating, increased losses, distorted current and voltage waveforms, etc. Hence, a control strategy must be employed, to share the harmonics and to reduce the THD of the output voltage at

PCC point. The harmonic power drawn from each DG depends on the line impedance between the DG and the load. Harmonic power sharing can be achieved by changing the effective impedance between the DG unit and the load. Furthermore, if the equivalent harmonic impedance is reduced properly, the PCC voltage quality can be improved [110]. A simplified circuit of two DG units at harmonic frequencies is shown in Fig. 3.2. Note that, the DG interfaced converter acts as short circuit for harmonic currents, but there still exist output voltage harmonic contents due to existence of inverter output impedance as shown in the figure. In literature, two ways were reported for changing the effective line impedance. First, by changing the inverter output impedance by means of virtual conductance [109]. In this case, if the difference between the line impedances Z^h_{line1} and Z^h_{line2} is significant, harmonic sharing may not be accurate. The second way as suggested in [99, 36, 37, 100, 101, 102, 103, 105, 104], by adding a virtual impedance in series to the line at harmonic frequencies. When the virtual harmonic impedance is dominant compared to the line impedance, the equivalent impedance become approximately equal for the two DGs in Fig. 3.2. Thus, harmonic load sharing will be achieved and distributed equally between DGs. However, adding series impedance to the line increase load voltage distortion.

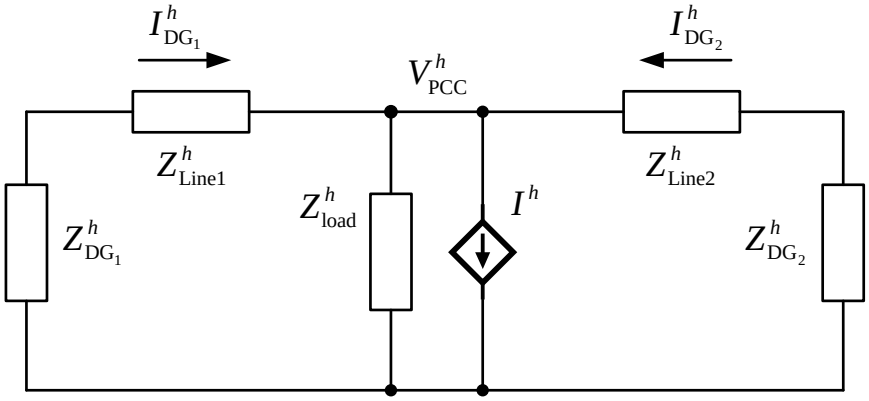

Figure 3.2: Equivalent circuit of two DGs at harmonic frequencies.

3.3 Proposed Harmonic Power Sharing

Instead of introducing complicated virtual impedance loops implemented in the inverter's control to improve the voltage harmonic distortion at the PCC and to share equally the harmonic currents between DGs, the proposed harmonic droop does the two functions in one loop design. Moreover, the proposed harmonic droop is unaffected by line mismatched impedances and grid disturbance. Thus, accurate harmonic sharing is achieved with reduced system complexity.

3.3.1 Principle of the proposed harmonic droop

The simplified equivalent circuit of two DGs supplying a common load is shown in Fig. 3.3, where the nonlinear load is modeled as a harmonic current source with passive load. The DGs are represented by a controlled voltage sources with DG feeder impedances (i=1, 2). If the DG harmonic voltage ($V^h_{DG_i}$) is controlled by using the PCC harmonic voltage (V^h_{PCC}) with a positive gain, G^h_i, as

$$V^h_{DG_i} = -G^h_i V^h_{PCC} \tag{3.3}$$

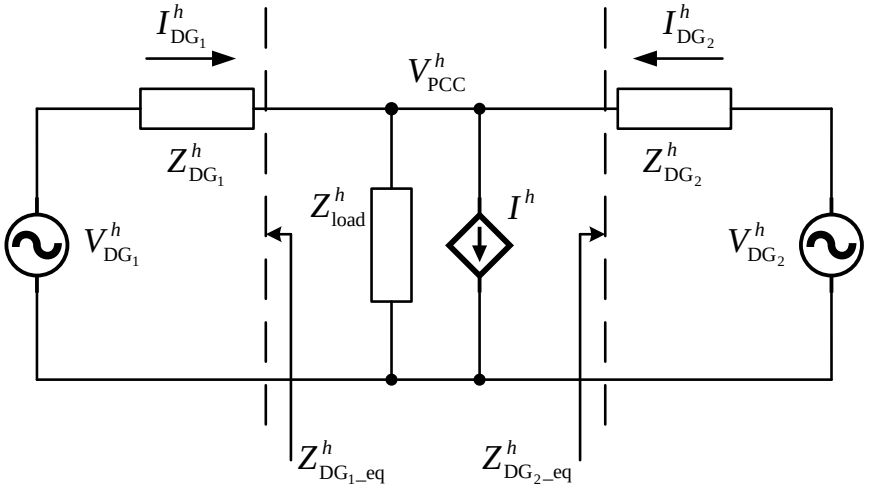

Figure 3.3: Simplified Equivalent circuit of two DGs based microgrid.

The equivalent harmonic impedance for DG_i at the PCC point can be derived as

$$\begin{aligned} I^h_{DG_i} &= (V^h_{DG_i} - V^h_{PCC})/Z^h_{DG_i} \\ &= -(1+G^h_i)V^h_{PCC}/Z^h_{DG_i} \\ Z^h_{DG_{i\_eq}} &= \frac{-V^h_{PCC}}{I^h_{DG_i}} = \frac{Z^h_{DG_i}}{(1+G^h_i)} \end{aligned} \tag{3.4}$$

where $I^h_{DG_i}$ is the DG_i harmonic current and $Z^h_{DG_i}$ is the DG_i feeder harmonic impedance.

It is clear from the above interpretation that, by properly controlling the DG_i harmonic voltage with a positive gain , the DG_i feeder harmonic impedance will be reduced by a factor of $(1+G^h_i)$. In order to share proportionally the harmonic power between different DGs, the selection of this gain is subject to a droop coefficient designed based on specific rating of harmonic power for each DG. It is obvious to say that multiple DGs with harmonic voltage controlled based on the reduction of DG harmonic impedance will further reduce the PCC voltage harmonics. Each DG will be subjected to a controlled positive gain G^h_i which is responsible for generating a reference harmonic voltage. More details of the design are given in the followed subsection.

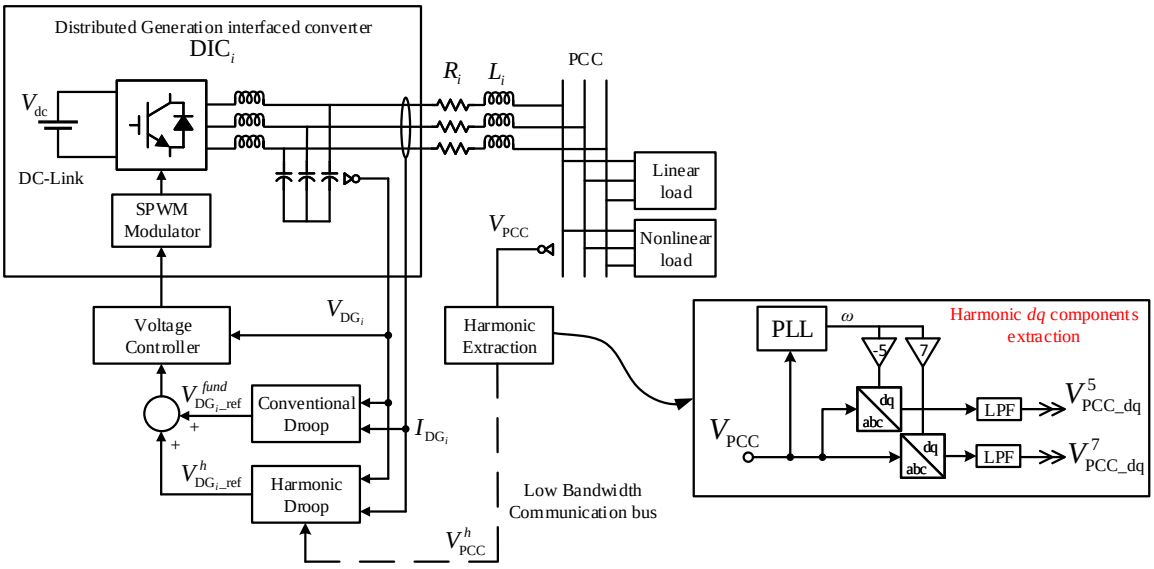

Figure 3.4: Proposed control strategy for DG interfaced converter.

3.3.2 Parameters identification of the proposed harmonic droop

The proposed control strategy is implemented as shown in Fig. 3.4. The harmonic voltages at the PCC are used to generate the inverter reference harmonic voltage by means of the harmonic droop. The voltage across filter capacitor is measured and controlled to be equal the total reference voltage generated by the two droop controllers. Thus, the dynamic behavior of a DG as regard to harmonic current is bound to the bandwidth of the voltage controller. The mechanism of the harmonic droop control is shown in Fig. 3.5. The essence of this controller comes from designing a harmonic droop function $(Q^h - G^h)$ that is able to define the gain G^h as function of the harmonic power rating of each DG. Similar to the characteristics defined for $P - f$ and $Q - V$ droop, that allow to share the fundamental power between DG units in proportion to the rated capacity, the proposed harmonic droop is defined in similar way by setting the droop coefficients b_i $(i{=}1 \ldots n)$ for all DG units as:

$$b_1 Q^h_{1\_\text{rated}} = b_2 Q^h_{2\_\text{rated}} = \ldots = b_n Q^h_{n\_\text{rated}} \tag{3.5}$$

where $Q^h_{i\_\text{rated}}$ $(i{=}1 \ldots n)$, is the rating value of harmonic power capacity of DG$_i$.

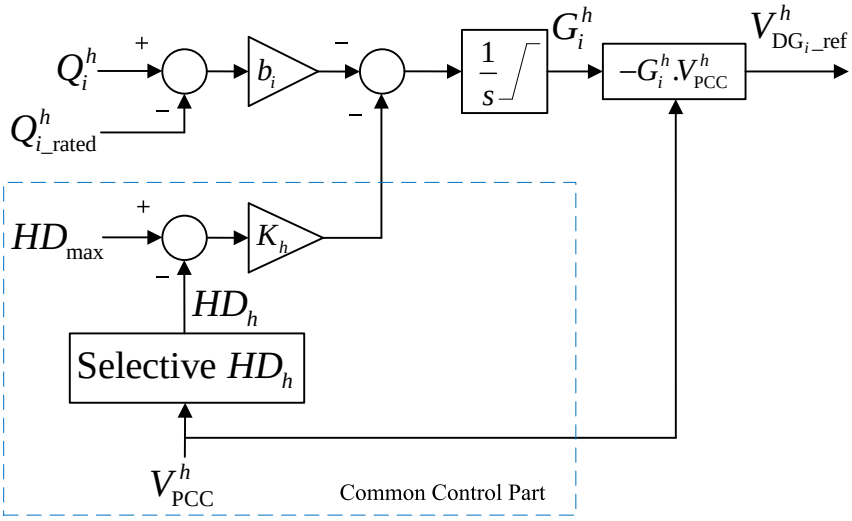

Figure 3.5: Proposed Harmonic Droop Controller.

However, the effect of the mismatch line impedances will prevent the proportional flow of harmonic power between DGs. For this case, a common control part for all DGs is proposed and added to the harmonic droop. It is represented by the selective harmonic distortion (HD_h) which is compared with an input value, HD_{max}, the maximal allowable variation of harmonic distortion. To illustrate the equally share of harmonic power between DGs, by referring to Fig. 3.5 and when steady state is reached, the input of the integrator is zero. Thus, Eq. (3.6) can be formed:

$$b_i(Q_i^h - Q_{i\_\text{rated}}^h) = K_h(HD_h - HD_{max}) \tag{3.6}$$

Since the output of the common control part is the same for all DGs, a proportional sharing of harmonic power between the units is satisfied by:

$$b_1 Q_1^h = b_2 Q_2^h = ... = b_n Q_n^h \tag{3.7}$$

As indicated in Fig. 5, the harmonic power Q_i^h is calculated for each DG as

$$Q_i^h = 3V_{DG_i}^{fund} I_{DG_i}^h \tag{3.8}$$

where $V_{DG_i}^{fund}$ is the fundamental rms-voltage across DG_i feeder.

The procedure of tuning the harmonic droop coefficients can be given as

$$b_i = b_0 / Q_{i\_\text{rated}}^h \tag{3.9}$$

The gain b_0 is set to be high enough, with system stability to be ensured, in order to adopt accurate harmonic power sharing. The gain K_h is chosen to be equal for all DGs and is defined by

$$K_h = b_0 / HD_{max} \tag{3.10}$$

Therefore, by setting b_0 and HD_{max}, the harmonic droop become simple to tune and flexible to work with the fundamental droop being reported previously. The proposed algorithm can dynamically change the positive gain for each harmonic frequency.

The selective HD_h represents the h-harmonic voltage distortion given as

$$HD_h = V_{PCC}^h / V_{PCC}^{fund} \tag{3.11}$$

where, V_{PCC}^{fund} represents the fundamental rms-voltage at the PCC, and V_{PCC}^h, the h-harmonic voltage component extracted using real time synchronous individual harmonic frame method.

To avoid saturation of the DG inner voltage controller when using the proposed harmonic droop which adds reference harmonic voltage to the input of the voltage controller, the integrator should be bound to the inverter voltage saturation value when using a specific modulator. For example, in sinusoidal PWM the saturation limit is given as:

$$V_{DG_{i\_\mathrm{ref}}} \leq \sqrt{\frac{3}{2}}.\frac{V_{dc}}{2} \tag{3.12}$$

And in the case of adding h-harmonic reference voltage to the DG inner controller the reference rms-voltage can be written as:

$$V_{DG_{i\_\mathrm{ref}}} = \sqrt{(V_{DG_{i\_\mathrm{ref}}}^{fund})^2 + (V_{DG_{i\_\mathrm{ref}}}^{h})^2} \tag{3.13}$$

Since the h-harmonic reference voltage is written as:

$$\begin{aligned} V_{DG_{i\_\mathrm{ref}}}^h &= -G_i^h V_{PCC}^h \\ V_{DG_{i\_\mathrm{ref}(max)}}^h &= -G_i^h HD_{max} V_{PCC}^{fund} \end{aligned} \tag{3.14}$$

Thus, introducing equations (3.13) and (3.14) in inequality (3.12) we obtain:

$$0 \leq G_i^h \leq \frac{\sqrt{\frac{3}{2}(V_{dc}/2)^2 - (V_{DG_i}^{fund})^2}}{HD_{max} V_{PCC}^{fund}} \tag{3.15}$$

Equation (3.15) can be re-written in another form, where only the DG input parameters can be used:

$$0 \leq G_i^h \leq \frac{\sqrt{\frac{3}{2}(V_{dc}/2)^2 - (V_{DG_i}^{fund})^2}}{HD_{max} V_{DG_i}^{fund}} \tag{3.16}$$

3.4 Control Model and Small-Signal Analysis

From the equivalent circuit in Fig. 3.3, (3.17) can be obtained at hth harmonic frequency for DG_i in synchronous rotating frame (dq) as

$$\begin{pmatrix} V^h_{DG_{i\_\mathrm{d}}} \\ V^h_{DG_{i\_\mathrm{q}}} \end{pmatrix} = Z^h_{DG_i} \begin{pmatrix} I^h_{DG_{i\_\mathrm{d}}} \\ I^h_{DG_{i\_\mathrm{q}}} \end{pmatrix} + L_i \frac{d}{dt} \begin{pmatrix} I^h_{DG_{i\_\mathrm{d}}} \\ I^h_{DG_{i\_\mathrm{q}}} \end{pmatrix} + \begin{pmatrix} V^h_{PCC\_\mathrm{d}} \\ V^h_{PCC\_\mathrm{q}} \end{pmatrix} \tag{3.17}$$

where $Z^h_{DG_i} = \begin{pmatrix} R_i & -h\omega L_i \\ h\omega L_i & R_i \end{pmatrix}$, $i \in \{1, 2\}$.

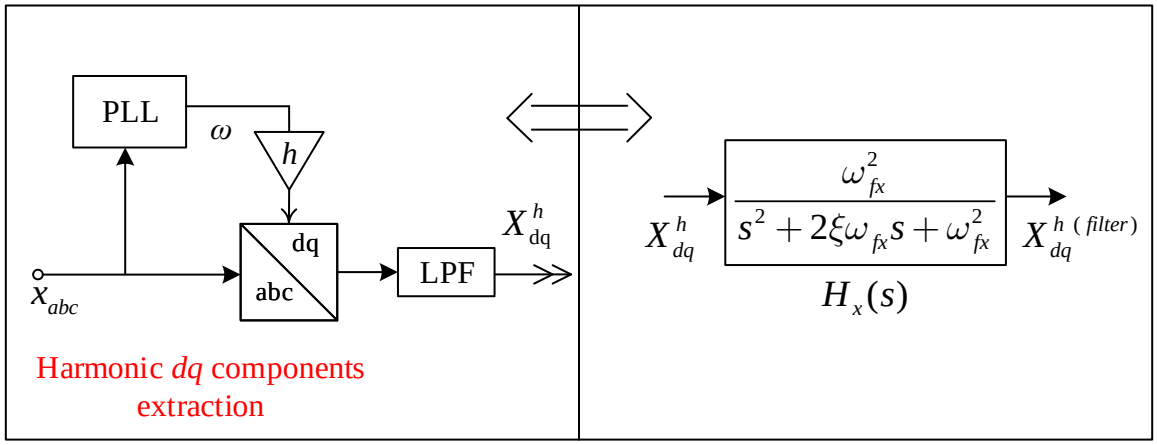

Figure 3.6: Synchronous individual harmonic "dq frame" extraction block.

It is to be noted that the DG voltage inner controller is of higher bandwidth compared to the bandwidth of droop control, thus the DG interfaced converter with its controller is modeled as a perfect voltage source as shown in Fig. 3.3. Fig. 3.6 shows the harmonic extraction method used to obtain the h-harmonic voltage/current components. The extraction of the harmonic current and voltage are based on time domain method which make use of generalized Park transformation to convert the measured quantity (current or voltage) from 3-phase stationary frame to the synchronous reference frame rotating at chosen frequency. The dc component is then filtered by using a simple low-pass filter. Thus, the harmonic extraction block can be modeled as a second order low-pass filter as

$$\frac{V^{h\ (filter)}_{PCC\_\mathrm{dq}}}{V^h_{PCC\_\mathrm{dq}}} = H_v(s) = \frac{\omega^2_{fv}}{s^2 + 2\xi_v\omega_{fv}s + \omega^2_{fv}} \tag{3.18}$$

$$\frac{I^{h\ (filter)}_{DG_{i\_\mathrm{dq}}}}{V^h_{DG_{i\_\mathrm{dq}}}} = H_i(s) = \frac{\omega^2_{fi}}{s^2 + 2\xi_i\omega_{fi}s + \omega^2_{fi}} \tag{3.19}$$

The DG_i harmonic voltage, is the reference set by the harmonic droop expressed as

$$\begin{pmatrix} V^h_{DG_{i\_\mathrm{d}}} \\ V^h_{DG_{i\_\mathrm{q}}} \end{pmatrix} = -G^h_i \begin{pmatrix} V^{h\ (filter)}_{PCC\_\mathrm{d}} \\ V^{h\ (filter)}_{PCC\_\mathrm{q}} \end{pmatrix} \tag{3.20}$$

Using Kirchhoff's current law, we can find from Fig. 3.3 in dq frame that

$$I^h_{DG_{2\_\mathrm{dq}}} = I^h_{\mathrm{dq}} - I^h_{DG_{1\_\mathrm{dq}}} \tag{3.21}$$

Assuming that the bandwidth of the extraction block along with the communication channel is lower enough to not interact with the dynamics of the harmonic current flowing across line impedances. Thus, (3.20) can be written as

$$\begin{pmatrix} V^h_{DG_{i\_\mathrm{d}}} \\ V^h_{DG_{i\_\mathrm{q}}} \end{pmatrix} = -G^h_i \begin{pmatrix} V^h_{PCC\_\mathrm{d}} \\ V^h_{PCC\_\mathrm{q}} \end{pmatrix} \tag{3.22}$$

For a microgrid with 2 DG sources ($i \in \{1, 2\}$), we substitute (3.22) in (3.17), to get $V^h_{DG_{2_\mathrm{dq}}}$as function of PCC and DG_1 harmonic voltages as:

$$\begin{aligned} \begin{pmatrix} V^h_{DG_{2\_\mathrm{d}}} \\ V^h_{DG_{2\_\mathrm{q}}} \end{pmatrix} &= Z^h_{DG_2} \begin{pmatrix} I^h_d - I^h_{DG_{1\_\mathrm{d}}} \\ I^h_q - I^h_{DG_{1\_\mathrm{q}}} \end{pmatrix} - \frac{L_2}{L_1} \left[\begin{pmatrix} V^h_{DG_{1\_\mathrm{d}}} \\ V^h_{DG_{1\_\mathrm{q}}} \end{pmatrix} - Z^h_{DG_1} \begin{pmatrix} I^h_{DG_{1\_\mathrm{d}}} \\ I^h_{DG_{1\_\mathrm{q}}} \end{pmatrix} \right] \\ &\quad + (1 + \frac{L_2}{L_1}) \begin{pmatrix} V^h_{PCC\_\mathrm{d}} \\ V^h_{PCC\_\mathrm{q}} \end{pmatrix} \end{aligned} \tag{3.23}$$

Rearranging (3.23) by taking into account (3.22), we can get:

$$V^h_{PCC\_\mathrm{dq}} = \frac{1}{G} . \left[-Z^h_{DG_2} (I^h_{\mathrm{dq}} - I^h_{DG_{1\_\mathrm{dq}}}) - \frac{L_2}{L_1} Z^h_{DG_1} I^h_{DG_{1\_\mathrm{dq}}} \right] \tag{3.24}$$

where, $G = \left(1 + G^h_2 + \frac{L_2}{L1}(1 + G^h_1)\right)$.

The coefficient G^h_i, the output of the droop can be given by

$$\frac{dG^h_i}{dt} = -b_i (Q^h_i - Q^h_{i\_\mathrm{rated}}) - K_h (HD_{max} - HD_h) \tag{3.25}$$

where, $Q^h_i = 3V^{fund}_{DG_i} I^h_{DG_i} = 3V^{fund}_{DG_i} \sqrt{\frac{1}{3}\left((I^h_{DG_{i\_\mathrm{d}}})^2 + (I^h_{DG_{i\_\mathrm{q}}})^2\right)}$ and $HD_h = \frac{V^h_{PCC}}{V^{fund}_{PCC}} = \frac{\sqrt{\frac{1}{3}\left((V^{h\,(filter)}_{PCC\_\mathrm{d}})^2 + (V^{h\,(filter)}_{PCC\_\mathrm{q}})^2\right)}}{V^{fund}_{PCC}}$.

Equations (3.17)-(3.25) can be combined to formulate the dynamics of the whole system as

$$\dot{x} = A(x).x \tag{3.26}$$

where, $x = \left[I^h_{DG_{1\_\mathrm{dq}}},\ I^{h\ (filter)}_{DG_{1\_\mathrm{dq}}},\ dI^{h\ (filter)}_{DG_{1\_\mathrm{dq}}},\ V^{h\ (filter)}_{PCC\_\mathrm{dq}},\ dV^{h\ (filter)}_{PCC\_\mathrm{dq}},\ G^h_1,\ G^h_2 \right]^t$.

Note that, $A(x)$ is not linear and has state variables as elements. Thus, the model is a nonlinear of order 12. In order to study the stability of the proposed harmonic droop and to understand the dynamic behavior which is affected by several control variables, an eigenvalue analysis by plotting the root locus is given. This is done by calculating the Jacobean matrix at each operating point to determine the stability of the system under the variations of different control parameters.

System Parameters	
Fundamental Line voltage (V)/frequency (Hz)	110V/60Hz
Feeder impedance $Z_{DG_1}(R_1,\ L_1)$	(0.1Ω, 1mH)
Feeder impedance $Z_{DG_2}(R_2,\ L_2)$	(0.2Ω, 5mH)
5th harmonic current source: $(I^5_{\mathrm{dq}} = I^5_{\mathrm{d}} + \mathrm{j}I^5_{\mathrm{q}})$	1-j0.5 (A)
DG Harmonic Droop	
$\mathrm{DG}_1:\ Q^h_{1\_\mathrm{rated}}$ (Var)	500
$\mathrm{DG}_2:\ Q^h_{2\_rated}$ (Var)	250
Max. Harmonic distortion $HD_{max}(\%)$	1%
Lowpass Filter Harmonic extraction	
ξ/ω_f (rad/sec)	1/100

Table 3.1: System Parameters for Dynamic Analysis.

The system parameters used for examination are given in table 3.1. The eigenvalues of the system at its nominal operating condition are shown in Fig. 3.7(a). It can be seen that the eigenvalues, are placed in three different clusters. The eigenvalues of cluster 1 are sensitive to the change of droop coefficients. The dynamics of the 2nd order lowpass filters used in extracting the harmonic contents (i.e. harmonic voltages and currents) are determined by the eigenvalues of cluster 2. The eigenvalues of cluster 3 represent the harmonic current dynamics before filtering $I^h_{DG_{1\_\mathrm{dq}}}$. Fig. 3.7(b) shows the locus of the dominant eigenvalues that affect the system stability as the harmonic droop coefficients change. The sense of variation of those coefficients is from lower to maximum value. The behavior of eigenvalues λ_7 and λ_8 are identical and tends to be unstable during the variation (at b_0=160). This interpret the appropriate choose of gain b_0, being positively high but not enough, to ensure stability of the system. As the droop coefficients increase the harmonic gains response become undamped which was noted from the behavior of eigenvalues λ_{11} and λ_{12}. Note that the conjugate pairs λ_1 and λ_2 are so far on the left-side of the s-plane and unaffected by the change, they are not shown here.

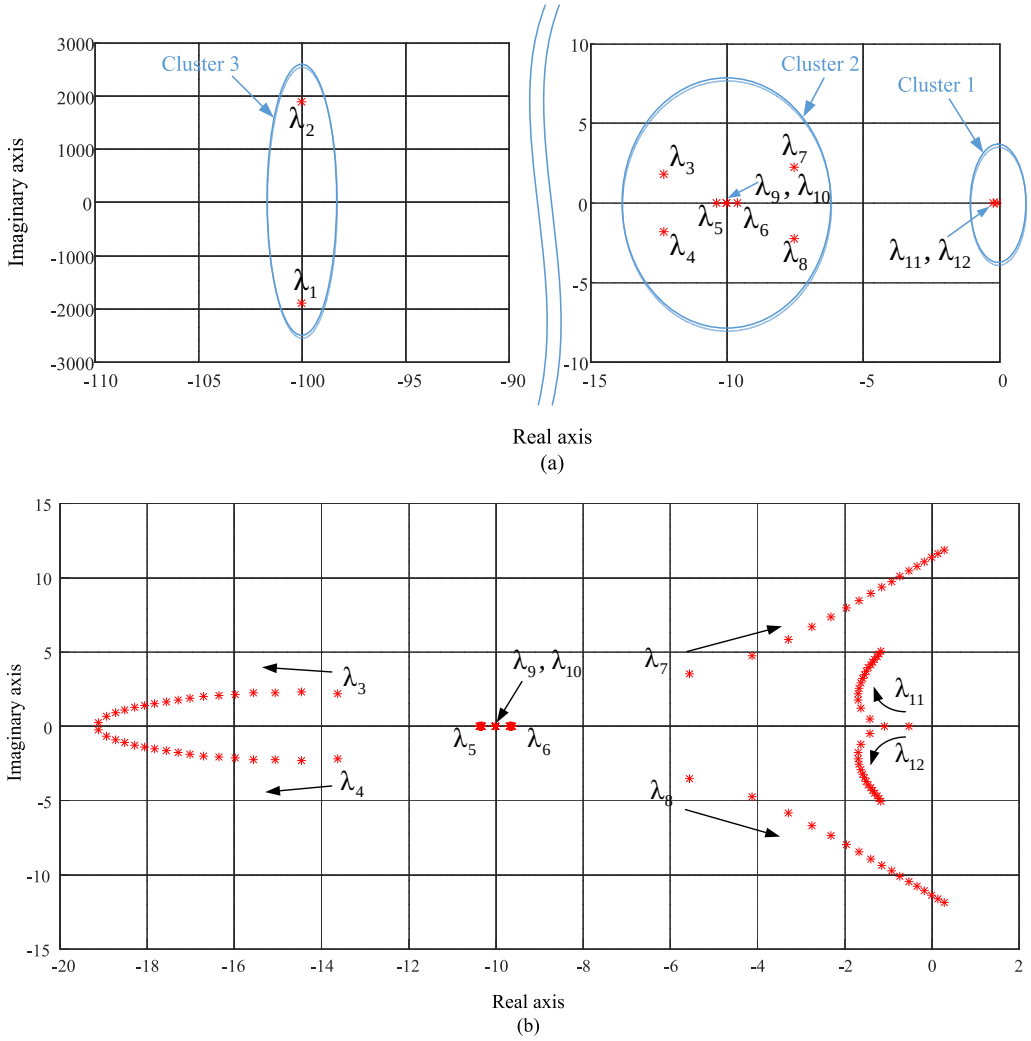

Figure 3.7: Eigenvalue analysis: (a) Eigenvalues for nominal condition (b_0=10): $b_1 = 2\times10^{-2}$, $b_2 = 4\times10^{-2}$; (b) Eigenvalues locus with harmonic droop coefficients change $b_i (0 \leq b_0 \leq 170)$: $2\times10^{-2} \leq b_1 \leq 3.4\times10^{-1}$, $4\times10^{-2} \leq b_2 \leq 6.8\times10^{-1}$.

3.5 Simulation Results

The proposed harmonic droop controller is tested by MATLAB-Simulink for different number of DGs as configured in Fig. 3.1. Firstly, the harmonic droop is applied for two DGs based-microgrid to demonstrate the harmonic sharing performance. Secondly, the proposed harmonic droop is tested in a system with three DGs to show if the it works with different condition. The linear load is defined as R-L and the nonlinear one is represented by current sources injected in the network. Note that, the study is done for sharing harmonics of 5th and 7th order.

3.5.1 Microgrid with two DGs

In this condition, DG_1 and DG_2 are supplying the R-L load with injection of 5th and 7th harmonic currents in the network. The system parameters for this simulation are given in Table 3.2. The two sources will share the fundamental real and reactive power equally by using the droop control with equal droop coefficients as set in Table 3.2. In the following, the proposed harmonic droop was tested for the two sources in two different cases.

System Parameters				
Fundamental line voltage (V)/frequency (Hz)	110 V/60 Hz			
Feeder impedance $Z_{DG_1}(R_1, L_1)$	(0.1Ω, 1mH)			
Feeder impedance $Z_{DG_2}(R_2, L_2)$	(0.2Ω, 5mH)			
5th harmonic current source: $(I^5_{\mathrm{dq}} = I^5_{\mathrm{d}} + \mathrm{j}I^5_{\mathrm{q}})$	1-j0.5 (A)			
7th harmonic current source: $(I^7_{\mathrm{dq}} = I^7_{\mathrm{d}} + \mathrm{j}I^7_{\mathrm{q}})$	-1 (A)			
Max. Harmonic distortion $HD_{max}(\%)$	1%			
DG Droop Characteristics				
Control parameter	**Case 1:**		**Case 2:**	
	DG_1	DG_2	DG_1	DG_2
m_i (rad/W)	5×10^{-5}	5×10^{-5}	5×10^{-5}	5×10^{-5}
n_i (V/Var)	6.7×10^{-3}	6.7×10^{-3}	6.7×10^{-3}	6.7×10^{-3}
$Q^h_{i\_\mathrm{rated}}$ (Var)	500	500	500	250
b_i (1/Var)	0.1	0.1	0.1	0.2

Table 3.2: Simulation Parameters for Two DGs configuration.

1. Case 1: The two sources are set to have equal harmonic power ratings. Fig. 3.8 shows the fundamental power sharing for this case. The fundamental active and reactive powers are equally shared between the two DGs. The reactive power sharing is compensated due to the fact that the method proposed in [54] is used. In Fig. 3.9 the harmonic power (5th and 7th orders) are shared equally between two DGs after starting the harmonic droop. The procedure also tests the dynamics of the controller under step load change which prove the effectiveness of the method proposed.

2. Case 2: The two DGs are set with different harmonic power ratings as indicated in Table II. The simulation test procedure is similar to the previous case, as shown in Fig. 3.10, DG_2 can share half the amount of harmonic power as regard to DG_1. Accurate proportional harmonic power sharing interprets the efficiency of the proposed controller. The positive gains given by the output of the harmonic droop control for each DG at 5th and 7th harmonics are shown in Fig. 3.11. The harmonic gains depend on the ratings and line impedance value separating each DG to the load.

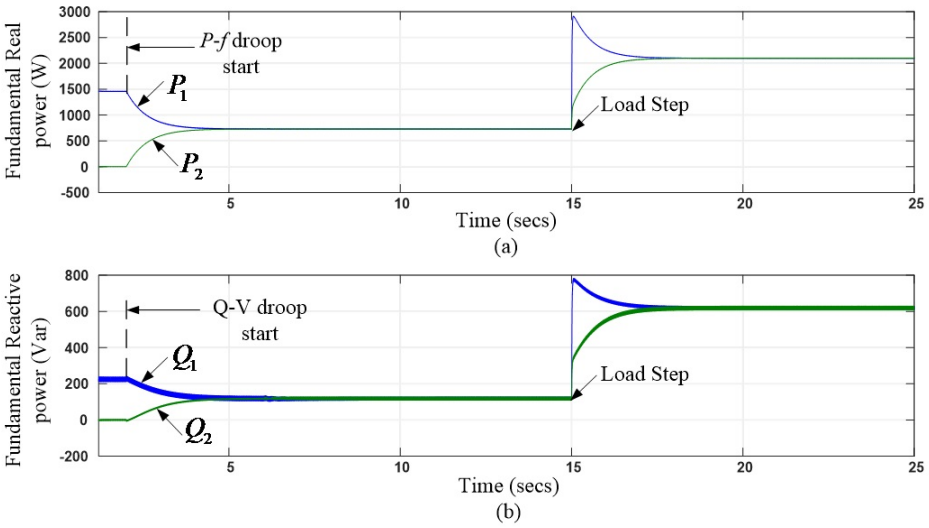

Figure 3.8: Simulation results for case 1: (a) Fundamental Real power: P_1, P_2; (b) Fundamental Reactive power: Q_1, Q_2.

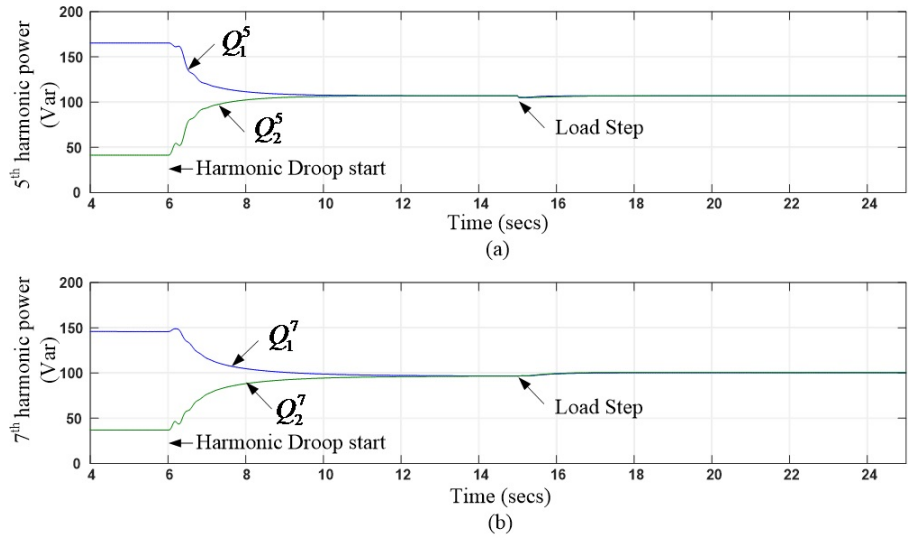

Figure 3.9: Simulation results for case 1. (a) 5th Harmonic power for two DGs: Q_1^5, Q_2^5; (b) 7th Harmonic power for two DGs: Q_1^7, Q_2^7.

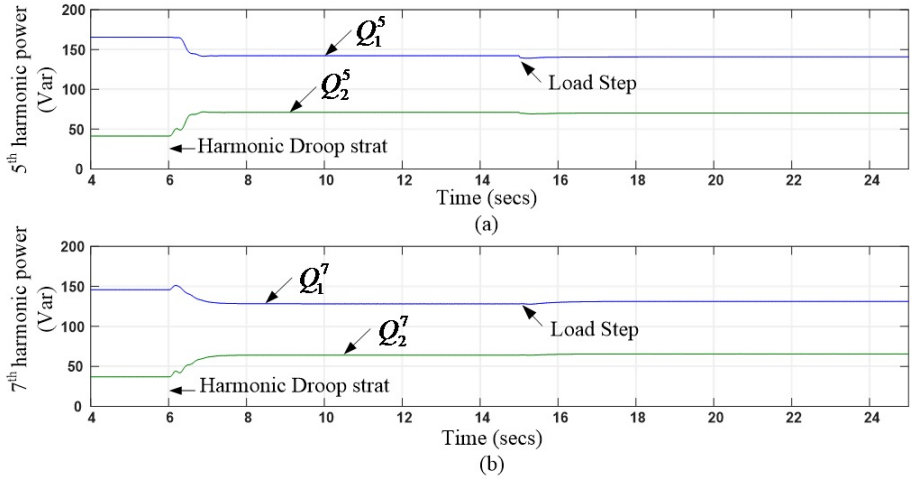

Figure 3.10: Simulation results for case 2. (a) 5th Harmonic power for two DGs: Q_1^5, Q_2^5; (b) 7th Harmonic power for two DGs: Q_1^7, Q_2^7.

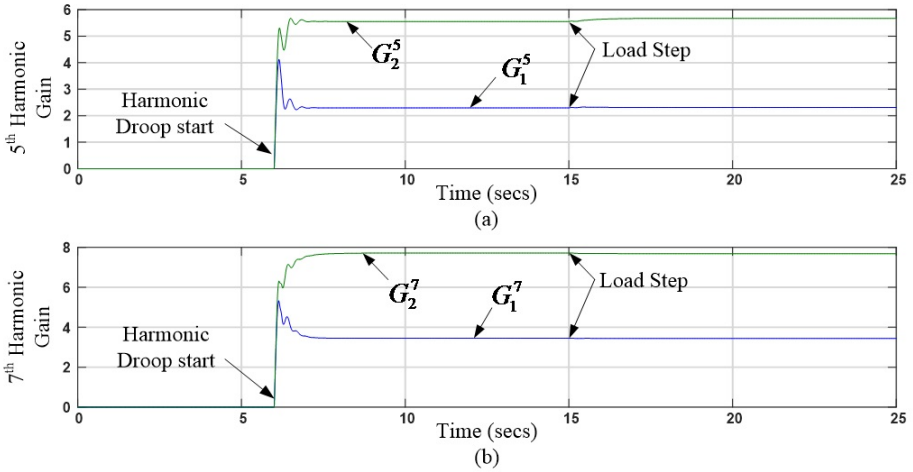

Figure 3.11: Simulation results for case 2. (a) 5th Harmonic Gains for two DGs: G_1^5, G_2^5; (b) 7th Harmonic Gains for two DGs: G_1^7, G_2^7.

3.5.2 System stability with high droop gains

As indicated before in Section 3.4, as the harmonic coefficients increase the system becomes unstable. The eigenvalues can predict system instability for such variation. To examine the system stability under high harmonic droop gains, the system is operated with different harmonic power ratings as in case 2, but first with limit droop gains ($b_0 = 160$) and at t=25sec. the droop gains are changed to higher values ($b_0 = 170$, i.e. $b_1 = 3.4 \times 10^{-1}$, $b_2 = 6.8 \times 10^{-1}$). Fig. 3.12 shows the system response under harmonic droop with higher gains where the power and current waveforms oscillate. Fig. 3.13 represents the output gains generated by the harmonic droop for both DGs in this case.

The undamped response validates the eigenvalue analysis of Fig. 3.7 where it predicts the instability behavior at the given droop parameters.

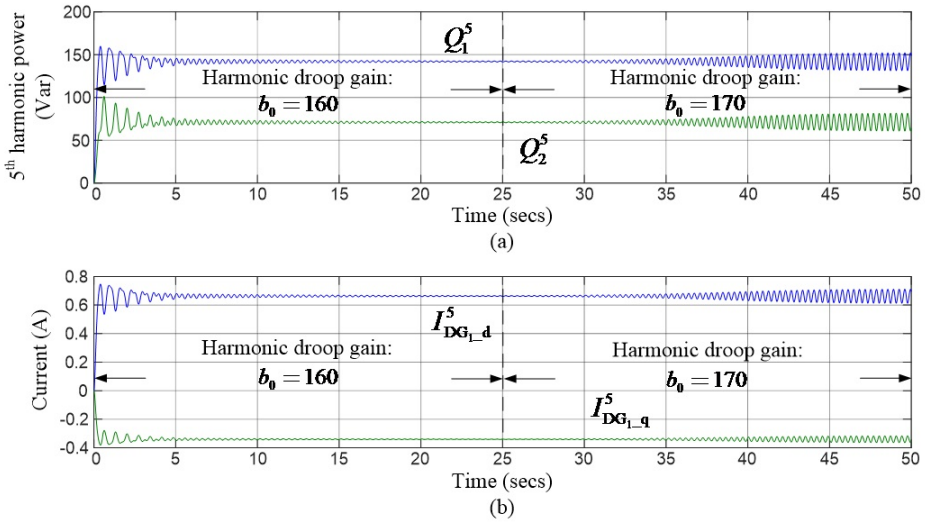

Figure 3.12: Simulation results for system stability: 5th Harmonic power distribution for both DGs with DG_1 harmonic current time response.

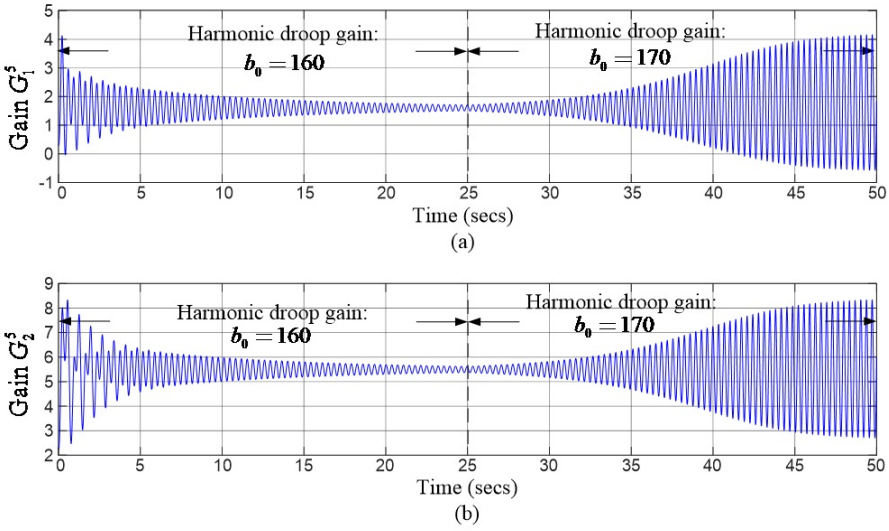

Figure 3.13: Simulation results for system stability: 5th Harmonic gain time response for both DGs.

System Parameters			
Fundamental line voltage (V)/frequency (Hz)	110 V/60 Hz		
Feeder impedance $Z_{DG_1}(R_1, L_1)$	(0.58Ω, 5mH)		
Feeder impedance $Z_{DG_2}(R_2, L_2)$	(0.2Ω, 2mH)		
Feeder impedance $Z_{DG_3}(R_3, L_3)$	(0.1Ω, 1mH)		
5th harmonic current source: $(I^5_{\mathrm{dq}} = I^5_{\mathrm{d}} + \mathrm{j}I^5_{\mathrm{q}})$	4-j2 (A)		
7th harmonic current source: $(I^7_{\mathrm{dq}} = I^7_{\mathrm{d}} + \mathrm{j}I^7_{\mathrm{q}})$	-5 (A)		
Max. Harmonic distortion $HD_{max}(\%)$	1%		
DG Droop Characteristics			
Control parameter	DG_1	DG_2	DG_3
m_i (rad/W)	5×10^{-5}	5×10^{-5}	5×10^{-5}
n_i (V/Var)	6.7×10^{-3}	6.7×10^{-3}	6.7×10^{-3}
$Q^h_{i\_\mathrm{rated}}$ (Var)	500/400	500/400	500/800
b_i (1/Var)	0.04/0.05	0.04/0.05	0.04/0.025

Table 3.3: Simulation Parameters for Three DGs configuration.

3.5.3 Microgrid with three DGs

To illustrate the performance of the proposed harmonic droop controller in different configurations, a simulation test was done in a microgrid of three DGs (as configured in Fig. 3.1), with two DGs near the nonlinear load while the third DG is set to be far from it. It is to be noted that all DGs are set to have equal fundamental power ratings. Furthermore, all DGs are supported by the harmonic droop to share the harmonic current and compensate the voltage distortion at the PCC. The system parameters for this simulation are given in Table 3.3. After connecting all DGs to the load, the fundamental output powers are distributed equally between DGs as given in Fig. 3.14. In Fig. 3.15, the harmonic power before starting the harmonic droop shows improper flow between DGs. It is evident that the most accompany source in supplying the harmonic power is the nearest one connected to the load (i.e. DG with less line impedance). After starting the droop, the harmonic power it is well compensated between all DG units. Furthermore, it was tested to stop harmonic sharing with DG_1, the source which is far away from the load, while the two other generators near the nonlinear load must participate in delivering harmonic power.

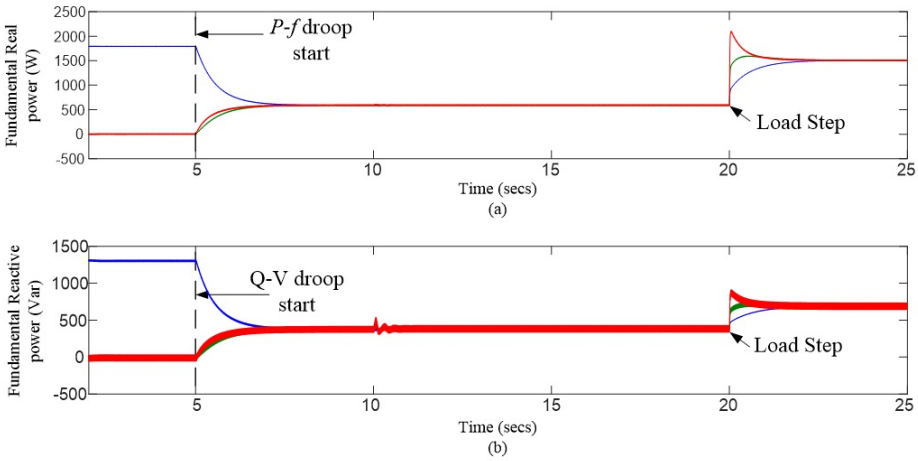

Figure 3.14: Simulation results for microgrid with three DGs: (a) Fundamental Real power: P_1, P_2 and P_3; (b) Fundamental Reactive power: Q_1, Q_2 and Q_3.

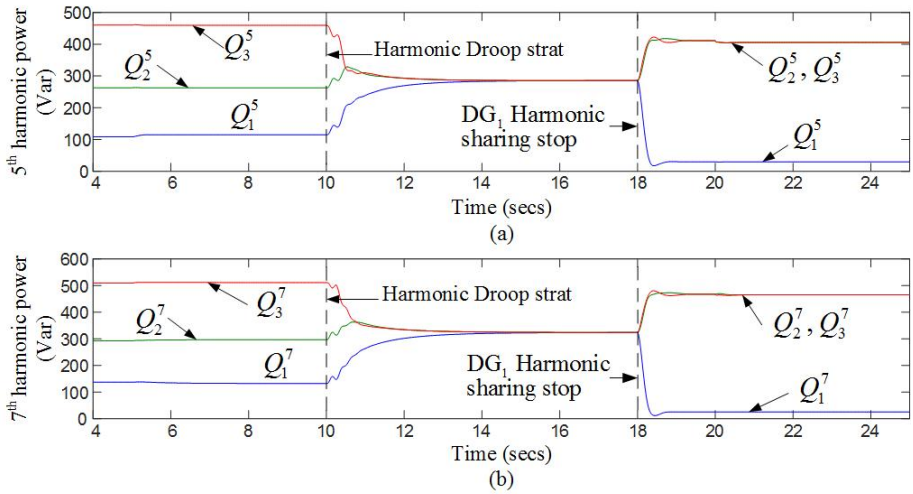

Figure 3.15: Simulation results for microgrid with three DGs with equal harmonic ratings: (a) 5th Harmonic power for two DGs: Q_1^5, Q_2^5, Q_3^5; (b) 7th Harmonic power for two DGs: Q_1^7, Q_2^7, Q_3^7.

Fig 3.16 shows the phase currents generated by each DG in two different stages. Firstly, Fig. 3.16(a) shows the phase currents after starting the droop in all DGs to see its effect in ameliorating the distribution of harmonic contents accurately between them. Furthermore, the phase currents after stopping the harmonic droop in DG_1 is shown in Fig. 3.16(b). It is clear that the phase current of DG_1 in Fig. 3.16(b) is pure sinusoidal which interpret the case of supplying the load with only fundamental power. In this case, the currents of DG_2 and DG_3 are the same and holding all harmonic contents of the load. For the PCC voltage distortion compensation with good amount of harmonic current injected by the load, Fig. 3.17 shows the FFT analysis before and after starting the harmonic droop. The THD has decreased from 5.86% to 1.23% when a harmonic

reference voltages are added to each DG. The same test is done after maintaining same fundamental ratings for all DGs but with different harmonic power as given in Table 3.3. Fig. 3.18 shows the harmonic power sharing between the three sources. When the harmonic droop start, eventually, the harmonic power is distributed proportionally between the DGs according to their ratings. After stopping the harmonic droop on DG_1, the 5th and 7th harmonic power will fall to zero. Meaning that no more harmonic power is delivered by DG_1 to the load. Fig. 3.19 interprets the result by showing the phase current generated by each DG. In Fig. 3.19(a) the phase current is shown when harmonic droop is running in all DGs. DG_1 and DG_2 will share same harmonic current which is half the amount supplied by DG_3. When the harmonic droop is stopped on DG_1, the phase current became sinusoidal and no harmonic power is yet supplied by this source as shown in Fig. 3.19(b).

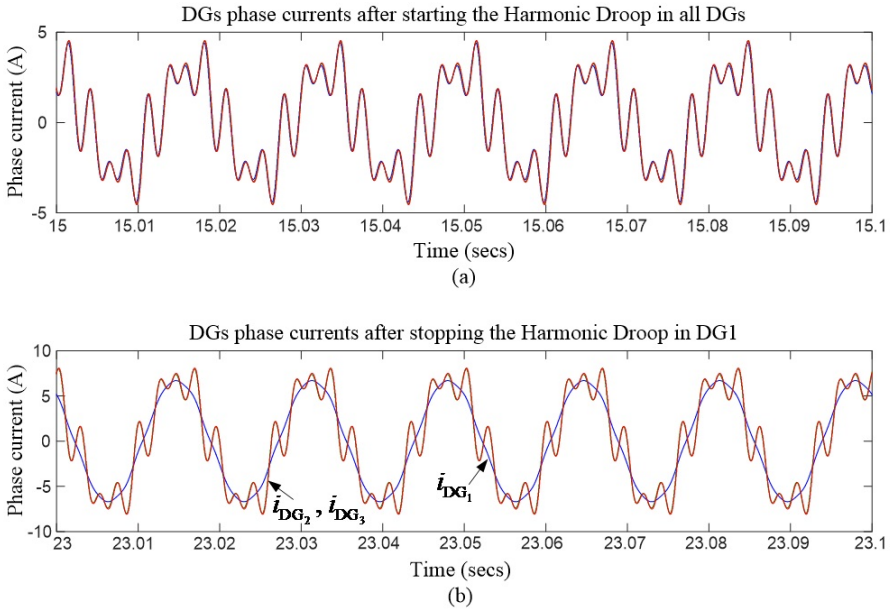

Figure 3.16: Simulation results for microgrid with three DGs: (a) Phase currents before Harmonic compensation: i_{DG_1}, i_{DG_2}, and i_{DG_3}; (b) Phase currents after Harmonic compensation.

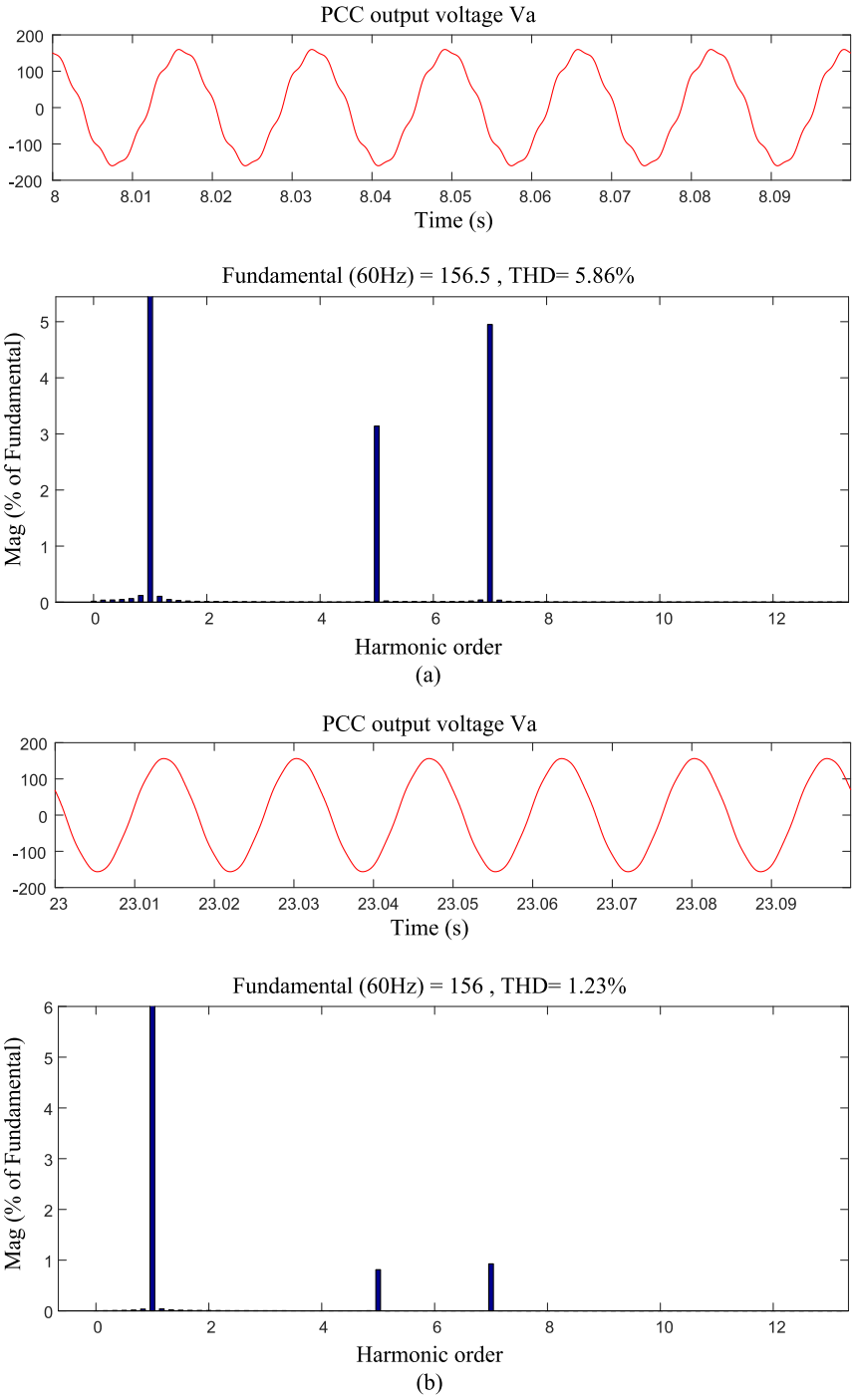

Figure 3.17: Simulation results for microgrid with three DGs: (a) Steady state PCC phase voltage and Harmonic analysis before starting the Harmonic droop: (b) PCC phase voltage and Harmonic analysis after starting the Harmonic droop.

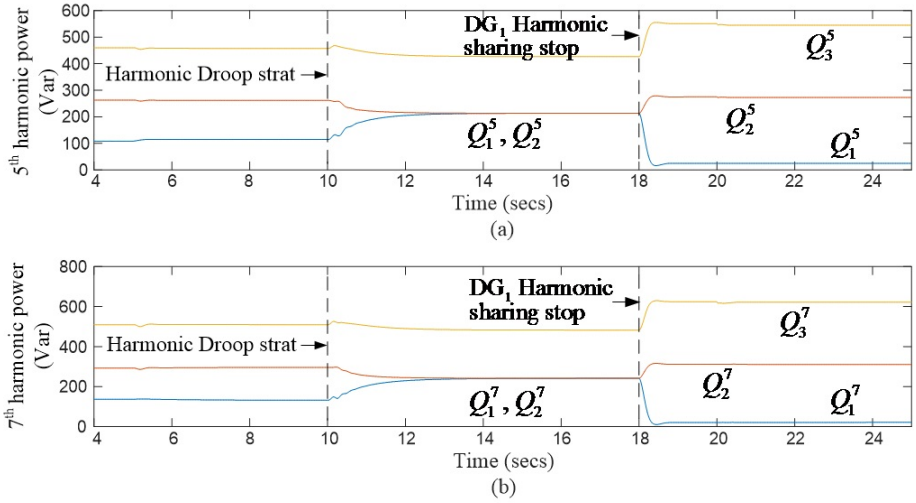

Figure 3.18: Simulation results for microgrid with three DGs with different harmonic ratings: (a) 5th Harmonic power for two DGs: Q_1^5, Q_2^5, Q_3^5; (b) 7th Harmonic power for two DGs: Q_1^7, Q_2^7, Q_3^7.

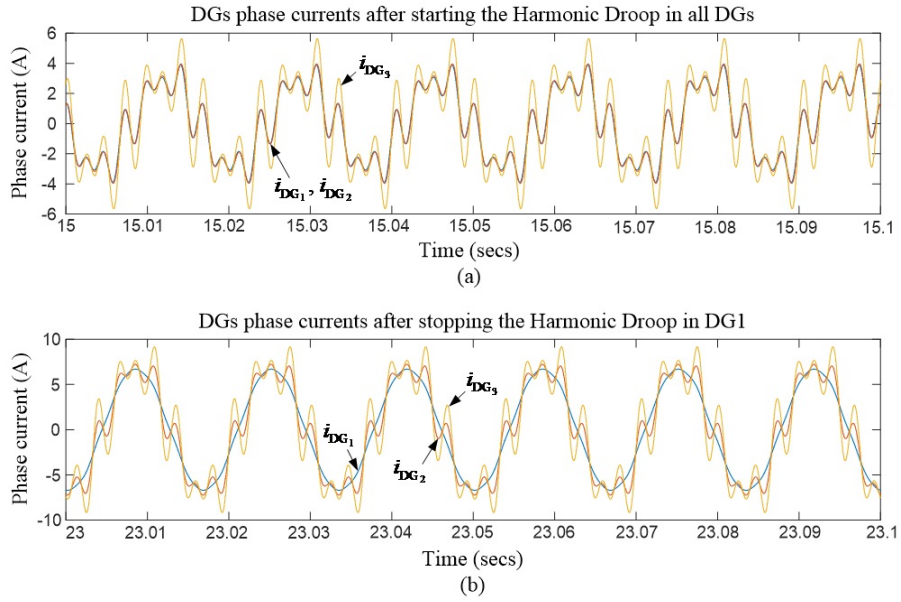

Figure 3.19: Simulation results for microgrid with three DGs: (a) Phase currents before Harmonic compensation: i_{DG_1}, i_{DG_2}, and i_{DG_3}; (b) Phase currents after Harmonic compensation.

3.6 Experimental Results

The Experimental test bench is constructed with two DGs (three-phase inverters 80V-60Hz) connected to a common linear R-L load and nonlinear full bridge rectifier load as

shown in Fig. 3.20. Similar to simulation given in section 3.5.1 with same system parameters given in table 3.2, experimental tests are conducted to validate the performance of the proposed harmonic droop in harmonic power sharing and compensation of voltage distortions. The conventional droop performance is tested first, where the fundamental active and reactive power waveforms for both DGs of equal power ratings are shown in Fig. 3.21.

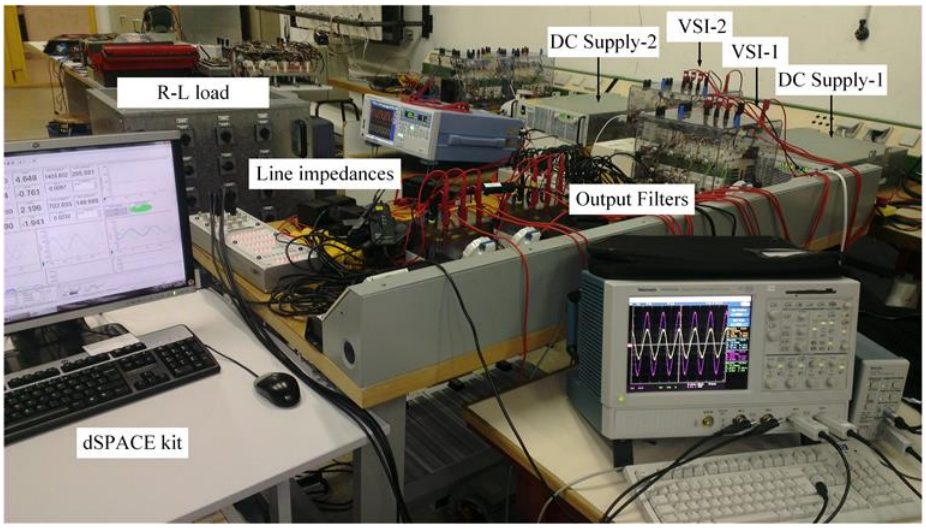

Figure 3.20: Experimental test bench constructed in the laboratory.

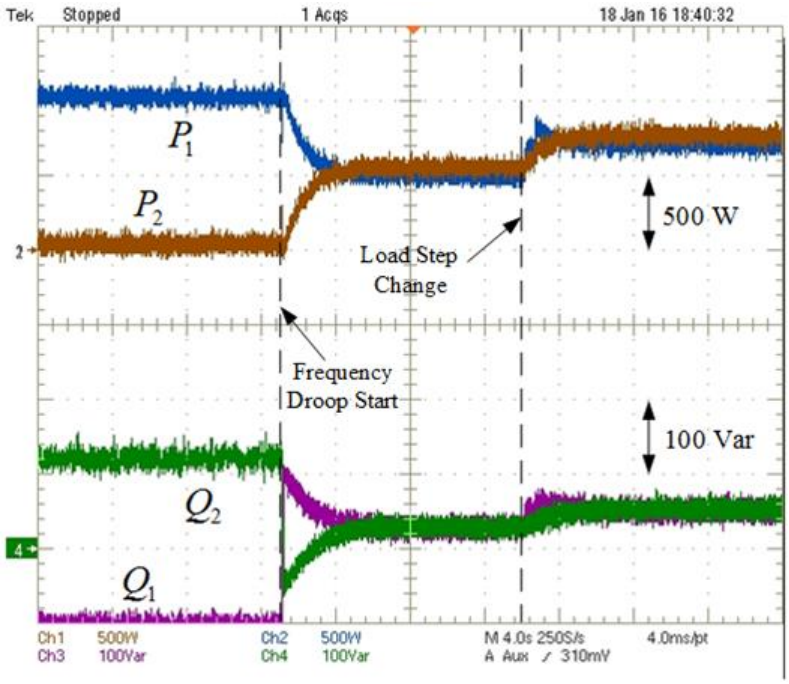

Figure 3.21: Experimental results for case 1: (a) Fundamental Real power: P_1, P_2 and Fundamental Reactive power: Q_1, Q_2 under different stages.

The fundamental Reactive power sharing is solved either by adding a redesigned virtual impedance method or by voltage compensation loop which ensures PCC voltage in nominal range as presented in [54]. This signal is added to the conventional droop controller to cancel the effect of line impedance mismatch thus enhancing the power sharing. Fig. 3.22 shows the 5th and 7th Harmonic Var for the two DGs, as well as the gain time response change to achieve proper sharing, the results are related to equal harmonic power ratings as given in table 3.2, case 1. Fig. 3.23 illustrates the operation of the harmonic droop controller under different rated capacity set to each DG as given in case 2. The steady state values show the harmonic power is shared between the two DGs in proportion to their rated capacity. The phase voltage and current waveforms for each DG before and after activating the harmonic droop are shown in Fig. 3.24. In this case, it is noted that DG_2 with its harmonic droop was able to add harmonic contents in its output voltage to absorb more harmonic current as seen in the figure. It is well interpreted by the waveform of DG_2 source current supplying the load. The compensating of voltage distortion at the PCC is verified with the proposed harmonic droop as shown in Fig. 3.25. The THD drops from 2.88% to 1.88%, since the 5th and 7th voltage components are widely reduced in this case (HD_5 drops from 1.85% to 0.6%, HD_7 drops from 1.37% to 0.34%).

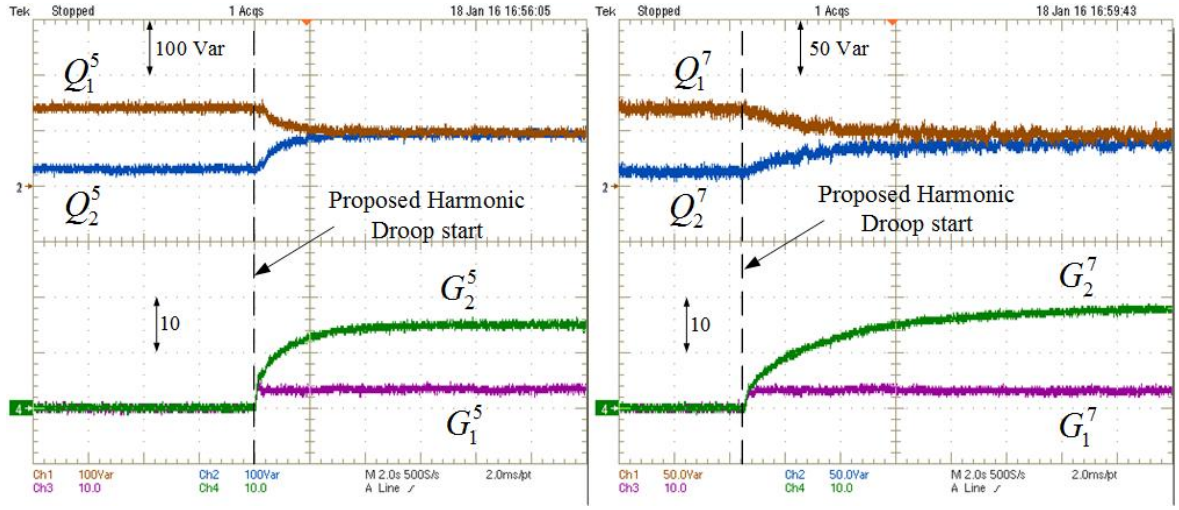

Figure 3.22: Experimental results for case 1: 5th and 7th Harmonic power distribution with gain time response for both DGs.

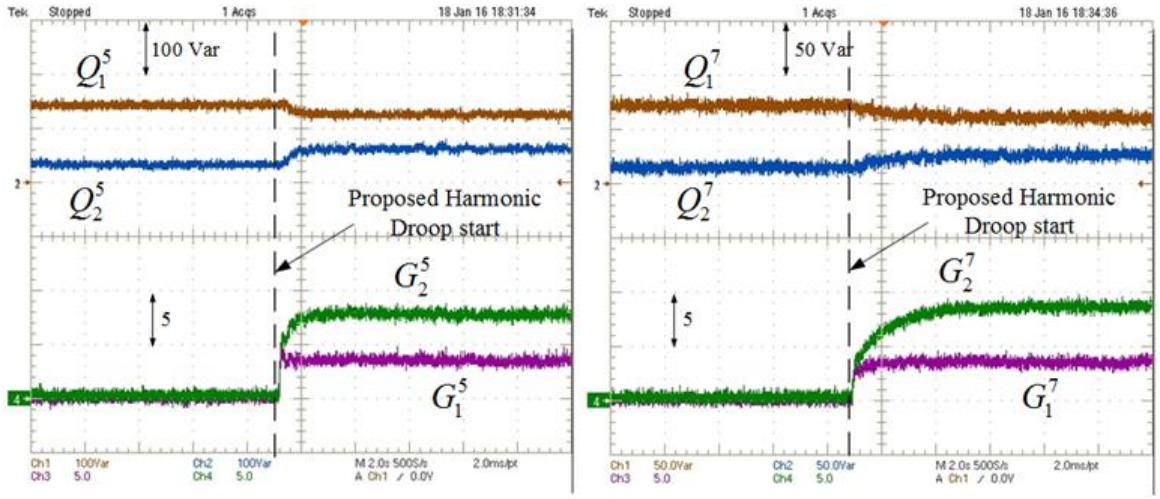

Figure 3.23: Experimental results for case 2: 5th and 7th Harmonic power distribution with gain time response for both DGs.

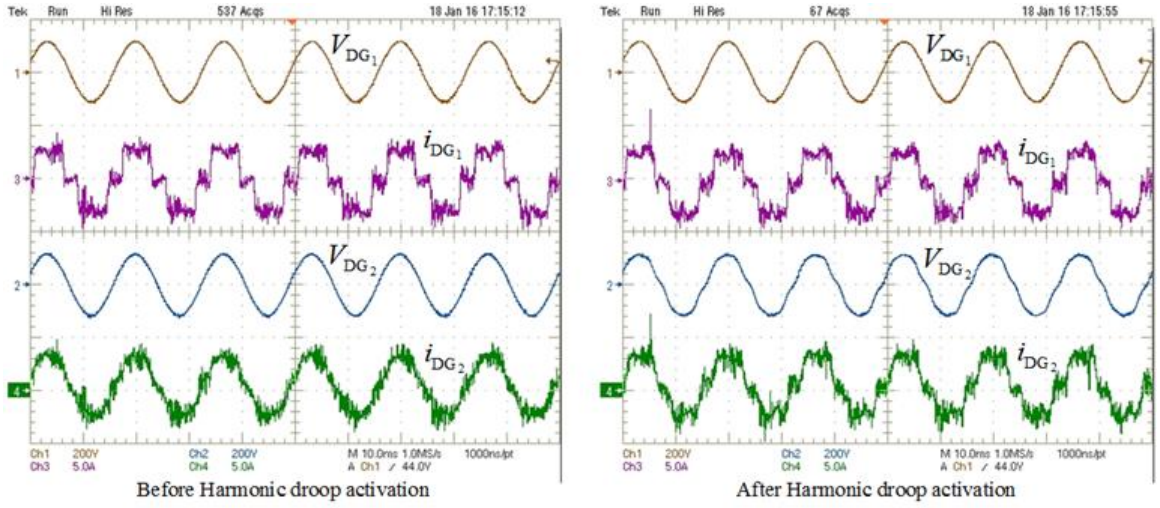

Figure 3.24: Experimental results: Phase voltage and current for each DG before and after Harmonic droop activation.

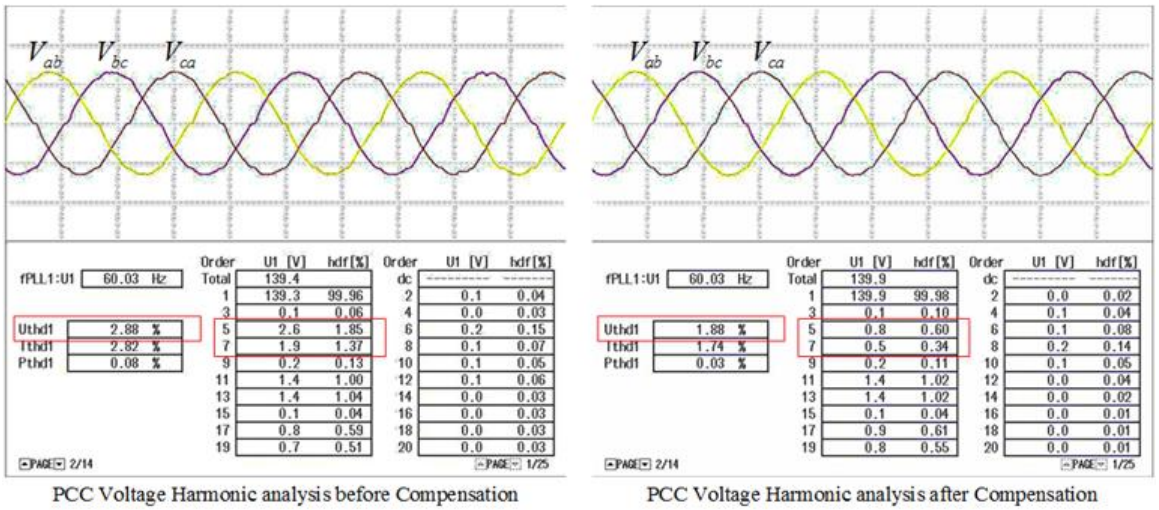

Figure 3.25: Experimental results: PCC phase-to-phase voltages with harmonic analysis before and after compensation.

3.7 Conclusion

This chapter has proposed a new harmonic droop control strategy for islanded AC microgrid with Distributed Generation Interfaced Converters (DICs). It has been shown that with proper settings of the proposed harmonic droop parameters and the choose of harmonic power rating for each DG unit, which depends on the distance separating the DG to the nonlinear load and its power capacity, each unit can supply harmonic power to the nonlinear loads as expected and can participate in filtering the voltage distortion at the PCC. The proposed method works in collaboration with conventional droop to share accurately the harmonic power Var consumed by the nonlinear loads. The harmonic sharing is not affected anymore by line impedance mismatches. Simulation results for different case studies show the effectiveness of the proposed harmonic droop. Finally, the proposed harmonic droop control is verified experimentally.

Chapter 4

OPTIMAL ANGLE DROOP FOR POWER SHARING ENHANCEMENT WITH STABILITY IMPROVEMENT IN ISLANDED MICROGRIDS

4.1 Introduction

The droop methods have many desirable features including flexibility, redundancy, expandability. However, the droop concept has limitations such as frequency and voltage variation, power quality problems, slow response and possibility of circulating current between inverters due to line impedance mismatches between inverters and the common bus. In literature, several improvements have been made for the conventional droop method to accurately share the power during weak islanding microgrid or during mismatch in line impedances [30, 26, 55, 57, 94, 113, 46, 54]. Recently, many researches extend the droop concept by adding low bandwidth communication link to enhance reactive power sharing, restore the frequency and voltage amplitude to their nominal values and to improve the power quality [94, 113, 46, 54, 114, 36, 115, 81, 116, 80]. In [114], the authors propose a new virtual flux droop. The objective is to obtain less frequency variation as compared to the conventional droop without the need of multi-feedback loops. Another way to share the real and reactive power in autonomous microgrid was introduced in [117, 28, 29], which is based on varying the angle and magnitude of the output voltage for distributed generators. The angle droop allows reducing the frequency deviation and improve the voltage quality. However, the main drawback is that power sharing with angle droop is poor as compared to frequency droop and it is highly affected by feeder impedance configuration. To alleviate the effect of the line impedance on power sharing, higher droop gains are required to overcome the higher existing line impedance. However, This causes instability behavior of the system. Additional loop was added to the droop to stabilize the overall system [29]. Furthermore, angle droop with its previous configuration have low dynamics and slow response.

This chapter proposes a new topology of an angle droop to share power among parallel

inverters in islanded microgrid. The aim is to insure a proper load sharing, robust against grid parameters and load changes that is stable for large range of operating conditions, with quietly no change in system frequency and less variation in voltage magnitude. The new topology adds an integral term to the controller for better transient response and it avoids the use of additional correcting loops. It is well known that the communication link has several benefits in improving conventional frequency droop control to share power accurately[94, 113, 46, 54, 114, 36, 115, 81, 116, 80]. While the angle droop, which already uses GPS signal in its configuration for time synchronization, can play an important role in gaining the same benefits. Currently, phasor measurement units (PMUs) are used for high-voltage power transmission and their deployment for low-voltage distribution systems, referred to as micro PMUs (µPMUs), is gaining momentum [118, 119, 120, 121, 122]. Thus the new feedback signals from µPMUs can play important role in improving the power sharing of the classical angle droop.

For further realization between system stability and its configuration, such as DGs capacity, droop gains and operating state, a small-signal analysis for a microgrid model is studied, the eigenvalues are identified to indicate the damping of the oscillatory terms under different operation conditions. Experimental results are introduced to validate the robustness of the proposed angle droop control.

4.2 Proposed Angle Droop Control for Power Sharing

Figure 4.1 shows two DGs connected to a common load across line impedances. The instantaneous real and reactive powers, p_i and q_i, respectively, can be derived as:

$$\begin{aligned} p_i &= \frac{3}{2}\frac{R_i}{Z_i}\left[\frac{V_i V_L}{Z_i}\cos\delta_{iL} - \frac{V_L^2}{Z_i}\right] + \frac{3}{2}\frac{X_i}{Z_i}\left[\frac{V_i V_L}{Z_i}\sin\delta_{iL}\right] \\ q_i &= -\frac{3}{2}\frac{R_i}{Z_i}\left[\frac{V_i V_L}{Z_i}\sin\delta_{iL}\right] + \frac{3}{2}\frac{X_i}{Z_i}\left[\frac{V_i V_L}{Z_i}\cos\delta_{iL} - \frac{V_L^2}{Z_i}\right] \end{aligned} \tag{4.1}$$

where $i = 1, 2$ represents the two branches in the simplified circuit, δ_{iL} represents the angle difference between the terminal voltages V_i and V_L.

If we make an assumption that the line impedance is pure inductive ($R_i = 0\Omega$), thus equation (4.1) can be written as follow:

$$\begin{aligned} p_i &= \frac{3}{2}\frac{V_i V_L}{X_i}\sin\delta_{iL} \\ q_i &= \frac{3}{2}\frac{V_L(V_i\cos\delta_{iL} - V_L)}{X_i} \end{aligned} \tag{4.2}$$

From (4.2) we can deduce that the active power is directly proportional to δ_i for a small variation, while the reactive power is directly proportional to V_i. In other words, the real power is controlled by controlling δ_i, and the reactive power is controlled by controlling V_i.

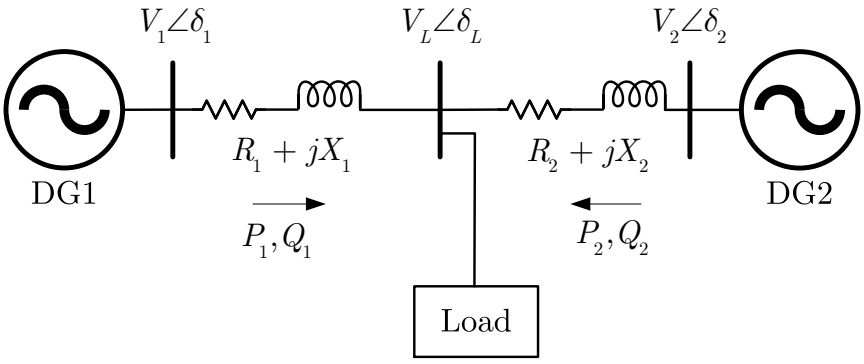

Figure 4.1: Simplified circuit of the system

4.2.1 Power Sharing in Classical Angle Droop

Unlike the conventional $P - f$ and $Q - V$ droop control that indirectly control the angle by varying the frequency of the grid, the $P - \delta$ and $Q - V$ droop control directly drop the voltage magnitude and the angle as

$$\begin{aligned} \delta_i &= \delta_{in} - m_i(P_i - P_{in}) \\ V_i &= V_{in} - n_i(Q_i - Q_{in}) \end{aligned} \tag{4.3}$$

where δ_{in} and V_{in} are the nominal voltage angle and magnitude, P_{in} and Q_{in} are the rated real and reactive power levels for a DG.

It is to be noted that the nominal voltage angle is defined according to IEEE Standard C37.118.1a-2014 [2]. The voltage angle (δ_i) represents the instantaneous phase angle relative to a cosine function at the nominal system frequency synchronized to UTC (Coordinated Universal Time). Respectively, δ_{in} (The nominal voltage angle) corresponds to a defined offset angle (set by the user) of the three-phase system with respect to the synchronization signal used by PMU and send from GPS.

The coefficients m_i and n_i are selected to set the voltage angle and magnitude drop. These coefficients are chosen for different DGs to share the load in proportion to their rating at a desired drop ratio, i.e., $m_i = \Delta\delta/P_{in}$ and $n_i = \Delta V/Q_{in}$.

For N-DGs in a microgrid, the power sharing between the DGs can be given as

$$\begin{aligned} m_1 \times P_{1n} &= m_2 \times P_{2n} = \cdots = m_N \times P_{Nn} \\ n_1 \times Q_{1n} &= n_2 \times Q_{2n} = \cdots = n_N \times Q_{Nn} \end{aligned} \tag{4.4}$$

It is to be noted that, the application of angle droop controller in DG interfaced Converter (DIC) was originally introduced in [29], which is a static control based on equation (4.3). Referring to Fig. 4.1, and applying all necessary assumptions we can get

$$\begin{aligned} \delta_1 - \delta_L &= \lambda_{L1} P_1 \\ \delta_2 - \delta_L &= \lambda_{L2} P_2 \end{aligned} \tag{4.5}$$

where, $\lambda_{L1} = \omega L_1/V_1V_L$ and $\lambda_{L2} = \omega L_2/V_2V_L$.

From (4.3) and (4.5), it was shown that the ratio of the output power is given as

$$\frac{P_1}{P_2} = \frac{\lambda_{L2} + m_2}{\lambda_{L1} + m_1} \tag{4.6}$$

Similarly, for the reactive power sharing, the output power ratio is given as

$$\frac{Q_1}{Q_2} = \frac{\lambda_{L2}V_2 + n_2}{\lambda_{L1}V_1 + n_1} \tag{4.7}$$

Thus, the error in proportional power sharing is due to line inductance mismatches. In real system with number of DGs and loads in different location, line impedance will have an impact on the load sharing [29]. High droop gains will play a dominant role in alleviating power sharing error as presented. However, high droop gains have a negative impact on the overall stability of the system. Moreover, the study in [29] is focused on improving only the active power sharing where the droop gains are set as

$$m_1 \gg \lambda_{L1} \text{ and } m_2 \gg \lambda_{L2}$$

4.2.2 Proposed Angle Droop Method

In order to obtain a proper load sharing and to ensure stability of the system at the same time, an improvement in the angle droop control is needed. In addition to the droop gain impact, the load change has an important effect on the dynamics and stability of the system. Figure 2 represents a microgrid with multiple DGs and loads connected to a common point. The overall block diagram of the proposed angle droop for power sharing is also shown in the figure. By which, a GPS signal is used for time synchronization of droop control local processor. Similar to the classical angle droop, the angle of the reference voltage of an inverter can control the real power produced.

However, the proposed angle droop keeps the angle drop in a defined range, where a feedback of the difference between the measured PCC voltage angle and the nominal value is added to the angle droop which specifies the closed-loop dynamics of the controller. To share the reactive power, the output voltage magnitude of the inverter V_i is drooped as function of the reactive power output Q_i where the voltage at the PCC is fed back and compared to the rated value to insure a less voltage drop, less affected by the load and guarantee the accuracy in reactive power sharing.

In the steady state, the input of the integrators should be zero, hence:

$$\begin{aligned} K_a(\delta_{in} - \delta_L) &= m_i(P_i - P_{in}) \\ K_e(V_{in} - V_L) &= n_i(Q_i - Q_{in}) \end{aligned} \tag{4.8}$$

The proposed angle droop aims to indirectly control the voltage at the PCC to be equal to the rated values (i.e. V_{in} and δ_{in}). The added integrators can minimize the static error between the feedback signal and the corresponding rated values. Thus, $K_a(\delta_{in} - \delta_L)$ and $K_e(V_{in} - V_L)$ are the same for all inverters, if we choose K_a and K_e the same, which

results in accurate real and reactive power sharing that is no longer depends on the system impedance and immune to numerical errors and disturbances.

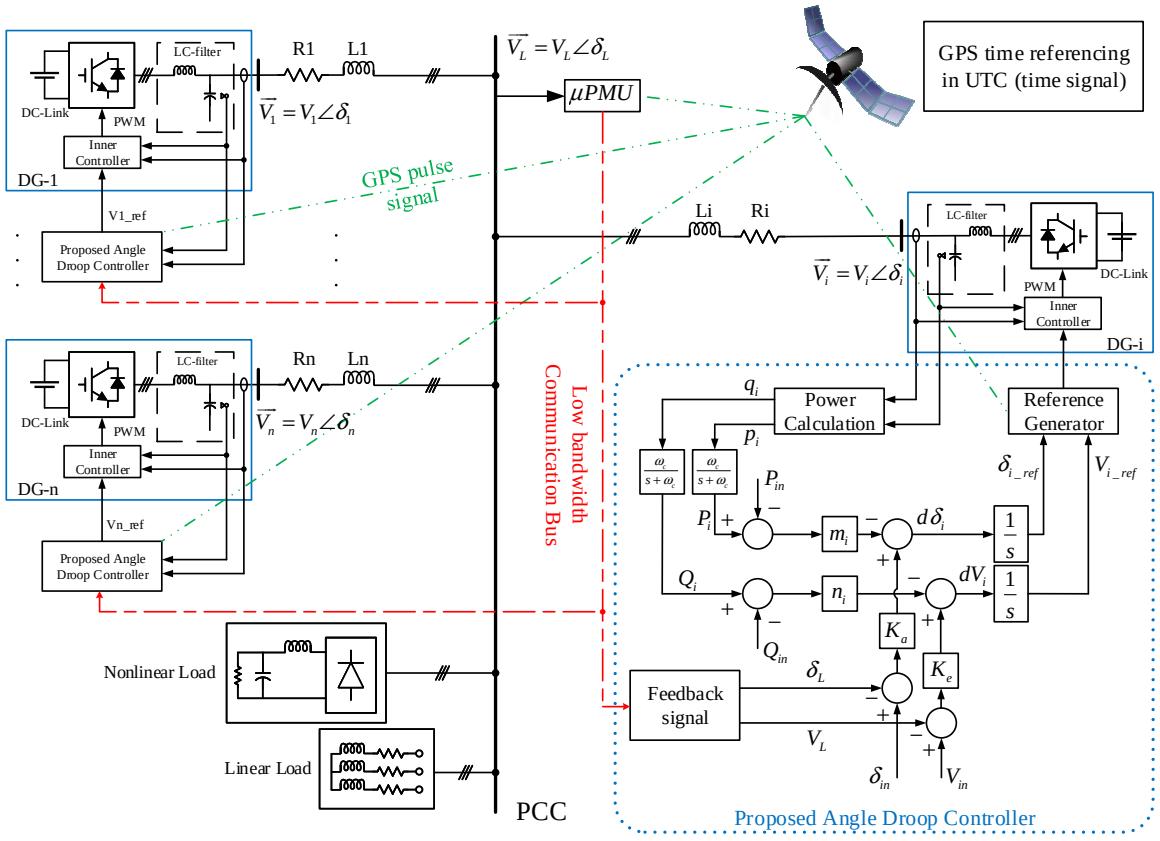

Figure 4.2: Microgrid with Proposed Angle droop control overall block diagram

The only possible error in power sharing here is due to different PCCs with different load locations. This results in multiple voltage magnitude and angle feedback signals in different locations. In real cases, the separation between different position of loads are done by the connection of tie lines which usually have lower impedance values. From (4.8), the deviation of reactive power due to error in voltage magnitude ΔV_{Li} is:

$$\Delta Q_i = -\frac{K_e}{n_i}\Delta V_{Li} \tag{4.9}$$

For two DICs sharing power common loads with equal power ratings, the relative reactive power sharing error due to different PCC voltages $\Delta V_L = \Delta V_{L2} - \Delta V_{L1}$ is

$$\varepsilon_Q = \frac{\Delta Q_1}{Q_{1n}} - \frac{\Delta Q_2}{Q_{2n}} = \frac{K_e \Delta V_L}{n_i Q_{in}} \tag{4.10}$$

The same interpretation is given to the real power sharing error, caused by the error in voltage angle signals, $\Delta\delta_L = \Delta\delta_{L2} - \Delta\delta_{L1}$, which can be written in the form:

$$\varepsilon_P = \frac{\Delta P_1}{P_{1n}} - \frac{\Delta P_2}{P_{2n}} = \frac{K_a \Delta\delta_L}{m_i P_{in}} \tag{4.11}$$

It can be seen that the error in real and reactive power sharing are inversely proportional to m_i/K_a and n_i/K_e respectively. Decreasing the gains K_a and K_e can play a dominant role in reducing errors in power sharing. If all the DGs are connected to same PCC, then the errors ΔV_L and $\Delta\delta_L$ are zero and accurate proportional power sharing can be achieved.

The proposed angle droop control often reduces the voltage magnitude and angle drop at the PCC. From (4.8) the PCC voltage is

$$V_L = V_{in} - \frac{n_i}{K_e}(Q_i - Q_{in}) = V_{in}\left(1 - \frac{n_i(Q_i - Q_{in})}{K_e V_{in}}\right) \tag{4.12}$$

Similarly, the PCC voltage angle can be expressed as:

$$\delta_L = \delta_{in} - \frac{m_i}{K_a}(P_i - P_{in}) = \delta_{in}\left(1 - \frac{m_i(P_i - P_{in})}{K_a \delta_{in}}\right) \tag{4.13}$$

Thus, the desired voltage drop ratio $n_i(Q_i–Q_{in})/(K_eV_{in})$ and angle drop ratio $m_i(P_i–P_{in})/(K_a\delta_{in})$ are no longer determined by the output impedance separating the inverter to the common load but by the parameters n_i, m_i, K_e, K_a and the actual power P_i, Q_i. It can be noted that the role of large gains K_e and K_a is to speed up the response and reduce the voltage and angle drop. However, a tradeoff should be done between the voltage magnitude and angle drop and the accuracy of power sharing because the voltage magnitude and angle drop are proportional to n_i/K_e and m_i/K_a, respectively, but the real and reactive power sharing errors are inverse proportional to m_i/K_a and n_i/K_e correspondingly. The experimental results presented in section V shows the effectiveness of the proposed control and validate the theoretical analysis.

4.3 State-Space model for a typical Microgrid

Modeling and stability analysis for islanded microgrid has been carried out in [4, 123, 124, 125, 126] using the conventional droop. For the proposed angle droop controller, which has several parameters to set, and in order to tune those parameters that are suitable for correct power sharing without affecting the system stability, a new state space model is to be realized for studying the operation under the variation of control parameters. In a microgrid that contains DICs only, a model of the converter inner controller, the droop controller, the line impedances that connect the converter to the network and the load are given. The state-space equations of DIC controller, droop, network and load are derived separately in a modular fashion using the synchronized reference frame. These are then combined together to get an overall microgrid model.

4.3.1 Angle Droop Control Model

Referring to Fig. 4.2, the reference dq voltages for a DICi can be written as:

$$V_{Cdi\_\mathrm{ref}} = \sqrt{3}V_i \cos\delta_i \text{ and } V_{Cqi\_\mathrm{ref}} = \sqrt{3}V_i \sin\delta_i \tag{4.14}$$

The Power Calculation block is useful for deriving the instantaneous powers as:

$$\begin{aligned} p_i &= V_{Cdi} i_{di} + V_{Cqi} i_{qi} \\ q_i &= V_{Cqi} i_{di} - V_{Cdi} i_{qi} \end{aligned} \tag{4.15}$$

Then passed through low-pass filters (cutoff frequency ω_c) to obtain the average real and reactive power P_i and Q_i. δ_L and V_L are the angle and the rms value of the voltage at the PCC side, they are given by a µPMU and send to the droop using a low bandwidth communication link. The droop controller state equation can be expressed as:

$$\frac{d}{dt}\begin{bmatrix} \delta_i \\ V_i \\ P_i \\ Q_i \end{bmatrix} = \begin{bmatrix} 0 & 0 & -m_i & 0 \\ 0 & 0 & -n_i & 0 \\ 0 & 0 & -\omega_i & 0 \\ 0 & 0 & 0 & -\omega_i \end{bmatrix} \times \begin{bmatrix} \delta_i \\ V_i \\ P_i \\ Q_i \end{bmatrix} + \begin{bmatrix} K_a(\delta_{in} - \delta_L) + m_i P_{in} \\ K_e(V_{in} - V_L) + n_i Q_{in} \\ p_i \\ q_i \end{bmatrix} \tag{4.16}$$

where, p_i and q_i represents the electrical state variables given in (4.15).

4.3.2 Flatness Controller Model

With Flatness based control unit, we can acheive a high bandwidth which plays a role in fast dynamic system and robust against grid distirbances. Fig. 4.3 shows the functional diagram of the one-loop based control method. It can be noted that the measure of the inductive filter currents is not useful to implement the control law. Only the capacitor voltage sensors are used for generating equations, while the load current sensors, that are used for power measuring in droop controller, could be useful for increasing dynamics of Flatness Controller as regard to load perturbation. More details about the controller are introduced in [1, 11]. Taking the assumption that the Flatness controller have much faster dynamics than the droop controller, so the *dq* voltages across capacitors (V_{Cdq_mes}) can be supposed to follow perfectly their respective *dq* references ($V^*_{Cdq\_f}$). We take into account the dynamic bound to the trajectory planning system. Thus, the DICi and its controller can be modeled as a second order filter.

$$\frac{V_{Cdqi}}{V^*_{Cdqi}} = \frac{\omega_{ei}^2}{s^2 + 2\xi_i \omega_{ei} s + \omega_{ei}^2} \tag{4.17}$$

The resulting dynamics for DICi controller can be expressed as:

$$\frac{d}{dt}\begin{bmatrix} V_{Cdi} \\ V_{Cqi} \\ \dot{V}_{Cdi} \\ \dot{V}_{Cqi} \end{bmatrix} = \begin{bmatrix} 0 & 0 & 1 & 0 \\ 0 & 0 & 0 & 1 \\ -\omega_{ei}^2 & 0 & -2\xi_i\omega_{ei} & 0 \\ 0 & -\omega_{ei}^2 & 0 & -2\xi_i\omega_{ei} \end{bmatrix} \times \begin{bmatrix} V_{Cdi} \\ V_{Cqi} \\ \dot{V}_{Cdi} \\ \dot{V}_{Cqi} \end{bmatrix} + \begin{bmatrix} 0 & 0 \\ 0 & 0 \\ \omega_{ei}^2 & 0 \\ 0 & \omega_{ei}^2 \end{bmatrix} \times \begin{bmatrix} V^*_{Cdi} \\ V^*_{Cqi} \end{bmatrix} \tag{4.18}$$

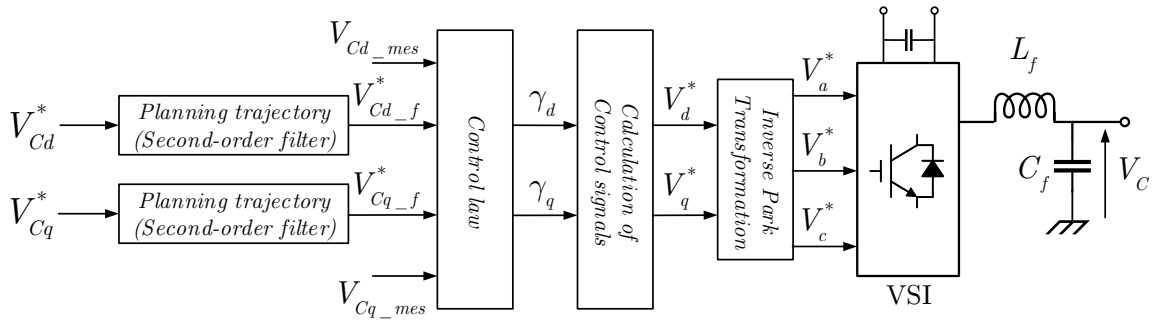

Figure 4.3: Flatness-based Control Functional Diagram.

4.3.3 Grid and Load Model

The Grid can be modeled based on the line impedances linking the DICi to the load ($\forall i \in \{1, \ldots, N\}$):

$$L_i \frac{d}{dt} i_{abci} + r_i i_{abci} = V_{Cabci} - V_{Labc} \tag{4.19}$$

In $\alpha\beta$ frame, equation (4.19) can be written as

$$L_i \frac{d}{dt} i_{\alpha\beta i} + r_i i_{\alpha\beta i} = V_{C\alpha\beta i} - V_{L\alpha\beta} \tag{4.20}$$

The state equation of a generalized R-L load can be expressed as

$$V_{L\alpha\beta} = L_L \frac{d}{dt} i_{L\alpha\beta} + R_L i_{L\alpha\beta} \tag{4.21}$$

where $i_{L\alpha\beta} = \sum_{i=1}^{N} i_{\alpha\beta i}$, is teh expression of the load current.

Equations (4.20) and (4.21) can be combined to get a model for the grid and the load together in $\alpha\beta$ frame represented as

$$[L] \frac{d}{dt} i_{\alpha\beta} = V_{C\alpha\beta} - [R]\, i_{\alpha\beta} \tag{4.22}$$

where, $i_{\alpha\beta} = [i_{\alpha 1}\, i_{\beta 1}\, \cdots\, i_{\alpha N}\, i_{\beta N}]^t$, $V_{C\alpha\beta} = [V_{C\alpha 1}\, V_{C\beta 1}\, \cdots\, V_{C\alpha N}\, V_{C\beta N}]^t$.

The line current equations can be obtained in the synchronous frames after Park's transformation. The resulting model can be defined as:

$$\frac{d}{dt} i_{dq} = [L_{net}]^{-1} . V_{Cdq} - [L_{net}]^{-1} . [R_{net}]\, i_{dq} \tag{4.23}$$

where, $i_{dq} = P_N . i_{\alpha\beta}$, $V_{Cdq} = P_N . V_{C\alpha\beta}$.

The matrices $[L_{net}]$ and $[R_{net}]$ are $(2N \times 2N)$ written as:

$$[L_{net}]^{-1} = P_N [L]^{-1} P_N^{-1} \text{ and } [R_{net}] = P_N [R] P_N^{-1} + P_N [L] \frac{dP_N^{-1}}{dt}$$

where $P_N = diag(P(\theta),\ldots,P(\theta))$, $P_N^{-1} = diag(P(-\theta),\ldots,P(-\theta))$ with $P(\theta) = \begin{bmatrix} \cos\theta & \sin\theta \\ -\sin\theta & \cos\theta \end{bmatrix}$, $P(-\theta) = \begin{bmatrix} \cos\theta & -\sin\theta \\ \sin\theta & \cos\theta \end{bmatrix}$.

For more clarification, the state equations of the line currents for $N = 2$ are shown as:

$$\frac{d}{dt}\begin{bmatrix} i_{d1} \\ i_{q1} \\ i_{d2} \\ i_{q2} \end{bmatrix} = \begin{bmatrix} \frac{L_2+L_L}{(L_1+L_2)L_L+L_1L_2} & 0 & \frac{-L_L}{(L_1+L_2)L_L+L_1L_2} & 0 \\ 0 & \frac{L_2+L_L}{(L_1+L_2)L_L+L_1L_2} & 0 & \frac{-L_L}{(L_1+L_2)L_L+L_1L_2} \\ \frac{-L_L}{(L_1+L_2)L_L+L_1L_2} & 0 & \frac{L_1+L_L}{(L_1+L_2)L_L+L_1L_2} & 0 \\ 0 & \frac{-L_L}{(L_1+L_2)L_L+L_1L_2} & 0 & \frac{L_1+L_L}{(L_1+L_2)L_L+L_1L_2} \end{bmatrix} \times \begin{bmatrix} V_{Cd1} \\ V_{Cq1} \\ V_{Cd2} \\ V_{Cq2} \end{bmatrix}$$
$$- \begin{bmatrix} \frac{L_2R_L+(L_2+L_L)r_1}{(L_1+L_2)L_L+L_1L_2} & -\omega & \frac{-r_2L_L+L_2R_L}{(L_1+L_2)L_L+L_1L_2} & 0 \\ \omega & \frac{L_2R_L+(L_2+L_L)r_1}{(L_1+L_2)L_L+L_1L_2} & 0 & \frac{-r_2L_L+L_2R_L}{(L_1+L_2)L_L+L_1L_2} \\ \frac{-r_1L_L+L_1R_L}{(L_1+L_2)L_L+L_1L_2} & 0 & \frac{L_1R_L+(L_1+L_L)r_2}{(L_1+L_2)L_L+L_1L_2} & -\omega \\ 0 & \frac{-r_1L_L+L_1R_L}{(L_1+L_2)L_L+L_1L_2} & \omega & \frac{L_1R_L+(L_1+L_L)r_2}{(L_1+L_2)L_L+L_1L_2} \end{bmatrix} \times \begin{bmatrix} i_{d1} \\ i_{q1} \\ i_{d2} \\ i_{q2} \end{bmatrix}$$

Equations (4.14)-(4.23) can be combined to formulate the dynamics of the whole system.

$$dz/dt = f(z) \tag{4.24}$$

where, $z = [x_{Droop\_1}\, x_{Flat\_1}\, x_{Grid\_1}\, \cdots\, x_{Droop\_i}\, x_{Flat\_i}\, x_{Grid\_i}]^t$
$x_{Droop\_i} = [\delta_i\, V_i\, P_i\, Q_i]^t$, $x_{Flat\_i} = \left[V_{Cdi}\, V_{Cqi}\, \dot{V}_{Cdi}\, \dot{V}_{Cqi}\right]^t$, $x_{Grid\_i} = [i_{di}\, i_{qi}]^t$.

4.4 Dynamic Stability Analysis of Microgrid

As mentioned previously, the angle droop introduced in [29] can share the power when using high droop gains which affect the system stability. A supplementary loop was added to insure a stable system. In order to study the stability of the proposed angle droop and to understand the dynamic behavior which is affected by several control variables, an eigenvalue analysis by plotting the root locus is needed. This will determine the stability of the system under the variations of different control parameters. The system parameters are given in table 4.1.

Fig. 4.4 shows the root locus diagrams after the variation of the most important parameters in droop control (i.e. coefficients m_i, n_i given in equation (4.8)). The sense of variation of those parameters is from lower to maximum value. It can be seen that the dominant eigenvalues that determine the system dynamics are λ_3, λ_4, λ_5, λ_6, λ_7, λ_8. They are sensitive to the changes in droop parameters.λ_5, λ_6, λ_7, and λ_8 are highly affected by the change in the droop coefficients m_i and n_i, as shown in Fig. 4.4(a) and (b), as the coefficients increase (dynamics will increase) the droop line becomes steeper and results to an underdamped dynamic response of the $P-\delta$ and $Q-V$. The behavior of eigenvalues λ_3 and λ_4 are identical and tends to be unstable during the variation. The dynamics of the low-pass filters used in droop control are determined by the eigenvalues λ_{17}, λ_{18}, λ_{19}, and λ_{20} ($\omega_c = 628.32$ rad/sec). The other clusters of eigenvalues are also changing their paths but they are less effective in the stability of the system.

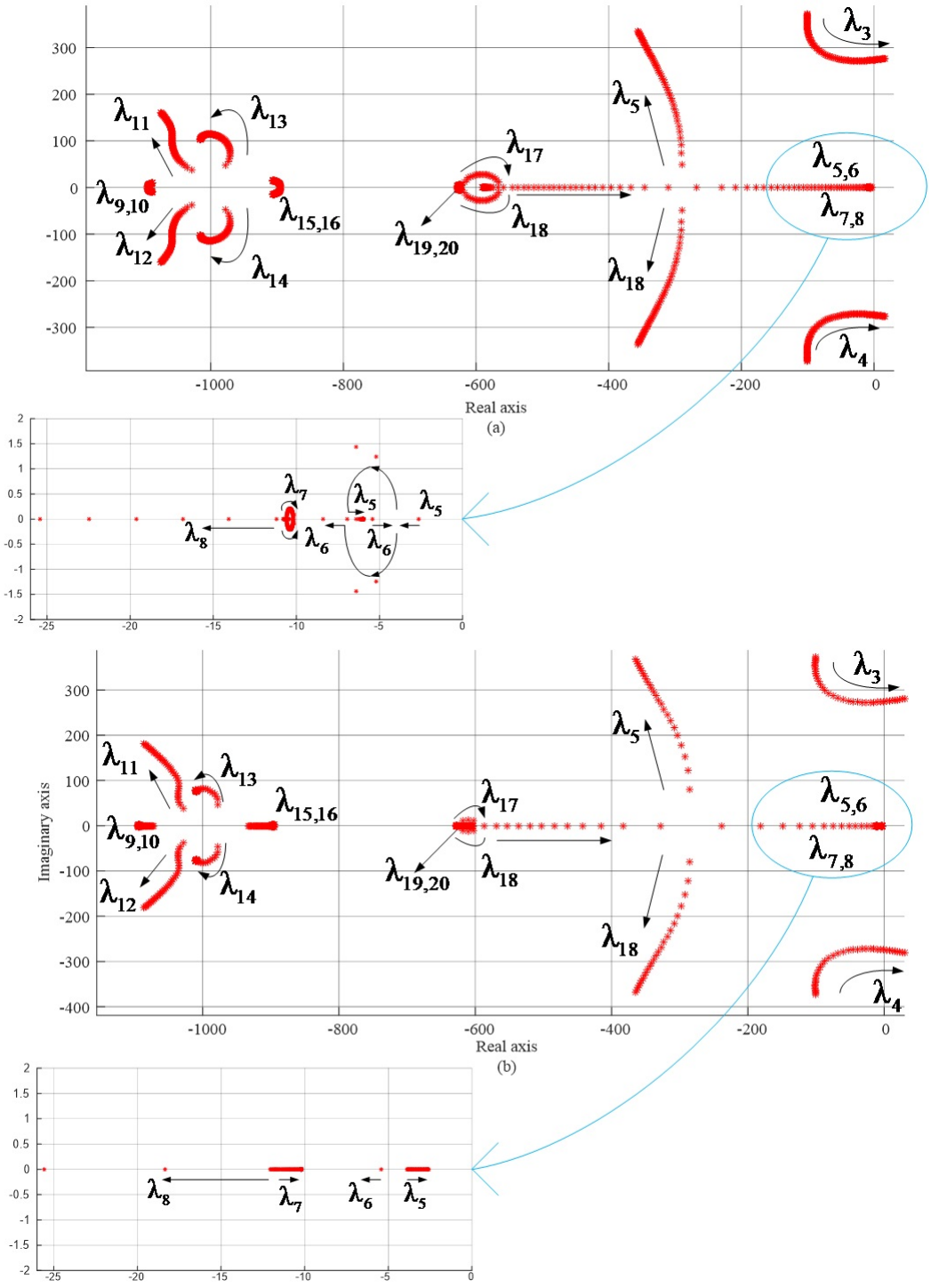

Figure 4.4: Root locus with the variation of parameters in the Droop control: (K_e = 10sec^{-1}, K_a = 10sec^{-1}). (a) Variation of m_i:$5 \times 10^{-5} \leq m_1 \leq 5 \times 10^{-3}$ (rad/W.sec), $1 \times 10^{-4} \leq m_2 \leq 1 \times 10^{-2}$ (rad/W.sec); (b) Variation of n_i: $1.33 \times 10^{-2} \leq n_1 \leq 0.53$ (V/Var.sec), $2.67 \times 10^{-2} \leq n_2 \leq 1.06$ (V/Var.sec).

System Parameters	
System frequency f	60Hz
$Z_1 = R_1 + \mathrm{j}X_1(\Omega)$	0.1+j0.377
$Z_2 = R_2 + \mathrm{j}X_2(\Omega)$	0.5+j1.885
$Z_L = R_L + \mathrm{j}X_L(\Omega)$	25+j3.5
DG Ratings	
DG_1 : P(W)/Q(Var)	2000/750
DG_2 : P(W)/Q(Var)	1000/375
rms-voltage $V_{1n}/V_{2n}(V)$	110/110
Angle δ_{1n}/δ_{2n}(rad)	0/0
Flatness Control trajectory dynamics	
ξ/ω_e(rad/sec)	1/1000
Angle Droop Control Parameters	
Voltage angle drop $\Delta\delta$ (rad/sec)	$0.1 \leq \Delta\delta \leq 10$
Voltage drop ΔV (V/sec)	$10 \leq \Delta V \leq 400$
Low pass filter cutoff frequency ω_c (rad/sec)	628.3
Integrator gains K_a/K_e (1/sec)	10/10

Table 4.1: System Parameters for Dynamic Analysis

Please note that λ_1 and λ_2 are so far on the left-side of the s-plane and unaffected by the parameters change, they are not shown in Fig. 4.4.

The stability margin of the proposed controller is studied by observing the maximum eigenvalues real part with respect to the variation of the droop parameters. Furthermore, the relationship between the bandwidth of the droop controller and the values of the integral gains (i.e. K_a and K_e) was deduced based on the plotting of Fig. 4.5. Fig. 4.5(a) shows the area where the system is stable during the change of the angle and voltage drop settings. As the droop coefficients are small, the response of the angle droop is slow, thus the corresponding real eigenvalues will be near zero. The increase in the droop parameters will increase the dynamics of the angle droop till reaching a limiting value determined by the integrator gains as indicated in Fig. 4.5(a) which is around 10 rad/sec. In Fig. 4.5(b), the integrator gain value is changed to $20\mathrm{sec}^{-1}$, the same procedure is done here where the minimum real part of the eigenvalues is around -20 which corresponds to a bandwidth of 20 rad/sec for droop controller. It is to be noted that, for a wide range of droop parameters ($\Delta\delta$ and ΔV), the dynamic of the proposed angle droop is highly determined by the values of the integrator gains (i.e. K_e and K_a). In this case, the droop settings permit to optimize the performance of the proposed angle droop during disturbances and numerical errors, to accurately share the power in case of weak microgrid and to overcome the high line impedance mismatches. This study also interprets the stability of the system for a wide range of operating conditions. In the simulation and experimental tests, presented in the next sections, the optimal droop parameters are chosen in the middle of the plan (i.e. $\Delta\delta = 3$rad/sec, $\Delta V = 50$V/sec). In this case the maximum angle and voltage drop are $\Delta\delta/K_a = 0.3$rad and $\Delta V/K_e = 5$V respectively. The communication

link is not presented in this study since its bandwidth is widely large as regard to the bandwidth of the droop controller. PMUs support IEEE C37.118.1a protocols for data communication [2]. Some of the most used methods include: serial-, UDP/IP-, TCP/IP-based communication scheme. The PMU shall support data reporting at sub-multiples of the nominal power line (system) frequency as given in table 4.2. Since, in our case study, the bandwidth of the droop controller is around 10 rad/sec ($\approx$ 1.6Hz) and based on IEEE C37.118.1a protocols for data communication, the minimum data reporting rate is 10 frames/sec which is applicable with this study.

System frequency	**50 Hz**			**60 Hz**					
Reporting rates (F_s-Frames per second)	10	25	50	10	12	15	20	30	60

Table 4.2: Required PMU reporting rates [2].

4.5 Simulation Results

The new angle droop controller is tested by MATLAB-Simulink for different configuration and number of DGs in a microgrid as presented in Fig. 4.2. Firstly, the proposed angle droop is applied for two DGs connected to a common load characterized by a linear R-L load and a nonlinear full bridge rectifier load. In the second case, the proposed angle droop is tested in a system with three DGs to show its effectiveness in different condition. Furthermore, the communication failure is elaborated in this case to see its effect in power sharing and the continuity of work with the proposed angle droop.

4.5.1 Microgrid Configuration with Two DGs

In this system, two DGs are supplying a linear R-L load and a non-linear full rectifier bridge. Different stages are considered to share the fundamental power between both DGs. The system parameters used for simulation test and droop coefficients are given in Table 4.3. The two sources will share the real and reactive power in proportion to their ratings. Fig. 4.6 shows the fundamental power sharing for this case. At t=4sec, DG_2 is connected to the microgrid to share power with DG_1. Before this period DG_2 is synchronized with the grid by applying a reference voltage angle and rms value equal to that at the PCC side. The wave forms of the shared power show the high performance of the proposed droop controller as given in Fig 4.6(a), (b). The higher value of DG_2 line impedance results in high reference output voltage V_2 than V_1 as in Fig. 4.7(a). The same result appears in voltage reference angle δ_2 which is higher than δ_1 as indicated in Fig. 4.7(b). The phase voltage and current waveforms for the two sources are shown in Fig. 4.8. The current of DG_1 contains more harmonics than DG_2, which is normal for this case, since the line impedance separating DG_1 from the nonlinear load is smaller than that separating DG_2.

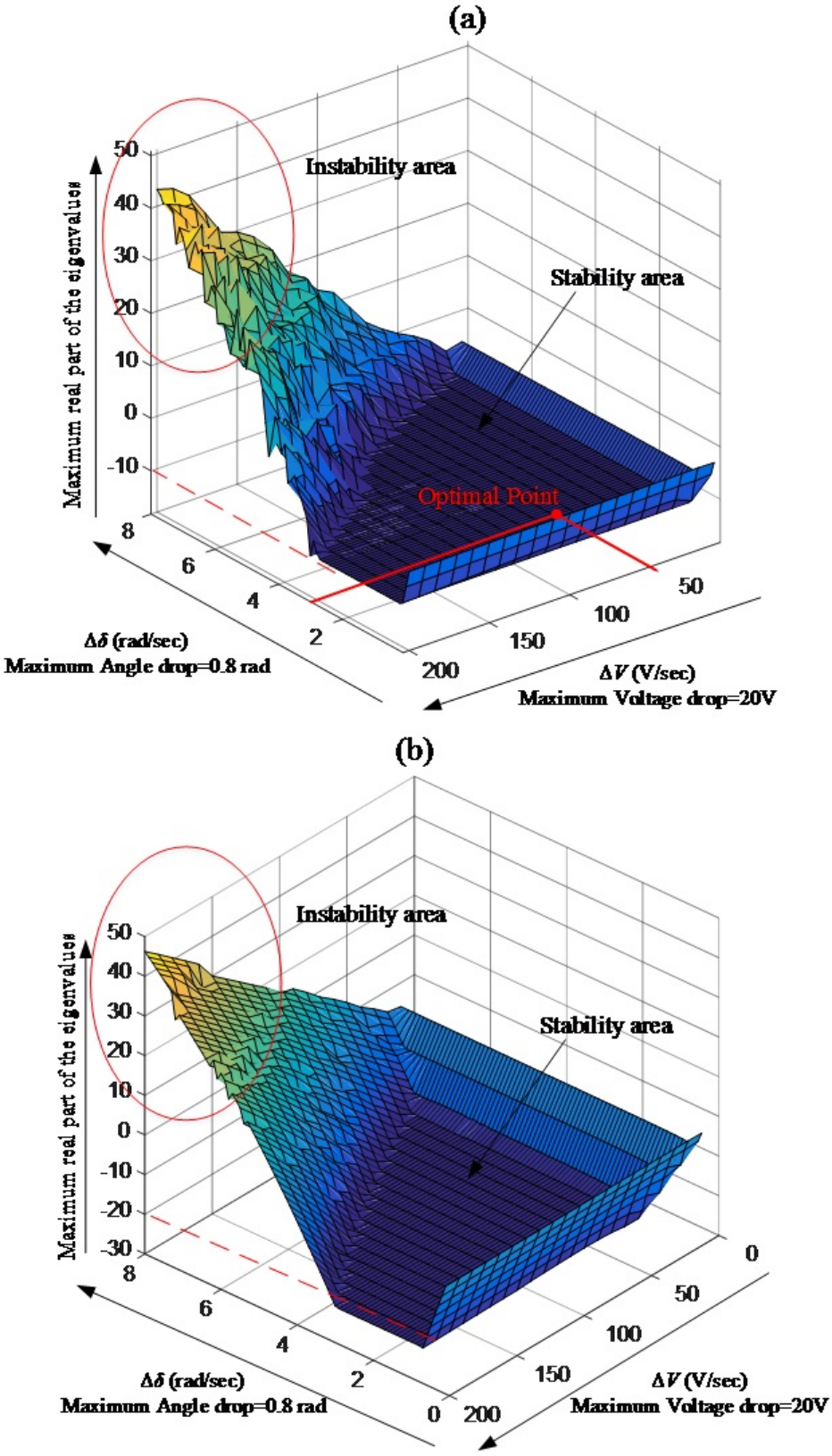

Figure 4.5: Stability margin study by observing the maximum real part of the eigenvalues with respect to the variation of the angle and voltage drop set parameters for: (a) $K_e = 10\text{sec}^{-1}$, $K_a = 10\text{sec}^{-1}$; (b) $K_e = 20\text{sec}^{-1}$, $K_a = 20\text{sec}^{-1}$.

System Parameters					
Fundamental Line voltage (V)/frequency (Hz)	110V/60Hz				
Feeder impedance $Z_{DG1}(R_1, L_1)$	(0.1Ω, 1mH)				
Feeder impedance $Z_{DG2}(R_2, L_2)$	(0.5Ω, 5mH)				
Feeder impedance $Z_{DG3}(R_3, L_3)$	(0.2Ω, 2mH)				
Nominal voltage angle δ_{in} (rad)	0 rad				
Nominal rms-voltage V_{in} (V)	110 V				
Angle Droop Characteristics					
Control Parameters	μGrid with 2 DGs		μGrid with 3 DGs		
	$\mathbf{DG}_1$	$\mathbf{DG}_2$	$\mathbf{DG}_1$	$\mathbf{DG}_2$	$\mathbf{DG}_3$
P_{in} (W)	2000	2000	4000	4000	2000
Q_{in} (Var)	750	750	1500	1500	750
$\Delta\delta$ (rad/sec)/ΔV (V/sec)	3 / 50	3 / 50	3 / 50		
K_a/K_e (1/sec)	10 / 10	10 / 10	10 / 10		
m_i (rad/W.sec)	0.0015	0.0015	0.0007	0.0007	0.0015
n_i (V/Var.sec)	0.066	0.066	0.066	0.066	0.13
Hierarchical Droop Parameters [55]					
$\Delta\omega$ (rad/sec)/ΔV (V)			1 / 5		
m_i (rad/W.sec)			0.0002	0.0002	0.0005
n_i (V/Var)			0.0033	0.0033	0.067
Secondary Loop					
Proportional frequency gain $K_{p\omega}$			1		
Integral frequency gain $K_{i\omega}$			10		
Proportional voltage gain K_{pE}			1		
Integral voltage gain K_{iE}			100		

Table 4.3: Droop Parameters for Simulation.

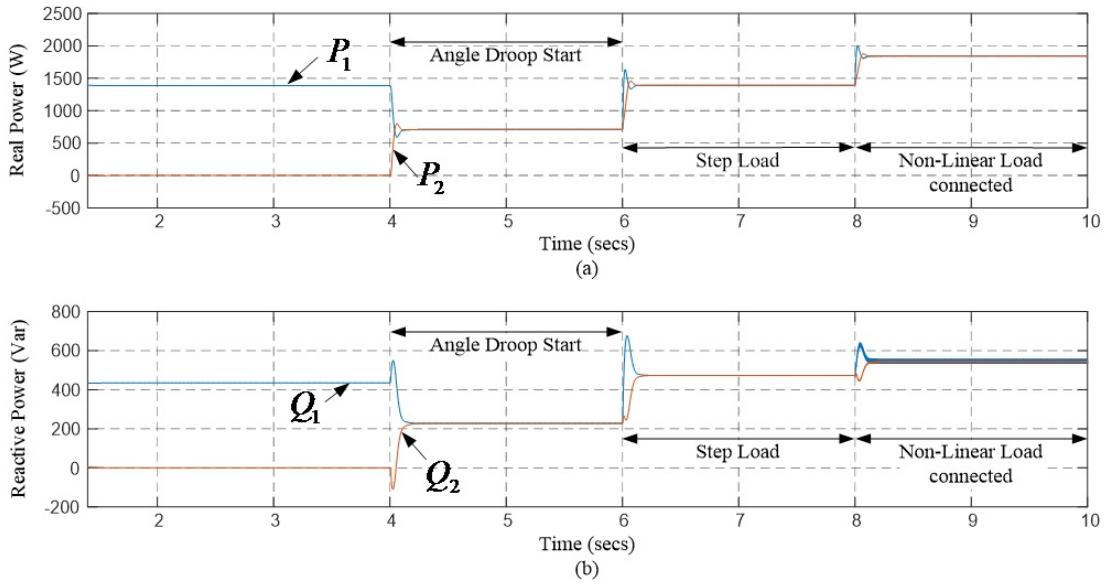

Figure 4.6: Simulation results for Microgrid with two DGs. (a) Real power: P_1, P_2; (b) Reactive power: Q_1, Q_2.

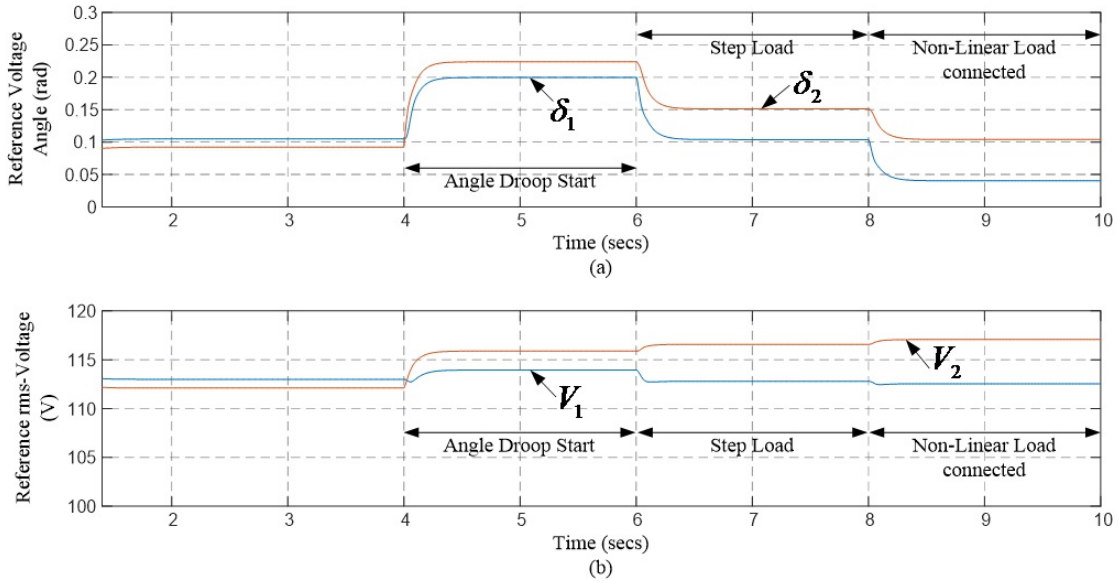

Figure 4.7: Simulation results Microgrid with two DGs. (a) Reference rms-Voltage: V_1, V_2; (b) Reference Voltage Angle: δ_1, δ_2.

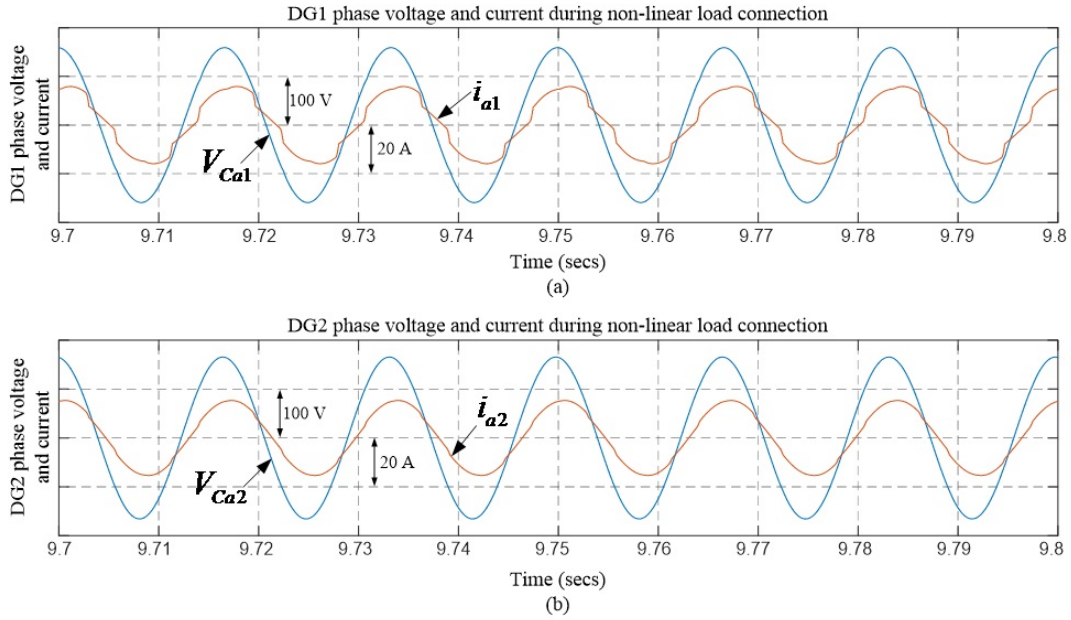

Figure 4.8: Simulation results for Microgrid with two DGs. (a) Phase voltage and current for DG_1; (b) Phase voltage and current for DG_2.

4.5.2 Microgrid Configuration with Three DGs

To illustrate the performance of the proposed angle droop controller with different configurations, a simulation test is constructed with a microgrid of three DGs connected to a common linear and nonlinear load. Furthermore, a comparison with Hierarchical Droop control proposed in [55] is presented. This will help identifying the main difference between the two controllers as regard to power flow transients and PCC output voltage characteristics. Off Corse, the Hierarchical droop controller proposed in [55], is mainly a classical frequency droop with virtual impedance loop for reactive power correction. And a secondary control loop is constructed to restore the PCC voltage and frequency to their nominal values. Thus, a communication signal is needed to send the errors in frequency and amplitude to all units. The procedure is similar to the previous simulation in case A. at t=4sec, DG_2 and DG_3 are turned on to share power with DG_1 as they are supported by droop method. The power sharing between the DGs is related to their parameter settings given in Table 4.3. Fig. 4.9 shows the power generated by the three DGs using the proposed angle droop. The power is distributed proportionally in different load stages. The PCC voltage and angle in this case are presented in Fig. 4.10. In the proposed angle droop, the frequency is fixed to nominal value, so there is no change in system frequency.

For the Hierarchical droop test, it can be seen from Fig. 4.11 that the power flow transient is affected by the droop dynamics and the virtual impedance loop. In this case, a virtual impedance design is needed to allow the units to share accurately the reactive power. The secondary restoration loop is designed based on [55]. Fig. 4.12 shows the PCC voltage characteristics during different power stages. The secondary control ensures

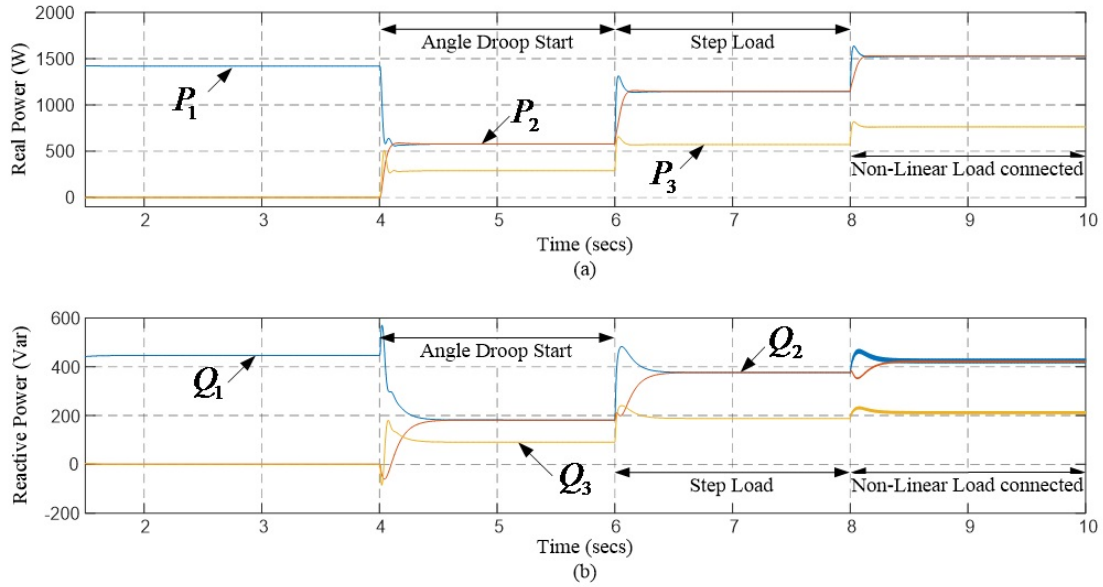

Figure 4.9: Simulation results for Microgrid with three DGs. (a) Real power: P_1, P_2 and P_3; (b) Reactive power: Q_1, Q_2 and Q_3.

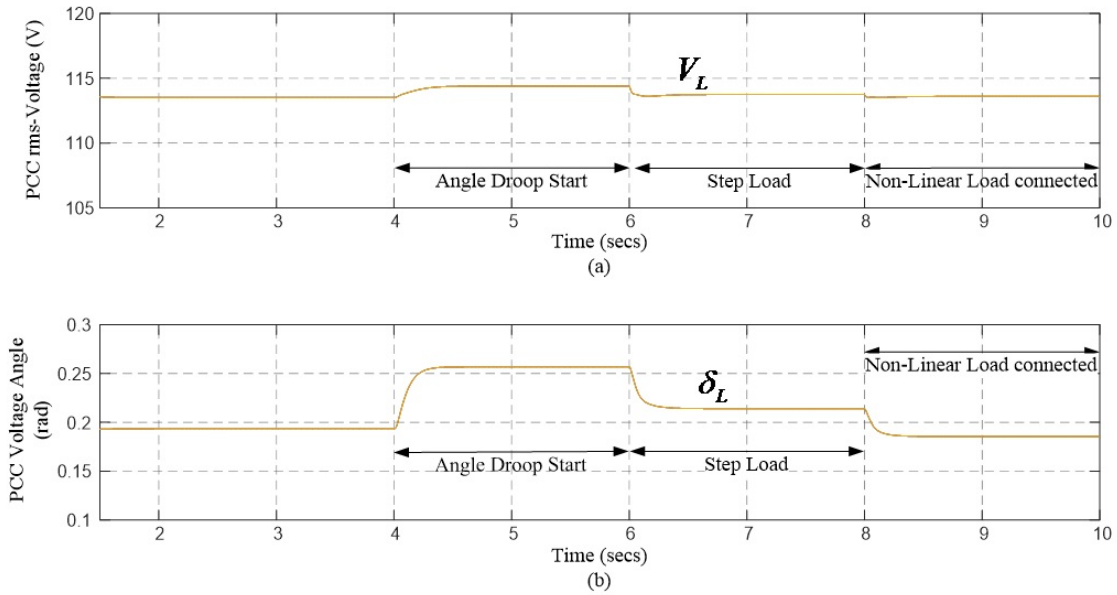

Figure 4.10: Simulation results for Microgrid with Three DGs. (a) PCC rms-Voltage; (b) PCC Voltage angle.

that the frequency and voltage deviations are regulated toward zero after every change of load and generation in microgrid. As a brief conclusion, this simulation part shows the difference between the proposed angle droop with the already used control in autonomous microgrid. Hierarchical droop control has multiple loops with complex design parameters (secondary control, virtual impedance, frequency droop control). Those designed loops are required to achieve the correct power sharing and voltage quality. In this case poor dynamic performance is an issue. Whereas in the proposed angle droop, the accurate power sharing and better voltage quality with fixed frequency are achieved in one loop control. Thus fast dynamic performance.

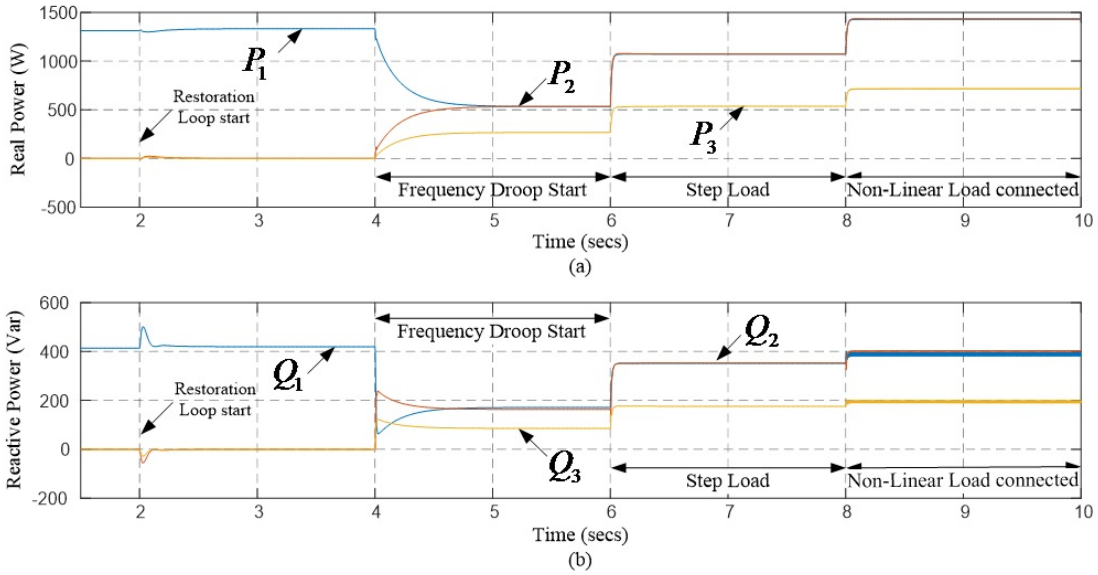

Figure 4.11: Simulation results for Microgrid with three DGs using Hierarchical Droop. (a) Real power: P_1, P_2 and P_3; (b) Reactive power: Q_1, Q_2 and Q_3.

4.5.3 Communication Failure

It is interesting to investigate the system performance under communication failure. Thus, a microgrid system is constructed same as that given in section 4.5.2, but with DG_2 and DG_3 loosing communication after power sharing activity. A load variation is also considered during each stage to see whether it affects the share of power and the attitude of each DG without the support of the communication link. When communication is lost, it is suggested to memorize the final values of the feedback signal inorder to keep working with the angle droop in this condition. It was noticed that in steady state condition without load change the system is not affected. Whereas, in load change condition the DG is able to keep supplying the load with constant power without proportional sharing with other DGs. Fig. 4.13 shows the simulation test that verify the procedure in different cases. It is indicated that at t=6sec, DG_3 lost the communication link, still share the power. After a load change, at t=8sec, it is noticed that the power remains the same without reacting with the load due to the previously memorized feedback signal. The

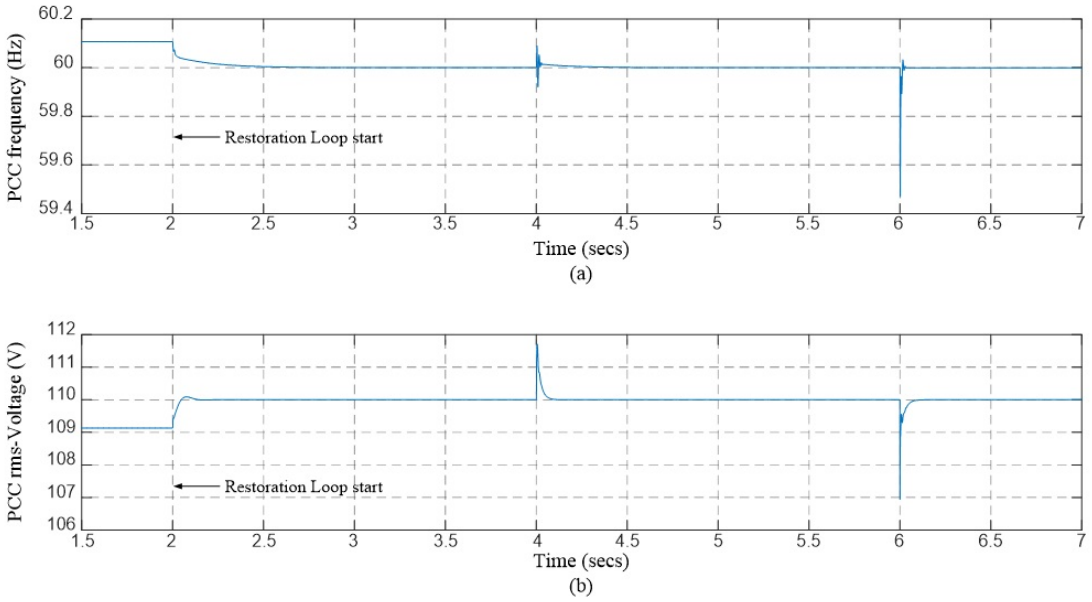

Figure 4.12: Simulation results for Microgrid with three DGs using Hierarchical Droop. (a) PCC frequency (Hz); (b) PCC rms-Voltage (V).

same procedure is made for DG_2. At t=10sec, a communication failure is presented. After that, at t=12sec, a load step is exerted by connecting a nonlinear load at the PCC. At t=16sec, the communication link is restored. The feedback values are now exactly the same for all DGs. In this case, the angle droop is able to reconfigure the reference voltage that allows to share the load proportionally as promised.

4.6 Experimental Results

To validate the performance of the proposed angle droop controller, a test bench of two DICs is constructed in the laboratory, Fig. 4.14, which consists of two isolated 500V DC voltage supplies, two three-phase inverters controlled by dSPACE 1005 kit, inductors for modeling the line impedance and a three phase R-L load and a full bridge rectifier. The system parameters are considered as follows:

1. The system voltage is 110V (RMS, Line-to-neutral), 60Hz.
2. Two three-phase PWM inverters, switching frequency 15kHz, the output filter inductor, $L_f = 3.4$ mH, the output filter capacitor $C_f = 40$ µF.
3. The proposed angle droop parameters are considered as given in Table 4.4.

4.6.1 Case1: Equal ratings of Power for DICs

In this case, we consider different line impedances set as $R_1 + \mathrm{j}X_1 = 0.1 + \mathrm{j}0.377\Omega$ and $R_2 + \mathrm{j}X_2 = 0.5 + \mathrm{j}1.88\Omega$. DIC1 is supplying the R-L load, while DIC2 is connected to the

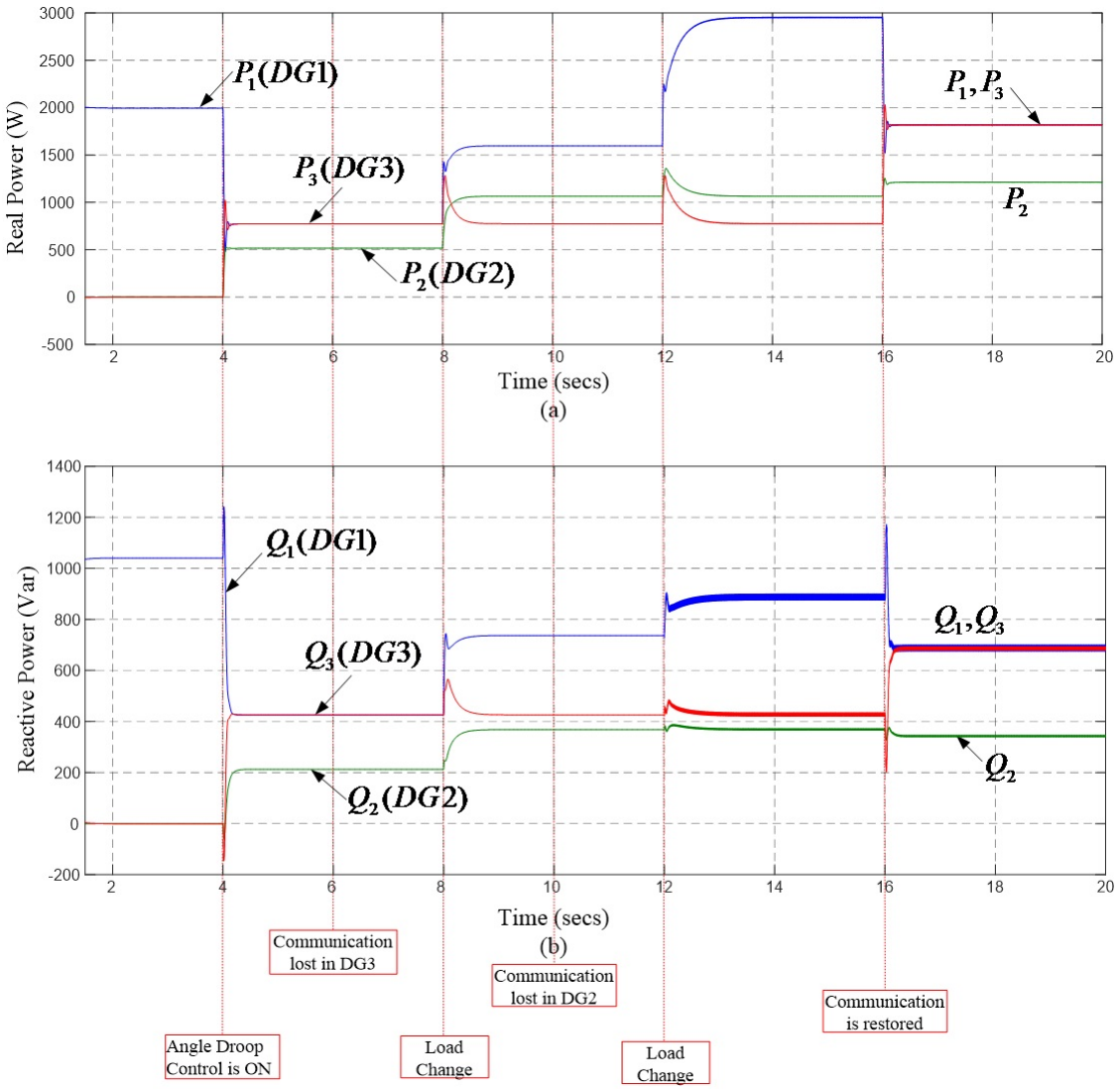

Figure 4.13: Simulation results for communication failure. (a) Real power: P_1, P_2 and P_3; (b) Reactive power: Q_1, Q_2 and Q_3.

Droop Control parameter	**Case 1: Equal Power ratings**	**Case 2: Different Power ratings**
P_{in}(W)	2000	2000/1000
Q_{in}(Var)	750	750/375
δ_{in}(rad) / V_{in}(V)	0/110	0/110
$\Delta\delta$(rad/sec) / ΔV(V/sec)	3/50	3/50
m_i(rad/W)	1.5×10^{-3}	$1.5 \times 10^{-3}/3 \times 10^{-3}$
n_i(V/Var)	6.67×10^{-2}	$6.67 \times 10^{-2}/1.34 \times 10^{-1}$
K_a/K_e(1/sec)	10/10	10/10

Table 4.4: Proposed Angle Droop Control Parameters.

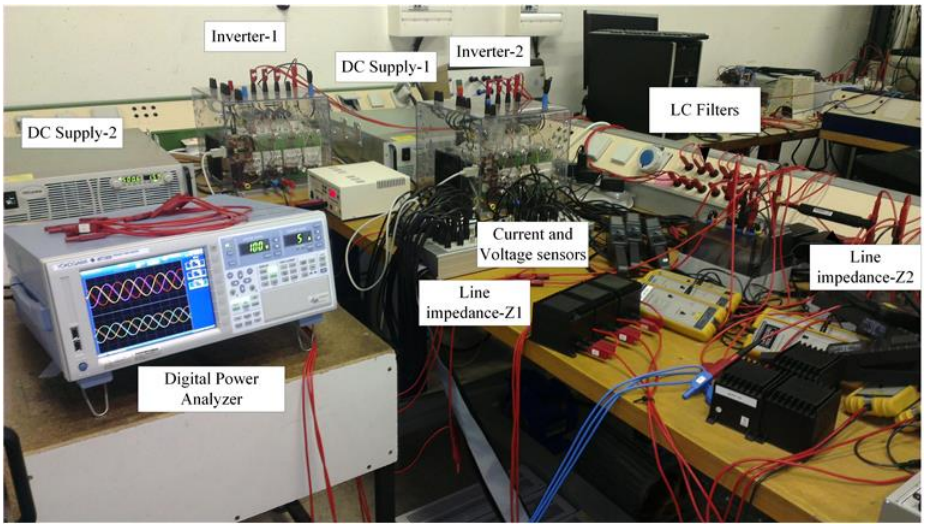

Figure 4.14: Experimental test bench constructed in the Laboratory.

grid at standby mode, at instant of turning on the Droop control for DIC2, the two sources will share the real and reactive power equally. Fig. 4.15 shows the power sharing for this case, where different stages are considered. At stage S1, DIC2 is connected to the grid in standby mode. At stage S2 the droop controller is running to share power between both converters as seen in the figure. At stage S3, a step load change is considered to study the dynamics and effectiveness of the droop controller. The phase voltage and phase current signals for the two DICs are given in Fig. 4.15(b), (c) which shows an equal magnitude of current in this case.

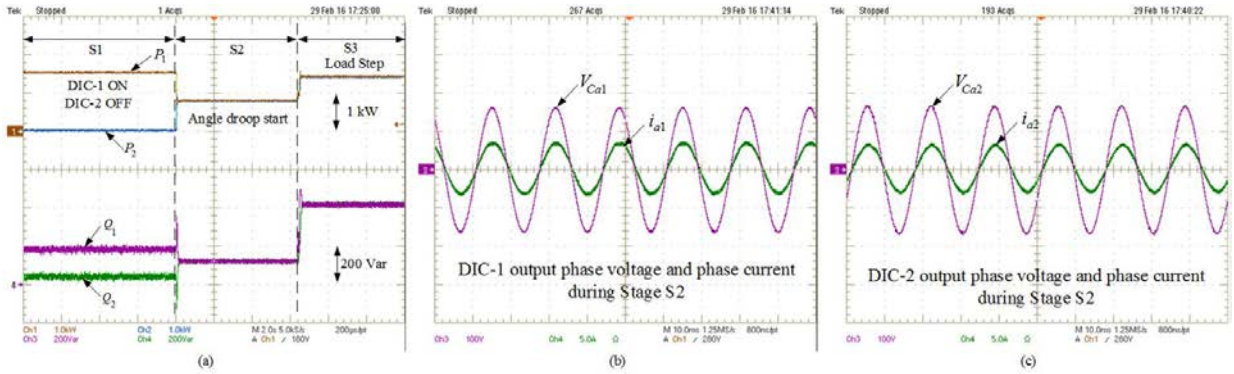

Figure 4.15: Experimental results of case 1: (a) real and reactive power sharing between two converters; (b) phase voltage and phase current for DIC-1; (c) phase voltage and phase current for DIC-2.

4.6.2 Case2: Different ratings of Power for DICs

The same line characteristics are considered, but now in this case the ratings of DIC1 is two times of DIC2. The droop parameters and the ratings are shown in Table 4.4. The

experimental test procedure is similar to the previous case. As shown in Fig. 4.16, DIC2 is put in standby mode first in stage S1, then sharing power with DIC1 at stage S2, and a step load was considered in stage S3. Accurate power sharing interprets the efficiency of the proposed controller. The steady state phase voltage and current for each converter are given in Fig 4.16(b), (c). The magnitude of i_{Ca2} is half the magnitude of i_{Ca1}.

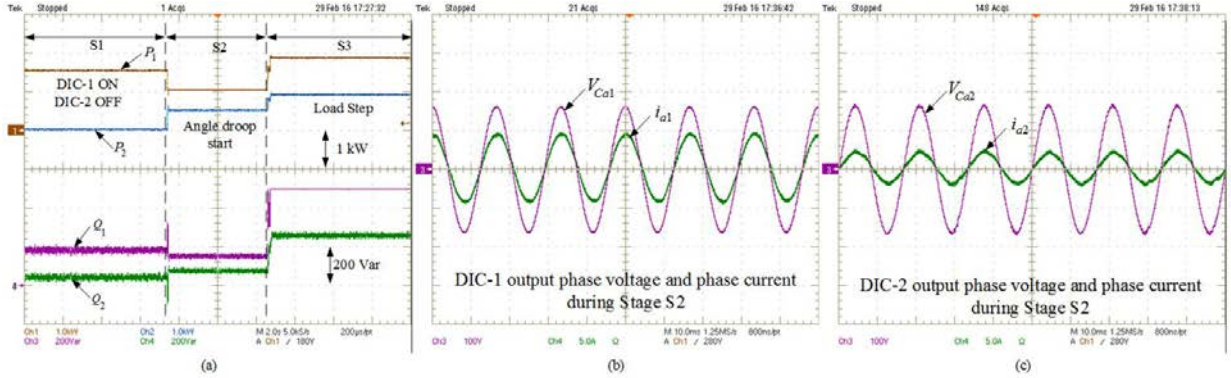

Figure 4.16: Experimental results of case 2: (a) real and reactive power sharing between two converters; (b) phase voltage and phase current for DIC-1; (c) phase voltage and phase current for DIC-2.

4.6.3 Case 3. Power Sharing in case of nonlinear Load

The droop parameters and line impedance characteristics are set as in case 2, but now with a three phase full bridge rectifier connected to 44Ω resistor and 14mH inductor. The same procedure is done for this case and the experimental results are shown in Fig. 4.17. The accurate load sharing demonstrates the robustness of the proposed droop controller even with non-linear load. This also proves that the Flatness controller can efficiently restrain the harmonic contents of the output voltage under nonlinear load condition. It is well adopted to ensure the output power of inverters to meet the load demand with reduced voltage harmonic.

4.7 Conclusion

It is well known that the frequency droop needs additional loops to restore the frequency and voltage magnitude to their nominal values, and to accurately share the power between distributed generations. In usual cases, a communication link is recommended for the purpose. Secondary loop design and virtual impedance are the rarely used methods in literature. Additional computational parameters are needed and dynamics must be taken in consideration with respect to droop control for insuring stability of the system. In this chapter, a new angle droop controller for parallel connected inverters in microgrid applications is proposed. Compared with modified frequency droop, the proposed angle droop offers no change in frequency and less voltage drop in one loop design. The µPMU,

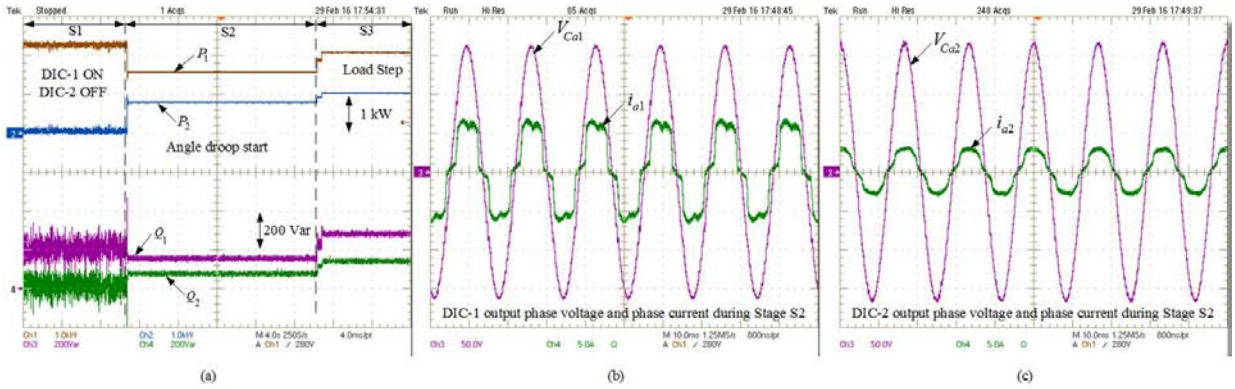

Figure 4.17: Experimental results of case 3: (a) fundamental real and reactive power sharing between two converters; (b) phase voltage and phase current for DIC-1; (c) phase voltage and phase current for DIC-2.

a promising new measurement technology for the AC microgrid, can simply be used in the proposed angle droop to define a feedback signal of the common point phasor. A robust Angle droop control is achieved during frequent load change microgrid. The proposed angle droop controller defines the dynamics of the droop and according to the stability analysis, it insures an accurate power sharing in a given range of parameters as shown in the results. The new angle droop method is tested and validated by using experiments which show the effectiveness of such control.

Chapter 5

MODELING AND STABILITY ANALYSIS FOR AC MICROGRID WITH HIGH PENETRATION OF INTERFACED-CONVERTER LOADS

5.1 Introduction

It is well known that the dynamic interaction between Distributed Generators (DG) and loads in a microgrid (MG) results to unstable behavior depending on the type of load being connected. Stability of ac-MG is influenced by high penetration of tightly regulated power converters used to interface distributed resources and loads. In this case, load converters behave as constant power loads (CPL) and introduce a negative incremental resistance feature which reduces the system stability.

In literature, some aspects of stability analysis are presented in [4, 27, 127, 128, 129, 130] where the major studies are based on small-signal linearization techniques [131]. By which, the non-linear model is linearized around an operating point and then studied by using linear analysis tools. Furthermore, the linearizing tools just predict the stability of the system for small perturbations [129, 130, 131]. The sub-system interaction and instability phenomena is a common problem in the Distributed Power System. The interaction arises because each individual converter has internal control function such as to regulate the converter dc/ac voltage, in order to keep a constant power and therefore has a negative incremental input impedance. The constant power and negative input resistance characteristic potentially have a destabilizing effect on the electrical supply system [129, 132, 133, 134]. When two stable sub-systems are combined, or integrated together, there is no guarantee that the combined system will be stable. There may be an interaction between the interconnected sub-systems, which can result in instability of the system. At the load side, a CPL is represented by an electronic power switches which regulate the supply voltage and current in order to keep a constant power consumption. Input filters must accompany power converters due to the switch-mode operation of semiconductor devices used. They have a drawback as tightly regulated power electronic converters tend

to show negative impedance characteristics and they lead to instability of the power system. In this chapter, modeling and stability analysis for ac microgrid with different load interactions are studied. The small signal analysis is studied first with different load interactions. After that, sensitivity analysis is also conducted which provides the sensitivity of different modes of the system state variables and estimates the effect of different parameter variations on each system state variables. However, it is well known that small-signal stability studies are only valid around the operating point and limited for a local domain of variation. Thus only small perturbations can be explored with small-signal analysis.

On the other hand, large-signal stability analysis for the ac microgrid is provided. A nonlinear model for inverter based microgrid is constructed taking into account the inverter inner controller, virtual impedance loop and different load types. Then, the domain of attraction of the system is developed based on *Marx et al.'s* approach [134]. The effect of CPL load as well as other loads on the domain of attraction is studied. Furthermore, the effect of virtual impedance loop on system stability is explored.

5.2 Small-Signal analysis study

In an islanded microgrid, all DGs are intended to maintain a stable system voltage and frequency when sharing the real and reactive powers. In this section, stability of multiple Distributed Generators (DGs) with different loads connected to a microgrid is applied using the eigenvalue analysis. A state-space model for the distributed interfaced converter (DIC) in a DG, with all state feedback and droop control, is performed. Each DG is referred to a common reference frame selected from any DG connected to the microgrid. Furthermore, the network and different loads are also modeled with respect to this common frame. The models of DGs, network and loads are combined together to formulate a complete generalized model for an islanded mcrogrid. A detail eigenvalue analysis is constructed to identify the effect of the droop parameters on the stability of the system. Also, for a system structure change especially when load power varies, the trajectory of dominant eigenvalues is investigated.

5.2.1 System structure and modeling

Figure 5.1 shows a simplified diagram of the microgrid system, where N-Distributed Generators (DGs) supplying a CPL load, resistive load and a constant current load represented by a current source. A capacitor bank, represented by C_{PCC}, is connected at the load side to present a real type of a microgrid. In fact, reactive power compensation would be needed in order to avoid low power factor. More importantly, the microgrid system could not be able to island successfully without another reactive power source supplying the common loads. Furthermore, The capacitor bank will play a role in simplifying the order of the system model. As shown for DG_i, the measured output current (i_{abci}) and voltage (e_{abci}) are used by a Droop Controller for sharing the desired real and reactive power to different loads. The inner controller is there, in order to insure the tracking of the reference voltage (e^*_{abci}) generated by the Droop controller. For the power section part, a three-phase VSI and an output LC filter is commonly used to interface a distributed

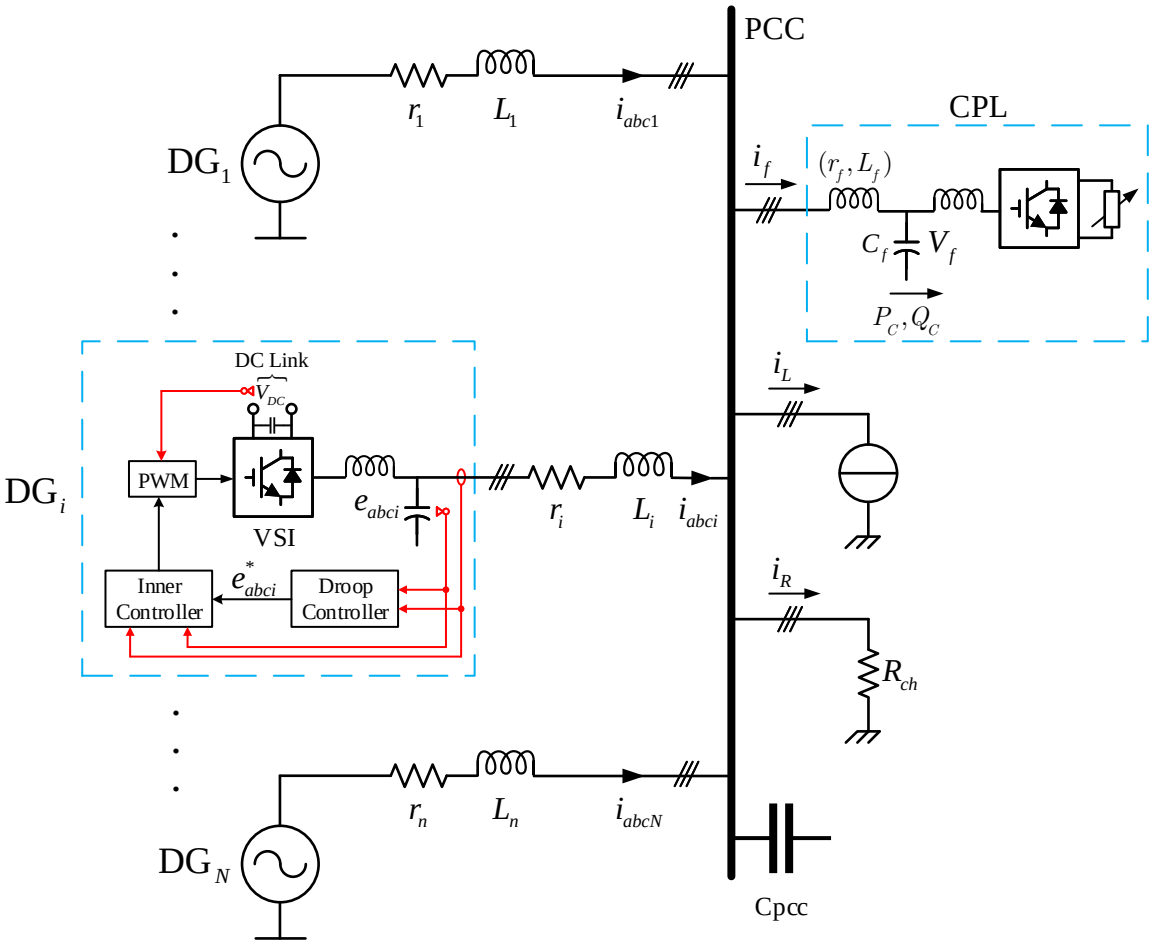

Figure 5.1: Simplified Diagram of the Microgrid system under study.

generator to a network. Assume that the inverter is represented by an ideal voltage source where the DC source dynamics are neglected as well as the switching frequency of the PWM is high enough (5-20kHz) to neglect its effect. For modeling the microgrid system, we divide the whole system into three major sub-modules: DG model, a network model for representing the line impedances and a model for different connected loads. Each DG is modeled on its individual reference frame whose rotation frequency is set by its local power sharing controller.

5.2.1.1 State-Space Model of a Distributed Generator (DG)

In order to formulate equations describing a DG_i system, an equivalent block diagram is represented in Fig. 5.2, where a virtual impedance loop is added to the reference signal generated by the droop function. This allows to model the whole DG and study the impact of virtual impedance on system stability. In this section, the state space model for a DG is formulated after presenting the three subsystems: power calculation, droop function and the inner controller.

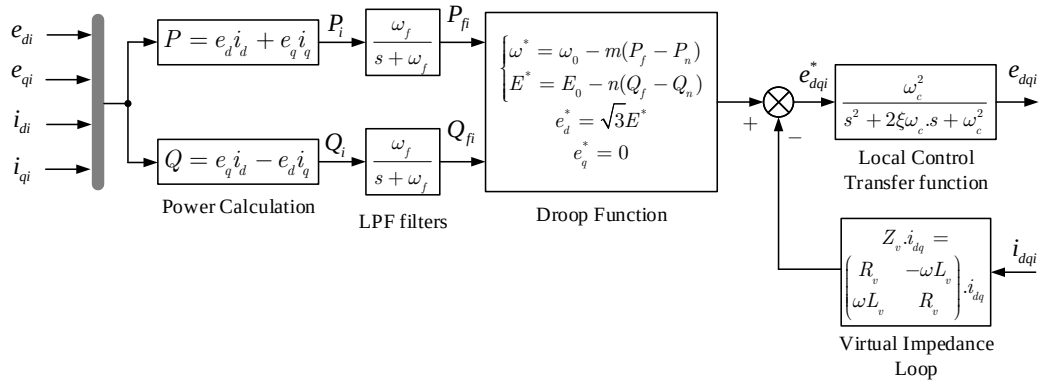

Figure 5.2: Equivalent Block diagram describing the Droop Control in DG_i.

- Power calculation:

As shown in Fig.5.2, the measured output voltage and output currents are used to calculate the instantaneous active and reactive power by using the following equations:

$$\begin{aligned} P_i &= e_d i_d + e_q i_q \\ Q_i &= e_q i_d - e_d i_q \end{aligned} \tag{5.1}$$

The instantaneous powers are passed through a first-order low pass filter, with ω_f representing the cut-off frequency of the filter, to get the average values P_{fi} and Q_{fi} as

$$\begin{aligned} P_{fi} &= \frac{\omega_f}{s+\omega_f} \cdot P_i \\ Q_{fi} &= \frac{\omega_f}{s+\omega_f} \cdot Q_i \end{aligned} \tag{5.2}$$

- Droop Function

The droop control allows each DG in a microgrid to share their real and reactive power proportional to their ratings. The real power is shared by drooping the frequency (ω) by a droop gain m, whereas the reactive power sharing is achieved by drooping the output voltage with a droop gain n. To obtain a reference voltage for DG_i, the droop function is performed to generate the frequency and voltage magnitude as shown in Fig.5.2 and given as

$$\begin{cases} \omega_i^* = & \omega_0 - m_i(P_i - P_{in}) \\ E_i^* = & E_0 - n_i(Q_i - Q_{in}) \end{cases} \tag{5.3}$$

The droop coefficients m_i and n_i can be calculated applying a given range of frequency and voltage variations, given as

$$m_i = \frac{\omega_{max} - \omega_{min}}{P_{in}},\ n_i = \frac{E_{max} - E_{min}}{Q_{in}} \tag{5.4}$$

- Inner Controller:

The inner controller is modeled as a second-order filter. The reason of taking this assumption, is that usually the inner controller has a fast dynamic as compared to the outer droop control loop. Thus the output voltages across capacitors (e_{dqi}) can be supposed to follow perfectly their reference (e^*_{dqi}). Thus, the inner controller model can be written in the form:

$$\frac{e_{dqi}}{e^*_{dqi}} = \frac{\omega_c^2}{s^2 + 2\xi\omega_c \cdot s + \omega_c^2} \tag{5.5}$$

where, ω_c represents the cut-off frequency of the inner controller.

The state equations are represented on the reference frame of one of the individual DG. This reference frame is considered as the common reference frame. All the other inverters are translated to this common reference frame using the transformation technique depicted in Fig. 5.3 and defined in (5.6) [4].

$$\begin{aligned} [X_{DQ}] &= [T_i] \cdot [X_{dq}] \\ [T_i] &= \begin{bmatrix} \cos(\delta_i) & -\sin(\delta_i) \\ \sin(\delta_i) & \cos(\delta_i) \end{bmatrix} \end{aligned} \tag{5.6}$$

Here, the DQ axis represents the common reference frame rotating at a frequency ω_{com}. This common reference frame is chosen by any DG in the system (for example the first one), and ω_{com} represents the angular frequency of the reference DG generated by the droop controller. Whereas axes $(d-q)_i$ and $(d-q)_j$ are the reference frame of ith and jth inverters rotating at ω_i and ω_j, respectively. Indeed, at steady state condition, the system frequency is the same (i.e. $\omega_i = \omega_j = \omega_{com}$) but there exist a phase shift created by each DG local controller regarding their time reference and the synchronization process. Where, δ_i is the phase angle of the reference frame of ith inverter with respect to the common reference frame. In this case, δ_i is a state variable expressed as:

$$\frac{d\delta_i}{dt} = \omega_i - \omega_{com} \tag{5.7}$$

Thus, the equivalent DG_i model in common reference frame, can be described by using the following equations:

$$\begin{cases} \frac{d}{dt}e_{DQi} = & \dot{e}_{DQi} - \begin{pmatrix} 0 & (\omega_i - \omega_{com}) \\ -(\omega_i - \omega_{com}) & 0 \end{pmatrix} e_{DQi} \\ \frac{d}{dt}\dot{e}_{DQi} = & -2\zeta\omega_c \cdot \dot{e}_{DQi} - \omega_c^2(e^*_{DQi} - e_{DQi}) - \begin{pmatrix} 0 & (\omega_i - \omega_{com}) \\ -(\omega_i - \omega_{com}) & 0 \end{pmatrix} \dot{e}_{DQi} \\ \frac{d}{dt}P_{fi} = & \omega_f(e_{Di}i_{Di} + e_{Qi}i_{Qi}) - \omega_f P_{fi} \\ \frac{d}{dt}Q_{fi} = & \omega_f(e_{Qi}i_{Di} - e_{Di}i_{Qi}) - \omega_f Q_{fi} \end{cases} \tag{5.8}$$

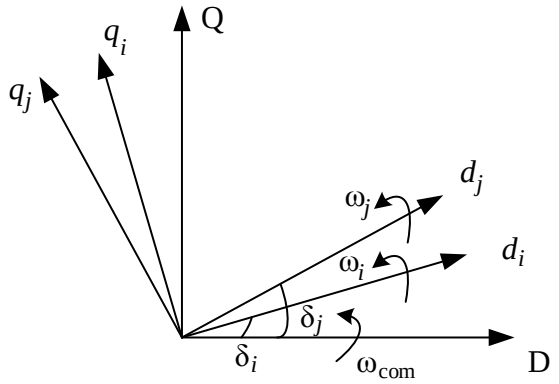

Figure 5.3: Reference Frame Transformation.

with e^*_{DQi}, the reference voltage of DG_i is expressed as:

$$\begin{bmatrix} e^*_{Di} \\ e^*_{Qi} \end{bmatrix} = [T_i] \cdot \begin{bmatrix} \sqrt{3}E^*_i \\ 0 \end{bmatrix} + \begin{bmatrix} -R_{vi} \cdot i_{Di} + \omega_{com} L_{vi} \cdot i_{Qi} \\ -\omega_{com} L_{vi} \cdot i_{Di} - R_{vi} \cdot i_{Qi} \end{bmatrix} \tag{5.9}$$

where R_{vi} and L_{vi} represent, respectively, the resistive and inductive values of the virtual output impedance loop.

5.2.1.2 Network Model

A simple example of a network of N feeder lines, connected to N inveters from one side and to a common coupling point (PCC) from the other side, is shown in Fig. 5.1. With respect to the common reference frame, the state equations of line current of the ith line connected to DG_i are:

$$\begin{aligned} \frac{d}{dt} i_{Di} &= \frac{1}{L_i}(e_{Di} - V_{PCCD}) - \frac{r_i}{L_i} i_{Di} + \omega_{com} \cdot i_{Qi} \\ \frac{d}{dt} i_{Qi} &= \frac{1}{L_i}(e_{Qi} - V_{PCCQ}) - \frac{r_i}{L_i} i_{Qi} - \omega_{com} \cdot i_{Di} \end{aligned} \tag{5.10}$$

5.2.1.3 Load Model

Many types of load can exist in a microgrid. Here, we are going to consider a resistive, constant current and CPL loads. The capacitor bank allows the formulation of the PCC voltages as function of other state variables. The state equations of the PCC can be written as:

$$\begin{aligned} \frac{d}{dt} V_{PCCD} &= \frac{1}{C_{PCC}} \left(\sum_{i=1}^{N} i_{Di} - \frac{V_{PCCD}}{R_{ch}} - i_{LD} - i_{fD} \right) + \omega_{com} \cdot V_{PCCQ} \\ \frac{d}{dt} V_{PCCQ} &= \frac{1}{C_{PCC}} \left(\sum_{i=1}^{N} i_{Qi} - \frac{V_{PCCQ}}{R_{ch}} - i_{LQ} - i_{fQ} \right) - \omega_{com} \cdot V_{PCCD} \end{aligned} \tag{5.11}$$

where, R_{ch} represents the resistance of the resistive load, i_{LD}, i_{LQ} are the constant current load in DQ frame and i_{fD}, i_{fQ} are the input current of the CPL load.

The electrical equations loaded by a CPL with its input filter are:

$$\begin{aligned} L_f \frac{d}{dt} i_{f(abc)} &= -r_f \cdot i_{f(abc)} + V_{PCC(abc)} - V_{f(abc)} \\ C_f \frac{d}{dt} V_{f(abc)} &= i_{f(abc)} - I_{(abc)} \end{aligned} \tag{5.12}$$

The three-phase CPL system described in (5.12), in (abc) frame, is reduced to a system described respectively in (dq) frame by applying Park transformation:

$$\begin{aligned} \frac{d}{dt}\begin{pmatrix} i_{fD} \\ i_{fQ} \end{pmatrix} &= \frac{-r_f}{L_f}\begin{pmatrix} i_{fD} \\ i_{fQ} \end{pmatrix} + \frac{1}{L_f}\begin{pmatrix} V_{PCCD} \\ V_{PCCQ} \end{pmatrix} - \frac{1}{L_f}\begin{pmatrix} V_{fD} \\ V_{fQ} \end{pmatrix} - \begin{pmatrix} 0 & -\omega_{com} \\ \omega_{com} & 0 \end{pmatrix} \cdot \begin{pmatrix} i_{fD} \\ i_{fQ} \end{pmatrix} \\ \frac{d}{dt}\begin{pmatrix} V_{fD} \\ V_{fQ} \end{pmatrix} &= \frac{1}{C_f}\begin{pmatrix} i_{fD} \\ i_{fQ} \end{pmatrix} - \frac{1}{C_f}\begin{pmatrix} I_D \\ I_Q \end{pmatrix} - \begin{pmatrix} 0 & -\omega_{com} \\ \omega_{com} & 0 \end{pmatrix} \cdot \begin{pmatrix} V_{fD} \\ V_{fQ} \end{pmatrix} \end{aligned} \tag{5.13}$$

where $\begin{pmatrix} I_D \\ I_Q \end{pmatrix} = \frac{1}{V_{fD}^2 + V_{fQ}^2}\begin{pmatrix} P_c & Q_c \\ -Q_c & P_c \end{pmatrix} \cdot \begin{pmatrix} V_{fD} \\ V_{fQ} \end{pmatrix}$, the current representing the consumed constant power P_c, Q_c.

For simplicity, we consider a microgrid with two DGs. The overall system model can be described as:

$$\frac{dx}{dt} = A(x) \cdot x \tag{5.14}$$

where,

$$\begin{aligned} x^T = [\ & i_{D1}\ \ i_{Q1}\ \ i_{D2}\ \ i_{Q2}\ \ V_{PCCD}\ \ V_{PCCQ}\ \ i_{fD}\ \ i_{fQ}\ \ V_{fD}\ \ V_{fQ} \\ & e_{D1}\ \ e_{Q1}\ \ \dot{e}_{D1}\ \ \dot{e}_{Q1}\ \ e_{D2}\ \ e_{Q2}\ \ \dot{e}_{D2}\ \ \dot{e}_{Q2}\ \ P_{f1}\ \ Q_{f1}\ \ P_{f2}\ \ Q_{f2}\ \ \delta_2] \end{aligned}$$

Note that, $A(x)$ is not linear and has state variables as elements. Thus, the model is nonlinear of order 23.

5.2.2 Eigenvalue and Sensitivity analysis

In order to study the stability of a microgrid and to understand the dynamic behavior which is affected by several control parameters, an eigenvalue analysis by plotting the root locus is given. This is done by calculating the Jacobean matrix at each operating point. The system parameters are given in table 5.1. When the system operates under those given parameters, it is assumed to be operating in the nominal operating condition.

The eigenvalues of the system under its nominal operating condition are shown in table 5.2. It can be seen in Fig. 5.4 that the eigenvalues are placed in different clusters. The large range of frequency components corresponds to the line currents (Fig. 5.4a) and

System Parameters	
Nominal frequency/voltage f /V	60 Hz, 110 V
Feeder 1 (r_1, L_1)	0.1Ω, 1mH
Feeder 2 (r_2, L_2)	0.1Ω, 1mH
DG Ratings	
DG_1 $P(W)/Q(Var)$	3000/1500
DG_2 $P(W)/Q(Var)$	3000/1500
Load Parameters	
Resistive Load R_{ch}	100Ω
Constant current load: i_{LD}, i_{LQ}	0, -3 A
Constant power load (CPL) (r_f, L_f, C_f)	(0.1Ω, 0.4mH, 40μF)
PCC Capacitor Bank C_{PCC}	100 nF
Virtual impedance	
(R_{v1}, L_{v1})	(0Ω, 0mH)
(R_{v2}, L_{v2})	(0Ω, 0mH)
Flatness Control trajectory dynamics	
ζ/ω_c (rad/sec)	1/5000
Frequency Droop Control Parameters	
Frequency drop $\triangle\omega$ (rad/sec)	$\triangle\omega = 0.1$
Voltage drop $\triangle V$ (V)	$\triangle V = 1$
Low pass filter cutoff frequency ω_f (rad/sec)	100

Table 5.1: System Parameters for stability analysis.

Eigenvalues	
$\lambda_{1,2}$	$-5 \times 10^4 \pm 2.066 \times 10^5$j
$\lambda_{3,4}$	$-5 \times 10^4 \pm 2.058 \times 10^5$j
$\lambda_{5,6}$	$-122.02 \pm 5.63 \times 10^3$j
$\lambda_{7,8}$	$-121.75 \pm 4.89 \times 10^3$j
λ_9	-160.77
$\lambda_{10,11}$	-70.28 ± 375.57j
λ_{12}	-3.18
λ_{13}	-96.54
λ_{14}	-99.99
λ_{15}	-99.83
λ_{16}	-4.95×10^3
λ_{17}	-5.04×10^3
$\lambda_{18,19}$	$-5 \times 10^3 \pm 16.65$j
$\lambda_{20,21}$	$-5 \times 10^3 \pm 2.02$j
λ_{22}	-4.99×10^3
λ_{23}	-5×10^3

Table 5.2: Eigenvalues under nominal operating condition.

voltage controller (Fig. 5.4b). The other clusters correspond to the PCC and CPL load voltages (i.e. $\lambda_{5,6,7,8}$), the input filter for power calculation (i.e. $\lambda_{9,13,14,15}$), the CPL input current (i.e. $\lambda_{10,11}$) and the phase angle (i.e. λ_{12}).

Eigenvalue reveal different frequency components in the system and their available damping. Further information about the origin of different frequency components can be obtained by observing the participation (sensitivity) of different state variables in a particular mode. In order to have a mathematical criteria of this observation, we can use a modal approach which will give us the sensitivity of the eigenvalues with respect to coefficients of the state matrix. The modal approach described in [135] makes it possible to quantify the sensitivity, and therefore the influence of each element of a state matrix on its eigenvalues. In [4], it is used to study the sensitivity of eigenvalues with respect to the parameters of microgrid system, more specifically, the droop coefficients. Here, we will simply study the influence of not only the droop parameters, but also the load powers on the system eigenvalues. In his book [135], Kundur *et al.* give the relation (5.15) where the sensitivity of eigenvalue λ_i to the element a_{kj} of the state matrix is equal to the product of the left eigenvector element Ψ_{ik} and the right eigenvector element Φ_{ji} given as:

$$\frac{\partial \lambda_i}{\partial a_{kj}} = \Psi_{ik}\Phi_{ji} \tag{5.15}$$

Since the real part of the eigenvalues indicate the stability of the system, we will only look at the real part of the sensitivity factor which gives information about the evolution of the real part of the eigenvalues. The real parts of the sensitivity values computed with the modal approach are given in Table 2.2. To obtain the sensitivity with respect to the power of the loads, we will take the coefficients of the state matrix which include them,

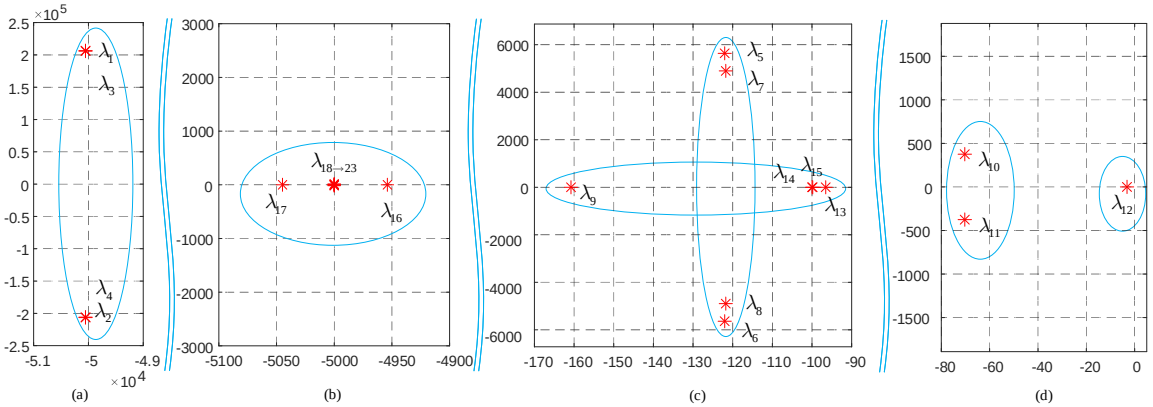

Figure 5.4: Eigenvalues spectrum of the system indicating different clusters.

	Sensitivity factor of $\lambda_{1,2,3,4}$ for (i_{dq1}, i_{dq2})	Sensitivity factor of $\lambda_{5,6,7,8}$ for (V_{PCCdq}, V_{fdq})	Sensitivity factor of $\lambda_{10,11}$ for (i_{fdq})	Sensitivity factor of λ_{12} for (δ_2)	Sensitivity factor of $\lambda_{9,13,14,15}$ for (PQ_{f1}, PQ_{f2})
$a_{9,9}$, $a_{10,10}$ (P_c)	0.00015	0.25	$\simeq 0$	$\simeq 0$	$\simeq 0$
$a_{5,5}$, $a_{6,6}$ (R_{ch})	0.25	0.0002	$\simeq 0$	$\simeq 0$	$\simeq 0$
$a_{13,20}$, $a_{17,22}$ (n_1, n_2)	$\simeq 0$	$\simeq 0$	$s_{\lambda 10} = -5 \times 10^{-4}$	0.001	$s_{\lambda 9} = -5 \times 10^{-4}$
					$s_{\lambda 13} \simeq 0$
			$s_{\lambda 11} = 3.6 \times 10^{-4}$		$s_{\lambda 14} \simeq 0$
					$s_{\lambda 15} \simeq 0$
$a_{23,19}$, $a_{23,21}$ (m_1, m_2)	$\simeq 0$	$s_{\lambda 5} = 3.5$	$s_{\lambda 10} \mp 1624.1$	$\mp 7.4 \times 10^2$	$s_{\lambda 9} = \mp 1619$
		$s_{\lambda 6} \simeq 3.5$			$s_{\lambda 13} = \pm 5 \times 10^4$
		$s_{\lambda 7} = -5.5$	$s_{\lambda 11} \mp 5.5 \times 10^4$		$s_{\lambda 14} = \pm 5.4 \times 10^4$
		$s_{\lambda 8} = -5.5$			$s_{\lambda 15} = 43.45$

Table 5.3: Sensitivity of the dominant eigenvalues.

that is to say $a_{9,9} = a_{10,10} = -Pc/(C_f V^2)$ which correspond to the real power of the CPL load and $a_{5,5} = a_{6,6} = -1/R_{ch}$ related to the resistive load. The droop control parameters appear in coefficients $a_{13,20}$ and $a_{17,22}$ respectively for voltage droop parameters n_1 and n_2 and coefficients $a_{23,19}$ and $a_{23,21}$ respectively for frequency droop parameters m_1 and m_2. With these coefficients of the state matrix, we will have the sensitivity of each eigenvalue with respect to load powers and droop parameters.

From Table 2.2, we see that the load powers have higher sensitivity values in $\lambda_{1,2,3,4}$ and $\lambda_{5,6,7,8}$ that correspond to DGs output current and voltage across the PCC and CPL filter capacitor. The droop parameters have high participation or sensitivity factors in λ_{12}, $\lambda_{10,11}$ and $\lambda_{9,13,14,15}$. It was shown that the voltage droop parameters (n_1, n_2) also affect the eigenvalue λ_{12} that corresponds to the phase angle difference between the two DGs in the microgrid system. The reason behind this case came from the coupling effect between active and reactive powers in a microgrid. Thus, the voltage droop control will affect the phase angle and the same scenario will appear in frequency droop, where the parameters (m_1, m_2) can affect the reactive power sharing.

In order to verify these results, Figs. 5.5, 5.6, 5.7, 5.8, 5.9 represent the evolution of the system eigenvalues with respect to droop parameters and different loads power variation. Fig. 5.5 shows the trajectory of the dominant low-frequency eigenvalues as function of the frequency drop $(\triangle\omega)$. It can be seen that as $\triangle\omega$ is increased, the eigenvalues λ_{12} and λ_{13} moves toward each other, to improve transient response for the active power flow of the

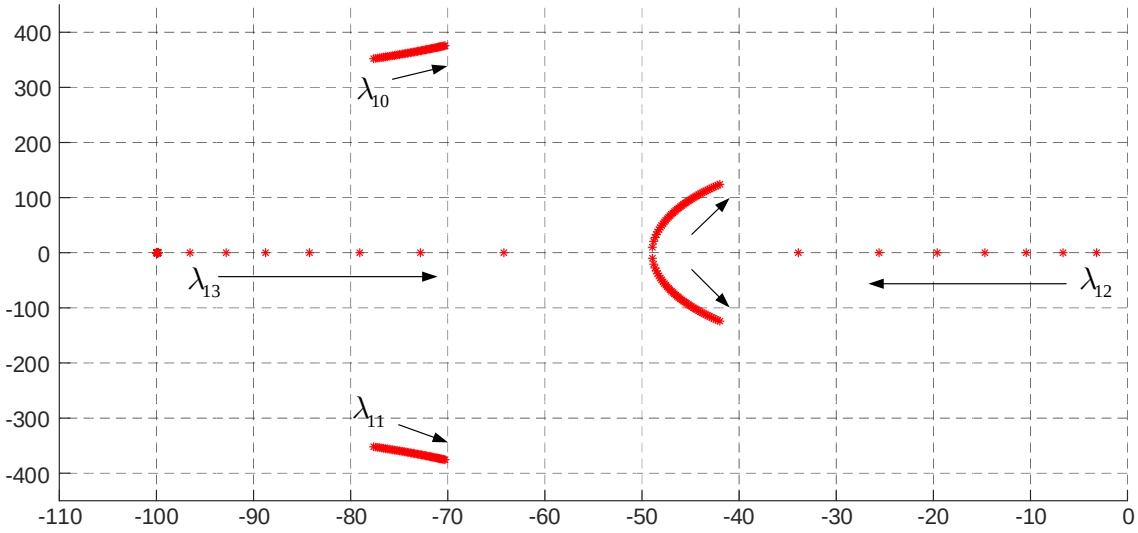

Figure 5.5: Low-frequency eigenvalues as function of frequency drop (increasing variation): $0.1 \leq \triangle\omega \leq 5$ (rad/sec).

DGs, and deflecting their path after collision toward the right side of the real axis. λ_{10} and λ_{11} are also sensitive to the change of frequency drop as seen in the figure, but they are less affected than eigenvalues λ_{12} and λ_{13}. Although the system remains stable, but a large frequency drop could affect the system stability. In Fig. 5.6, the low-frequency dominant eigenvalues that are sensitive to the voltage drop (reactive power droop) are λ_9, $\lambda_{10,11}$.The eigenvalue λ_{12} remains stable and not affected to the change of voltage drop parameters.Whereas, $\lambda_{10,11}$ move to the right side of the real axis and tend to be positive. Thus, the modeled system shift to unstable case after setting a large value of voltage drop ($\triangle V$).

To explain the effect of load variation on system stability, a study for the most dominant eigenvalues trajectory change as function of different load condition is established. Starting from the CPL type, Fig. 5.7 shows the eigenvalues trajectory under the effect of CPL real power change. As the power P_c increased, the dominant eigenvalues that are sensitive to the change are $\lambda_{5,6}$ and $\lambda_{7,8}$. The rest low-frequency eigenvalues remain stable. The next step is to change the resistive load (R_{ch}) and see its effect on each eigenvalue. Fig. 5.8 represents this case study. It can be seen that, as the resistance became large, the most effected eigenvalues are $\lambda_{1,3}$ and $\lambda_{2,4}$ that correspond to the line currents. For low-frequency eigenvalues, the most moving ones are $\lambda_{5,6,7,8}$ that correspond to the PCC and CPL voltages. The same study is done by changing the constant current source values, system condition will change and the eigenvalues trajectory is given in Fig. 5.9. It is noticed that, all the eigenvalues remain stable with no remarkable change. From the last three studies, it can be noticed that the eigenvalues related to the droop control (i.e. λ_9, $\lambda_{13,14,15}$ and λ_{12}) are not influenced with the change in all types of load. Indeed, the load change has no effect on droop dynamics as presented earlier from the eigenvalues and sensitivity analysis.

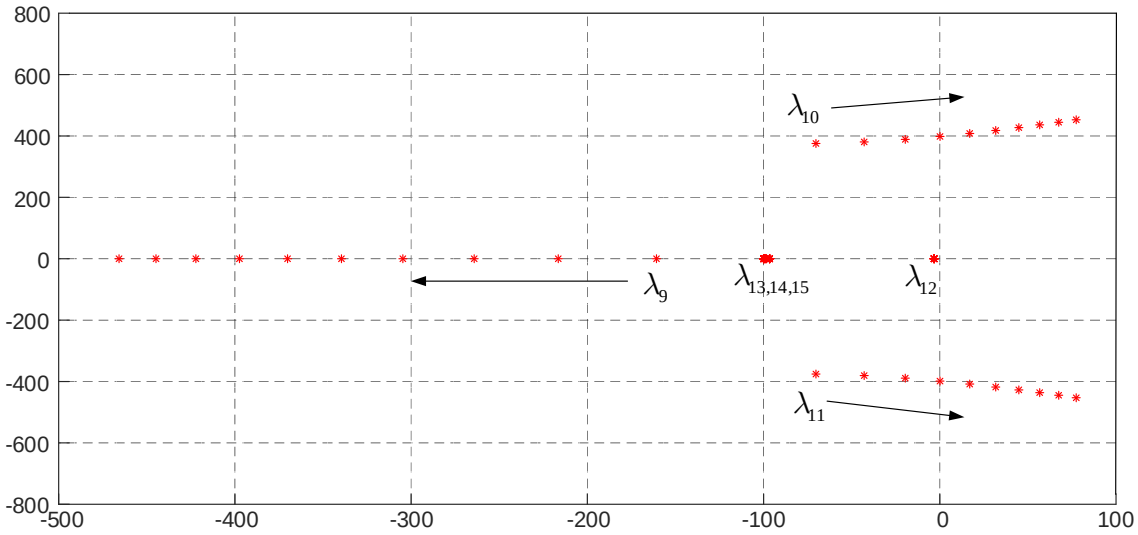

Figure 5.6: Low-frequency eigenvalues as function of voltage drop (increasing variation): $1 \leq \triangle V \leq 10\,(V)$.

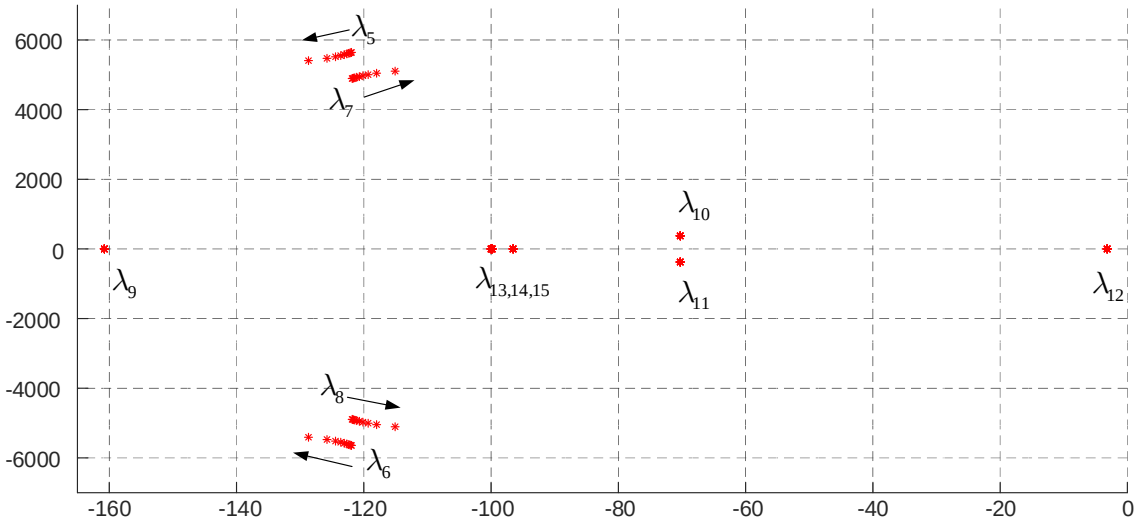

Figure 5.7: Low-frequency eigenvalues as function of CPL real power (increasing): $100 \leq P_c \leq 1000\,(W)$.

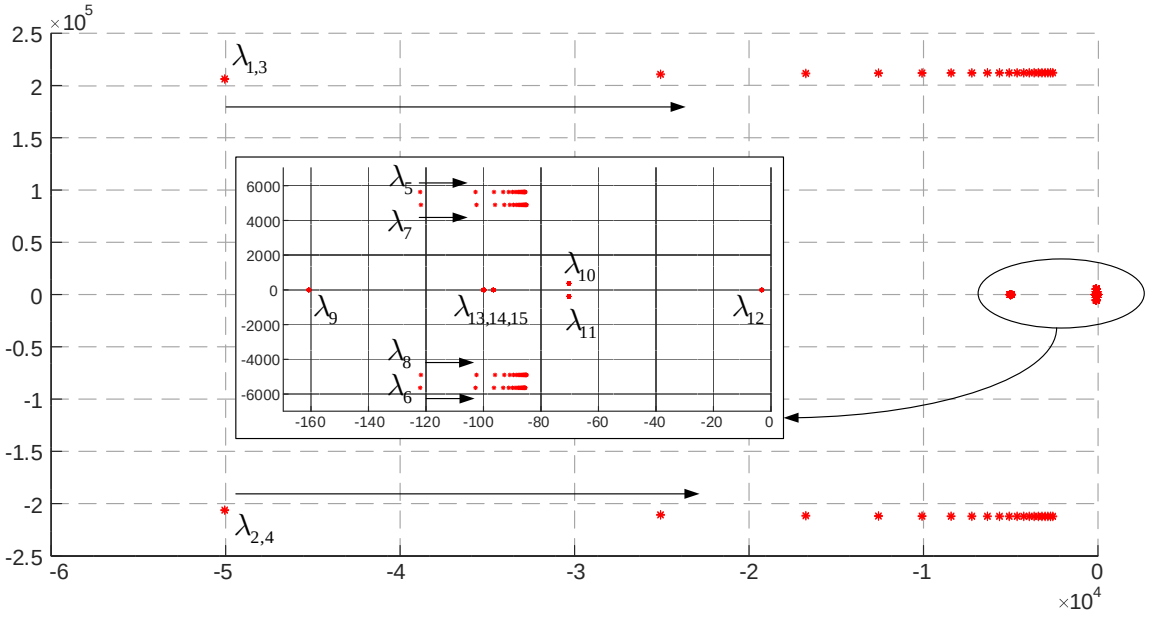

Figure 5.8: Low-frequency eigenvalues as function of R_{ch} load change (increasing): $100 \leq R_{ch} \leq 2000\,(\Omega)$.

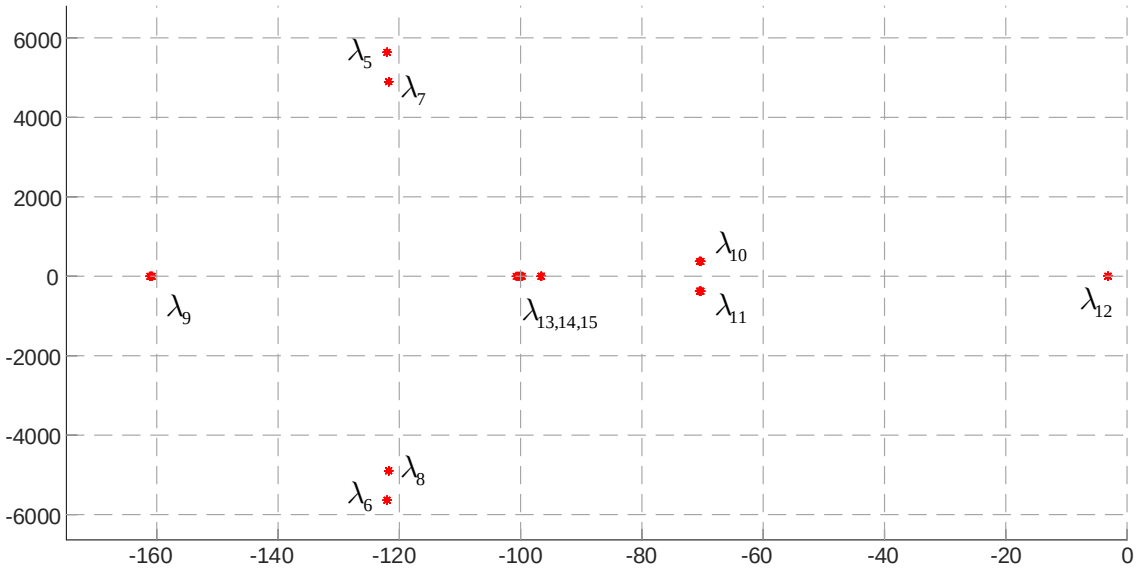

Figure 5.9: Low-frequency eigenvalues as function of I_{Lq} current source load change (increasing): $0 \leq I_{Lq} \leq 20\,(A)$.

5.3 Conclusion for Small-Signal analysis

As a conclusion, the small-signal analysis for ac microgrid is elaborated. Furthermore, the study considers different types of load where eigenvalue and sensitivity analysis are given for the microgrid model. Sensitivity study is presented by the method of [135], where the approach demonstrates clearly the lesser effect of CPL and other loads on the droop controller by calculating the sensitivity factor of each dominant eigenvalues that represent load change as well as droop parameters change. It was found that the eigenvalues that represent the dynamics of the droop control are not affected by the load variation. In the next section we are going to study the large-signal stability for the ac-microgrid which will focus on the effect of load interaction with the ac grid. We will assume each DG is perfectly controlled by the droop control without taking into consideration its dynamics in the analysis. As it corresponds to low-frequency mode and is not affected by the load interaction.

5.4 Large-Signal analysis

In this section, we propose to study the large-signal stability of ac-microgrid supplying different types of load. Indeed, Lyapunov-based techniques are the commonly used tool for nonlinear stability study. The main advantage of Lyapunov-based approach lies in the fact that Lyapunov function provides an estimation of the region of attraction of a stable operating point, allowing to predict the size of disturbance that can be tolerated. The domain of validity and effectiveness of large-signal nonlinear stability analysis is much larger than that of small-signal linear analysis [136, 137]. Indeed, a large-signal stable system is small-signal stable but the reverse is not necessarily true.

Power electronic converters are an enabling technology for integrating renewable energy sources such as wind turbines and solar photovoltaics (PV) systems. Furthermore, microgrids provide opportunities for small-scale renewable implementation. Hence, microgrids are technically feasible due to these power electronic converters. However, these converters are effectively nonlinear since the differential-algebraic dynamic equations describing those converters are nonlinear [138]. In literature, large-signal stability of power electronic converters have been studied in [139, 140]. Then, Lyapunov-based stability analysis tools are applicable to study, analyze and optimize the nonlinear stability problems within microgrids. In this section, we propose to analyze the stability of microgrids by using Takagi-Sugeno multi-modeling [141] for generating a Lyapunov function which not only proves the asymptotic stability of the system at a given operating point, but also determines an estimation of the domain of attraction around this point [142, 143]. This approach needs a linear matrix inequalities (LMI) solver to maximize the size of the estimated domain [144].

5.4.1 Microgrid Full-Order Model

The system model formulated in section 5.2 is used here. The microgrid system is represented by Fig. 5.10. As concluded in the small-signal analysis, in ac-microgrid, the poles

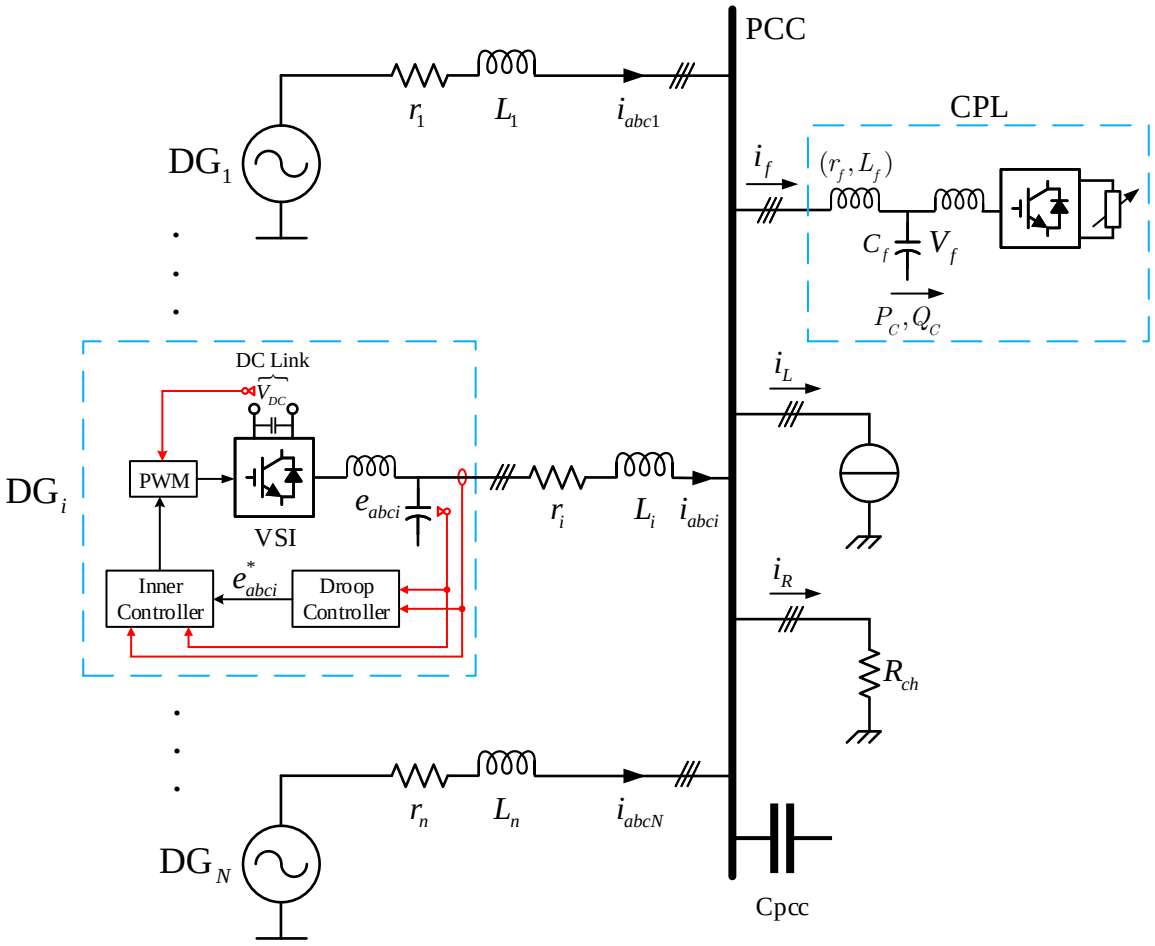

Figure 5.10: Simplified Diagram of the Microgrid system under study.

associated to the DG droop control dynamics are weakly affected by the load interaction and power change. Thus, the only change in the system model is that the state equations related to power sharing and droop control are neglected from the analysis. The state variables take the form:

$$x^T = [\ i_{D1}\ \ i_{Q1}\ \ i_{D2}\ \ i_{Q2}\ \ V_{PCCD}\ \ V_{PCCQ}\ \ i_{fD}\ \ i_{fQ}\ \ V_{fD}\ \ V_{fQ}$$
$$e_{D1}\ \ e_{Q1}\ \ \dot{e}_{D1}\ \ \dot{e}_{Q1}\ \ e_{D2}\ \ e_{Q2}\ \ \dot{e}_{D2}\ \ \dot{e}_{Q2}]$$

For Large-Signal analysis, the system should be written around its operating point. Thus, taking the change of origin as $x = X_0 + \tilde{x}$, the 18^{th} order model can be expressed as:

$$
\begin{cases}
\frac{d}{dt}\tilde{i}_{D1} & = \frac{-r_1}{L_1}\tilde{i}_{D1} + \omega\tilde{i}_{Q1} - \frac{1}{L_1}\tilde{e}_{D1} + \frac{1}{L_1}\tilde{v}_{PCCD} \\
\frac{d}{dt}\tilde{i}_{Q1} & = -\omega\tilde{i}_{D1} - \frac{r_1}{L_1}\tilde{i}_{Q1} - \frac{1}{L_1}\tilde{e}_{Q1} + \frac{1}{L_1}\tilde{v}_{PCCQ} \\
\frac{d}{dt}\tilde{i}_{D2} & = \frac{-r_2}{L_2}\tilde{i}_{D2} + \omega\tilde{i}_{Q2} - \frac{1}{L_2}\tilde{e}_{D2} + \frac{1}{L_2}\tilde{v}_{PCCD} \\
\frac{d}{dt}\tilde{i}_{Q2} & = -\omega\tilde{i}_{D2} - \frac{r_2}{L_2}\tilde{i}_{Q2} - \frac{1}{L_2}\tilde{e}_{Q2} + \frac{1}{L_2}\tilde{v}_{PCCQ} \\
\frac{d}{dt}\tilde{v}_{PCCD} & = \frac{1}{C_{PCC}}\tilde{i}_{D1} + \frac{1}{C_{PCC}}\tilde{i}_{D2} - \frac{1}{R_{ch}}\tilde{v}_{PCCD} + \omega\tilde{v}_{PCCQ} - \frac{1}{C_{PCC}}\tilde{i}_{fD} \\
\frac{d}{dt}\tilde{v}_{PCCQ} & = \frac{1}{C_{PCC}}\tilde{i}_{Q1} + \frac{1}{C_{PCC}}\tilde{i}_{Q2} - \omega\tilde{v}_{PCCD} - \frac{1}{R_{ch}}\tilde{v}_{PCCQ} - \frac{1}{C_{PCC}}\tilde{i}_{fQ} \\
\frac{d}{dt}\tilde{i}_{fD} & = \frac{1}{L_f}\tilde{v}_{PCCD} - \frac{r_f}{L_f}\tilde{i}_{fD} + \omega\tilde{i}_{fQ} - \frac{1}{L_f}\tilde{v}_{fD} \\
\frac{d}{dt}\tilde{i}_{fQ} & = \frac{1}{L_f}\tilde{v}_{PCCQ} - \omega\tilde{i}_{fD} - \frac{r_f}{L_f}\tilde{i}_{fQ} - \frac{1}{L_f}\tilde{v}_{fQ} \\
\frac{d}{dt}\tilde{v}_{fD} & = \frac{1}{C_f}\tilde{i}_{fD} + \left[(V_{fD0}I_{D0} - V_{fQ0}I_{Q0})f_1 + I_{D0}f_1f_2\right]\tilde{v}_{fD} \\
& \quad + \left[\omega + (V_{fD0}I_{Q0} + V_{fQ0}I_{D0})f_1 + I_{D0}f_1f_3\right]\tilde{v}_{fQ} \\
\frac{d}{dt}\tilde{v}_{fQ} & = \frac{1}{C_f}\tilde{i}_{fQ} + \left[-\omega + (V_{fD0}I_{Q0} + V_{fQ0}I_{D0})f_1 + I_{Q0}f_1f_2\right]\tilde{v}_{fD} \\
& \quad + \left[-(V_{fD0}I_{D0} - V_{fQ0}I_{Q0})f_1 + I_{Q0}f_1f_3\right]\tilde{v}_{fQ} \\
\frac{d}{dt}\tilde{e}_{D1} & = \tilde{\dot{e}}_{D1} \\
\frac{d}{dt}\tilde{e}_{Q1} & = \tilde{\dot{e}}_{Q1} \\
\frac{d}{dt}\tilde{\dot{e}}_{D1} & = -R_{v1}\omega_{c1}^2\tilde{i}_{D1} + \omega L_{v1}\omega_{c1}^2\tilde{i}_{Q1} - \omega_{c1}^2\tilde{e}_{D1} - 2\zeta_1\omega_{c1}\tilde{\dot{e}}_{D1} \\
\frac{d}{dt}\tilde{\dot{e}}_{Q1} & = -\omega L_{v1}\omega_{c1}^2\tilde{i}_{D1} - R_{v1}\omega_{c1}^2\tilde{i}_{Q1} - \omega_{c1}^2\tilde{e}_{Q1} - 2\zeta_1\omega_{c1}\tilde{\dot{e}}_{Q1} \\
\frac{d}{dt}\tilde{e}_{D2} & = \tilde{\dot{e}}_{D2} \\
\frac{d}{dt}\tilde{e}_{Q2} & = \tilde{\dot{e}}_{Q2} \\
\frac{d}{dt}\tilde{\dot{e}}_{D2} & = -R_{v2}\omega_{c2}^2\tilde{i}_{D2} + \omega L_{v2}\omega_{c2}^2\tilde{i}_{Q2} - \omega_{c2}^2\tilde{e}_{D2} - 2\zeta_2\omega_{c2}\tilde{\dot{e}}_{D2} \\
\frac{d}{dt}\tilde{\dot{e}}_{Q2} & = -\omega L_{v2}\omega_{c2}^2\tilde{i}_{D2} - R_{v2}\omega_{c2}^2\tilde{i}_{Q2} - \omega_{c2}^2\tilde{e}_{Q2} - 2\zeta_2\omega_{c2}\tilde{\dot{e}}_{Q2}
\end{cases}
\tag{5.16}
$$

where, f_1, f_2 and f_3 are the repeating nonlinear functions defined as:

$$
\begin{cases}
f_1 & = \frac{1}{C_f\left[(V_{fD0}+\tilde{v}_{fD})^2+(V_{fQ0}+\tilde{v}_{fQ})^2\right]} \\
f_2 & = \tilde{v}_{fD} \\
f_3 & = \tilde{v}_{fQ}
\end{cases}
\tag{5.17}
$$

5.4.2 Large-Signal stability analysis tool

As proposed in [134], Takagi-Sugeno (TS) multi-modeling is used to determine the estimated domain of attraction. TS multi-model are a useful tool for studying the stability of nonlinear system. In this method, a set of r linear local models are deduced from the nonlinear system and are interconnected by nonlinear scalar activation functions μ_i verifying the property of convex sums. To obtain a TS model for the nonlinear system, a general form can be written as

$$
\begin{cases}
\dot{x}(t) = & \sum_{i=1}^{r}\mu_i[A_ix(t) + B_iu(t)] \\
y(t) = & \sum_{i=1}^{r}\mu_iC_ix(t)
\end{cases}
\tag{5.18}
$$

The principle of modeling the system in TS form is to consider a nonlinear model as a weighted sum of r linear models. In this way, it is possible to transpose a nonlinear problem into a sum of linear problems. The weighting of the sub-modules is done via the activation functions μ_i which are function of the state of the system. These activation functions must respect the convex sum property (5.19).

$$\begin{cases} \sum_{i=1}^{r} \mu_i(x(t)) & = 1 \\ \mu_i(x(t)) & \geqslant 0, \forall t \end{cases} \tag{5.19}$$

This method uses "$if-then$" rules that represent the input-output linear local relations of the nonlinear system. Thus, the ith fuzzy rule defines a local linear behavior by a linear model of the type $\dot{x}(t) = A_i.x(t)+B_i.u(t)$. It is possible to obtain a TS model representing exactly the nonlinear system using a limited number of local models. Each nonlinearity $(f_j(x),\ j = 1,\ 2, \cdots,\ r)$ may admit two values: its minimum value f_{jmin} and its maximum value f_{jmax}. This gives rise for two matrices A_i. Thus, for r nonlinearities in the system, 2^r matrices should be formed. In order to use Lyapunov method for the TS model, Marx *et al.* state that the system is asymptotically stable if the following $(r+1)$ Linear Matrix Inequalities (LMI) hold [134]:

$$\begin{cases} M = M^T & > 0 \\ A_i^T \cdot M + M \cdot A_i & < 0,\ \forall i \in \{1,\ 2,\ \cdots\ 2^r\} \end{cases} \tag{5.20}$$

The existence of M depends on two conditions: the first one is that any matrix A_i is Hurwitz and the second condition considers the convex sum property described earlier. Thus, it is necessary (but not sufficient) that the local models are stable. Now, the asymptotic stability is proved if the LMI (5.20) is feasible. Once the matrix M is determined, the following Lyapunov function is completely known:

$$V(x) = x^T \cdot M \cdot x \tag{5.21}$$

The LMI algorithm is studied by fixing each r nonlinearity to a constant limit value (min. and max. value). These limits are obtained once the LMI is not yet feasible. In this case, the estimated domain of attraction is bordered by x_{jmin} and x_{jmax}, $j = 1,\ 2,\ \cdots r$. In fact, we need only the knowledge of the local state matrices A_i that can be directly obtained from the nonlinear model by fixing each of r nonlinearities to a constant limit value (min or max value). These limit values determine a domain in which the stability analysis is valid. In other words, the estimation of the domain of attraction of the operating point is deduced from the domain delimited by the aforementioned limit values. Therefore, for estimating the domain of attraction, the following algorithm can be proposed:

1. Set all nonlinearities to their operating point values: $f_{jmin} = f_{jmax} = f_j(0)$, $j = 1, 2, \cdots, r$ $(x^j_{min} = x^j_{max} = 0)$.

2. If the LMI problem (5.20) is not feasible, then go to 4.

3. Else, decrease f_{jmin} and increase f_{jmax} by modifying x^j_{min} and x^j_{max}, $j = 1, 2, \cdots, r$. Then go to 2.

4. The estimated domain of attraction is bordered by x^j_{min} and x^j_{max}, $j = 1, 2, \cdots, r$.

It is obvious that such estimation is conservative because of the nature of this approach based on the second method of Lyapunov. However, the main drawback of this method lies in the fact that the complexity of the problem grows rapidly with the number of nonlinearities. Indeed, 2^r matrices should be processed if there are r nonlinearities.

5.4.3 Application of the Large-Signal stability analysis and Simulation Results

For the system described in (5.16), the nonlinearities are given as f_1, f_2 and f_3. Thus, we have $r = 3$. And suppose that $\tilde{v}_{fD}$ belongs to the interval $[\ v_{fDmin},\ \ v_{fDmax}\ ]$ and $\tilde{v}_{fQ}$ belongs to the interval $[\ v_{fQmin},\ \ v_{fQmax}\ ]$, with those intervals to be determined. Let:

$$\begin{cases} f_{1min} = \frac{1}{C_f\left[(V_{fD0}+\tilde{v}_{fDmax})^2+(V_{fQ0}+\tilde{v}_{fQmax})^2\right]} & , f_{1max} = \frac{1}{C_f\left[(V_{fD0}+\tilde{v}_{fDmin})^2+(V_{fQ0}+\tilde{v}_{fQmin})^2\right]} \\ f_{2min} = \tilde{v}_{fDmin} & , f_{2max} = \tilde{v}_{fDmax} \\ f_{3min} = \tilde{v}_{fQmin} & , f_{3max} = \tilde{v}_{fQmax} \end{cases} \tag{5.22}$$

As $r = 3$, there exist 8 local models and 8 fuzzy rules. The TS fuzzy models are developed based on the following rules:

- Rule 1: if $f_1 = f_{1min}$, $f_2 = f_{2min}$ and $f_3 = f_{3min}$, then the model is written as: $\dot{x} = A_1 \cdot x$.
- Rule 2: if $f_1 = f_{1min}$, $f_2 = f_{2min}$ and $f_3 = f_{3max}$, then the model is written as: $\dot{x} = A_2 \cdot x$.
- Rule 3: if $f_1 = f_{1min}$, $f_2 = f_{2max}$ and $f_3 = f_{3min}$, then the model is written as: $\dot{x} = A_3 \cdot x$.
- Rule 4: if $f_1 = f_{1min}$, $f_2 = f_{2max}$ and $f_3 = f_{3max}$, then the model is written as: $\dot{x} = A_4 \cdot x$.
- Rule 5: if $f_1 = f_{1max}$, $f_2 = f_{2min}$ and $f_3 = f_{3min}$, then the model is written as: $\dot{x} = A_5 \cdot x$.
- Rule 6: if $f_1 = f_{1max}$, $f_2 = f_{2min}$ and $f_3 = f_{3max}$, then the model is written as: $\dot{x} = A_6 \cdot x$.
- Rule 7: if $f_1 = f_{1max}$, $f_2 = f_{2max}$ and $f_3 = f_{3min}$, then the model is written as: $\dot{x} = A_7 \cdot x$.
- Rule 8: if $f_1 = f_{1max}$, $f_2 = f_{2max}$ and $f_3 = f_{3max}$, then the model is written as: $\dot{x} = A_8 \cdot x$.

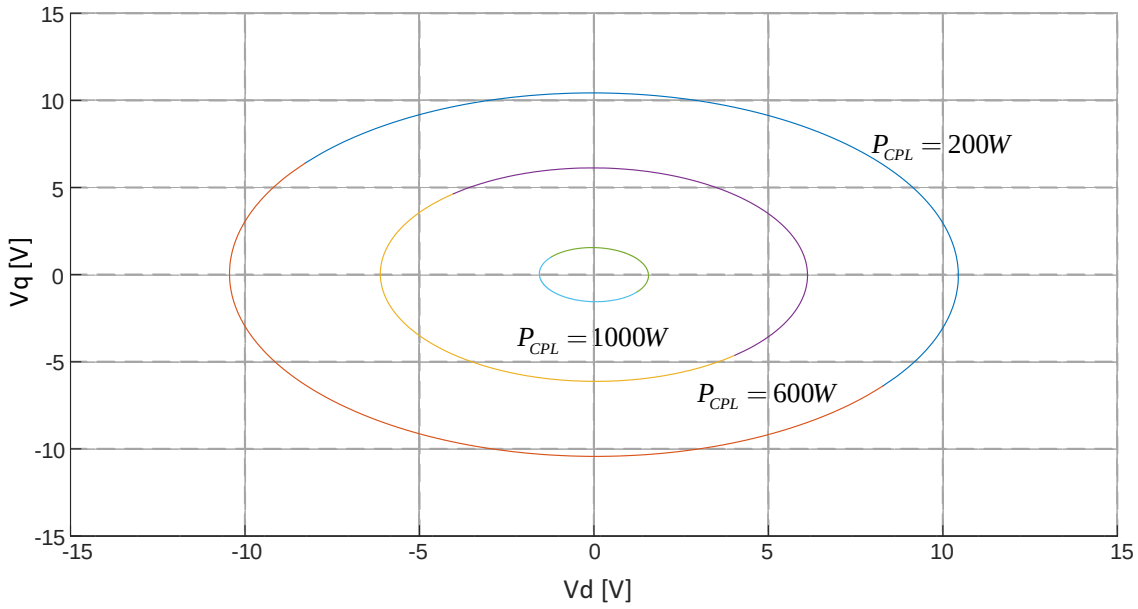

Figure 5.11: Estimated Domain of attraction for the system under the effect of CPL active power ($R_{ch} = 100\Omega$, $I_{Ld} = 0$, $I_{Lq} = -3$A).

Now, we apply the proposed algorithm in Section 5.4.2 to the 8 local models with the following LMI:

$$\begin{cases} M = M^T & > 0 \\ A_1^T \cdot M + M \cdot A_1 & < 0 \\ A_2^T \cdot M + M \cdot A_2 & < 0 \\ A_3^T \cdot M + M \cdot A_3 & < 0 \\ A_4^T \cdot M + M \cdot A_4 & < 0 \\ A_5^T \cdot M + M \cdot A_5 & < 0 \\ A_6^T \cdot M + M \cdot A_6 & < 0 \\ A_7^T \cdot M + M \cdot A_7 & < 0 \\ A_8^T \cdot M + M \cdot A_8 & < 0 \end{cases} \tag{5.23}$$

A MATLAB simulation is implemented to solve LMI for the nonlinear model represented in (5.23) using the explained algorithm. The system parameters used in simulation are given in Table 5.1. Following the algorithm, the min. and max. values of $\tilde{v}_{fD}$ and $\tilde{v}_{fQ}$ were obtained, and the estimated domain of attraction is plotted in the $x_5 - x_6$ plane (i.e. $v_{PCCD} - v_{PCCQ}$ plane). The effect of CPL load in the domain of attraction is first studied. Fig. 5.11 shows the estimated domain of attraction for three values of CPL active power. In this case, the resistive load is fixed to 100Ω and the constant current load is given as $I_{LD} = 0$, $I_{LQ} = -3A$. It can be noticed that, as the power of the CPL increases the domain of attraction become narrower. This interprets the destabilizing effect of the CPL on ac-MG when connected to some intensive active loads.

The effect of the Resistive load when connected to a microgrid is explored in Fig. 5.12. It is evident that the more resistive load in a microgrid, the less damping factor obtained and the more stable is the system. When we increase the consumed resistive power, the estimated domain of attraction become wider for a specific CPL load. Indeed, a parallel resistive load plays an important role in damping the oscillation resulted from a CPL load on ac-MG. For constant current load, the increase in direct current I_{Ld} will increase the size of the domain of attraction as seen in Fig. 5.13. This behavior is similar to adding more resistive load to the microgrid.

As a speculation, one can say that a virtual resistive impedance is a solution. But, its effect on high-frequency range is bound to inverter voltage controller. Furthermore, adding a virtual impedance to the output of the DG in series with the feeder impedance will have a destabilizing effect on the MG-system. To illustrate this, we did a test with inverters having a bandwidth equal 5000 rad/sec which is less than the oscillating frequency generated by the input filter of the CPL which is around 8×10^3 rad/sec. Fig. 5.14 shows a case study, where the domain of attraction region is plotted for three values of R_v which is the virtual resistance introduced in the two inverters inner controller. It can be seen that the domain of attraction decreases as the virtual resistance increases. Thus, the virtual resistive component has a negative effect on the stability of the microgrid with intensive use of CPL load. Similarly, the effect of virtual inductive impedance is realized. It should be noted that, the virtual inductance is usually used in microgrid application to enhance the reactive power sharing. For that reason, its effect on the stability of microgrid should be elaborated. In Fig. 5.15 the domain of attraction region is plotted for different values of virtual inductive impedance. As the value of L_v increases, the estimated domain of attraction decreases. Exceeding a value of $L_v = 1.6mH$ will allow the system to lose stability.

To verify the validity of the large-signal stability analysis, a small test was performed using the model presented in (5.16). The MATLAB model for the microgrid system is simulated based on parameters listed in Table 5.1. The CPL load varies its power consumption from 200W to 1000W. Referring to the estimated domain of attraction in Fig. 5.11, that corresponds to this case, the system remains stable. To prove this, Fig. 5.16 shows the PCC voltage waveform under a step change of CPL load power consumption. The results in Fig. 5.16 is compatible with the estimated domain of attraction. If the active power of the CPL is changed to 1150W the system will lose stability and the PCC voltage waveform will diverge. Fig. 5.17 shows the simulation result for $P_{CPL} = 1150$W which explains our estimated domain of attraction has been verified. For the effect of virtual impedance loop, the modeled system is tested without adding virtual resistance and with an additional value $R_v = 5\Omega$. According to the estimated domain of attraction, the system will lose stability when this value is added to the inverters inner controller. To verify this fact, Fig. 5.18 shows the evolution of the PCC *dq* voltages under the two situations. We have seen that the voltage waveforms diverge and tend to oscillate when introducing the virtual resistance to the inverters. The virtual inductive impedance is also introduced in the inverter inner controller to verify its impact on system stability. Fig. 5.19 indicates the behavior of PCC voltage when increasing the virtual inductance beyond its limit as predicted by the domain of attraction given in Fig. 5.15. It can be seen

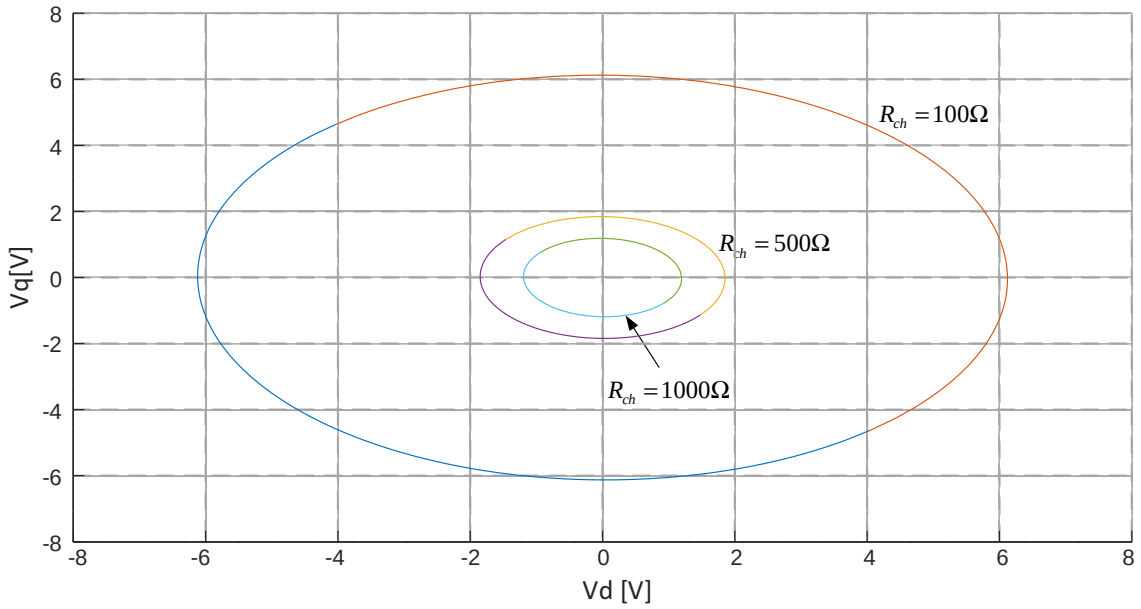

Figure 5.12: Estimated Domain of attraction for the system under the effect of Resistive Load, R_{ch} (P_c(CPL) = 600W, $I_{Ld} = 0$, $I_{Lq} = -3$A).

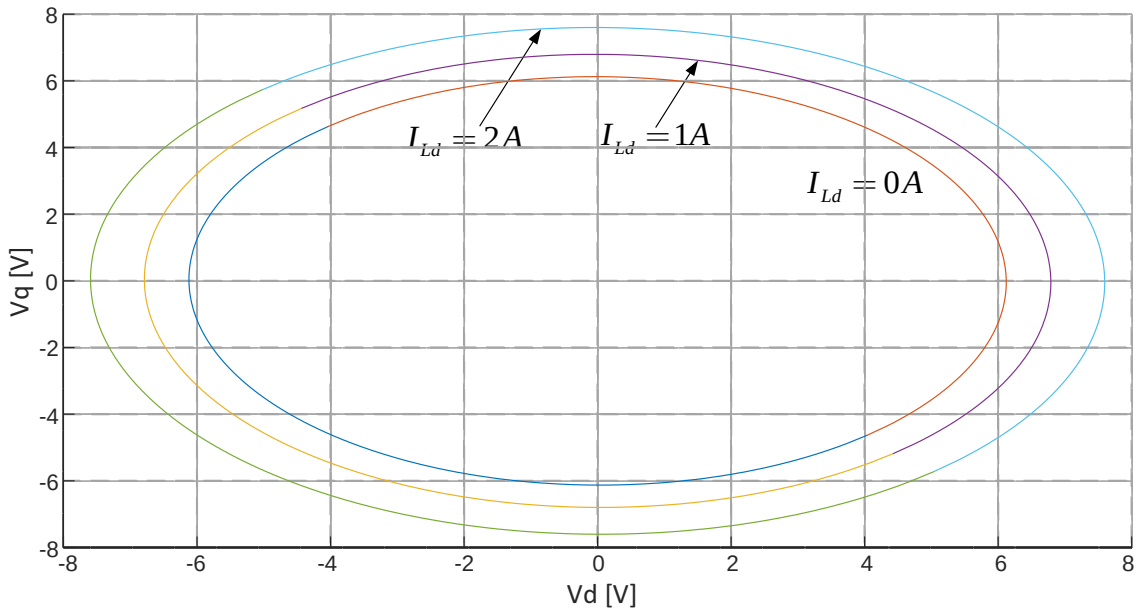

Figure 5.13: Estimated Domain of attraction for the system under the effect of constant current load (P_c(CPL) = 600W, $R_{ch} = 100\Omega$).

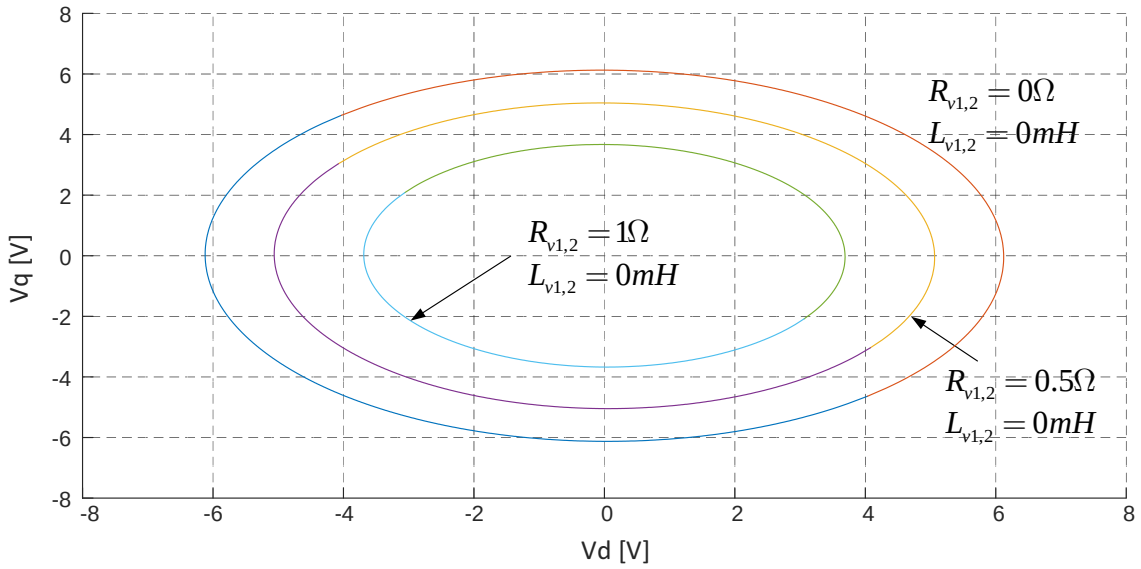

Figure 5.14: Effect of virtual resistance R_v on the estimated domain of asymptotic stability when the bandwidth of inverters controller ($\omega_c = 5000$ rad/sec) is lower than the cutoff frequency of the CPL input filter ($\omega_f = 8000$ rad/sec). Load condition: P_c(CPL) = 600W, $I_{Ld} = 0$, $I_{Lq} = -3$A, $R_{ch} = 100\Omega$.

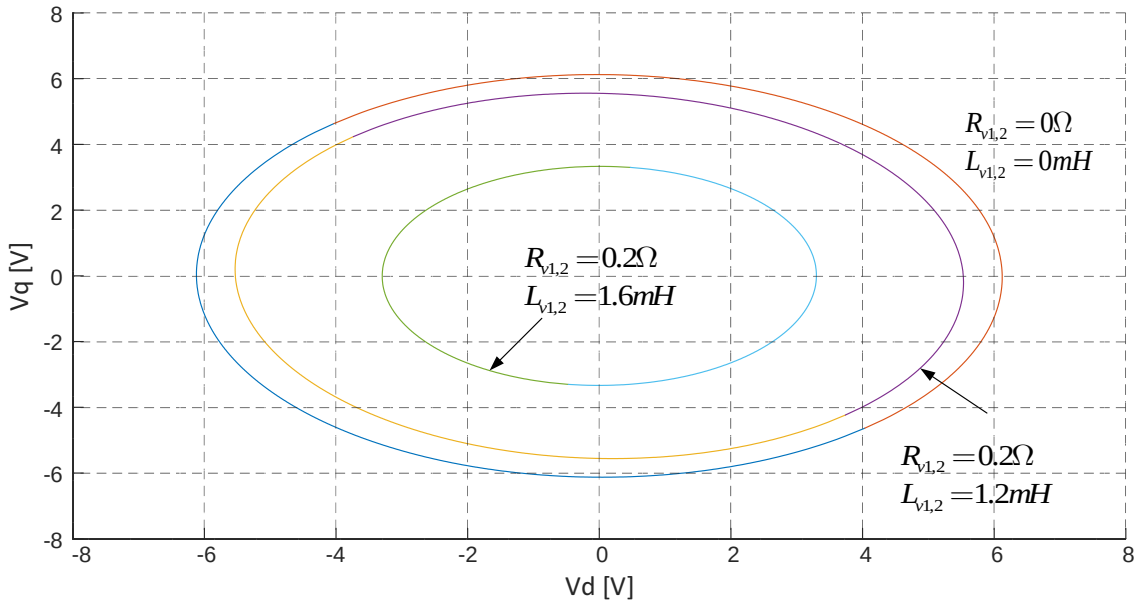

Figure 5.15: Effect of virtual resistance L_v on the estimated domain of asymptotic stability when the bandwidth of inverters controller ($\omega_c = 5000$ rad/sec) is lower than the cutoff frequency of the CPL input filter ($\omega_f = 8000$ rad/sec). Load condition: P_c(CPL) = 600W, $I_{Ld} = 0$, $I_{Lq} = -3$A, $R_{ch} = 100\Omega$.

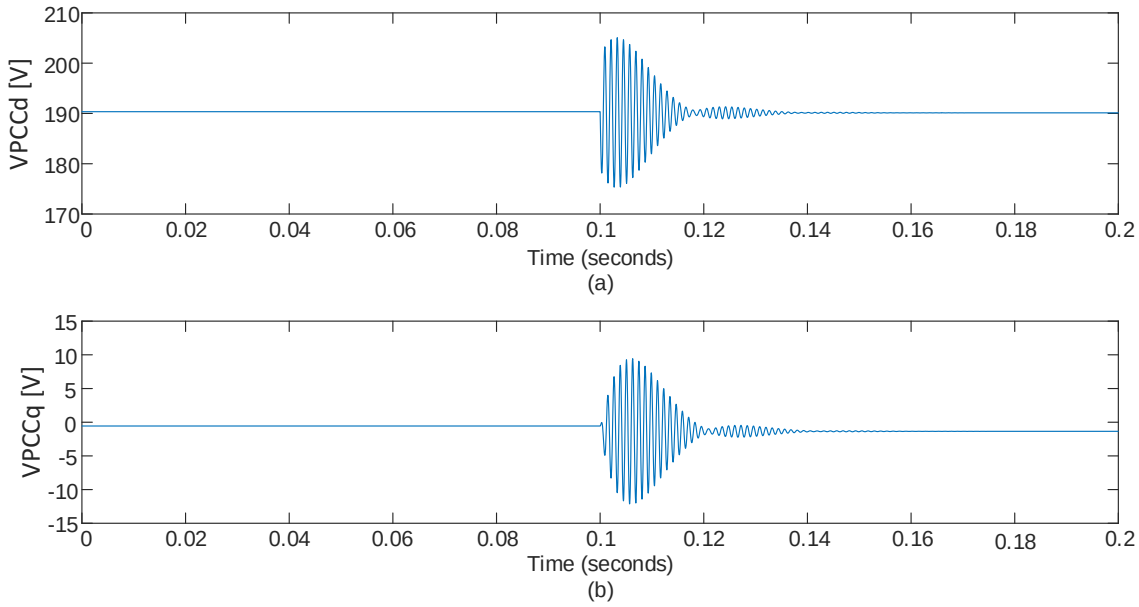

Figure 5.16: PCC *dq* voltage waveform evolution inside the predicted domain of attraction for CPL load change: $P_{CPL} = 200 - 1000W$.

that also the PCC voltage diverges when $L_v = 2.2mH$ and the system become unstable. The large-signal analysis allows us to formulate the overall conclusion given in the next section.

5.5 Conclusion for Large-Signal analysis

The large signal stability for ac microgrid was explored. The study focused on the effect of load interaction with the ac-MG. The effect of CPL load on the estimated domain of attraction was realized. It was shown also that excessive resistive load can play an important role in insuring asymptotic stability of the system. However, one of the characteristics of an islanded microgrid is the load shedding where different loads, predominantly the resistive loads, are disconnected from the grid to ensure balanced generation-consumption. Thus, this scenario should be taken into consideration when subjected to ac microgrid with CPL load being connected. Load shedding must not affect system stability. The effect of constant current load in system stability is also explored. It was shown that excess direct current will damp oscillations in microgrid and preserves stable system. Furthermore, the effect of virtual impedance loop in system stability is pointed out. It should be noted that, the virtual impedance loop is commonly used to compensate reactive power sharing for droop control based-microgrids. The aforementioned results, show that the virtual impedance loop has a negative impact on system stability and additional impedance loop tends to destabilize the system especially when supplying a CPL load. These results are verified by simulating the effect of adding additional resistive and inductive terms at the output of inverters on the evolution of the PCC voltage. Thus, the strategy of adding

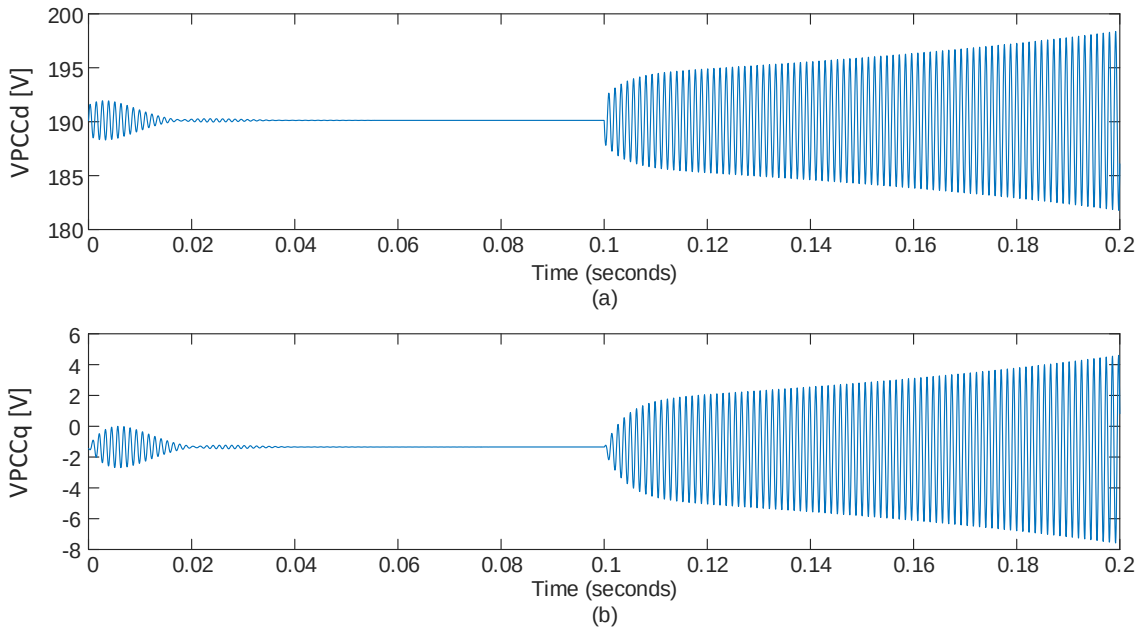

Figure 5.17: PCC *dq* voltage waveforms evolution outside the predicted domain of attraction for CPL load change: $P_{CPL} = 1000 - 1150W$.

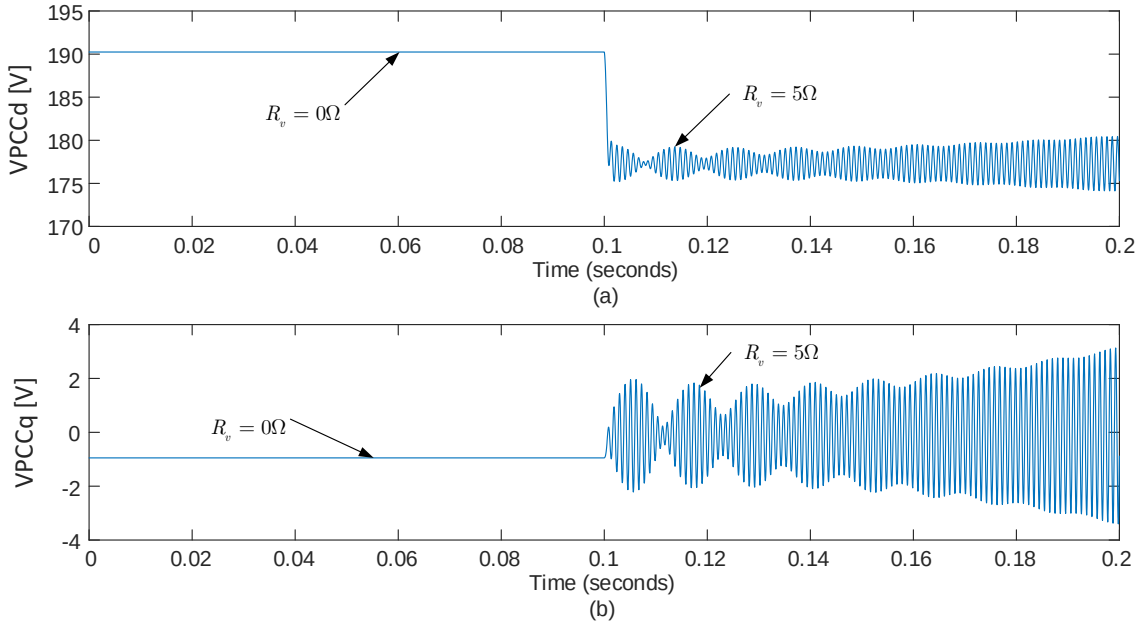

Figure 5.18: PCC *dq* voltage waveforms evolution inside/outside the predicted domain of attraction for virtual resistance: $R_v = 0 - 5\Omega$.

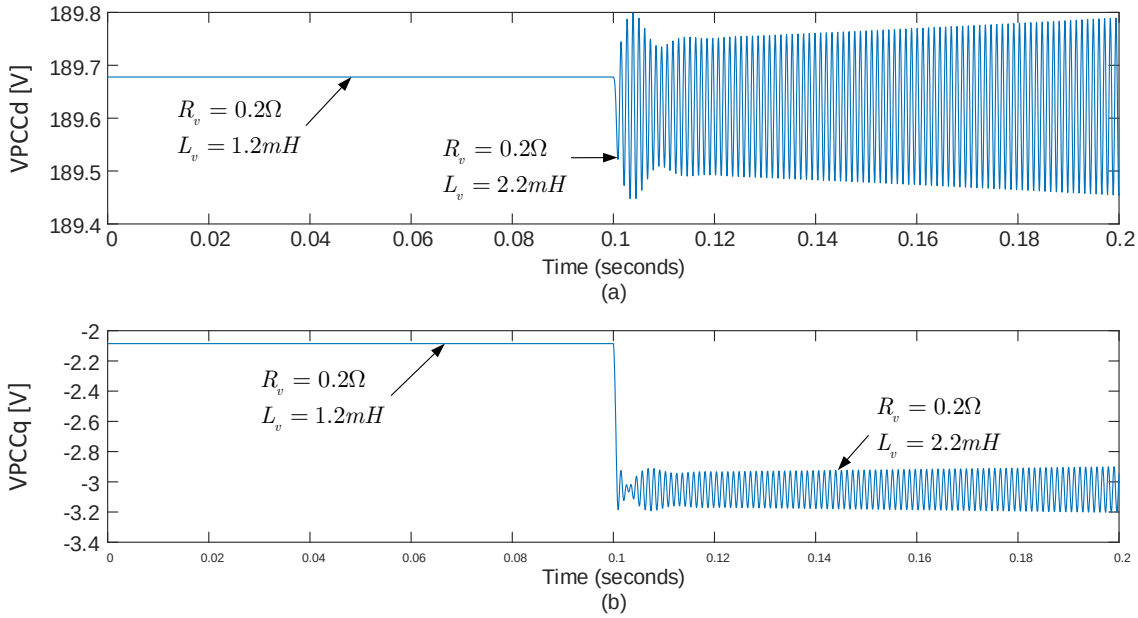

Figure 5.19: PCC *dq* voltage waveforms evolution inside/outside the predicted domain of attraction for virtual resistance: $L_v = 1.2 - 2.2mH$.

virtual impedance loop should be studied carefully before introducing it to the system. One opinion that should be verified in the future, is the use of parallel virtual resistive impedance. In this case, the virtual impedance loop could damp oscillations result from different load interactions. The load interaction using the CPL active power is simulated in order to verify the results of the estimated domain of attraction. The PCC voltage waveform is compatible with the large-signal stability analysis.

General Conclusion and Perspectives

This thesis focuses on the decentralized control strategies for AC islanded Microgrids, especially on the Droop Control in order to enhance system reliability, power sharing and system stability. The main objectives is to solve problems and find improvements related to the control and power management for distributed generation (DG) systems. The thesis starts with reviewing various droop methods proposed recently to improve different drawbacks related to the aforementioned aspects. The first chapter summarizes the most important control approaches and are compared in terms of their respective advantages and disadvantages.

Secondly in chapter 2, the Flatness-based control for converters is developed. Modeling, analysis and implementation of the controller are done for DC/AC inverter with LC filter which is applicable to what so called Distributed Generation Interfaced Converter (DIC). Furthermore, the Flatness-based controller is applied to the case of modular inverter design (i.e. parallel connected inverters). A flood analysis was presented to model the system and the test results are derived to verify the effectiveness of the flatness-based controller on maintaining a regulated ac-voltages at the output of the module with minimized circulating currents between parallel inverters. The next part of chapter 2 deals with the proposed state-observer used in microgrid application which is considered to be a prospect tool for enhancing the power sharing between droop-based converters. The state estimation of the point of power coupling (PCC) rms-voltage can be utilized to retrieve the drop voltages across the mismatched feeder lines that are mainly affecting the reactive power sharing. In this way, the proposed $Q - V$Est is more efficient for accurate load sharing. The performance of such droop control is validated experimentally where its advantages over other proposals are presented.

Next, the power quality issues in distributed generation are studied when linear and nonlinear loads are connected to the microgrid. It was shown that the proposed harmonic droop controller has superior behavior in sharing the harmonic power between distributed generators and compensating the harmonic distortion at the PCC. At the same time, the fundamental active and reactive powers are shared proportional to the ratings of each DG. Thus, the two droop controllers work separately to enhance system reliability. A microgrid decomposed of two or three inverters was implemented using simulation to verify the operation and validity of the proposed control technique. Furthermore, Experimental results are given to support the effectiveness of this method.

In chapter 4, an optimal angle droop control was proposed to share active and reactive powers between DGs without affecting system frequency which remains constant in this case. Modeling and small-signal stability analysis are performed for a generalized

microgrid system based on the proposed angle droop, in order to specify the range of design parameters that ensure proper load sharing with system stability being maintained. Perfect results were obtained with this method, where a one-loop design of the proposed angle droop control is found to have better results as compared with Hierarchical droop control with multiple loops for the same objectives.

Finally, chapter 5 discussed the stability analysis of AC islanded microgrid with high penetration of Interfaced converter loads. The effect of intensive use of converter loads (such as a constant power load, CPL) on system stability are analyzed using small-signal stability tool. And according to sensitivity analysis, it was found that whatever the load interacted with the grid, the eigenvalues that corresponds to droop control are with lower sensitivity factor. Which means that the droop control is not affected by the change of load and an assumption can be considered by neglecting the droop control model from large-signal stability analysis in order to decrease the number of nonlinearities and simplify system equations. The large-signal analysis shows that excessive resistive load can guarantee a stable system in case of a CPL load also connected. Furthermore, it was shown that the virtual impedance loop can not be considered as an effective tool to stabilize the system due to the limitation of inverter inner control bandwidth design. Simulation results are provided to demonstrate the aforementioned interpretation.

The aforementioned conclusions in this thesis lead to several proposals for future research work to be developed at present, at both a scientific and technical level development of projects as:

- DC coupling microgrids: This line of research will expose new challenge of modeling and practical work when the interaction between AC and DC microgrids (Hybrid microgrids) is studied. This will open new fields for renewable energy power-management control strategies. New scenarios for Distributed Generation systems, reliability and flexibility operation as well as power quality enhancement.

- Based on the proposed Harmonic droop control developed in chapter 3, The effect of imbalance loads should be adopted with a strategy to study their issues and attenuate their transient's variations in islanded microgrid.

- The proposed angle droop control scheme can be modified by emulating the state-observe to estimate the PCC voltage amplitude and angle in order to perform an improved control strategy when communication is lost or can't be used in some applications.

- The stability analysis for ac microgrid in chapter 5 gives some important aspects for future work to design a stabilization method for the system. The stabilization method should be based on the Lyapunov theory. It would be interesting and useful to realize the network configurations for testing the stabilization method which could be well suited for industrial applications.

- Due to inherently distributed and heterogeneous nature of microgrid, it becomes an ideal platform for applications of consensus algorithms. Several attempts have been made to utilize consensus-based control algorithms for smart grid applications,

including 1) voltage support on distribution feeders; 2) smart economic dispatch; 3) smart load shedding; 4) inverter-based power sharing, etc.

List of Publications

Journal Publications

1. Ahmed Shahin; **Hassan Moussa**; Ivano Forrisi; Jean-Philippe Martin; Babak Nahid-Mobarakeh; Serge Pierfederici, "Reliability Improvement Approach Based on Flatness Control of Parallel-Connected Inverters," IEEE Transaction on Power Electronics, vol. 32, no. 1, pages 681-692, Feb. 2016.

2. **Hassan Moussa**; Ahmed Shahin; Jean-Philippe Martin; Serge Pierfederici; Nazih Moubayed, "Optimal Angle Droop for Power Sharing Enhancement with Stability Improvement in Islanded Microgrids," IEEE Transaction on Smart Grid, vol. PP, no. 99, pages 1-12, early access article, 2017.

3. **Hassan Moussa**; Ahmed Shahin; Jean-Philippe Martin; Babak Nahid-Mobarakeh; Serge Pierfederici; Nazih Moubayed, "Harmonic Power Sharing with Voltage Distortion Compensation of Droop controlled Islanded microgrids," IEEE Transaction on Smart Grid, vol. PP, no. 99, pages 1-12, early access article, 2017.

Conference Publications

1. A. Shahin, **H. Moussa**, H. Renaudineau, A. Houari, J.-P. Martin, B. Nahid-Mobarakeh, S. Pierfederici and A. M. Sharaf, "Optimal Efficiency Optimization through Power-Sharing for Paralleled DC-AC Inverters with Parameters Estimator," in the 11th international conference on Modeling and Simulation of Electric Machines, Converters and Systems (ELECTRIMACS 2014)-Valencia, Spain.

2. **H. Moussa**, A. Shahin, F. Sharif, J.-P. Martin, S. Pierfederici and N. Moubayed, "Optimal Angle Droop Power Sharing Control for Autonomous Microgrid," in the 7th Annual IEEE Energy Conversion Congress and Exposition (ECCE 2015)-Montreal, Canada.

3. A. Shahin, S. Eskander, **H. Moussa**, J. -P. Martin, B. Nahid-Mobarakeh; S. Pierfederici, "A New Approach based on Flatness Control to improve reliability of parallel connected inverters," in the 7th Annual IEEE Energy Conversion Congress and Exposition (ECCE 2015)-Montreal, Canada.

4. **H. Moussa**, J.-P. Martin, S. Pierfederici and N. Moubayed, "Power Sharing Enhancement for Islanded Microgrid Based on State estimation of PCC rms-Voltage,"

in the 42nd Annual Conference of IEEE Industrial Electronics Society (IECON 2016)-Florence, Italy.

5. **H. Moussa**, J.-P. Martin, S. Pierfederici and N. Moubayed, "Different Virtual Impedance Loops for Power Sharing Enhancement in Islanded Microgrid," in the 3rd International Conference on Electrical and Electronic Engineering, Telecommunication Engineering and Mechatronics (EEETEM2017)-Beirut, Lebanon.

6. **H. Moussa**, J.-P. Martin, S. Pierfederici, Farid Meibody-Tabar and N. Moubayed, "Voltage Harmonic Distortion Compensation with non-Linear Load Sharing of Droop Controlled Islanded Microgrids," in the 12th international conference on Modeling and Simulation of Electric Machines, Converters and Systems (ELECTRIMACS 2017)-Toulouse, France.

Bibliography

[1] A. Houari, "Contribution à l'étude de micro-réseaux autonomes alimentés par des sources photovoltaïques," Ph.D. dissertation, Université de Lorraine, 2012.

[2] "IEEE standard for synchrophasor measurements for power systems – amendment 1: Modification of selected performance requirements," *IEEE Std C37.118.1a-2014 (Amendment to IEEE Std C37.118.1-2011)*, pp. 1–25, Apr. 2014.

[3] P. C. Loh, M. J. Newman, D. N. Zmood, and D. G. Holmes, "A comparative analysis of multiloop voltage regulation strategies for single and three-phase ups systems," *Power Electronics, IEEE Transactions on*, vol. 18, no. 5, pp. 1176–1185, 2003.

[4] N. Pogaku, M. Prodanović, and T. C. Green, "Modeling, analysis and testing of autonomous operation of an inverter-based microgrid," *Power Electronics, IEEE Transactions on*, vol. 22, no. 2, pp. 613–625, 2007.

[5] M. Prodanović and T. C. Green, "Control and filter design of three-phase inverters for high power quality grid connection," *Power Electronics, IEEE Transactions on*, vol. 18, no. 1, pp. 373–380, 2003.

[6] E. Twining and D. G. Holmes, "Grid current regulation of a three-phase voltage source inverter with an lcl input filter," *Power Electronics, IEEE Transactions on*, vol. 18, no. 3, pp. 888–895, 2003.

[7] J.-I. Jang and D.-C. Lee, "High performance control of three-phase pwm converters under nonideal source voltage," in *Industrial Technology, 2006. ICIT 2006. IEEE International Conference on*. IEEE, 2006, pp. 2791–2796.

[8] L. Li and K. M. Smedley, "A new analog controller for three-phase four-wire voltage generation inverters," *Power Electronics, IEEE Transactions on*, vol. 24, no. 7, pp. 1711–1721, 2009.

[9] T. Liu, X. Hao, X. Yang, J. Liu, B. Zhang, and L. Huang, "A novel current dual-loop control strategy for three-phase grid-connected vsi with lcl filter," in *Power Electronics and Motion Control Conference (IPEMC), 2012 7th International*, vol. 1. IEEE, 2012, pp. 626–630.

[10] H. Renaudineau, "Hybrid renewable energy sourced system: Energy management & self-diagnosis," Ph.D. dissertation, Université de Lorraine, 2013.

[11] A. E. M. Shahin, "Contribution à l'optimisation des structures de conversion dc/dc non isolées," Ph.D. dissertation, PhD thesis, Institut National Polytechnique de Lorraine, 2011.

[12] M. Fliess, J. Lévine, P. Martin, and P. Rouchon, "Flatness and defect of non-linear systems: introductory theory and examples," *International journal of control*, vol. 61, no. 6, pp. 1327–1361, 1995.

[13] P. Martin, R. M. Murray, and P. Rouchon, "Flat systems, equivalence and trajectory generation," 2003.

[14] M. J. Van Nieuwstadt and R. M. Murray, "Real time trajectory generation for differentially flat systems," 1997.

[15] F. Rotella and I. Zambettakis, "Commande des systèmes par platitude," *Techniques de l'ingénieur S*, vol. 7450, p. 2007, 2007.

[16] M. C. Chandorkar, D. M. Divan, and R. Adapa, "Control of parallel connected inverters in standalone ac supply systems," *Industry Applications, IEEE Transactions on*, vol. 29, no. 1, pp. 136–143, 1993.

[17] M. Chandrokar, D. Divan, and B. Banerjee, "Control of distributed ups systems," in *Power Electronics Specialists Conference, PESC'94 Record., 25th Annual IEEE*. IEEE, 1994, pp. 197–204.

[18] P. Piagi and R. H. Lasseter, "Autonomous control of microgrids," in *Power Engineering Society General Meeting, 2006. IEEE*. IEEE, 2006, pp. 8–pp.

[19] M. N. Marwali and A. Keyhani, "Control of distributed generation systems-part i: Voltages and currents control," *Power Electronics, IEEE Transactions on*, vol. 19, no. 6, pp. 1541–1550, 2004.

[20] K. De Brabandere, B. Bolsens, J. Van den Keybus, A. Woyte, J. Driesen, and R. Belmans, "A voltage and frequency droop control method for parallel inverters," *Power Electronics, IEEE Transactions on*, vol. 22, no. 4, pp. 1107–1115, 2007.

[21] J. M. Guerrero, J. Matas, D. Vicuna, L. García, M. Castilla, and J. Miret, "Wireless-control strategy for parallel operation of distributed-generation inverters," *Industrial Electronics, IEEE Transactions on*, vol. 53, no. 5, pp. 1461–1470, 2006.

[22] J. M. Guerrero, L. Hang, and J. Uceda, "Control of distributed uninterruptible power supply systems," *Industrial Electronics, IEEE Transactions on*, vol. 55, no. 8, pp. 2845–2859, 2008.

[23] J. M. Guerrero, J. Matas, L. G. de Vicuna, M. Castilla, and J. Miret, "Decentralized control for parallel operation of distributed generation inverters using resistive output impedance," *IEEE Transactions on Industrial Electronics*, vol. 54, no. 2, pp. 994–1004, Apr. 2007.

[24] X. Yu, A. M. Khambadkone, H. Wang, and S. T. S. Terence, "Control of parallel-connected power converters for low-voltage microgrid —part i: A hybrid control architecture," *IEEE Transactions on Power Electronics*, vol. 25, no. 12, pp. 2962–2970, Dec. 2010.

[25] C. K. Sao and P. W. Lehn, "Control and power management of converter fed microgrids," *Power Systems, IEEE Transactions on*, vol. 23, no. 3, pp. 1088–1098, 2008.

[26] W. Yao, M. Chen, J. Matas, J. M. Guerrero, and Z.-M. Qian, "Design and analysis of the droop control method for parallel inverters considering the impact of the complex impedance on the power sharing," *Industrial Electronics, IEEE Transactions on*, vol. 58, no. 2, pp. 576–588, 2011.

[27] R. Majumder, A. Ghosh, G. Ledwich, and F. Zare, "Stability analysis and control of multiple converter based autonomous microgrid," in *Control and Automation, 2009. ICCA 2009. IEEE International Conference on*. IEEE, 2009, pp. 1663–1668.

[28] R. Majumder, G. Ledwich, A. Ghosh, S. Chakrabarti, and F. Zare, "Droop control of converter-interfaced microsources in rural distributed generation," *Power Delivery, IEEE Transactions on*, vol. 25, no. 4, pp. 2768–2778, 2010.

[29] R. Majumder, B. Chaudhuri, A. Ghosh, R. Majumder, G. Ledwich, and F. Zare, "Improvement of stability and load sharing in an autonomous microgrid using supplementary droop control loop," *Power Systems, IEEE Transactions on*, vol. 25, no. 2, pp. 796–808, 2010.

[30] J. Kim, J. M. Guerrero, P. Rodriguez, R. Teodorescu, and K. Nam, "Mode adaptive droop control with virtual output impedances for an inverter-based flexible ac microgrid," *Power Electronics, IEEE Transactions on*, vol. 26, no. 3, pp. 689–701, 2011.

[31] J. M. Guerrero, D. Vicuña, L. García, J. Matas, M. Castilla, and J. Miret, "Output impedance design of parallel-connected ups inverters with wireless load-sharing control," *Industrial Electronics, IEEE Transactions on*, vol. 52, no. 4, pp. 1126–1135, 2005.

[32] J. M. Guerrero, N. Berbel, J. Matas, J. L. Sosa, D. Vicuña, and L. García, "Droop control method with virtual output impedance for parallel operation of uninterruptible power supply systems in a microgrid," in *Applied Power Electronics Conference, APEC 2007-Twenty Second Annual IEEE*. IEEE, 2007, pp. 1126–1132.

[33] S. Golestan, F. Adabi, H. Rastegar, and A. Roshan, "Load sharing between parallel inverters using effective design of output impedance," in *Power Engineering Conference, 2008. AUPEC'08. Australasian Universities*. IEEE, 2008, pp. 1–5.

[34] J. He and Y. W. Li, "Analysis, design, and implementation of virtual impedance for power electronics interfaced distributed generation," *Industry Applications, IEEE Transactions on*, vol. 47, no. 6, pp. 2525–2538, 2011.

[35] J. He, Y. W. Li, J. M. Guerrero, J. C. Vasquez, and F. Blaabjerg, "An islanding microgrid reactive power sharing scheme enhanced by programmed virtual impedances," in *Power Electronics for Distributed Generation Systems (PEDG), 2012 3rd IEEE International Symposium on*. IEEE, 2012, pp. 229–235.

[36] J. He, Y. W. Li, and F. Blaabjerg, "An enhanced islanding microgrid reactive power, imbalance power, and harmonic power sharing scheme," *Power Electronics, IEEE Transactions on*, vol. 30, no. 6, pp. 3389–3401, 2015.

[37] J. He, Y. W. Li, J. M. Guerrero, F. Blaabjerg, and J. C. Vasquez, "An islanding microgrid power sharing approach using enhanced virtual impedance control scheme," *Power Electronics, IEEE Transactions on*, vol. 28, no. 11, pp. 5272–5282, 2013.

[38] C.-T. Lee, C.-C. Chuang, C.-C. Chu, and P.-T. Cheng, "Control strategies for distributed energy resources interface converters in the low voltage microgrid," in *Energy Conversion Congress and Exposition, 2009. ECCE 2009. IEEE*. IEEE, 2009, pp. 2022–2029.

[39] Y. Li and Y. W. Li, "Virtual frequency-voltage frame control of inverter based low voltage microgrid," in *Electrical Power & Energy Conference (EPEC), 2009 IEEE*. IEEE, 2009, pp. 1–6.

[40] ——, "Power management of inverter interfaced autonomous microgrid based on virtual frequency-voltage frame," *Smart Grid, IEEE Transactions on*, vol. 2, no. 1, pp. 30–40, 2011.

[41] T. Wu, Z. Liu, J. Liu, S. Wang, and Z. You, "A unified virtual power decoupling method for droop controlled parallel inverters in microgrids," *Power Electronics, IEEE Transactions on*, vol. 31, no. 8, pp. 5587–5603, 2016.

[42] J. M. Guerrero, D. Vicuña, L. García, J. Matas, M. Castilla, and J. Miret, "A wireless controller to enhance dynamic performance of parallel inverters in distributed generation systems," *Power Electronics, IEEE Transactions on*, vol. 19, no. 5, pp. 1205–1213, 2004.

[43] G. Yajuan, W. Weiyang, G. Xiaoqiang, and G. Herong, "An improved droop controller for grid-connected voltage source inverter in microgrid," in *Power Electronics for Distributed Generation Systems (PEDG), 2010 2nd IEEE International Symposium on*. IEEE, 2010, pp. 823–828.

[44] Y. A.-R. I. Mohamed and E. F. El-Saadany, "Adaptive decentralized droop controller to preserve power sharing stability of paralleled inverters in distributed generation microgrids," *Power Electronics, IEEE Transactions on*, vol. 23, no. 6, pp. 2806–2816, 2008.

[45] A. Salamah, S. Finney, and B. Williams, "Autonomous controller for improved dynamic performance of ac grid, parallel-connected, single-phase inverters," *Generation, Transmission & Distribution, IET*, vol. 2, no. 2, pp. 209–218, 2008.

[46] N. Soni, S. Doolla, and M. C. Chandorkar, "Improvement of transient response in microgrids using virtual inertia," *Power Delivery, IEEE Transactions on*, vol. 28, no. 3, pp. 1830–1838, 2013.

[47] Y. W. Li and C.-N. Kao, "An accurate power control strategy for power-electronics-interfaced distributed generation units operating in a low-voltage multibus microgrid," *Power Electronics, IEEE Transactions on*, vol. 24, no. 12, pp. 2977–2988, 2009.

[48] J. C. Vasquez, J. M. Guerrero, A. Luna, P. Rodríguez, and R. Teodorescu, "Adaptive droop control applied to voltage-source inverters operating in grid-connected and islanded modes," *Industrial Electronics, IEEE Transactions on*, vol. 56, no. 10, pp. 4088–4096, 2009.

[49] E. Rokrok and M. E. H. Golshan, "Adaptive voltage droop scheme for voltage source converters in an islanded multibus microgrid," *Generation, Transmission & Distribution, IET*, vol. 4, no. 5, pp. 562–578, 2010.

[50] C. T. Lee, C. C. Chu, and P. T. Cheng, "A new droop control method for the autonomous operation of distributed energy resource interface converters," in *Proc. IEEE Energy Conversion Congress and Exposition*, Sep. 2010, pp. 702–709.

[51] C.-T. Lee, C.-C. Chu, and P.-T. Cheng, "A new droop control method for the autonomous operation of distributed energy resource interface converters," *Power Electronics, IEEE Transactions on*, vol. 28, no. 4, pp. 1980–1993, 2013.

[52] C.-T. Lee, R.-P. Jiang, and P.-T. Cheng, "A grid synchronization method for droop-controlled distributed energy resource converters," *Industry Applications, IEEE Transactions on*, vol. 49, no. 2, pp. 954–962, 2013.

[53] C. K. Sao and P. W. Lehn, "Autonomous load sharing of voltage source converters," *Power Delivery, IEEE Transactions on*, vol. 20, no. 2, pp. 1009–1016, 2005.

[54] Q.-C. Zhong, "Robust droop controller for accurate proportional load sharing among inverters operated in parallel," *Industrial Electronics, IEEE Transactions on*, vol. 60, no. 4, pp. 1281–1290, 2013.

[55] J. M. Guerrero, J. C. Vasquez, J. Matas, D. Vicuna, L. García, and M. Castilla, "Hierarchical control of droop-controlled ac and dc microgrids—a general approach toward standardization," *Industrial Electronics, IEEE Transactions on*, vol. 58, no. 1, pp. 158–172, 2011.

[56] A. Bidram and A. Davoudi, "Hierarchical structure of microgrids control system," *Smart Grid, IEEE Transactions on*, vol. 3, no. 4, pp. 1963–1976, 2012.

[57] J. M. Guerrero, M. Chandorkar, T.-L. Lee, and P. C. Loh, "Advanced control architectures for intelligent microgrids, part i: decentralized and hierarchical control," *IEEE Transactions on Industrial Electronics*, vol. 60, no. 4, pp. 1254–1262, 2013.

[58] L. Meng, F. Tang, M. Savaghebi, J. C. Vasquez, and J. M. Guerrero, "Tertiary control of voltage unbalance compensation for optimal power quality in islanded microgrids," *Energy Conversion, IEEE Transactions on*, vol. 29, no. 4, pp. 802–815, 2014.

[59] D.-E. Kim and D.-C. Lee, "Feedback linearization control of three-phase ups inverter systems," *industrial Electronics, iEEE Transactions on*, vol. 57, no. 3, pp. 963–968, 2010.

[60] H. Mahmood, D. Michaelson, and J. Jiang, "Accurate reactive power sharing in an islanded microgrid using adaptive virtual impedances," *IEEE Transactions on Power Electronics*, vol. 30, no. 3, pp. 1605–1617, Mar. 2015.

[61] Z. Shao, X. Zhang, F. Wang, and R. Cao, "Modeling and elimination of zero-sequence circulating currents in parallel three-level t-type grid-connected inverters," *IEEE Transactions on Power Electronics*, vol. 30, no. 2, pp. 1050–1063, Feb. 2015.

[62] W. Lu, K. Zhou, D. Wang, and M. Cheng, "A general parallel structure repetitive control scheme for multiphase DC –AC PWM converters," *IEEE Transactions on Power Electronics*, vol. 28, no. 8, pp. 3980–3987, Aug. 2013.

[63] B. M. H. Jassim, D. J. Atkinson, and B. Zahawi, "Modular current sharing control scheme for parallel-connected converters," *IEEE Transactions on Industrial Electronics*, vol. 62, no. 2, pp. 887–897, Feb. 2015.

[64] A. Houari, A. Battiston, J. P. Martin, S. Pierfederici, and F. Meibody-Tabar, "Flatness-based-control for parallel operation of n voltage-source inverters," in *Proc. 15th European Conf. Power Electronics and Applications (EPE)*, Sep. 2013, pp. 1–10.

[65] B. Cougo, T. Meynard, and G. Gateau, "Parallel three-phase inverters: Optimal PWM method for flux reduction in intercell transformers," *IEEE Transactions on Power Electronics*, vol. 26, no. 8, pp. 2184–2191, Aug. 2011.

[66] X. Yu and A. M. Khambadkone, "Reliability analysis and cost optimization of parallel-inverter system," *IEEE Transactions on Industrial Electronics*, vol. 59, no. 10, pp. 3881–3889, Oct. 2012.

[67] M. A. Abusara and S. M. Sharkh, "Design and control of a grid-connected interleaved inverter," *IEEE Transactions on Power Electronics*, vol. 28, no. 2, pp. 748–764, Feb. 2013.

[68] G. Perez-Ladron, V. Cardenas, and G. Espinosa, "Analysis and implementation of a master-slave control based on a passivity approach for parallel inverters operation," in *Proc. IEEE Int. Power Electronics Congress*, Oct. 2006, pp. 1–5.

[69] D. E. Kim and D. C. Lee, "Feedback linearization control of three-phase UPS inverter systems," *IEEE Transactions on Industrial Electronics*, vol. 57, no. 3, pp. 963–968, Mar. 2010.

[70] M. Borrega, L. Marroyo, R. González, J. Balda, and J. L. Agorreta, "Modeling and control of a master –slave PV inverter with n-paralleled inverters and three-phase three-limb inductors," *IEEE Transactions on Power Electronics*, vol. 28, no. 6, pp. 2842–2855, Jun. 2013.

[71] T. P. Chen, "Zero-sequence circulating current reduction method for parallel hepwm inverters between AC bus and DC bus," *IEEE Transactions on Industrial Electronics*, vol. 59, no. 1, pp. 290–300, Jan. 2012.

[72] G. Gohil, R. Maheshwari, L. Bede, T. Kerekes, R. Teodorescu, M. Liserre, and F. Blaabjerg, "Modified discontinuous PWM for size reduction of the circulating current filter in parallel interleaved converters," *IEEE Transactions on Power Electronics*, vol. 30, no. 7, pp. 3457–3470, Jul. 2015.

[73] D. J. Tschirhart and P. K. Jain, "Design procedure for high-frequency operation of the modified series-resonant apwm converter to reduce size and circulating current," *IEEE Transactions on Power Electronics*, vol. 27, no. 10, pp. 4181–4191, Oct. 2012.

[74] J. Liu, X. Qin, H. Lin, and L. Bu, "Analysis on circulating current of parallel inverter with spwm modulation for AC motor drive," in *Proc. Int. Conf. Modelling Identification and Control 2012*, Jun. 2012, pp. 1080–1086.

[75] D. Zhang, F. F. Wang, R. Burgos, and D. Boroyevich, "Common-mode circulating current control of paralleled interleaved three-phase two-level voltage-source converters with discontinuous space-vector modulation," *IEEE Transactions on Power Electronics*, vol. 26, no. 12, pp. 3925–3935, Dec. 2011.

[76] T. P. Chen, "Dual-modulator compensation technique for parallel inverters using space-vector modulation," *IEEE Transactions on Industrial Electronics*, vol. 56, no. 8, pp. 3004–3012, Aug. 2009.

[77] Y. Zhang, Y. Kang, and J. Chen, "The zero-sequence circulating currents between parallel three-phase inverters with three-pole transformers and reactors," in *Proc. APEC '06. Twenty-First Annual IEEE Applied Power Electronics Conf. and Exposition*, Mar. 2006, pp. 7 pp.–.

[78] B. Zhao, Q. Song, W. Liu, and Y. Sun, "Overview of dual-active-bridge isolated bidirectional DC –DC converter for high-frequency-link power-conversion system," *IEEE Transactions on Power Electronics*, vol. 29, no. 8, pp. 4091–4106, Aug. 2014.

[79] M. Narimani and G. Moschopoulos, "Three-phase multimodule vsis using she-PWM to reduce zero-sequence circulating current," *IEEE Transactions on Industrial Electronics*, vol. 61, no. 4, pp. 1659–1668, Apr. 2014.

[80] H. Zhang, S. Kim, Q. Sun, and J. Zhou, "Distributed adaptive virtual impedance control for accurate reactive power sharing based on consensus control in microgrids," *IEEE Transactions on Smart Grid*, vol. PP, no. 99, pp. 1–13, 2016.

[81] H. Mahmood, D. Michaelson, and J. Jiang, "Reactive power sharing in islanded microgrids using adaptive voltage droop control," *IEEE Transactions on Smart Grid*, vol. 6, no. 6, pp. 3052–3060, Nov. 2015.

[82] L.-Y. Lu and C.-C. Chu, "Consensus-based droop control synthesis for multiple dics in isolated micro-grids," *Power Systems, IEEE Transactions on*, vol. 30, no. 5, pp. 2243–2256, 2015.

[83] A. Solanki, A. Nasiri, V. Bhavaraju, Y. L. Familiant, and Q. Fu, "A new framework for microgrid management: Virtual droop control," *IEEE Transactions on Smart Grid*, vol. 7, no. 2, pp. 554–566, Mar. 2016.

[84] W.-H. Chen, "Disturbance observer based control for nonlinear systems," *Mechatronics, IEEE/ASME Transactions on*, vol. 9, no. 4, pp. 706–710, 2004.

[85] K.-S. Kim and K.-H. Rew, "Reduced order disturbance observer for discrete-time linear systems," *Automatica*, vol. 49, no. 4, pp. 968–975, 2013.

[86] H. K. Khalil, *Nonlinear Systems*. Prentice-Hall, New Jersey, 1996.

[87] C.-T. Lee, C.-C. Chu, and P.-T. Cheng, "A new droop control method for the autonomous operation of distributed energy resource interface converters," *Power Electronics, IEEE Transactions on*, vol. 28, no. 4, pp. 1980–1993, 2013.

[88] A. A. A. Radwan and Y. A. R. I. Mohamed, "Networked control and power management of AC/DC hybrid microgrids," *IEEE Systems Journal*, vol. PP, no. 99, pp. 1–12, 2014.

[89] H. Zhang, J. Zhou, Q. Sun, J. M. Guerrero, and D. Ma, "Data-driven control for interlinked AC/DC microgrids via model-free adaptive control and dual-droop control," *IEEE Transactions on Smart Grid*, vol. 8, no. 2, pp. 557–571, Mar. 2017.

[90] L. Che, M. Shahidehpour, A. Alabdulwahab, and Y. Al-Turki, "Hierarchical coordination of a community microgrid with AC and DC microgrids," *IEEE Transactions on Smart Grid*, vol. 6, no. 6, pp. 3042–3051, Nov. 2015.

[91] J. M. Guerrero, P. C. Loh, T. L. Lee, and M. Chandorkar, "Advanced control architectures for intelligent microgrids —part ii: Power quality, energy storage, and AC/DC microgrids," *IEEE Transactions on Industrial Electronics*, vol. 60, no. 4, pp. 1263–1270, Apr. 2013.

[92] D. E. Olivares, A. Mehrizi-Sani, A. H. Etemadi, C. A. Cañizares, R. Iravani, M. Kazerani, A. H. Hajimiragha, O. Gomis-Bellmunt, M. Saeedifard, R. Palma-Behnke *et al.*, "Trends in microgrid control," *IEEE Transactions on smart grid*, vol. 5, no. 4, pp. 1905–1919, 2014.

[93] H. Xin, L. Zhang, Z. Wang, D. Gan, and K. P. Wong, "Control of island AC microgrids using a fully distributed approach," *IEEE Transactions on Smart Grid*, vol. 6, no. 2, pp. 943–945, Mar. 2015.

[94] H. Han, Y. Liu, Y. Sun, M. Su, and J. M. Guerrero, "An improved droop control strategy for reactive power sharing in islanded microgrid," *IEEE Transactions on Power Electronics*, vol. 30, no. 6, pp. 3133–3141, Jun. 2015.

[95] J. He and Y. W. Li, "An enhanced microgrid load demand sharing strategy," *Power Electronics, IEEE Transactions on*, vol. 27, no. 9, pp. 3984–3995, 2012.

[96] R. I. Bojoi, L. R. Limongi, D. Roiu, and A. Tenconi, "Enhanced power quality control strategy for single-phase inverters in distributed generation systems," *IEEE Transactions on Power Electronics*, vol. 26, no. 3, pp. 798–806, Mar. 2011.

[97] R. B. Gonzatti, S. C. Ferreira, C. H. da Silva, R. R. Pereira, L. E. B. da Silva, and G. Lambert-Torres, "Smart impedance: A new way to look at hybrid filters," *IEEE Transactions on Smart Grid*, vol. 7, no. 2, pp. 837–846, Mar. 2016.

[98] M. M. Hashempour, M. Savaghebi, J. C. Vasquez, and J. M. Guerrero, "A control architecture to coordinate distributed generators and active power filters coexisting in a microgrid," *IEEE Transactions on Smart Grid*, vol. 7, no. 5, pp. 2325–2336, Sep. 2016.

[99] T. Vandoorn, B. Meersman, J. D. Kooning, and L. Vandevelde, "Controllable harmonic current sharing in islanded microgrids: Dg units with programmable resistive behavior toward harmonics," *IEEE Transactions on Power Delivery*, vol. 27, no. 2, pp. 831–841, Apr. 2012.

[100] M. Savaghebi, J. C. Vasquez, A. Jalilian, J. M. Guerrero, and T. L. Lee, "Selective harmonic virtual impedance for voltage source inverters with LCl filter in microgrids," in *Proc. IEEE Energy Conversion Congress and Exposition (ECCE)*, Sep. 2012, pp. 1960–1965.

[101] M. Savaghebi, A. Jalilian, J. C. Vasquez, and J. M. Guerrero, "Secondary control for voltage quality enhancement in microgrids," *Smart Grid, IEEE Transactions on*, vol. 3, no. 4, pp. 1893–1902, 2012.

[102] P. Sreekumar and V. Khadkikar, "A new virtual harmonic impedance scheme for harmonic power sharing in an islanded microgrid," *IEEE Transactions on Power Delivery*, vol. 31, no. 3, pp. 936–945, Jun. 2016.

[103] X. Wang, F. Blaabjerg, and Z. Chen, "Autonomous control of inverter-interfaced distributed generation units for harmonic current filtering and resonance damping in an islanded microgrid," *IEEE Transactions on Industry Applications*, vol. 50, no. 1, pp. 452–461, Jan. 2014.

[104] A. Micallef, M. Apap, C. Spiteri-Staines, and J. M. Guerrero, "Mitigation of harmonics in grid-connected and islanded microgrids via virtual admittances and impedances," *IEEE Transactions on Smart Grid*, vol. PP, no. 99, pp. 1–11, 2015.

[105] A. Micallef, M. Apap, C. Spiteri-Staines, J. M. Guerrero, and J. C. Vasquez, "Reactive power sharing and voltage harmonic distortion compensation of droop controlled single phase islanded microgrids," *IEEE Transactions on Smart Grid*, vol. 5, no. 3, pp. 1149–1158, May 2014.

[106] H. Han, X. Hou, J. Yang, J. Wu, M. Su, and J. M. Guerrero, "Review of power sharing control strategies for islanding operation of AC microgrids," *IEEE Transactions on Smart Grid*, vol. 7, no. 1, pp. 200–215, Jan. 2016.

[107] M. Hamzeh, H. Karimi, and H. Mokhtari, "Harmonic and negative-sequence current control in an islanded multi-bus MV microgrid," *IEEE Transactions on Smart Grid*, vol. 5, no. 1, pp. 167–176, Jan. 2014.

[108] Q. C. Zhong, "Harmonic droop controller to reduce the voltage harmonics of inverters," *IEEE Transactions on Industrial Electronics*, vol. 60, no. 3, pp. 936–945, Mar. 2013.

[109] T. L. Lee and P. T. Cheng, "Design of a new cooperative harmonic filtering strategy for distributed generation interface converters in an islanding network," *IEEE Transactions on Power Electronics*, vol. 22, no. 5, pp. 1919–1927, Sep. 2007.

[110] J. He, Y. W. Li, and M. S. Munir, "A flexible harmonic control approach through voltage-controlled dg –grid interfacing converters," *IEEE Transactions on Industrial Electronics*, vol. 59, no. 1, pp. 444–455, Jan. 2012.

[111] j. zhou, S. Kim, H. Zhang, Q. Sun, and R. Han, "Consensus-based distributed control for accurate reactive, harmonic and imbalance power sharing in microgrids," *IEEE Transactions on Smart Grid*, vol. PP, no. 99, p. 1, 2016.

[112] Y. Han, P. Shen, X. Zhao, and J. M. Guerrero, "An enhanced power sharing scheme for voltage unbalance and harmonics compensation in an islanded AC microgrid," *IEEE Transactions on Energy Conversion*, vol. 31, no. 3, pp. 1037–1050, Sep. 2016.

[113] F. Guo, C. Wen, J. Mao, and Y. D. Song, "Distributed secondary voltage and frequency restoration control of droop-controlled inverter-based microgrids," *IEEE Transactions on Industrial Electronics*, vol. 62, no. 7, pp. 4355–4364, Jul. 2015.

[114] J. Hu, J. Zhu, D. G. Dorrell, and J. M. Guerrero, "Virtual flux droop method — a new control strategy of inverters in microgrids," *IEEE Transactions on Power Electronics*, vol. 29, no. 9, pp. 4704–4711, Sep. 2014.

[115] A. Kahrobaeian and Y. A. R. I. Mohamed, "Networked-based hybrid distributed power sharing and control for islanded microgrid systems," *IEEE Transactions on Power Electronics*, vol. 30, no. 2, pp. 603–617, Feb. 2015.

[116] C. Ahumada, R. Cárdenas, D. Sáez, and J. M. Guerrero, "Secondary control strategies for frequency restoration in islanded microgrids with consideration of communication delays," *IEEE Transactions on Smart Grid*, vol. 7, no. 3, pp. 1430–1441, May 2016.

[117] R. Majumder, A. Ghosh, G. Ledwich, and F. Zare, "Angle droop versus frequency droop in a voltage source converter based autonomous microgrid," in *Proc. IEEE Power Energy Society General Meeting*, Jul. 2009, pp. 1–8.

[118] J. D. L. Ree, V. Centeno, J. S. Thorp, and A. G. Phadke, "Synchronized phasor measurement applications in power systems," *IEEE Transactions on Smart Grid*, vol. 1, no. 1, pp. 20–27, Jun. 2010.

[119] A. Borghetti, C. A. Nucci, M. Paolone, G. Ciappi, and A. Solari, "Synchronized phasors monitoring during the islanding maneuver of an active distribution network," *IEEE Transactions on Smart Grid*, vol. 2, no. 1, pp. 82–91, Mar. 2011.

[120] V. Salehi, A. Mohamed, A. Mazloomzadeh, and O. A. Mohammed, "Laboratory-based smart power system, part ii: Control, monitoring, and protection," *IEEE Transactions on Smart Grid*, vol. 3, no. 3, pp. 1405–1417, Sep. 2012.

[121] K. G. Nagananda, S. Kishore, and R. S. Blum, "A pmu scheduling scheme for transmission of synchrophasor data in electric power systems," *IEEE Transactions on Smart Grid*, vol. 6, no. 5, pp. 2519–2528, Sep. 2015.

[122] H. Gharavi and B. Hu, "Scalable synchrophasors communication network design and implementation for real-time distributed generation grid," *IEEE Transactions on Smart Grid*, vol. 6, no. 5, pp. 2539–2550, Sep. 2015.

[123] A. Kahrobaeian and Y. A. R. I. Mohamed, "Analysis and mitigation of low-frequency instabilities in autonomous medium-voltage converter-based microgrids with dynamic loads," *IEEE Transactions on Industrial Electronics*, vol. 61, no. 4, pp. 1643–1658, Apr. 2014.

[124] A. H. Etemadi, E. J. Davison, and R. Iravani, "A generalized decentralized robust control of islanded microgrids," *IEEE Transactions on Power Systems*, vol. 29, no. 6, pp. 3102–3113, Nov. 2014.

[125] M. J. Hossain, M. A. Mahmud, F. Milano, S. Bacha, and A. Hably, "Design of robust distributed control for interconnected microgrids," *IEEE Transactions on Smart Grid*, vol. 7, no. 6, pp. 2724–2735, Nov. 2016.

[126] I. P. Nikolakakos, H. H. Zeineldin, M. S. El-Moursi, and N. D. Hatziargyriou, "Stability evaluation of interconnected multi-inverter microgrids through critical clusters," *IEEE Transactions on Power Systems*, vol. 31, no. 4, pp. 3060–3072, Jul. 2016.

[127] E. A. A. Coelho, P. C. Cortizo, and P. F. D. Garcia, "Small-signal stability for parallel-connected inverters in stand-alone AC supply systems," *IEEE Transactions on Industry Applications*, vol. 38, no. 2, pp. 533–542, Mar. 2002.

[128] R. Majumder, "Some aspects of stability in microgrids," *IEEE Transactions on Power Systems*, vol. 28, no. 3, pp. 3243–3252, Aug. 2013.

[129] N. Bottrell, M. Prodanovic, and T. C. Green, "Dynamic stability of a microgrid with an active load," *IEEE Transactions on Power Electronics*, vol. 28, no. 11, pp. 5107–5119, Nov. 2013.

[130] M. Rasheduzzaman, J. A. Mueller, and J. W. Kimball, "An accurate small-signal model of inverter- dominated islanded microgrids using *dq* reference frame," *IEEE Journal of Emerging and Selected Topics in Power Electronics*, vol. 2, no. 4, pp. 1070–1080, Dec. 2014.

[131] M. Kabalan, P. Singh, and D. Niebur, "Large signal Lyapunov-based stability studies in microgrids: A review," *IEEE Transactions on Smart Grid*, vol. PP, no. 99, pp. 1–9, 2016.

[132] A. B. Jusoh, "The instability effect of constant power loads," in *Proc. National Power and Energy Conf. PECon 2004*, Nov. 2004, pp. 175–179.

[133] M. Cespedes, L. Xing, and J. Sun, "Constant-power load system stabilization by passive damping," *IEEE Transactions on Power Electronics*, vol. 26, no. 7, pp. 1832–1836, Jul. 2011.

[134] D. Marx, P. Magne, B. Nahid-Mobarakeh, S. Pierfederici, and B. Davat, "Large signal stability analysis tools in DC power systems with constant power loads and variable power loads —a review," *IEEE Transactions on Power Electronics*, vol. 27, no. 4, pp. 1773–1787, Apr. 2012.

[135] P. Kundur, N. J. Balu, and M. G. Lauby, *Power system stability and control*. McGraw-hill New York, 1994, vol. 7.

[136] U. Topcu and A. Packard, "Linearized analysis versus optimization-based nonlinear analysis for nonlinear systems," in *American Control Conference, 2009. ACC'09.* IEEE, 2009, pp. 790–795.

[137] W. Du, J. Zhang, Y. Zhang, and Z. Qian, "Stability criterion for cascaded system with constant power load," *IEEE Transactions on Power Electronics*, vol. 28, no. 4, pp. 1843–1851, 2013.

[138] A. Griffo and J. Wang, "Large signal stability analysis of'more electric'aircraft power systems with constant power loads," *IEEE Transactions on Aerospace and Electronic Systems*, vol. 48, no. 1, pp. 477–489, 2012.

[139] F. Andrade, K. Kampouropoulos, L. Romeral, J. C. Vasquez, and J. M. Guerrero, "Study of large-signal stability of an inverter-based generator using a lyapunov function," in *Industrial Electronics Society, IECON 2014-40th Annual Conference of the IEEE*. IEEE, 2014, pp. 1840–1846.

[140] F. Umbría, J. Aracil, and F. Gordillo, "Singular perturbation stability analysis of three phase two-level power converters," in *Control & Automation (MED), 2010 18th Mediterranean Conference on*. IEEE, 2010, pp. 123–128.

[141] T. Takagi and M. Sugeno, "Fuzzy identification of systems and its applications to modeling and control," *IEEE transactions on systems, man, and cybernetics*, no. 1, pp. 116–132, 1985.

[142] Y. Blanco, W. Perruquetti, and P. Borne, "Non quadratic stability of nonlinear systems in the takagi-sugeno form," in *Control Conference (ECC), 2001 European*. IEEE, 2001, pp. 3917–3922.

[143] M. Chadli, D. Maquin, and J. Ragot, "An lmi formulation for output feedback stabilization in multiple model approach," in *Decision and Control, 2002, Proceedings of the 41st IEEE Conference on*, vol. 1. IEEE, 2002, pp. 311–316.

[144] S. Boyd, L. El Ghaoui, E. Feron, and V. Balakrishnan, *Linear matrix inequalities in system and control theory*. SIAM, 1994.